

DANIEL TOLD

**GYROKINETIC MICROTURBULENCE IN
TRANSPORT BARRIERS**

GYROKINETIC MICROTURBULENCE IN TRANSPORT BARRIERS

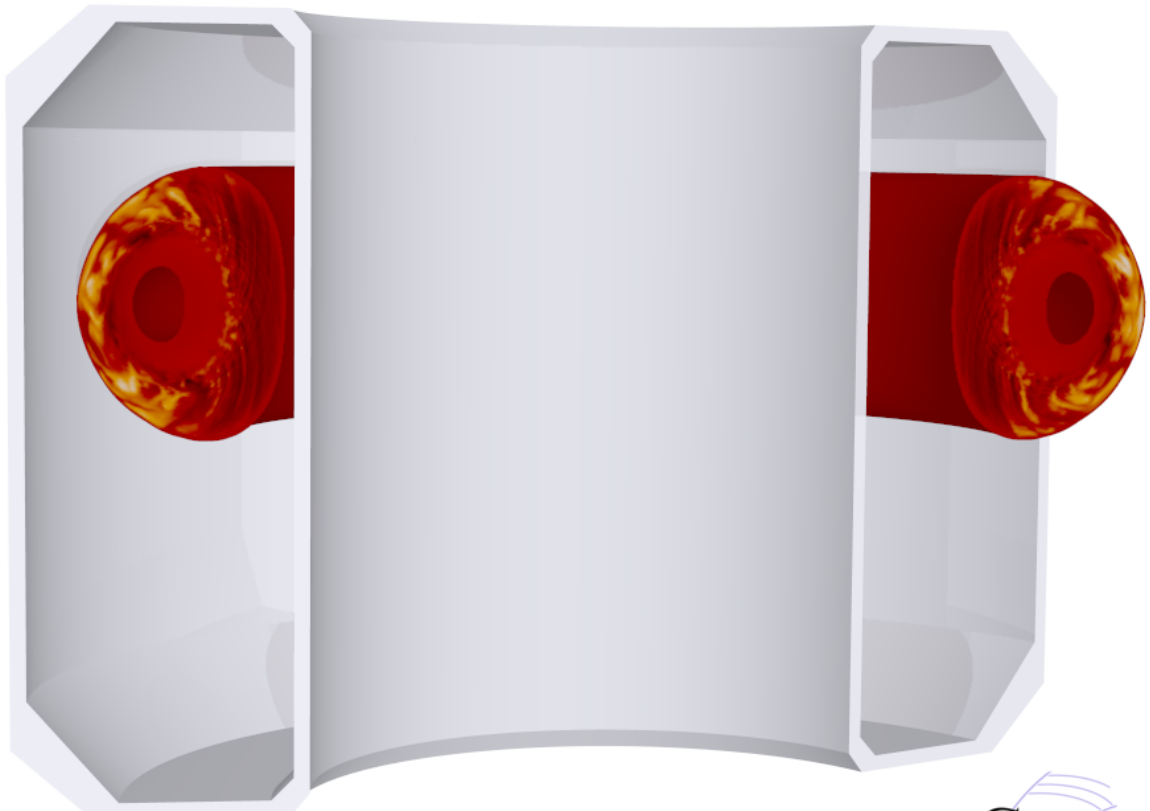
Dissertation zur Erlangung
des Doktorgrades Dr. rer. nat
der Fakultät für Naturwissenschaften
der Universität Ulm

vorgelegt von

Daniel Told

aus Illertissen

2012



gene.rzg.mpg.de



Fluctuations of the electron temperature due to plasma turbulence in an internal transport barrier discharge of the TCV tokamak.

Dekan: Prof. Dr. Axel Groß
Erstgutachter: apl. Prof. Dr. Frank Jenko
Zweitgutachter: Prof. Dr. Peter Reineker
Drittgutachter: Prof. Dr. T. Fülöp
Tag der Promotion: 25. Oktober 2012

ABSTRACT

Modern fusion research aims at making the energy source of the sun accessible for electricity generation on earth. For this purpose, magnetically confined plasmas must be heated to very high temperatures of 100 million Kelvin. The resulting steep pressure gradients lead to turbulent mixing in the plasma, causing a drastic deterioration of particle and energy confinement. Under certain conditions, however, self-organized transport barriers can form in the plasma, which allow for extremely steep density and temperature gradients, and substantially improved confinement. Understanding the physical mechanisms of transport barriers is thus a key step toward increasing the feasibility and competitiveness of fusion power plants.

This work aims to advance the theoretical understanding of transport barriers occurring both in the core and in the edge of the plasma. In order to study such conditions, the effect of strongly varying temperature and density profiles must be considered, as well as the complex shaping of today's tokamak plasmas. The gyrokinetic turbulence code `GENE` has in recent years been extended to include such capabilities, and is in this work for the first time applied to the conditions of both core and edge transport barriers.

As an example of internal transport barriers, discharges of the Swiss tokamak TCV are examined. Experimentally, the steepness of the barrier in these discharges can be controlled by varying the plasma current profile. This in turn leads to changes in the geometry of the magnetic field, which stabilizes the turbulence and results in a steeper barrier. In the present thesis, the global version of `GENE` is used to study turbulence under these conditions with a comprehensive physical model. While for low ion temperature, trapped electron mode (TEM) turbulence is responsible for the heat and particle transport, it is found that for higher ion temperature, small-scale electron temperature gradient driven modes (ETG) can play a key role in determining the steepness of the barrier. The use of a global model in such studies turns out to be crucial, as the transport due to large-scale turbulence is otherwise overestimated by orders of magnitude.

Next, the `GENE` code is used to study plasma edge turbulence in a discharge of the German tokamak ASDEX Upgrade. In the linear regime, the spatial mode structures are strongly affected by the complex geometry of the magnetic field. It turns out that ETG instabilities dominate over a wide range of the wavenumber spectrum, hinting at their possible importance. In nonlinear simulations, it is then confirmed that these instabilities are indeed able to drive a large fraction of the experimental heat transport levels, making them a key candidate for the residual turbulence in the edge transport barrier of high-confinement discharges.

ZUSAMMENFASSUNG

Die moderne Kernfusionsforschung verfolgt das Ziel, die Energiequelle der Sonne zur irdischen Energieerzeugung nutzbar zu machen. Magnetisch eingeschlossene Plasmen müssen zu diesem Zweck auf sehr hohe Temperaturen von mehr als 100 Mio. Kelvin geheizt werden. Daraus resultieren steile Druckgradienten, die im Plasma für eine turbulente Durchmischung sorgen, welche den Einschluss von Wärme und Teilchen drastisch verschlechtert. Unter bestimmten Bedingungen entstehen in den Fusionsplasmen jedoch Transportbarrieren, welche extrem steile Druckgradienten erlauben und den Einschluss deutlich verbessern. Das Verständnis der physikalischen Vorgänge in solchen Barrieren ist daher von großer Bedeutung für die Realisierbarkeit und die Wettbewerbsfähigkeit zukünftiger Fusionskraftwerke.

Die vorliegende Dissertation soll das theoretische Verständnis von Transportbarrieren im Plasmakern und auch im Plasmarand vertiefen. Um Plasmaturbulenz unter solchen Bedingungen zu untersuchen, müssen sowohl die stark variierenden Temperatur- und Dichteprofile, als auch die komplexe Form heutiger Tokamakplasmen in Betracht gezogen werden. Der gyrokinetische Turbulenzcode GENE wurde in den letzten Jahren mit den nötigen Fähigkeiten ausgestattet und wird in dieser Arbeit erstmals auf Kern- und Randtransportbarrieren angewandt.

Zur Untersuchung von internen Transportbarrieren dienen Plasmaentladungen, die am Schweizer Tokamak TCV durchgeführt wurden. Im Experiment kann die Güte dieser Barrieren durch Variation des Plasmastromprofils kontrolliert werden. Dieses beeinflusst die Magnetfeldgeometrie und erlaubt durch Stabilisierung der Turbulenz eine Transportbarriere mit steilerem Druckgradienten. In der vorliegenden Arbeit wird die globale Version von GENE verwendet, um Plasmaturbulenz unter solchen Bedingungen mit einem umfassenden physikalischen Modell zu studieren. Während bei niedriger Ionentemperatur die Turbulenz von Gefangen-Elektronen-Moden (TEM) getrieben wird, steigt bei höherer Ionentemperatur der Anteil kleinskaliger, vom Elektronentemperaturgradienten getriebener Turbulenz (ETG). Die Verwendung eines globalen Modells, welches die radiale Profilvariation berücksichtigt, erweist sich als zwingend, da der Transport durch großskalige Turbulenz anderenfalls um Größenordnungen überschätzt wird.

Schließlich wird GENE zur Untersuchung von Plasmarand-Turbulenz einer Entladung des Garching Tokamaks ASDEX Upgrade verwendet. In linearen Simulationen zeigt sich, dass die räumliche Struktur der Instabilitäten stark durch die komplexe Geometrie des Magnetfelds beeinflusst wird. Über ein breites Wellenzahlspektrum hinweg dominieren hier ETG-Instabilitäten. In nichtlinearen Simulationen wird schließlich gezeigt, dass diese kleinskalige Turbulenzart einen großen Teil des Wärmeflusses treiben kann. Damit ist ETG-Turbulenz ein Hauptkandidat zur Erklärung des residuellen Transports in Plasmarandbarrieren.

CONTENTS

1	INTRODUCTION	1
2	THEORETICAL BACKGROUND	9
2.1	Overview	9
2.2	Gyrokinetic ordering	10
2.3	Gyrokinetic single-particle dynamics	12
2.3.1	Transformation to guiding-center coordinates	12
2.3.2	Transformation to gyrocenter coordinates	15
2.3.3	Gyrocenter equations of motion	19
2.4	Gyrokinetic Vlasov equation	22
2.4.1	Definition of the equilibrium distribution	23
2.4.2	Expansion of vector expressions	24
2.4.3	Collisional gyrokinetic equation	26
2.5	Maxwell's equations	26
2.5.1	Pull-back operator	27
2.5.2	Moments of the gyrocenter distribution	28
2.5.3	Gyrokinetic Poisson equation	30
2.5.4	Gyrokinetic Ampere's law	31
2.5.5	Simplified versions of the field equations	33
2.6	Summary	35
3	NUMERICAL IMPLEMENTATION OF THE GYROKINETIC EQUATIONS	37
3.1	Overview	37
3.2	Gyrokinetic Vlasov equation	37
3.2.1	Field-aligned coordinates	38
3.2.2	Physical boundary conditions	38
3.2.3	Representation of derivatives	41
3.2.4	Discretization of the nonlinearity	43
3.2.5	Phase-shift dealiasing	44
3.3	Gyrophase averaging	47
3.3.1	Implementation of the gyroaveraging operator	47
3.3.2	Consecutive gyroaverages	50
3.4	Normalization	50
3.4.1	Definition of normalization rules	50
3.4.2	Dimensionless equations	52
3.5	Observables	53
3.5.1	Transport quantities	54
3.6	Heat and particle sources	56
3.6.1	Krook-type heat and particle sources	57

3.6.2	Localized heat sources	60
3.7	Sheared equilibrium flows in GENE	61
3.8	Summary	64
4	OPTIMIZED TREATMENTS OF MAGNETIC GEOMETRY	67
4.1	TRACER-EFIT interface	67
4.1.1	Conversion to a radially independent binormal coordinate	68
4.1.2	Local benchmark of the TRACER-EFIT interface	70
4.1.3	Global benchmark of the TRACER-EFIT interface	74
4.2	Geometry treatment in strongly sheared plasma regions	75
4.2.1	Properties of field-aligned coordinate systems	76
4.2.2	Numerical tests of standard and shifted metric	80
4.2.3	Discussion of the numerical results	85
4.2.4	Invariance of physics	89
4.2.5	Implications for turbulence simulations	92
4.2.6	Generalization to global simulations	93
4.3	Treatment of strongly shaped plasmas	93
4.4	Summary	96
5	GLOBAL SIMULATIONS OF INTERNAL TRANSPORT BARRIERS	99
5.1	Overview	99
5.2	Experimental situation and previous findings	101
5.2.1	Electron internal transport barriers in TCV	101
5.2.2	Previous theoretical results	102
5.3	Setup of the simulations	103
5.3.1	Some general remarks	103
5.3.2	Input parameters	106
5.4	Simulation results	108
5.4.1	Linear simulations	108
5.4.2	Turbulence simulations	112
5.5	Sensitivity study of ETG stability	115
5.5.1	Linear simulations at low ion temperature	115
5.5.2	Nonlinear simulations at low ion temperature	116
5.5.3	Pure ETG turbulence simulations	117
5.5.4	Interaction with large-scale turbulence	118
5.5.5	Effect of experimental uncertainty	120
5.6	Comparison to local simulations	123
5.7	Discussion of the simulation results	124
5.8	Summary	127
6	ELECTRON TEMPERATURE GRADIENT DRIVEN TURBULENCE IN THE PLASMA EDGE	129
6.1	Overview	129
6.2	Discharge 20431	130
6.3	Instabilities in the plasma edge	130

6.3.1	Linear simulation results	131
6.3.2	Geometric considerations	131
6.3.3	Brief history of ETG turbulence	136
6.4	Numerical setup and convergence	137
6.4.1	Initializing a nonlinear ETG simulation	137
6.4.2	Optimized parallel coordinate	138
6.4.3	Role of dissipation	140
6.4.4	Numerical convergence criteria	141
6.4.5	Verification against shifted metric simulations	149
6.5	Physical properties of edge ETG turbulence	150
6.5.1	Radial dependence of the electron heat flux	150
6.5.2	Absence of streamers	153
6.5.3	Influence of impurities and temperature ratio	155
6.6	Summary	156
7	CONCLUSIONS	159
7.1	Summary	159
7.2	Outlook	161
A	REMARKS ON CURVILINEAR GEOMETRY	163
A.1	Field-aligned coordinates	164
A.2	Visualizing curvilinear geometry	165
A.3	Definition of wavenumbers	167
B	GENE LAUNCHER TOOL	171
	Bibliography	173

1

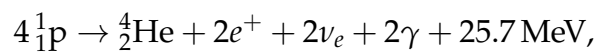
INTRODUCTION

For the past decades, scientists have been striving to make possible the utilization of nuclear fusion as a power source. As the name suggests, the process of nuclear fusion involves the combination of lighter atomic nuclei into heavier ones. For elements lighter than iron, such a reaction often involves an energy release, since the binding energy of its product will be larger than that of the initial nuclei (Fig. 1). On the other hand, nuclear fission works by splitting heavy atoms into lighter ones, which is also accompanied by an energy release due to the peaked shape of the binding energy curve.

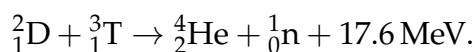
For all such reactions, the energy difference between the initial and final state is roughly a million times larger than that of a typical chemical reaction taking place in the atomic shell. A power plant harnessing fusion reactions for the generation of electricity would therefore require only small amounts of fuel compared to conventional power plants, making such an approach a very promising candidate for a long-term energy supply.

NUCLEAR FUSION

A very well-known fusion reaction is the proton-proton cycle, which is the main source of the continuous energy conversion occurring in the sun. This reaction, which takes place in several stages, can be summarized as



i.e. four protons are combined into a helium nucleus, and two positrons, electron-neutrinos and gamma particles are emitted. The total energy distributed to all products then amounts to 25.7 MeV. Unfortunately, the first stage of this reaction, which involves the fusion of two protons via the weak interaction, has a very low reaction cross-section and thus prevents the exploitation of the proton-proton cycle in a terrestrial fusion power plant. Instead, the most promising fusion reaction begins with the next heavier isotopes of hydrogen and relies on the combination of deuterium and tritium into a helium nucleus,



In this process, a neutron is released, which carries 80 % of the released energy of 17.6 MeV. Deuterium is a naturally abundant isotope of hydrogen and can be

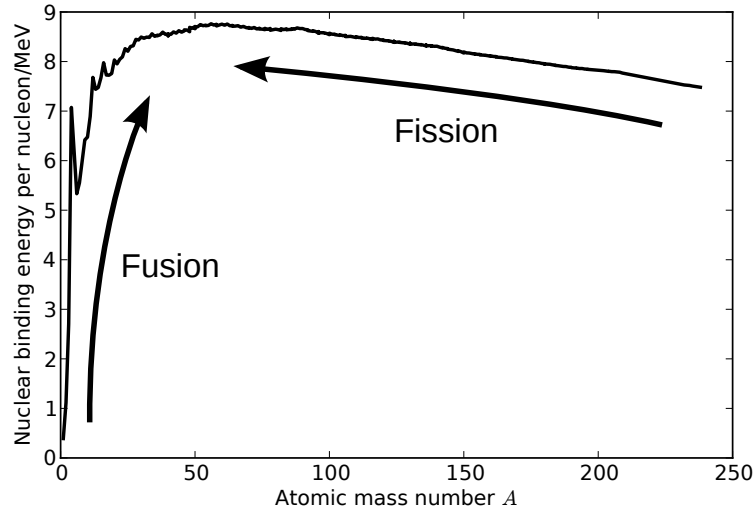


Figure 1: Illustration of energy gain by fusion and fission due to varying nuclear binding energy. The graph depicts the binding energy per nucleon in MeV versus the atomic mass number. Data source: [1]

extracted from ocean water, in which it can be found in the form of D₂O and HDO molecules. Tritium, on the other hand, is radioactive and due to its short half-life of 12.3 years, it does not occur naturally in sufficient amounts and must instead be bred by neutron activation of lithium, its neighbor in the periodic table of elements. This can be achieved by the reaction



By lining the wall blankets of a fusion reactor with lithium¹, the tritium supplies of the power plant can be regenerated within the reactor, so that deuterium and lithium can be regarded as the primary resources required for power generation via nuclear fusion. Both these elements are available in large amounts, although concerns about the competition of lithium requirements with the batteries of electric cars have recently been voiced [2].

BENEFITS

While both fission and fusion power plants virtually eliminate the immense CO₂ emission of fossil fuel combustion, the safety and environmental properties of future fusion power plants are far superior compared to those of today's fission reactors. Unlike the latter, fusion reactors do not rely on a critically balanced chain reaction, eliminating the risk of a run-away reaction as in the Chernobyl accident. The more recent Fukushima accident, on the other hand, was not caused by a lack of control of the chain-reaction, but by the inability to remove the decay heat,

¹ A neutron-multiplying layer of beryllium is also necessary to compensate the loss of neutrons which are absorbed by other wall components.

which is generated by residual nuclear reactions continuing *after* the shutdown of the reactor. This problem is also much less of a concern for a fusion power plant, since the fusion reactions immediately cease after shutdown (or damaging) of the reactor; remaining nuclear reactions in the reactor walls will *not* be able to endanger the reactor structures [3].

Finally, the terminal storage problem does not exist on the same scope as for fission power plants. The waste produced by the latter contains a large variety of radioactive isotopes, some of which have a half-life on the order of 100,000 years. The targeted fusion reactions, on the other hand, do not directly produce radioactive waste, but the fast neutrons will activate the materials of the reactor walls. Unlike in the case of fission, the relevant materials can be *selected* to have good activation properties. Thus, it is foreseen that the majority of the activated components will have a short enough half-life to enable their recycling after less than 100 years of safe storage (see Ref. [3] and references therein). Finding suitable storage areas (e.g. buildings) for such a timescale is, of course, a much simpler task than finding a repository that remains safe for 100,000 years.

FUSION REQUIREMENTS

The principal challenge of achieving nuclear fusion is the requirement that the participating nuclei must overcome their mutual Coulomb repulsion, before the strong nuclear interaction becomes dominant and leads to the fusion of both nuclei. Thus, the latter have to collide with a large kinetic energy, which must in principle be larger than the height of the Coulomb barrier of 415 keV. Fortunately, the required energy is substantially reduced by the quantum tunneling effect, which leads to a finite probability of penetrating the Coulomb wall even if the particles' energy is actually smaller than the barrier energy.

The most promising approach to achieving sufficiently large kinetic energies for a large number of particles is to heat a gas of deuterium and tritium to a very high temperature, so that the particles' random motion becomes fast enough. In a Maxwellian velocity distribution, there always exists a fraction of particles with large velocity, so that fusion reactions will set in at temperatures far below the above mentioned energies. Even with these favorable effects, in order to achieve a practically usable fusion rate, the fuel gas must still be heated to a temperature of 100 – 200 million Kelvin, which corresponds to a thermal energy of roughly 10 – 20 keV. These energies far exceed the electron binding energies in the atomic shell of light elements, so that the fuel gases are fully ionized, i.e. they exist in the *plasma* state.

PLASMA CONFINEMENT

At such extreme temperatures, it is no longer possible to confine the plasma solely with material walls, since no material would withstand the continued exposure to the hot plasma. Instead, use is made of the fact that the plasma consists of

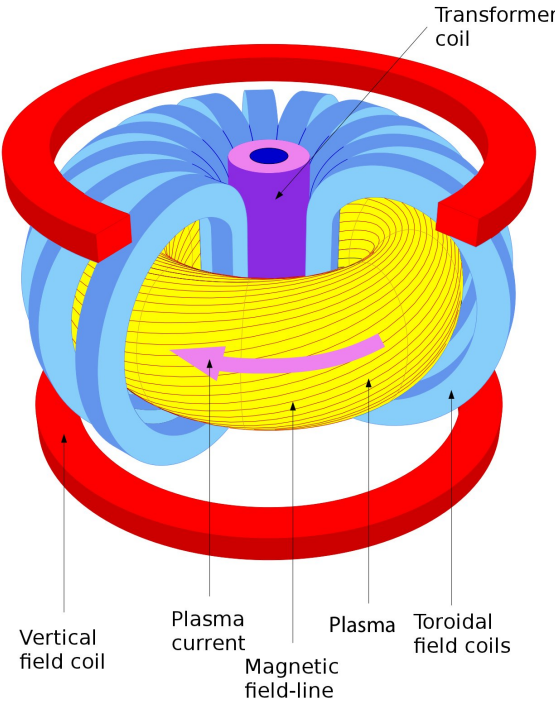


Figure 2: Illustration of the tokamak principle. (Source: IPP, adapted)

charged particles, whose motion can be influenced by magnetic fields. By placing coils around the plasma, a strong magnetic field is imposed, which confines the plasma particles to helical orbits around the field by means of the Lorentz force

$$\mathbf{F}_L = \frac{q}{c} \mathbf{v} \times \mathbf{B}.$$

The Lorentz force, however, acts only in the plane perpendicular to the magnetic field. To contain the particles also *along* the field lines, a straightforward approach would be to close the magnetic field in a ring. Unfortunately, the resulting inhomogeneity of the field leads to particle drifts, which make such a configuration intrinsically unstable.

By twisting the field lines into a helical shape, it is possible to overcome this problem and obtain a macroscopically stable plasma containment. This additional twisting of the field lines can be achieved by driving a current in the plasma, which induces an additional (poloidal) magnetic field, adding to the external (purely toroidal) field. To drive the current, usually the transformer principle is employed by placing the primary coil in the center of the plasma ring, and using the plasma itself as secondary coil. This approach is, following a Russian acronym for 'toroidal chamber with magnetic field coils', called the *tokamak* principle (see Fig. 2).

Another approach, the *stellarator*, generates the helical magnetic field purely by external coils, so that no plasma current is required. This is an intrinsic advantage, since it allows for steady-state operation, while a (standard) tokamak must be operated in a pulsed fashion due to the limitations of the transformer principle.

ple. On the other hand, simple stellarator designs are subject to strong transport losses, and stellarator designs thus have to rely on computer-aided optimization of the coil shapes to overcome this problem. Both the tokamak and the stellarator concepts are being actively researched and developed, with the ultimate goal of producing an efficient and commercially competitive power plant reactor.

By means of magnetic plasma confinement, the walls of the vacuum vessel are no longer in direct contact with the hot plasma and thus have a much increased lifetime. Due to the requirement of low temperature (at most about 1300 K) at the walls, but very high temperature ($\sim 10^8$ K) in the plasma core, the region in between—which in many experiments is only a few ten centimeters wide—must obviously be characterized by a large temperature gradient. While the plasma is macroscopically stable, the gradients of temperature and density drive microinstabilities which lead to turbulent transport of heat, particles and momentum. The timescale on which the heat losses occur is measured by the energy confinement time τ_E , and is given by

$$\tau_E = \frac{E}{P_{\text{ext}}},$$

where E is the energy contained in the plasma, and P_{ext} denotes the amount of external heating required in the steady state. A criterion for the ‘break-even’ condition, at which the produced fusion power balances the required external heating (corresponding to a fusion power gain of $Q = 1$), is given by the triple product $nT\tau_E$ (density \times temperature \times confinement time) exceeding a value of

$$nT\tau_E \gtrsim 10^{21} \frac{\text{s} \cdot \text{keV}}{\text{m}^3}.$$

Due to turbulent transport, the confinement times are much smaller in practice than anticipated in the early days of fusion research, and fusion reactors must in turn be built much larger in size to overcome these additional losses. For this reason, understanding and improving the transport properties of fusion plasmas is crucial to ensuring the feasibility and also the commercial competitiveness of future power plants.

IMPROVED CONFINEMENT REGIMES

Significant progress in improving the plasma confinement was achieved with the discovery of the ‘H-mode’ regime (“high-confinement mode”) [4], which the plasma enters when the external heating power exceeds a given threshold value. In this regime, the energy confinement time τ_E is roughly twice as large as in the low-confinement ‘L-mode’. The improved confinement results from the formation of a transport barrier at the very edge of the plasma (see Fig. 3), which permits extremely steep temperature and density gradients in that region. Naturally, such a region is not easily accessible to either experimental measurement or theoretical description, although significant progress in both areas has been made since the experimental discovery of the H-mode (see Ref. [5] for a review). The generally

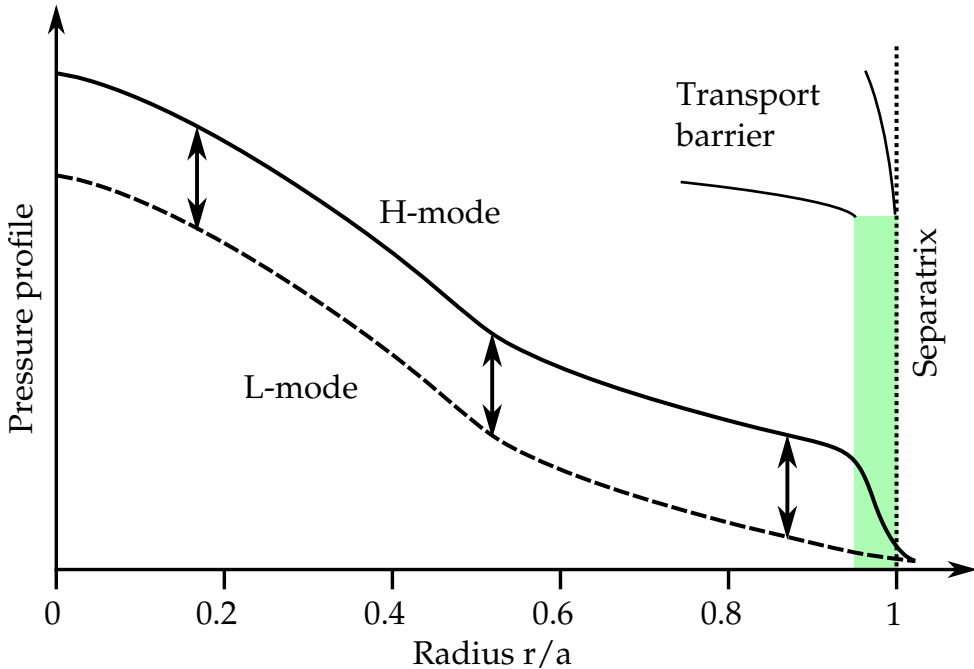


Figure 3: Illustration of the confinement improvement in the H-mode regime.

accepted picture of the H-mode barrier is that fast, sheared plasma flows suppress large-scale turbulence in the barrier region, which in turn leads to substantially reduced heat and particle transport. While many theoretical studies support this picture, a fully self-consistent numerical simulation of an edge transport barrier has not yet been achieved, and many questions concerning the relevant turbulence mechanisms are still open.

In addition to the exploration of the H-mode regime, experiments have in recent years also successfully obtained discharges with *internal* transport barriers, which form—as their name suggests—not in the very edge, but in the core of the plasma. This kind of barrier is usually obtained by a combination of induced plasma rotation and reversed magnetic shear, which act to stabilize the turbulence in the core region of the plasma (see, e.g., Ref. [6] for a review of such barriers).

In both edge and core transport barriers, it is usually observed that the ion heat diffusivity is reduced to very low levels, close to what would be expected in the case of purely collisional diffusion (see Ref. [7] for an extensive review of this topic). Both the particle and the electron heat fluxes, on the other hand, clearly exceed such levels, and are therefore likely to be caused by turbulence. The mechanisms governing these phenomena are the subject of this work.

LINKS TO FUNDAMENTAL RESEARCH

Apart from the obvious application of the present studies to fusion research, many of the phenomena occurring in the context of plasma turbulence are interesting in their own right. In recent decades, interdisciplinary science fields such as systems

theory and complexity theory have gained attention by aiming for a description of phenomena like self-regulation, self-organization, and emergence, which can be observed in many different fields of science ranging from biology, chemistry, and physics to sociology and economics.

Self-organization and emergence are features of complex systems, which in general consist of a large number of individual agents with a given set of properties. Emergence is the appearance of new—often surprising—collective phenomena in such systems, which become possible by the interaction of the individual agents. Basic examples of such systems can be examined using cellular automata, e.g. in Conway’s Game of Life [8], in which agents with a single property (“dead” or “alive”), under a given set of rules, are able to form complex objects and behaviors.

In the present case, the plasma itself can be viewed as a complex system, which consists of many individual particles with given charge and mass. The evolution of these particles is determined by their mutual interaction through self-generated fields, allowing for a host of collective phenomena like waves, instabilities and flows. The plasmas considered here are in a state far from thermodynamic equilibrium, and are exposed to a continuous input and outflow of energy, particles and momentum. Often, self-organization in parts of the plasma can be observed: Turbulence in a plasma can regulate itself—similar to a predator-prey relationship—by the generation of zonal flows, which back-react on the turbulence by breaking up convective cells, thus limiting the transport levels. Transitions to improved confinement states, as studied in this thesis, are also self-organized phenomena, which can be triggered by exceeding a given threshold heating power to the plasma, or by manipulating macroscopic properties like the profile of the plasma current.

SCOPE OF THE PRESENT WORK

The present thesis aims to make a useful contribution to the theoretical understanding of both edge and core transport barriers. To this end, the gyrokinetic turbulence code GENE is extended with several useful features, including the possibility to study the effect of sheared $E \times B$ rotation, a new interface to magnetic geometries reconstructed from actual experiments, a conservative global discretization of the nonlinear terms in the gyrokinetic equations, and an adaptive particle source for gradient-driven global simulations. Furthermore, improvements to the treatment of complex magnetic field geometries are introduced, including a shifted-metric approach for strongly sheared magnetic fields, and a remapping of the parallel coordinate grid to remedy resolution problems occurring in simulations of the plasma edge.

With these improvements, the GENE code is used to study an electron internal transport barrier in comprehensive global simulations, including both kinetic ions and electrons. In all three examined cases, it is found that electron temperature gradient driven (ETG) modes are strongly unstable, indicating their possible importance in determining the electron heat transport, and thus the strength of the

transport barrier. Indeed, nonlinear simulations reveal substantial transport contributions at electron gyroradius scales, indicating that there is no clear separation of the latter from the ion scales. Simulations of both pure ETG turbulence and pure ion-scale turbulence are then used to show that a large fraction of the total heat transport is indeed driven at electron scales, underscoring their importance under these conditions. A sensitivity study proves the robustness of this statement by showing that ETG contributions persist also in presence of impurities, weaker profile gradients, and lower ion temperature.

As another application, the local version of GENE is used to study instabilities and turbulence in a high-confinement ASDEX Upgrade discharge, focusing on the edge region. It is found that ETG turbulence is able to carry a significant fraction of the experimentally expected heat flux, even though commonly expected features like radially elongated streamers are absent. Various positions across the pedestal of the discharge are examined, yielding substantial ETG-driven transport levels from the middle of the pedestal to the pedestal top. This result is shown to be robust also for rather impure edge plasmas. Due to the challenging magnetic background geometry in the plasma edge, various numerical optimizations are employed, and extensive convergence tests are performed to validate the obtained results.

This thesis is structured as follows. In Chapter 2, the theoretical framework of gyrokinetic theory is introduced, and the derivation of the GENE equations is detailed. Chapter 3 describes the numerical implementation of the equations, along with several new features introduced during the course of this thesis. These include changes to the implementation of multiple gyroaverages, a conservative discretization of the nonlinearity in the global version of GENE, as well as additional features allowing the inclusion of sheared perpendicular and parallel equilibrium $E \times B$ flows. In Chapter 4, improvements to the geometry capabilities of GENE are detailed. In particular, the implementation and benchmarking of a new interface to the widely-used EFIT output files, using a GENE-internal field-line tracing module is described. Furthermore, a shifted metric procedure, which facilitates simulations in presence of strongly sheared magnetic fields, is implemented and thoroughly examined, and an optimized treatment of the parallel coordinate is introduced in order to alleviate resolution issues occurring in simulations of the plasma edge. Chapter 5 describes global simulations of an electron internal transport barrier discharge of the TCV tokamak. In Chapter 6, local simulations of an ASDEX Upgrade plasma pedestal are shown. In Chapter 7, finally, conclusions are drawn from the obtained results, and an outlook to future necessary and planned work is given.

2

THEORETICAL BACKGROUND

2.1 OVERVIEW

The present chapter is dedicated to the theoretical framework that will be used throughout this work to describe phenomena of plasma turbulence under conditions found in transport barriers. After a short description of the kinetic equations governing the dynamics of plasmas, in Sec. 2.2 several ordering assumptions about plasma fluctuations are introduced, which determine fundamentally the physics retained in the final equations. In Sec. 2.3, equations of motion, suitable to describe the motion of single particles in strongly magnetized plasmas with fluctuating electromagnetic fields, are derived. Using the results of that section along with the ordering assumptions introduced before, the gyrokinetic Vlasov equation, describing the evolution of a gyrocenter distribution, is constructed in Sec. 2.4. Finally, Maxwell's equations are adapted to the gyrokinetic model in Sec. 2.5, providing a means to calculate the fields generated by the gyrocenter distribution and thereby closing the system of equations.

The magnetically confined plasmas studied for fusion applications are characterized by their very high temperature and low density. They are therefore essentially collision-free², contradicting the usual fluid theory assumption of strong particle collisions. While the latter assumption still proves to be adequate when describing the large-scale behavior of the plasma, for the description of microstability phenomena it is necessary to employ a kinetic description which includes the velocity space dynamics.

Neglecting collisional particle interactions, the equations describing plasma dynamics are given by the Vlasov equation

$$\frac{Df_j}{Dt} = \frac{\partial f_j}{\partial t} + \mathbf{v} \cdot \nabla_x f_j + \frac{\mathbf{F}}{m} \cdot \nabla_v f_j = 0, \quad (2.1)$$

which relates the spatio-temporal evolution of the particle distribution $f_j(\mathbf{x}, \mathbf{v}, t)$ (j denoting the index of the particle species) to a self-consistently generated force-field $\mathbf{F} = q(\mathbf{E} + \mathbf{v} \times \mathbf{B})$, which is in turn given by the Maxwell equations

² See plasma physics textbooks such as Refs. [9, 10, 11].

$$\begin{aligned}
\nabla \times \mathbf{E} &= -\frac{1}{c} \frac{\partial \mathbf{B}}{\partial t} \\
\nabla \times \mathbf{B} &= \frac{4\pi}{c} \sum_j q_j \int v f_j d\mathbf{v} + \frac{1}{c} \frac{\partial \mathbf{E}}{\partial t} \\
\nabla \cdot \mathbf{E} &= 4\pi \sum_j q_j \int f_j d\mathbf{v} \\
\nabla \cdot \mathbf{B} &= 0.
\end{aligned}$$

While it is feasible (but computationally expensive) to solve these kinetic equations numerically, they can be further reduced and adapted to the problem at hand, while keeping the physics of interest intact. The most important reduction in this context is made possible by the strong magnetization of the fusion plasmas studied here, which forces particles into helical gyro-orbits and thereby limits their mobility in the perpendicular plane³. The averaged particle motion in that plane is thus slowed down by orders of magnitude, and the turbulence dynamics of interest becomes much slower than the timescale on which gyration takes place. By exploiting this fact, it is possible to derive an approximate set of equations which describes only low-frequency phenomena in a reduced five-dimensional phase space (three space, two velocity space dimensions). This set of equations, which is known as the gyrokinetic Vlasov-Maxwell system, will form the theoretical background for the studies performed in the present thesis.

In the following sections, the derivation of the gyrokinetic equations will be outlined. Starting from an analysis of single-particle motion, we will construct a set of equations for the gyrocenter distribution function and its self-consistently generated fields. Here, we will follow the Hamiltonian approach detailed in the publications [12] and [13], and further references therein.

2.2 GYROKINETIC ORDERING

During the derivation of the gyrokinetic equation system, assumptions about the magnitude of various quantities will be used. These assumptions are motivated by experimental observations as well as some basic properties of plasmas. For instance, our equations will consider small perturbations of the distribution function about a Maxwellian background, and potential energy perturbations that are small compared to the background temperature, which we will characterize by an expansion parameter denoted by ϵ_δ . The aforementioned orderings are summarized by the estimates

$$\frac{f_1}{F_0} \sim \frac{q\phi_1}{T_e} \sim q \frac{v_{\parallel}}{c} \frac{A_{1\parallel}}{T_e} \sim \frac{B_{1\parallel}}{B} \sim \epsilon_\delta. \quad (2.2)$$

³ From now on, the terms ‘parallel’ and ‘perpendicular’ will always refer to the direction of the background magnetic field.

Here, f_1 denotes the deviation of the distribution function from its stationary background F_0 ; c is the speed of light, q the electric charge, ϕ_1 the perturbed electrostatic potential, v_{\parallel} the velocity along the background magnetic field, $A_{1\parallel}$ the perturbed parallel magnetic potential, T_e the electron temperature, B the background magnetic field and $B_{1\parallel}$ the parallel magnetic field perturbation. The magnetic vector potential is related to the magnetic field by the relation

$$\mathbf{B} = \nabla \times \mathbf{A}.$$

Aside from the orderings regarding the magnitude of perturbations, equilibrium quantities are assumed to vary slowly in space, which can be expressed by stating

$$\begin{aligned}\frac{\rho_i \nabla F_0}{F_0} &\sim \epsilon_F \\ \frac{\rho_i \nabla B}{B} &\sim \epsilon_B.\end{aligned}$$

Moreover, these quantities are taken to be static in time. We will usually assume that⁴ $\epsilon_B \sim \epsilon_F$. Finally, the highly anisotropic particle mobility in the plasma—parallel motion is not affected by the background magnetic field—causes parallel derivatives of fluctuating quantities to be much smaller than perpendicular derivatives, which will be taken into account by the wavenumber ordering

$$\frac{k_{\parallel}}{k_{\perp}} \sim \epsilon_{\parallel}.$$

On the other hand, to allow studies of turbulence at arbitrary spatial scales, its perpendicular fluctuation scale lengths are allowed to be comparable to the gyroradius

$$k_{\perp} \rho_{i/e} \sim 1$$

of the considered particle species. The gyroradius is—for a particle of species j —given by

$$\rho_j = \frac{v_j}{\Omega_j},$$

with the gyrofrequency

$$\Omega_j = \frac{q_j B}{m_j c}.$$

⁴ In fact, in toroidal plasmas, the magnetic field variation is weaker than that of the other profiles roughly by a factor $\epsilon = a/R$, with a and R the minor and major radii, respectively.

Here, m_j is the particle mass, v_j its velocity and q_j its charge. Combining the ordering of the perpendicular wavenumber with that of the potentials ϕ_1 and $A_{1\parallel}$, gives an ordering for the electromagnetic fields

$$\frac{c |E_{1\perp}|}{v_{th} B} \sim \frac{|B_1|}{B} \sim \epsilon_\delta,$$

with the perpendicular electric field perturbation $E_{1\perp} = -\nabla_\perp \phi_1$, the thermal velocity v_{th} , the background magnetic field B , and its perturbation B_1 .

2.3 GYROKINETIC SINGLE-PARTICLE DYNAMICS

As a first step in the derivation of the gyrokinetic equation system, we will examine the gyrokinetic equations of motion for single particles. We start from the Lagrangian

$$L(\mathbf{x}, \dot{\mathbf{x}}, t) = \frac{1}{2} m v^2 - q\phi(\mathbf{x}, t) = \mathbf{p}(v) \cdot \dot{\mathbf{x}} - H(\mathbf{x}, \mathbf{p}(v), t),$$

which can be used to obtain the Euler-Lagrange equations of a particle in the presence of electromagnetic potentials ϕ and \mathbf{A} (see, e.g., Ref. [14]). In this equation, $\mathbf{p}(v) = mv + q\mathbf{A}(\mathbf{x})/c$ is the canonical momentum of the particle. The techniques we are going to employ in this chapter usually use the associated one-form γ instead of the Lagrangian, which is defined via the action integral

$$\int L dt = \int \gamma. \quad (2.3)$$

Inserting the single-particle Hamiltonian $H(\mathbf{x}, \mathbf{p}(v), t) = \frac{1}{2}mv^2 + q\phi(\mathbf{x}, t)$ yields the one-form

$$\gamma = \left(mv + \frac{q}{c} \mathbf{A}(\mathbf{x}) \right) \cdot d\mathbf{x} - \left(\frac{1}{2}mv^2 + q\phi(\mathbf{x}, t) \right) dt. \quad (2.4)$$

This one-form is now subjected to a two-step transformation, the first of which will yield the one-form for guiding center motion in a stationary electromagnetic field. In the second step, field perturbations—which are required for the description of turbulent plasmas—are allowed, and a new set of gyrocenter equations of motion is found, which retains the average effect of the gyromotion without depending explicitly on the gyroangle.

2.3.1 TRANSFORMATION TO GUIDING-CENTER COORDINATES

In a strong magnetic field, it is advantageous to describe the motion of charged particles as a superposition of the motion of its guiding center, and a fast gyration of the particle around the latter. For many investigations, it is sufficient to examine the guiding center motion and disregard the exact dynamics of the fast gyration,

saving many orders of magnitude in both temporal and spatial resolution, and gaining also analytical simplicity.

The instantaneous position of the guiding center can be derived from a particle's trajectory $\mathbf{x}(t)$ by splitting its velocity vector $\mathbf{v} = \dot{\mathbf{x}}(t)$ into parts that are parallel and perpendicular to the background magnetic field, yielding

$$\mathbf{v} = v_{\parallel} \hat{\mathbf{b}} + v_{\perp} \hat{\mathbf{c}}.$$

Here, $\hat{\mathbf{b}}$ is the unit vector parallel to the magnetic field, and $\hat{\mathbf{c}}$ is the unit vector following the perpendicular part of the velocity vector. Since the gyration frequency of a charged particle⁵ with mass m and charge q in a magnetic field is the cyclotron frequency, given by

$$\Omega(\mathbf{x}) = \frac{qB(\mathbf{x})}{mc},$$

we can derive the gyroradius to be

$$\rho(\mathbf{x}, v_{\perp}) = \frac{v_{\perp}}{\Omega(\mathbf{x})}.$$

This allows us to establish the relationship between the gyroradius vector and the perpendicular part of the velocity as

$$\mathbf{v}_{\perp} = v_{\perp} \hat{\mathbf{c}} = \frac{d\rho}{dt}.$$

A very common parametrization of the gyromotion, which forms also the basis of the theory in this work, is achieved by describing the perpendicular gyromotion in polar coordinates. This approach is justified by the assumption that the background magnetic field varies on much larger scale lengths, and that the particle can complete many gyrations before moving significantly in the perpendicular plane. We can then define the gyroradius vector as

$$\boldsymbol{\rho} = \frac{v_{\perp}}{\Omega} \hat{\mathbf{a}}(\theta) = \frac{v_{\perp}}{\Omega} (\cos \theta \hat{\mathbf{e}}_1 - \sin \theta \hat{\mathbf{e}}_2).$$

Here, we have introduced the gyrophase or gyroangle θ and two orthogonal unit vectors $\hat{\mathbf{e}}_1, \hat{\mathbf{e}}_2$ spanning the perpendicular plane. From the above definition, upon using $d\theta/dt = \Omega$ we get

$$\mathbf{v}_{\perp} = v_{\perp} \hat{\mathbf{c}} = -v_{\perp} (\sin \theta \hat{\mathbf{e}}_1 + \cos \theta \hat{\mathbf{e}}_2).$$

Having defined the gyroradius vector, we can give the position of the guiding center as

$$\mathbf{X} = \mathbf{x} - \boldsymbol{\rho} = \mathbf{x} - \rho(\mathbf{x}, v_{\perp}) \hat{\mathbf{a}}(\theta).$$

⁵ Unless they are necessary, we will usually suppress species indices for better readability.

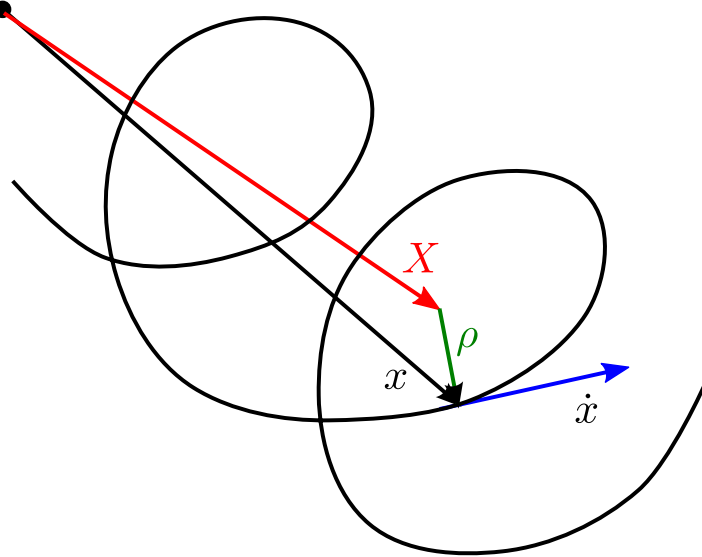


Figure 4: Depiction of a particle trajectory and the vectors describing the particle position, velocity, the guiding-center position and the gyroradius vector (x , \dot{x} , X and ρ respectively).

The relations between the above defined vectors are also indicated in Fig. 4. In many practical applications such as the fusion plasmas considered in this work, the background magnetic field varies on a much slower temporal and spatial scale than the gyromotion. In such situations, the magnetic moment

$$\mu = \frac{mv_{\perp}^2}{2B(X)}$$

is an adiabatic invariant (see classical mechanics textbooks such as Ref. [14]), i.e. an approximate constant of motion. With the above definitions, it is possible to transform the one-form from Eq. 2.4 to guiding-center coordinates $\{X, v_{\parallel}, \mu\}$. Applying this transformation and keeping only terms of first order in $\epsilon_B = \rho/L_B$, one can derive the gyrophase-averaged guiding center one-form (see, e.g. Refs. [15, 16])

$$\Gamma_0 = \left[m\hat{\mathbf{b}}v_{\parallel} + \frac{q}{c}A_0(X) \right] \cdot d\mathbf{X} + \frac{\mu B(X)}{\Omega(X)} d\theta - \left[\frac{1}{2}mv_{\parallel}^2 + \mu B(X) + e\phi_0(X) \right] dt,$$

with the equilibrium electrostatic potential ϕ_0 associated to the plasma rotation. This contribution will be neglected from now on, and rotation will only be considered in the co-moving frame, in which the equilibrium potential vanishes. At this point, it is useful to introduce the abbreviation

$$A_0^* = A_0 + \frac{mc}{q}v_{\parallel}\hat{\mathbf{b}}$$

and the zeroth-order guiding center Hamiltonian

$$H_0(\mathbf{X}, v_{\parallel}, \mu) = \frac{1}{2}mv_{\parallel}^2 + \mu B(\mathbf{X}).$$

Using this notation, we can express the unperturbed guiding-center one-form in a compact way as

$$\Gamma_0 = \frac{q}{c} \mathbf{A}_0^*(\mathbf{X}) \cdot d\mathbf{X} + \frac{\mu B(\mathbf{X})}{\Omega(\mathbf{X})} d\theta - H_0(\mathbf{X}, v_{\parallel}, \mu) dt. \quad (2.5)$$

This one-form describes the motion of charged particles in a slowly-varying electromagnetic field and can be used to derive the associated equations of motion to yield the so-called drift-kinetic Vlasov equation, which is already very useful to investigate effects of particle motion in given background fields.

2.3.2 TRANSFORMATION TO GYROCENTER COORDINATES

In order to describe turbulent transport, it is necessary to extend the guiding-center one-form from the previous section and allow for perturbations in the electromagnetic potentials. We start by extending the previous definitions of the one-forms and the Hamiltonian function by perturbed contributions

$$\begin{aligned} \gamma &= \gamma_0 + \gamma_1 \\ \Gamma &= \Gamma_0 + \Gamma_1 \\ H &= H_0 + H_1, \end{aligned}$$

which are of order $\mathcal{O}(\epsilon_{\delta})$ compared to their background counterparts. The perturbed parts of the one-form and the Hamiltonian are given by

$$\begin{aligned} \gamma_1 &= \frac{q}{c} \mathbf{A}_1(\mathbf{x}, t) \cdot d\mathbf{x} - H_1 dt \\ H_1 &= q\phi_1(\mathbf{x}, t). \end{aligned} \quad (2.6)$$

Here, γ denotes again the one-form in particle phase space, while Γ denotes its guiding-center coordinate counterpart. Taking into account that $\mathbf{x} = \mathbf{X} + \boldsymbol{\rho}(\mathbf{X}, \mu, \theta)$, we can see that the total one-form as well as the Hamiltonian have again acquired a gyrophase dependence, which had been averaged out of the guiding center one-form Γ_0 . Here, however, it is not possible to remove the dependence on the gyroangle by simply taking a gyroaverage, since the potential perturbations vary on the gyroradius scale. Instead, to derive a reduced version of the perturbed one-form, we will use the formalism of Lie perturbation theory (an introduction can be found, e.g., in Ref. [17]) to find a new set of gyrocenter equations of motion, which do not depend on the gyrophase. The Lie-transformed gyrocenter one-form $\bar{\Gamma}_1$ is marked with an overbar to distinguish it from its guiding-center counterpart.

There are various ways to find simplified equations, which differ by the choice of which parts of the gyrocenter one-form should retain perturbed fields. For instance, in the Hamiltonian approach (see, e.g., Ref. [18]) one chooses to set all components of $\bar{\Gamma}_1$ to zero, except for $\bar{\Gamma}_{1t} = -\bar{H}_1$. This approach has the advantage of leaving the equations of motion unchanged compared to the guiding center equations.

Here, however, we employ the so-called symplectic approach (see, e.g., Ref. [19]), which allows the symplectic part of the gyrocenter one-form (i.e. the components multiplied by dX , dv_{\parallel} , $d\mu$ and $d\theta$) to retain gyroangle-independent parts of the perturbed fields. The advantage of this approach compared to the Hamiltonian one is that the parallel momentum coordinate does not acquire a dependence on the perturbed magnetic potential and remains a kinetic momentum. All approaches, however, have in common that all dependences of the perturbed potentials on the gyroangle are at each order moved into a gauge function denoted by S_n , while the resulting equations of motion are independent of the gyroangle.

The actual transformation to the gyrocenter one-form is (up to second order in ϵ) given by

$$\begin{aligned}\bar{\Gamma}_0 &= \Gamma_0 + dS_0 \\ \bar{\Gamma}_1 &= \Gamma_1 - G_1 \cdot \omega_0 + dS_1 \\ \bar{\Gamma}_2 &= -G_2 \cdot \omega_0 - \frac{1}{2}G_1 \cdot (\omega_1 + \bar{\omega}_1) + dS_2,\end{aligned}$$

where the functions G_n are the generating functions of the Lie transformation and ω_n is the nth-order Lagrange-tensor, defined as

$$\omega_{n,\alpha\beta} = \frac{\partial \Gamma_{n,\beta}}{\partial z^\alpha} - \frac{\partial \Gamma_{n,\alpha}}{\partial z^\beta} \quad (2.7)$$

and the derivatives are taken with respect to the phase-space coordinates z^μ accurate to $\mathcal{O}(\epsilon^n)$. The first-order Hamiltonian function, on the other hand, is given by

$$\bar{H}_1 = \langle H_1 - G_1 \cdot dH_0 \rangle, \quad (2.8)$$

where the brackets $\langle \dots \rangle$ denote an average over the gyrophase, which is for an arbitrary quantity Q defined as

$$\langle Q \rangle = \frac{1}{2\pi} \oint Q(X + \rho) d\theta.$$

As a first step in our derivation, we have to transform the first order perturbed one-form to guiding-center coordinates. Expanding Eq. 2.6 to zeroth order in ϵ_B yields

$$\begin{aligned}\Gamma &= \Gamma_0 + \Gamma_1 = \left(\frac{q}{c} \mathbf{A}_0^* + \frac{q}{c} \mathbf{A}_1 \right) \cdot d\mathbf{X} + \frac{q}{c} \left(\mathbf{A}_1 \cdot \frac{\partial \rho}{\partial \mu} \right) d\mu \\ &\quad + \left(\frac{\mu B}{\Omega} + \frac{q}{c} \mathbf{A}_1 \cdot \frac{\partial \rho}{\partial \theta} \right) d\theta - (H_0 + q\phi_1) dt\end{aligned}$$

It is sufficient to carry the calculation of the perturbed one-form to $\mathcal{O}(\epsilon_B^0)$, as the terms contributing to the equations of motion will then be of the same order as the $\mathcal{O}(\epsilon_B)$ corrections from the zeroth-order one-form (assuming that $\epsilon_B \sim \epsilon_\delta$). The derivation proceeds now in a very similar way as in Ref. [20], except that we choose to keep only

$$\bar{\Gamma}_{1X} = \frac{q}{c} \hat{\mathbf{b}} \langle A_{1\parallel} \rangle$$

in the perturbed gyrocenter one-form⁶. The component $\bar{\Gamma}_{1\mu}$ is chosen to be zero, which is a necessary requirement to establish the new gyrocenter magnetic moment as an adiabatic invariant⁷. Another requirement to achieve this property is that the total $\bar{\Gamma}_\theta$ depend only on μ ; we therefore choose $\bar{\Gamma}_{1\theta} = 0$ as well. The component $\Gamma_{1v\parallel}$ vanishes already in the above equation and we accordingly set $\bar{\Gamma}_{1v\parallel} = 0$ in the gyrocenter one-form. The approach of keeping only the $A_{1\parallel}$ component in $\bar{\Gamma}_{1X}$ corresponds to the \parallel -symplectic gyrocenter model ($\alpha = 0, \beta = 1$ in Eq. (157) of Ref. [13]). The generating functions G_1 then have to be chosen as

$$\begin{aligned}G_1^\mu &= \frac{\Omega}{B} \left(\frac{m}{B} \mathbf{A}_1 \cdot \mathbf{v}_\perp + \frac{\partial S_1}{\partial \theta} \right) \\ G_1^{v\parallel} &= \frac{\Omega}{B} \frac{\mathbf{B}_0^*}{B_{0\parallel}^*} \cdot \left(\mathbf{A}_1 - \hat{\mathbf{b}} \langle A_{1\parallel} \rangle + \frac{c}{q} \nabla S_1 \right) \\ G_1^\theta &= -\frac{\Omega}{B} \left(\frac{1}{v_\perp} \mathbf{A}_1 \cdot \hat{\mathbf{a}} + \frac{\partial S_1}{\partial \mu} \right) \\ G_1^X &= -\frac{1}{B_{0\parallel}^*} \left[\hat{\mathbf{b}} \times \left(\mathbf{A}_1 + \frac{c}{q} \nabla S_1 \right) + \frac{\mathbf{B}_0^*}{m} \frac{\partial S_1}{\partial v_\parallel} \right],\end{aligned}$$

where $\mathbf{B}_0^* = \nabla \times \mathbf{A}_0^*$. Note that in comparison to Ref. [20], due to our slightly different choice of $\bar{\Gamma}_{1X}$, the definition of G_1^X contains the full magnetic potential instead of only the fluctuations, and $G_1^{v\parallel}$ contains the full perpendicular potential, but only the fluctuations of the parallel one. Comparing the derivatives of the

⁶ To the order of accuracy of our final equations, this yields the same result as in Ref. [20], where the perpendicular component of \mathbf{A}_1 was also kept, but neglected later on to derive the equations of motion.

⁷ This property simplifies the final equations in the sense that only X and v_\parallel are dynamic variables with a time evolution, while the magnetic moment μ enters as a mere parameter.

gauge function S_1 in magnitude (see Ref. [20]), we retain only $\partial S_1 / \partial \theta$, which then has to be chosen to fulfill

$$\frac{\partial S_1}{\partial \theta} = \frac{1}{\Omega} \left\{ q\tilde{\phi}_1 + \frac{\hat{\mathbf{b}}}{B_{0\parallel}^*} \times \tilde{\mathbf{A}}_1 \cdot \mu \nabla B - \frac{qv_\parallel}{c} \frac{\mathbf{B}_0^*}{B_{0\parallel}^*} \cdot \tilde{\mathbf{A}}_1 - \frac{\Omega}{B} \left(\widetilde{\mathbf{A}_1 \cdot \mathbf{v}_\perp} \right) \right\}. \quad (2.9)$$

In the last equation, we introduced the notation

$$\tilde{Q} = Q - \langle Q \rangle$$

to denote the gyroangle-dependent part of a fluctuating quantity Q . From Eq. 2.8, the perturbed Hamiltonian can be found to be

$$\bar{H}_1 = q \left\langle \phi_1 - \frac{\mathbf{v}_\perp}{c} \cdot \mathbf{A}_{1\perp} \right\rangle.$$

By expanding the magnetic potential \mathbf{A}_1 as

$$\mathbf{A}_1(\mathbf{X} + \boldsymbol{\rho}) = \sum_{n=0}^{\infty} \frac{1}{n!} (\boldsymbol{\rho} \cdot \nabla_\perp)^n \mathbf{A}_1(\mathbf{X}),$$

the term

$$\langle \mathbf{v}_\perp \cdot \mathbf{A}_{1\perp} / c \rangle = \frac{1}{2\pi c} \int \mathbf{v}_\perp \cdot \mathbf{A}_{1\perp} d\theta$$

can be identified [21] as

$$\langle \mathbf{v}_\perp \cdot \mathbf{A}_{1\perp} / c \rangle = -\frac{\mu}{q} I_1(\lambda) B_{1\parallel} = -\frac{\mu}{q} \left\langle B_{1\parallel} \right\rangle.$$

Here, we introduced the abbreviation

$$I_1(\lambda) = \frac{2}{\lambda} J_1(\lambda)$$

in terms of $\lambda^2 = -\rho^2 \nabla_\perp^2$ and the n th order Bessel functions

$$J_n(\lambda) = \sum_{k=0}^{\infty} \frac{(-1)^k}{k! (n+k)!} \left(\frac{\lambda}{2} \right)^{n+2k}.$$

Replacing the gyroaverage accordingly, we can define

$$\bar{H}_1 = q \left\langle \phi_1 + \frac{\mu}{q} B_{1\parallel} \right\rangle \equiv q \langle \psi_1 \rangle,$$

where ψ_1 is the effective potential in the perturbed Hamiltonian. Summing up all relations derived up to now, the full gyrocenter one-form reads

$$\bar{\Gamma} = \left[\frac{q}{c} \mathbf{A}_0^* + \frac{q}{c} \left\langle A_{1\parallel} \right\rangle \hat{\mathbf{b}} \right] \cdot d\mathbf{X} + \frac{\mu B}{\Omega} d\theta - [H_0 + q \langle \psi_1 \rangle] dt. \quad (2.10)$$

Note that the above Taylor expansion in ρ is only valid if all orders are kept, since A_1 varies on the gyroradius scale. As we will see later on, keeping all orders is only possible in a local model, which treats a thin sheet of the plasma and therefore allows for periodic boundary conditions. In the more general global model, only the perpendicular magnetic field fluctuations described by $A_{1\parallel}$ will be kept, so that ψ_1 reduces to ϕ_1 . With this restriction, the latter model is valid in the limit of low plasma β ; i.e. the plasma pressure must be small compared to the magnetic pressure, which is usually well-fulfilled for the systems studied here.

2.3.3 GYROCENTER EQUATIONS OF MOTION

Using the gyrocenter one-form of Eq. 2.10, we can write down its associated equations of motion. One possibility is to use Definition 2.7 and calculate the Euler-Lagrange equations of motion

$$\omega_{\alpha\beta} \frac{\partial z^\beta}{\partial t} = \frac{\partial H}{\partial z^\alpha};$$

alternatively, one can employ the associated Poisson bracket (see Eq. (159) of Ref. [13]). Calculating $\dot{X} = \{X, H\}$ and $\dot{v}_\parallel = \{v_\parallel, H\}$ yields the equations of motion

$$\dot{X} = \frac{c\hat{b}}{qB_\parallel^*} \times \nabla H + \frac{\partial H}{\partial v_\parallel} \frac{\mathbf{B}^*}{mB_\parallel^*} \quad (2.11)$$

$$\dot{v}_\parallel = -\frac{\mathbf{B}^*}{mB_\parallel^*} \cdot \left(\nabla H + \frac{q}{c} \hat{b} \dot{\bar{A}}_{1\parallel} \right). \quad (2.12)$$

Here, we have started to denote gyroaveraged quantities appearing in the equations of motion by an overbar⁸. Using the above equations, we can straightforwardly calculate the collisionless (single-particle) Vlasov equation via

$$\frac{\partial F}{\partial t} + \dot{X} \cdot \nabla F + \dot{v}_\parallel \frac{\partial F}{\partial v_\parallel} = 0.$$

Note that the terms containing $\dot{\mu}$ and $\dot{\theta}$ are absent from the gyrokinetic Vlasov equation, because $\dot{\mu} = 0$ and the gyrocenter distribution does not depend on the gyrophase ($\partial F / \partial \theta = 0$). Before proceeding to write down the Vlasov equation, we will first examine the equations of motion more closely.

⁸ Gyroaverages in the equations of motion are taken about the gyrocenter position X , whereas in the field equations they are taken about the particle position x . The latter gyrophase averages will be denoted by brackets $\langle \dots \rangle$.

Due to the introduction of perturbed fields, the effective magnetic field B^* appearing in the above equations now contains a term due to magnetic fluctuations, and can be written as

$$\begin{aligned} B^* &= B_0^* + \nabla \times (\hat{\mathbf{b}} \bar{A}_{1\parallel}) = \mathbf{B} + \frac{B}{\Omega} v_{\parallel} \nabla \times \hat{\mathbf{b}} + \nabla \times (\hat{\mathbf{b}} \bar{A}_{1\parallel}) \\ &\approx \mathbf{B} + \frac{B}{\Omega} v_{\parallel} \nabla \times \hat{\mathbf{b}} - \hat{\mathbf{b}} \times \nabla \bar{A}_{1\parallel}. \end{aligned}$$

In the last step, a term of order $\epsilon_B \epsilon_{\delta}$ was dropped. Separating the parallel and perpendicular parts of B^* then allows us to write

$$B^* = B_{\parallel}^* \hat{\mathbf{b}} + \frac{B}{\Omega} v_{\parallel} (\nabla \times \hat{\mathbf{b}})_{\perp} - \hat{\mathbf{b}} \times \nabla \bar{A}_{1\parallel}$$

with $B_{\parallel}^* = B_{0\parallel}^*$. The second and third term can be cast in terms of drift speeds due to the curvature and the perpendicular fluctuations of the magnetic field, and we can write

$$B^* = B_{\parallel}^* \hat{\mathbf{b}} + \frac{B}{v_{\parallel}} \mathbf{v}_c + \frac{B}{v_{\parallel}} \mathbf{v}_{A_{1\parallel}}, \quad (2.13)$$

where we have defined the curvature drift velocity

$$\mathbf{v}_c = \frac{v_{\parallel}^2}{\Omega} (\nabla \times \hat{\mathbf{b}})_{\perp}$$

and the drift velocity due to perpendicular magnetic field fluctuations (also known as magnetic flutter)

$$\mathbf{v}_{A_{1\parallel}} = -\frac{1}{m\Omega} \hat{\mathbf{b}} \times \left(\frac{qv_{\parallel}}{c} \nabla \bar{A}_{1\parallel} \right).$$

Note that both of the above $\mathcal{O}(\epsilon)$ corrections arise from the motion of particles along a perturbed or inhomogeneous background field.

Equation for the gyrocenter velocity

Using the explicit form from Eq. 2.13 of B^* , we can express the gyrocenter velocity (Eq. 2.11) as

$$\dot{\mathbf{X}} = v_{\parallel} \hat{\mathbf{b}} + \frac{B}{B_{\parallel}^*} \left[\frac{\hat{\mathbf{b}}}{m\Omega} \times \nabla H + \mathbf{v}_{A_{1\parallel}} + \mathbf{v}_c \right].$$

Taking into account that the Hamiltonian is given by

$$H = H_0 + H_1 = \frac{1}{2} m v_{\parallel}^2 + \mu B + q \bar{\psi}_1$$

and defining the modified potential

$$\bar{\chi}_1 = \bar{\psi}_1 - \frac{v_{\parallel}}{c} \bar{A}_{1\parallel} = \bar{\phi}_1 - \frac{v_{\parallel}}{c} \bar{A}_{1\parallel} + \frac{\mu}{q} \bar{B}_{1\parallel},$$

the grad-B drift velocity

$$\mathbf{v}_{\nabla B} = \frac{\mu}{\Omega m} \hat{\mathbf{b}} \times \nabla B$$

and the generalized $E \times B$ drift speed (which contains also the drifts due to parallel and perpendicular magnetic fluctuations)

$$\mathbf{v}_\chi = \frac{c}{B} \hat{\mathbf{b}} \times \nabla \bar{\chi}_1, \quad (2.14)$$

we can conveniently rewrite the equation for the gyrocenter velocity as

$$\dot{\mathbf{X}} = v_{\parallel} \hat{\mathbf{b}} + \frac{B}{B_{\parallel}^*} (\mathbf{v}_{\nabla B} + \mathbf{v}_\chi + \mathbf{v}_c). \quad (2.15)$$

The terms contained in this equation are slow perpendicular motion of the gyrocenter due to the grad-B drift, the generalized $E \times B$ drift, the curvature drift, and fast motion along the unperturbed magnetic field.

Equation for the gyrocenter acceleration

A more explicit form of Eq. 2.12 for the parallel gyrocenter acceleration is

$$\dot{v}_{\parallel} = -\frac{\mathbf{B}^*}{m B_{\parallel}^*} \cdot (\mu \nabla B + q \nabla \bar{\psi}_1) - \frac{q}{mc} \dot{A}_{1\parallel}.$$

Alternatively, we can write

$$\dot{v}_{\parallel} = -\frac{\dot{\mathbf{X}}}{mv_{\parallel}} \cdot (\mu \nabla B + q \nabla \bar{\psi}_1) - \frac{q}{mc} \dot{A}_{1\parallel}, \quad (2.16)$$

which can be verified by inserting Eq. 2.11 and using $\hat{\mathbf{b}} \cdot \dot{\mathbf{X}} = v_{\parallel}$. Using Eq. 2.15, we arrive at

$$\dot{v}_{\parallel} = - \left(\frac{1}{m} \hat{\mathbf{b}} + \frac{1}{mv_{\parallel}} \frac{B}{B_{\parallel}^*} (\mathbf{v}_{\nabla B} + \mathbf{v}_\chi + \mathbf{v}_c) \right) \cdot (\mu \nabla B + q \nabla \bar{\psi}_1) - \frac{q}{mc} \dot{A}_{1\parallel}.$$

2.4 GYROKINETIC VLASOV EQUATION

Using Eqs. 2.1, 2.15 and 2.16, the gyrokinetic Vlasov equation is obtained as

$$\begin{aligned}\frac{DF}{dt} &= \frac{\partial(F_0 + f_1)}{\partial t} + \dot{X} \cdot \nabla(F_0 + f_1) + \dot{v}_{\parallel} \frac{\partial(F_0 + f_1)}{\partial v_{\parallel}} \\ &= \frac{\partial f_1}{\partial t} + \left\{ \frac{c\hat{b}}{qB_{\parallel}^*} \times \nabla(\mu B + q\bar{\chi}_1) + v_{\parallel} \hat{b} + \frac{B}{B_{\parallel}^*} \mathbf{v}_c \right\} \\ &\quad \cdot \left\{ \nabla(F_0 + f_1) - \left[\frac{1}{mv_{\parallel}} \cdot (\mu \nabla B + q \nabla \bar{\psi}_1) \right] \frac{\partial(F_0 + f_1)}{\partial v_{\parallel}} \right\} \\ &\quad - \frac{q}{mc} \dot{\bar{A}}_{1\parallel} \frac{\partial(F_0 + f_1)}{\partial v_{\parallel}} = 0.\end{aligned}\tag{2.17}$$

In this equation, we introduced the delta- f splitting by setting $F = F_0 + f_1$ with the time-independent equilibrium distribution F_0 and a small perturbation f_1 . Employing the ordering defined in Sec. 2.2 (the orders given here are relative to Ωf_1), we can separate the above equation into terms of zeroth, first and second order in ϵ , where we assume different ϵ_{α} ($\alpha = \delta, F, B, \parallel, \omega$) to be of similar magnitude. To zeroth order, the equation reads

$$v_{\parallel} \hat{b} \cdot \left[\nabla F_0 - \frac{1}{mv_{\parallel}} \mu \nabla B \frac{\partial F_0}{\partial v_{\parallel}} \right] = 0.\tag{2.18}$$

This equation imposes a condition on the equilibrium distribution, which is not explicitly evolved in time; therefore, the equilibrium distribution will be chosen such that it fulfills Eq. 2.18 exactly at all times (see next section). Using this property and adding $\mathcal{O}(\epsilon)$ terms, the equation then reads

$$\begin{aligned}\frac{\partial f_1}{\partial t} &+ \left\{ \frac{c\hat{b}}{qB_{\parallel}^*} \times \nabla(\mu B + q\bar{\chi}_1) + \frac{B}{B_{\parallel}^*} \mathbf{v}_c \right\} \\ &\quad \cdot \left[\nabla(F_0 + f_1) - \frac{1}{mv_{\parallel}} (\mu \nabla B + q \nabla \bar{\psi}_1) \frac{\partial F_0}{\partial v_{\parallel}} \right] \\ &\quad + v_{\parallel} \hat{b} \cdot \left[\nabla f_1 - \frac{1}{mv_{\parallel}} q \nabla \bar{\psi}_1 \frac{\partial F_0}{\partial v_{\parallel}} - \frac{1}{mv_{\parallel}} \mu \nabla B \frac{\partial f_1}{\partial v_{\parallel}} \right] \\ &\quad - \frac{q}{mc} \dot{\bar{A}}_{1\parallel} \frac{\partial F_0}{\partial v_{\parallel}} = 0.\end{aligned}\tag{2.19}$$

The second (and higher) order terms—also known as parallel nonlinearity—will not be taken into account in this work⁹ and turn out to be (on the left hand side of the above equation)

$$\begin{aligned} - \left[\frac{c\hat{\mathbf{b}}}{qB_{\parallel}^*} \times \nabla (\mu B + q\bar{\chi}_1) + \frac{B}{B_{\parallel}^*} \mathbf{v}_c \right] \cdot \left[\frac{1}{mv_{\parallel}} (\mu \nabla B + q \nabla \bar{\psi}_1) \frac{\partial f_1}{\partial v_{\parallel}} \right] \\ + \frac{q}{m} \left(\frac{B}{B_{\parallel}^*} \hat{\mathbf{b}} \cdot \nabla \bar{\psi}_1 - \frac{1}{c} \dot{\mathbf{A}}_{1\parallel} \right) \frac{\partial f_1}{\partial v_{\parallel}}. \end{aligned} \quad (2.20)$$

The equation we will explicitly solve is therefore given by Eq. 2.19.

2.4.1 DEFINITION OF THE EQUILIBRIUM DISTRIBUTION

The equilibrium distribution F_0 is chosen to be a local (i.e. radially dependent) Maxwellian, which is for each species given by

$$F_0(x, v_{\parallel}, \mu) = \frac{n(x)}{\pi^{3/2} v_T^3(x)} \exp \left[-\frac{E(v_{\parallel}, \mu)}{T(x)} \right],$$

where both $n(x)$ and $T(x)$ are allowed to be species dependent and $E(v_{\parallel}, \mu) = mv_{\parallel}^2/2 + \mu B$. With this choice, the derivatives of the equilibrium distribution are

$$\begin{aligned} \partial_x F_0 &= \left[\partial_x \ln n + \partial_x \ln T \left(\frac{E}{T} - \frac{3}{2} \right) - \frac{\mu}{T} \partial_x B \right] F_0 \\ \partial_{y,z} F_0 &= -\mu \partial_{y,z} B \frac{F_0}{T} \\ \partial_{v_{\parallel}} F_0 &= -mv_{\parallel} \frac{F_0}{T} \\ \partial_{\mu} F_0 &= -B \frac{F_0}{T}. \end{aligned}$$

In addition, we define the radial derivative acting only on the density and temperature profiles¹⁰ as

$$\partial_x^{n,T} F_0 = \left[\partial_x \ln n + \partial_x \ln T \left(\frac{E}{T} - \frac{3}{2} \right) \right] F_0.$$

⁹ This is in accordance with previous simulation work [22, 23], which showed that for medium and large devices the parallel nonlinearity does not significantly influence the results.

¹⁰ This definition proves to be useful in deriving the final form of the Vlasov equation, since the term associated to the magnetic field derivative can be combined with other terms to yield the final curvature and grad-B drift terms.

Using this choice for the equilibrium distribution, the zeroth order Vlasov equation (Eq. 2.18) is automatically fulfilled. The Vlasov equation up to first order then turns into

$$\begin{aligned} \frac{\partial f_1}{\partial t} + & \left\{ \frac{c\hat{\mathbf{b}}}{qB_{\parallel}^*} \times \nabla (\mu B + q\bar{\chi}_1) + \frac{B}{B_{\parallel}^*} \mathbf{v}_c \right\} \cdot \left[\nabla (F_0 + f_1) + \nabla (\mu B + q\bar{\psi}_1) \frac{F_0}{T_0} \right] \\ & + v_{\parallel} \hat{\mathbf{b}} \cdot \left[\nabla f_1 + q\nabla\bar{\psi}_1 \frac{F_0}{T_0} - \frac{\mu}{mv_{\parallel}} \nabla B \frac{\partial f_1}{\partial v_{\parallel}} \right] + \frac{qv_{\parallel}}{c} \dot{\bar{A}}_{1\parallel} \frac{F_0}{T_0} = 0 \end{aligned}$$

As can be seen, apart from the time derivative of the distribution function f_1 , there is another time derivative acting on the perturbed magnetic potential $\bar{A}_{1\parallel}$. For numerical solution, however, it is advantageous to unite all time derivatives in one quantity, whose time derivative is then discretized using one of the available numerical schemes. Therefore, we define the modified distribution function

$$g_1 = f_1 - \frac{q}{mc} \frac{\partial F_0}{\partial v_{\parallel}} \bar{A}_{1\parallel} = f_1 + \frac{qv_{\parallel}}{c} \frac{F_0}{T_0} \bar{A}_{1\parallel}.$$

2.4.2 EXPANSION OF VECTOR EXPRESSIONS

For numerical implementation, we choose to rewrite the vector expressions in terms of their components (for an introduction to curvilinear coordinates, see Ref. [24] and also App. A), replacing the parallel gradient and the triple products appearing in the drift terms by

$$\begin{aligned} \nabla_{\parallel} &= \hat{\mathbf{b}} \cdot \nabla = \hat{\mathbf{e}}_z \cdot \mathbf{e}^z \frac{\partial}{\partial z} = \frac{1}{\sqrt{g_{zz}}} \frac{\partial}{\partial z} = \frac{\mathcal{C}}{JB} \frac{\partial}{\partial z} \\ \hat{\mathbf{b}} \times \nabla A \cdot \nabla B &= \hat{\mathbf{b}} \cdot \nabla A \times \nabla B = \hat{\mathbf{b}} \cdot \partial_i A \partial_j B \frac{\epsilon^{ijk}}{J} \mathbf{e}_k \\ &= \frac{g_{kz}}{J\sqrt{g_{zz}}} \partial_i A \partial_j B \epsilon^{ijk}. \end{aligned} \quad (2.21)$$

In these equations, the covariant metric coefficients, defined as $g_{ij} = \hat{\mathbf{e}}_i \cdot \hat{\mathbf{e}}_j$ and the Jacobian determinant, defined as $J = \sqrt{\det(g_{ij})}$ appear as a result of evaluating the vector expressions. The triple product expansion can be further rewritten by using the Clebsch coordinate formulation of the magnetic field

$$\mathbf{B} = \mathcal{C} \nabla x \times \nabla y, \quad (2.22)$$

with a radially dependent constant \mathcal{C} , leading to $B^2 = \mathcal{C}^2 \left(g^{xx} g^{yy} - (g^{xy})^2 \right)$, where $g^{ij} = \mathbf{e}^i \cdot \hat{\mathbf{e}}^j$ are the contravariant metric coefficients. We use the fact that

$$(g_{ij}) = (g^{ij})^{-1}$$

and replace the metric element appearing in Eqs. 2.21 by

$$g_{zz} = J^2 \left(g^{xx} g^{yy} - (g^{xy})^2 \right) = \frac{J^2 B^2}{\mathcal{C}^2}.$$

Therefore

$$\hat{\mathbf{b}} \times \nabla A \cdot \nabla B = \frac{\mathcal{C}}{J^2 B} \sum_{k=1}^3 g_{kz} \partial_i A \partial_j B \epsilon^{ijk}.$$

Depending on what A and B are, often several terms drop out of this expression, since we order parallel wavenumbers of fluctuating quantities to be small in comparison to the perpendicular ones. On the other hand, many of the involved background quantities have non-zero derivatives only in the radial direction, leading to further simplifications.

The curl term appearing in the curvature drift can be expanded by employing Ampère's law and the MHD equilibrium condition $\nabla p = \mathbf{j} \times \mathbf{B}/c$, yielding

$$\begin{aligned} (\nabla \times \hat{\mathbf{b}})_\perp &= \left(\nabla \times \frac{\mathbf{B}}{B} \right)_\perp = \left(\frac{4\pi}{cB} \mathbf{j} + \frac{1}{B} \hat{\mathbf{b}} \times \nabla B \right)_\perp \\ &= -\hat{\mathbf{b}} \times \left[\hat{\mathbf{b}} \times \left(\frac{4\pi}{cB} \mathbf{j} + \frac{1}{B} \hat{\mathbf{b}} \times \nabla B \right) \right] \\ &= \hat{\mathbf{b}} \times \left(\frac{\nabla B}{B} + \frac{\beta}{2} \frac{\nabla p}{p} \right). \end{aligned}$$

After applying the aforementioned expansions, the Vlasov equation in terms of vector components is finally given by

$$\begin{aligned} \frac{\partial g_1}{\partial t} &= +\frac{c}{\mathcal{C}} \frac{B}{B_\parallel^*} \partial_y \bar{\chi}_1 \partial_x^{n,T} F_0 - \frac{c}{\mathcal{C}} \frac{B}{B_\parallel^*} (\partial_x \bar{\chi}_1 \Gamma_y - \partial_y \bar{\chi}_1 \Gamma_x) \\ &\quad + \frac{c}{\mathcal{C}} \frac{B}{B_\parallel^*} \left[\frac{\mu B + mv_\parallel^2}{qB} (K_x \Gamma_x - K_y \Gamma_y) - \frac{mv_\parallel^2}{q} \frac{\beta}{2} \frac{\partial_x p}{p} \Gamma_y \right] \quad (2.23) \\ &\quad - \frac{\mathcal{C}}{JB} v_\parallel \Gamma_z + \frac{\mu}{m} \frac{\mathcal{C}}{JB} \partial_z B \frac{\partial f_1}{\partial v_\parallel} + \frac{c}{\mathcal{C}} \frac{B}{B_\parallel^*} \frac{\mu B + mv_\parallel^2}{qB} K_x \partial_x^{n,T} F_0, \end{aligned}$$

where we have introduced abbreviations for the frequently occurring expressions

$$\begin{aligned} \boldsymbol{\Gamma} &= \nabla f_1 + q \nabla \bar{\psi}_1 \frac{F_0}{T_0} \\ K_x &= \left(\partial_y B - \frac{g_{yz}}{g_{zz}} \partial_z B \right) \\ K_y &= \left(\partial_x B - \frac{g_{xz}}{g_{zz}} \partial_z B \right). \end{aligned}$$

This last version of the Vlasov equation is the one with the closest correspondence to its actual implementation in the GENE code, in which every expression has to be computed in terms of its components. Note that in the derivation of the last version of the Vlasov equation, extensive use has been made of simplifications due to the parallel wavenumber ordering, which implies

$$\hat{\mathbf{b}} \cdot \boldsymbol{\Gamma} \sim \epsilon_{\parallel} |\boldsymbol{\Gamma}_{\perp}|.$$

2.4.3 COLLISIONAL GYROKINETIC EQUATION

The gyrokinetic Vlasov equation derived in the last sections—in conjunction with Maxwell’s equations that will be discussed in Sec. 2.5—describes the interaction of a many-particle system with its collectively generated electromagnetic field, while neglecting the interaction of particles among themselves¹¹. The latter can, at next order, be taken into account by adding a collision operator to the collisionless Vlasov equation $Dg_{1j}/Dt = 0$ (D/Dt representing the total time derivative), such that

$$\frac{Dg_{1j}}{Dt} = C_j(F) = \sum_{j'} C(F_j, F_{j'}).$$

In the present work, a (linearized) Landau-Boltzmann collision operator will be considered, which is of the form

$$C(F_j, F_{j'}) = \nabla_v \cdot (\overleftrightarrow{\mathbf{D}} \cdot \nabla_v - \mathbf{R}) F_j,$$

where $\overleftrightarrow{\mathbf{D}}$ is the diffusion tensor, and \mathbf{R} a vectorial friction coefficient. A complete account of the gyrocenter version of this operator as well as of its numerical implementation in the GENE code can be found in Ref. [25].

2.5 MAXWELL’S EQUATIONS

Solving the gyrokinetic equations of motion requires the evaluation of the electric and magnetic fields that are self-consistently generated. These can be computed from the particle distribution function via Maxwell’s equations

$$-\nabla^2 \phi = 4\pi \rho(\mathbf{x}) = 4\pi \sum_j q_j n_j(\mathbf{x}) \quad (2.24)$$

$$-\nabla^2 \mathbf{A} = \frac{4\pi}{c} \mathbf{j}(\mathbf{x}) = \frac{4\pi}{c} \sum_j q_j n_j(\mathbf{x}) \mathbf{u}_j(\mathbf{x}). \quad (2.25)$$

Note that the moments in the above equations will only be taken of the perturbed distribution function and describe therefore only field perturbations; the equilib-

¹¹ This approximation is actually the lowest-order truncation of the BBGKY hierarchy (see, e.g. [11]), which exploits the fact that interactions among particles are weaker than particle-field interactions.

rium is assumed to be quasineutral and is therefore not explicitly considered in Maxwell's equations. Accordingly, the background current enters only the stationary background field, and Ampère's equation considers only current perturbations. The usual fluid moments like density, average fluid velocity and temperature are defined in terms of the total particle distribution F_j by

$$\begin{aligned} n_j(\mathbf{x}) &= \int F_j(\mathbf{x}, \mathbf{v}) d^3 v \\ \mathbf{u}_j(\mathbf{x}) &= \frac{1}{n_j(\mathbf{x})} \int \mathbf{v} F_j(\mathbf{x}, \mathbf{v}) d^3 v \\ T_j(\mathbf{x}) &= \frac{1}{n_j(\mathbf{x})} \int \frac{m}{2} (\mathbf{v} - \mathbf{u}_j)^2 F_j(\mathbf{x}, \mathbf{v}) d^3 v. \end{aligned}$$

2.5.1 PULL-BACK OPERATOR

Maxwell's equations as defined above are cast in terms of the particle distribution function; we therefore require an explicit transformation to calculate the particle distribution from a given gyrocenter distribution—which is the quantity evolved by the gyrokinetic Vlasov equation. The pull-back operator T^* which achieves this is, to first order in ϵ_δ , given in terms of the generating functions G_1^ν by

$$T^* s = s + \epsilon_\delta G_1^\nu \cdot \frac{\partial s}{\partial Z^\nu} \approx s_0 + \epsilon_\delta s_1 + \epsilon_\delta G_1^\nu \cdot \frac{\partial s_0}{\partial Z^\nu},$$

where the Z^ν are the gyrocenter phase space coordinates and we have employed an expansion of the scalar function $s = s_0 + \epsilon_\delta s_1$ as well as the Einstein summation convention. Letting the operator act on the perturbed gyrocenter distribution f_1 (i.e. we suppress the s_0 term for the moment) yields

$$\begin{aligned} T^* f_1 &= f_1 + G_1^X \cdot \nabla F_0 + G_1^{v_\parallel} \frac{\partial F_0}{\partial v_\parallel} + G_1^\mu \frac{\partial F_0}{\partial \mu} \\ &= f_1 - \frac{\hat{\mathbf{b}} \times \mathbf{A}_1}{B_\parallel^*} \cdot \nabla F_0 + \frac{\Omega}{B} \frac{\mathbf{B}^*}{B_\parallel^*} \cdot \left(\mathbf{A}_1 - \hat{\mathbf{b}} \overline{\mathbf{A}}_{1\parallel} \right) \frac{\partial F_0}{\partial v_\parallel} \\ &\quad + \frac{\Omega}{B} \left(\frac{m}{B} \mathbf{A}_1 \cdot \mathbf{v}_\perp + \frac{\partial S_1}{\partial \theta} \right) \frac{\partial F_0}{\partial \mu} \Big\}. \end{aligned}$$

Here, we again neglected all derivatives of S_1 except for the one with respect to the gyroangle θ , which is of the same order as the other terms in the above equation. Inserting Eq. 2.9, we arrive at

$$\begin{aligned} T^*f_1 &= f_1 - \frac{\hat{\mathbf{b}} \times \mathbf{A}_1}{B_{\parallel}^*} \cdot \nabla F_0 + \frac{\Omega}{B} \frac{\mathbf{B}^*}{B_{\parallel}^*} \cdot \left(\mathbf{A}_{1\perp} - \hat{\mathbf{b}} \bar{\mathbf{A}}_{1\parallel} \right) \frac{\partial F_0}{\partial v_{\parallel}} \\ &\quad + \left(\frac{\Omega}{B^2} \mathbf{A}_1 \cdot \mathbf{v}_{\perp} + \frac{1}{B} \left[q\tilde{\phi}_1 + \frac{\hat{\mathbf{b}}}{B_{\parallel}^*} \times \tilde{\mathbf{A}}_1 \cdot \mu \nabla B \right. \right. \\ &\quad \left. \left. - \frac{qv_{\parallel}}{c} \frac{\mathbf{B}^*}{B_{\parallel}^*} \cdot \tilde{\mathbf{A}}_1 - \frac{\Omega}{B} \left\{ \widetilde{\mathbf{A}_1 \cdot \mathbf{v}_{\perp}} \right\} \right] \right) \frac{\partial F_0}{\partial \mu} \end{aligned}$$

If one chooses F_0 to be a local Maxwellian (see Sec. 2.4.1), the expression reduces to

$$\begin{aligned} T^*f_1 &= f_1 - \frac{\hat{\mathbf{b}} \times \mathbf{A}_1}{B_{\parallel}^*} \cdot \nabla F_0 + \frac{qv_{\parallel}}{c} \frac{\mathbf{B}^*}{B_{\parallel}^*} \cdot \bar{\mathbf{A}}_{1\perp} \frac{F_0}{T_0} \\ &\quad - \left[\frac{\Omega}{B} \bar{\mathbf{A}}_1 \cdot \mathbf{v}_{\perp} + q\tilde{\phi}_1 + \frac{\hat{\mathbf{b}}}{B_{\parallel}^*} \times \tilde{\mathbf{A}}_1 \cdot \mu \nabla B \right] \frac{F_0}{T_0}. \end{aligned} \quad (2.26)$$

Note that when keeping only fluctuations of $A_{1\parallel}$, all terms containing the electromagnetic potential vanish, and one arrives at the expression

$$T^*f_1 = f_1 - q\tilde{\phi}_1 \frac{F_0}{T_0}.$$

Keeping full electromagnetic fluctuations but dropping, on the other hand, all terms of order ϵ_B inside the curled brackets of Eq. 2.26, we are left only with

$$\begin{aligned} T^*f_1 &= f_1 - \left\{ q\tilde{\phi}_1 + \frac{\Omega}{B} \bar{\mathbf{A}}_1 \cdot \mathbf{v}_{\perp} \right\} \frac{F_0}{T_0} \\ &= f_1 - \left\{ q\tilde{\phi}_1 - \mu \bar{B}_{1\parallel} \right\} \frac{F_0}{T_0}. \end{aligned} \quad (2.27)$$

This last expression will be used in the following sections to derive appropriate gyrokinetic versions of Maxwell's equations, which will close the system of equations under consideration. According to the above derivation, this form of the pull-back operator is, to first order in ϵ , valid for both local and global models including electromagnetic fluctuations.

2.5.2 MOMENTS OF THE GYROCENTER DISTRIBUTION

Introducing the delta- f splitting to the above moment equations separates their definitions into a term containing the equilibrium distribution, and another term containing the perturbed distribution. Since the former has a simple analytical

form¹², the moment evaluation is trivial. To calculate the parts containing the gyrocenter distribution f_1 , however, we have to perform the pull-back transformation to guiding center phase space, as well as the transformation from guiding center variables to the standard (x, v) phase space. An arbitrary velocity space moment of the gyrocenter distribution is then expressed as

$$M_{ab}(x) = \frac{1}{m} \int \delta(\mathbf{X} - \mathbf{x} + \boldsymbol{\rho}) T^* f_1 (\mathbf{X}, v_{\parallel}, \mu) B_{\parallel}^* v_{\parallel}^a v_{\perp}^b d^3 X d v_{\parallel} d \mu d \theta,$$

using the pull-back operator T^* in the appropriate limit as introduced in Sec. 2.5.1. With Eq. 2.27, we can write

$$M_{ab}(x) = \frac{1}{m} \int \delta(\mathbf{X} - \mathbf{x} + \boldsymbol{\rho}) \left[f_1 - \left(q\tilde{\phi}_1 - \mu \bar{B}_{1\parallel} \right) \frac{F_0}{T_0} \right] B_{\parallel}^* v_{\parallel}^a v_{\perp}^b d^3 X d v_{\parallel} d \mu d \theta.$$

As has already been discussed, the parallel component of the effective magnetic field can be written as

$$B_{\parallel}^* = B + \frac{mc}{q} v_{\parallel} \hat{\mathbf{b}} \cdot \nabla \times \hat{\mathbf{b}},$$

which allows us to separate the previous expression into two terms

$$\begin{aligned} M_{ab}(x) &= \frac{1}{m} \int \delta(\mathbf{X} - \mathbf{x} + \boldsymbol{\rho}) \left\{ B v_{\parallel}^a \left[f_1 - \left(q\tilde{\phi}_1 - \mu \bar{B}_{1\parallel} \right) \frac{F_0}{T_0} \right] \right. \\ &\quad \left. + \frac{mc}{q} v_{\parallel}^{a+1} \hat{\mathbf{b}} \cdot (\nabla \times \hat{\mathbf{b}}) \left[f_1 - \left(q\tilde{\phi}_1 - \mu \bar{B}_{1\parallel} \right) \frac{F_0}{T_0} \right] \right\} v_{\perp}^b d^3 X d v_{\parallel} d \mu d \theta. \end{aligned} \quad (2.28)$$

For the fluid moments relevant to Maxwell's equations, this yields

$$\begin{aligned} n(x) &= M_{00}(x) = \frac{1}{m} \int \delta(\mathbf{X} - \mathbf{x} + \boldsymbol{\rho}) \left\{ B \left[f_1 - \left(q\tilde{\phi}_1 - \mu \bar{B}_{1\parallel} \right) \frac{F_0}{T_0} \right] \right. \\ &\quad \left. + \frac{mc}{q} v_{\parallel} \hat{\mathbf{b}} \cdot (\nabla \times \hat{\mathbf{b}}) f_1 \right\} d^3 X d v_{\parallel} d \mu d \theta \end{aligned} \quad (2.29)$$

$$\begin{aligned} n(x) u_{\parallel}(x) &= M_{10}(x) = \frac{1}{m} \int \delta(\mathbf{X} - \mathbf{x} + \boldsymbol{\rho}) \left\{ B v_{\parallel} f_1 \right. \\ &\quad \left. + \frac{mc}{q} v_{\parallel}^2 \hat{\mathbf{b}} \cdot (\nabla \times \hat{\mathbf{b}}) \left[f_1 - \left(q\tilde{\phi}_1 - \mu \bar{B}_{1\parallel} \right) \frac{F_0}{T_0} \right] \right\} d^3 X d v_{\parallel} d \mu d \theta \end{aligned} \quad (2.30)$$

$$\begin{aligned} n(x) \mathbf{u}_{\perp}(x) &= M_{01}(x) = \frac{1}{m} \int \delta(\mathbf{X} - \mathbf{x} + \boldsymbol{\rho}) \hat{\mathbf{c}} \left\{ B \left[f_1 - \left(q\tilde{\phi}_1 - \mu \bar{B}_{1\parallel} \right) \frac{F_0}{T_0} \right] \right. \\ &\quad \left. + \frac{mc}{q} v_{\parallel} \hat{\mathbf{b}} \cdot (\nabla \times \hat{\mathbf{b}}) f_1 \right\} \sqrt{\frac{2B}{m}} \sqrt{\mu} d^3 X d v_{\parallel} d \mu d \theta. \end{aligned} \quad (2.31)$$

¹² In addition, we can neglect the difference between particle and gyrocenter position for the equilibrium distribution.

In the last equation, the factor $\sqrt{2B/m}$ arises from the substitution of v_\perp with $\sqrt{\mu}$. Note that in GENE the terms involving $\hat{\mathbf{b}} \cdot \nabla \times \hat{\mathbf{b}}$ (which are of order $\mathcal{O}(\epsilon_B)$ compared to the other terms) are currently not taken into account, which simplifies and partly decouples the field equation system.

2.5.3 GYROKINETIC POISSON EQUATION

Combining Eqs. 2.24 and 2.29 and assuming a quasineutral equilibrium, the gyrokinetic Poisson equation can be written as

$$\begin{aligned}\nabla_\perp^2 \phi &= -4\pi \sum_j \frac{q_j}{m_j} \int \delta(\mathbf{X} - \mathbf{x} + \boldsymbol{\rho}) \\ &\quad \cdot \left\{ B \left[f_{1j} - \left(q_j \tilde{\phi}_{1j} - \mu \bar{B}_{1\parallel j} \right) \frac{F_{0j}}{T_{0j}} \right] \right\} \Big|_{\mathbf{x}} d^3 \mathbf{X} dv_\parallel d\mu d\theta \\ &= -8\pi^2 \sum_j \frac{q_j}{m_j} \int \left[\left\langle \{Bf_{1j}\} \Big|_{\mathbf{x}-\boldsymbol{\rho}} \right\rangle - q_j \phi_1 \left\langle \left\{ B \frac{F_{0j}}{T_{0j}} \right\} \Big|_{\mathbf{x}-\boldsymbol{\rho}} \right\rangle \right. \\ &\quad \left. + \left\langle \left\{ \left[q_j \bar{\phi}_{1j} + \mu \bar{B}_{1\parallel j} \right] B \frac{F_{0j}}{T_{0j}} \right\} \Big|_{\mathbf{x}-\boldsymbol{\rho}} \right\rangle \right] dv_\parallel d\mu.\end{aligned}$$

Here, we have applied the parallel wavenumber ordering to the Laplacian operator and introduced the species label j . Note that in these equations, we have employed the notation $\{\cdots\}|_{\mathbf{x}-\boldsymbol{\rho}}$, which implies that all spatially dependent quantities contained in the curled brackets are to be evaluated at position $\mathbf{x} - \boldsymbol{\rho}$. In addition, in the last line the integral over $d\theta$ has been replaced by gyroaverage brackets $\langle \cdots \rangle$. Note that $\tilde{\phi}_{1j}(\mathbf{x} - \boldsymbol{\rho}) = \phi_1(\mathbf{x}) - \bar{\phi}_{1j}(\mathbf{x} - \boldsymbol{\rho})$; therefore the term with $\phi_1(\mathbf{x})$ is not affected by the gyroaverage. This form of the Poisson equation shows that consecutive gyroaverages have to be taken of the electrostatic potential and of the parallel magnetic field perturbation in order to solve this equation. Furthermore, the equilibrium quantities F_0 , T_0 and B are kept within the gyroaverages here in order to preserve the symmetry property of the field equation also in its global version. Rearranging the above equation such that all terms involving ϕ_1 are on the left hand side, we can write the gyrokinetic Poisson equation as

$$\begin{aligned}\nabla_\perp^2 \phi_1 - 8\pi^2 \sum_j \frac{q_j^2}{m_j} \int \left[\phi_1 B \frac{F_{0j}}{T_{0j}} - \left\langle \left\{ B \bar{\phi}_{1j} \frac{F_{0j}}{T_{0j}} \right\} \Big|_{\mathbf{x}-\boldsymbol{\rho}} \right\rangle \right] dv_\parallel d\mu \\ = -8\pi^2 \sum_j \frac{q_j}{m_j} \int \left[\left\langle \{Bg_{1j}\} \Big|_{\mathbf{x}-\boldsymbol{\rho}} \right\rangle + \left\langle \left\{ \mu B \bar{B}_{1\parallel j} \frac{F_{0j}}{T_{0j}} \right\} \Big|_{\mathbf{x}-\boldsymbol{\rho}} \right\rangle \right] dv_\parallel d\mu.\end{aligned}\tag{2.32}$$

Note that we replaced the distribution f_{1j} with g_{1j} , since the latter is the quantity evolved by the gyrokinetic Vlasov equation. This substitution does not alter the

above Poisson equation due to the symmetry of the equilibrium distribution F_0 with respect to v_{\parallel} . In some of the above terms, it is possible to evaluate the velocity space integration analytically. In particular,

$$\int_0^\infty \int_{-\infty}^\infty F_{0j} dv_{\parallel} d\mu = \frac{n_{0j} m_j}{2\pi T_{0j}} \int_0^\infty e^{-\mu B/T_{0j}} d\mu = \frac{n_{0j} m_j}{2\pi B}.$$

For the numerical solution of the Poisson equation, its left hand side can be regarded as an operator $\mathcal{P}[\phi_1]$, whose inverse is then applied to the right hand side of Eq. 2.32 to yield the electrostatic potential. One complication arises due to the fact that the parallel magnetic perturbation $B_{1\parallel}$ must be solved for as well; when the latter is kept, the above scheme must be extended to solve the coupled system of equations for $\{\phi_1, B_{1\parallel}\}$.

2.5.4 GYROKINETIC AMPERE'S LAW

Employing the pullback operator and fluid moments introduced in the last sections, the parallel component of Ampere's law can be written as

$$\begin{aligned} \nabla_{\perp}^2 A_{1\parallel} &= -\frac{4\pi}{c} \sum_j \frac{q_j}{m_j} \int \delta(\mathbf{X} - \mathbf{x} + \boldsymbol{\rho}) v_{\parallel} \langle \{Bf_{1j}\} |_{x-\rho} \rangle d^3X dv_{\parallel} d\mu d\theta \\ &= -\frac{8\pi^2}{c} \sum_j \frac{q_j}{m_j} \int v_{\parallel} \langle \{Bf_{1j}\} |_{x-\rho} \rangle dv_{\parallel} d\mu. \end{aligned}$$

Note that no current contribution from the equilibrium is taken into account, since only the perturbed magnetic field is evolved and the equilibrium current is assumed to be stationary and taken care of in the background magnetic field. As in the Poisson equation, we replace the distribution f_{1j} with its counterpart g_{1j} , which results in an additional term leading to

$$\nabla_{\perp}^2 A_{1\parallel} = -\frac{8\pi^2}{c} \sum_j \frac{q_j}{m_j} \int v_{\parallel} \left\langle \left\{ Bg_{1j} - \frac{q_j v_{\parallel}}{c} \frac{F_{0j}}{T_{0j}} B \bar{A}_{1\parallel j} \right\} \Big|_{x-\rho} \right\rangle dv_{\parallel} d\mu.$$

Rearranging again the equation so that all terms containing $A_{1\parallel}$ are on the left hand side, we arrive at

$$\begin{aligned} \nabla_{\perp}^2 A_{1\parallel} - \frac{8\pi^2}{c^2} \sum_j \frac{q_j^2}{m_j} \int v_{\parallel}^2 \left\langle \left\{ \frac{F_{0j}}{T_{0j}} B \bar{A}_{1\parallel j} \right\} \Big|_{x-\rho} \right\rangle dv_{\parallel} d\mu &= \\ -\frac{8\pi^2}{c} \sum_j \frac{q_j}{m_j} \int v_{\parallel} \langle \{Bg_{1j}\} |_{x-\rho} \rangle dv_{\parallel} d\mu. & \end{aligned} \quad (2.33)$$

Similarly as for the Poisson equation, the left hand side operator $\mathcal{A}[A_{1\parallel}]$ can be numerically inverted to solve for the parallel magnetic potential. In all cases considered here, this equation remains decoupled from the others.

Finally, we will also evaluate the perpendicular part of Ampère's law in terms of the magnetic field $B_{1\parallel}$. We write

$$(\nabla \times B_1)_\perp = \frac{4\pi}{c} j_\perp$$

and evaluate the curl expression to

$$\partial_y B_{1\parallel} \hat{e}_1 - \partial_x B_{1\parallel} \hat{e}_2.$$

Introducing the perpendicular current from Eq. 2.31, we arrive at

$$\begin{aligned} \begin{pmatrix} \partial_y B_{1\parallel} \\ -\partial_x B_{1\parallel} \end{pmatrix} &= \frac{2\pi}{c} \sum_j q_j \left(\frac{2}{m_j} \right)^{\frac{3}{2}} \int \delta(\mathbf{X} - \mathbf{x} + \boldsymbol{\rho}) \left\{ \hat{c} B^{3/2} \left[f_{1j} \right. \right. \\ &\quad \left. \left. - \left(q_j \tilde{\phi}_{1j} - \mu \bar{B}_{1\parallel j} \right) \frac{F_{0j}}{T_{0j}} \right] \right\} \Big|_{\mathbf{X}} \sqrt{\mu} d^3 X d\mathbf{v}_\parallel d\mu d\theta \\ &= \frac{4\pi^2}{c} \sum_j q_j \left(\frac{2}{m_j} \right)^{\frac{3}{2}} \\ &\quad \cdot \int \left\langle \left\{ \hat{c} B^{3/2} \left[f_{1j} - \left(q_j \tilde{\phi}_{1j} - \mu \bar{B}_{1\parallel j} \right) \frac{F_{0j}}{T_{0j}} \right] \right\} \Big|_{\mathbf{x}-\boldsymbol{\rho}} \right\rangle \sqrt{\mu} d\mathbf{v}_\parallel d\mu, \end{aligned}$$

where

$$\hat{c} = \frac{\partial \hat{\mathbf{a}}}{\partial \theta} = -\sin \theta \hat{e}_1 - \cos \theta \hat{e}_2.$$

Again, we rearrange the equation such that all terms involving $B_{1\parallel}$ appear on the left hand side, yielding

$$\begin{aligned} \begin{pmatrix} \partial_y B_{1\parallel} \\ -\partial_x B_{1\parallel} \end{pmatrix} - \frac{4\pi^2}{c} \sum_j q_j \left(\frac{2}{m_j} \right)^{\frac{3}{2}} \int \left\langle \left\{ \hat{c} B^{3/2} \bar{B}_{1\parallel j} \frac{F_{0j}}{T_{0j}} \right\} \Big|_{\mathbf{x}-\boldsymbol{\rho}} \right\rangle \mu^{\frac{3}{2}} d\mathbf{v}_\parallel d\mu \\ = \frac{4\pi^2}{c} \sum_j q_j \left(\frac{2}{m_j} \right)^{\frac{3}{2}} \int \left\langle \left\{ \hat{c} B^{3/2} \left[f_{1j} - q_j \tilde{\phi}_{1j} \frac{F_{0j}}{T_{0j}} \right] \right\} \Big|_{\mathbf{x}-\boldsymbol{\rho}} \right\rangle \sqrt{\mu} d\mathbf{v}_\parallel d\mu. \end{aligned} \tag{2.34}$$

The numerical solution of the coupled $\{\phi_1, B_{1\parallel}\}$ system of equations is described in Ref. [25].

2.5.5 SIMPLIFIED VERSIONS OF THE FIELD EQUATIONS

Depending on the problem studied, considerable simplifications can be applied to the field equations.

Local version

In a local flux-tube model, all equilibrium quantities can be taken out of the gyroaverages, leading to simplified versions of Maxwell's equations. Poisson's equation is then given by

$$\begin{aligned} \nabla_{\perp}^2 \phi_1 - 8\pi^2 \sum_j \frac{q_j^2}{m_j T_{0j}} B \int F_{0j} (\phi_1 - \langle \bar{\phi}_{1j} \rangle) dv_{\parallel} d\mu \\ = -8\pi^2 \sum_j \frac{q_j}{m_j} B \int \left[\langle g_{1j} \rangle + \mu \frac{F_{0j}}{T_{0j}} \langle \bar{B}_{1\parallel j} \rangle \right] dv_{\parallel} d\mu, \end{aligned}$$

the parallel component of Ampere's equation can be written as

$$\begin{aligned} \nabla_{\perp}^2 A_{1\parallel} - \frac{8\pi^2}{c^2} \sum_j \frac{q_j^2}{m_j T_{0j}} B \int v_{\parallel}^2 F_{0j} \langle \bar{A}_{1\parallel j} \rangle dv_{\parallel} d\mu \\ = -\frac{8\pi^2}{c} \sum_j \frac{q_j}{m_j} B \int v_{\parallel} \langle g_{1j} \rangle dv_{\parallel} d\mu, \end{aligned}$$

and its perpendicular component is given by

$$\begin{pmatrix} \partial_y B_{1\parallel} \\ -\partial_x B_{1\parallel} \end{pmatrix} = \frac{4\pi^2}{c} \sum_j q_j \left(\frac{2B}{m_j} \right)^{\frac{3}{2}} \int \left[\left\langle \hat{c} \left(f_{1j} - q_j \tilde{\phi}_{1j} \frac{F_{0j}}{T_{0j}} + \mu \bar{B}_{1\parallel j} \frac{F_{0j}}{T_{0j}} \right) \right\rangle \right] \sqrt{\mu} dv_{\parallel} d\mu.$$

Moreover, the gyrophase averages denoted by $\langle \dots \rangle$ and $\overline{\dots}$ are identical in this limit and can be represented by simple multiplications with Bessel functions (see Refs. [25, 26]).

Adiabatic electrons

In this limit, the electrons are taken to be massless and therefore infinitely fast along the magnetic field, and at all times there is a perfect balance between the parallel electric field and the parallel pressure gradient¹³. The electron density perturbation is then at each instant given by a modified Boltzmann response

$$\frac{n_{1e}}{n_{0e}} = \frac{e}{T_{0e}} (\phi_1 - \langle \phi_1 \rangle_{FS}),$$

¹³ This behavior is similar to that of a driven oscillator, where the oscillator is exactly in phase with the driver if the driving frequency is very slow compared to the oscillator's resonant frequency.

so that Eq. 2.32 becomes

$$\begin{aligned} & - \sum_{j \setminus e} \frac{m_e}{m_j} q_j^2 \int \left[\phi_1 \left\langle \left\{ B \frac{F_{0j}}{T_{0j}} \right\} \Big|_{x-\rho} \right\rangle - \left\langle \left\{ B \bar{\phi}_{1j} \frac{F_{0j}}{T_{0j}} \right\} \Big|_{x-\rho} \right\rangle \right] dv_{\parallel} d\mu \\ & = Be^2 \frac{n_{0e}}{T_{0e}} (\phi_1 - \langle \phi_1 \rangle_{FS}) - \sum_{j \setminus e} \frac{m_e}{m_j} q_j \int \left\langle \left\{ B g_{1j} \right\} \Big|_{x-\rho} \right\rangle dv_{\parallel} d\mu \end{aligned}$$

or

$$\begin{aligned} & - \sum_{j \setminus e} \frac{m_e}{m_j} q_j^2 \int \frac{F_{0j}}{T_{0j}} (\phi_1 - \langle \bar{\phi}_{1j} \rangle) dv_{\parallel} d\mu \\ & = e^2 \frac{n_{0e}}{T_{0e}} (\phi_1 - \langle \phi_1 \rangle_{FS}) - \sum_{j \setminus e} \frac{m_e}{m_j} q_j \int \langle g_{1j} \rangle dv_{\parallel} d\mu \end{aligned}$$

in the local model. The Ampère equation for the electromagnetic field is not solved in the adiabatic electron approximation, since the ion contribution to $A_{1\parallel}$ is smaller than that of the electrons by a factor m_e/m_i and a Maxwellian velocity space structure is assumed for the electron distribution, excluding any currents.

Adiabatic ions

A similar simplification, but taking the *ion* response to be adiabatic, is possible in the limit of large wavenumbers¹⁴. In this limit, all ion gyroaverages evaluate to zero, yielding the ion density perturbation

$$\frac{n_{1i}}{n_{0i}} = -\frac{q_i \phi_1}{T_{0i}}$$

for each ion species. With this approximation, the Poisson equation takes the form

$$\begin{aligned} & \nabla_{\perp}^2 \phi_1 - 4\pi \frac{n_{0e}}{T_{0e}} (1 + \tau) \phi_1 + \frac{8\pi^2}{m_e} \int \left[\left\langle \left\{ B \bar{\phi}_1 \frac{F_{0e}}{T_{0e}} \right\} \Big|_{x-\rho} \right\rangle \right] dv_{\parallel} d\mu \\ & = \frac{8\pi^2}{m_e} e \int \left[\left\langle \left\{ B g_{1e} \right\} \Big|_{x-\rho} \right\rangle + \left\langle \left\{ \mu B \bar{B}_{1\parallel e} \frac{F_{0e}}{T_{0e}} \right\} \Big|_{x-\rho} \right\rangle \right] dv_{\parallel} d\mu. \quad (2.35) \end{aligned}$$

Here, the parameter $\tau = Z_{\text{eff}} T_e / T_i$ appears, which represents the effect of multiple adiabatic ion species with equal temperatures and the effective charge number $Z_{\text{eff}} = \sum_j q_j^2 n_{0j} / n_{0e}$. Note that for adiabatic ions—in contrast to the adiabatic electron limit—the adiabaticity constraint is also valid for the zonal flow mode, which constitutes an important difference in the nonlinear saturation mechanism between ITG and ETG instabilities [27]. In this limit, both the parallel and perpen-

¹⁴ In the driven oscillator picture, this time the driver (the electromagnetic fields) is much faster than the characteristic frequency of the oscillator (the ion response), leading to an opposite phase relation.

dicular Ampère's law are simply given by Eqs. 2.33 and 2.34, with the species sum including only the electron species.

2.6 SUMMARY

In this chapter, the gyrokinetic system of equations has been derived, which will form the basis for the numerical investigations performed in this work. The equations are accurate to first order in the generic ordering parameter ϵ and are suitable for studies of electromagnetic fluctuations in fusion plasmas with arbitrary geometry, taking into account the radial variation of temperature and density profiles. Simplified equations for studies in the limit of heavy ions or massless electrons were given, as well as equations valid in the local limit, when the background profiles vary only weakly in the considered plasma region. The following chapter will detail the numerical implementation of the equations in the gyrokinetic turbulence code GENE.

3

NUMERICAL IMPLEMENTATION OF THE GYROKINETIC EQUATIONS

3.1 OVERVIEW

As has been discussed in the last chapter, the gyrokinetic turbulence problem can, for realistic scenarios, only be solved by numerical methods. A widely used code, developed at IPP since 1999, which implements the gyrokinetic equations is `GENE` [25, 27, 28, 29]; the present chapter will give a detailed explanation of the numerical methods employed in this code. In Sec. 3.2, the discretization schemes used to represent the gyrokinetic Vlasov equation will be elucidated, paying particular attention to the applied boundary conditions, and detailing also a newly implemented numerical representation for the nonlinear term. Sec. 3.3 is dedicated to a discussion of the gyroaveraging operations occurring in the global version of the `GENE` code. As it turns out, the linearized gyroaveraging operator is not Hermitian, and therefore the gyrophase averages appearing in the field equations and the equations of motion have to be represented by different, but mutually adjoint operators. Sec. 3.4 is concerned with deriving the dimensionless forms of the gyrokinetic equations, which are actually implemented in `GENE`. Furthermore, Sec. 3.5 details the measurement of transport quantities in simulations, and in Sec. 3.6, heat and particle sources for a controlled background profile evolution in global simulations are introduced. Sec. 3.7, finally, elaborates on the implementation of equilibrium flow shear in `GENE`, taking into account both its perpendicular and parallel components.

3.2 GYROKINETIC VLASOV EQUATION

At the most basic level, `GENE` uses the method-of-lines approach, meaning that spatial and temporal derivatives are discretized independently. Much attention has always been paid to selecting discretizations which are computationally efficient and which can be easily scaled to very large numbers of processors in the range of 100,000 and more. Thus, well-established schemes like finite difference, finite volume, finite element and spectral approaches are employed for the spatial discretization, whereas a Runge-Kutta scheme is used to compute temporal derivatives. Using these schemes, the `GENE` code has been shown to scale efficiently up to tens of thousands of processors, and more [30, 31].

3.2.1 FIELD-ALIGNED COORDINATES

The dynamics in gyrokinetic theory takes place in a five-dimensional phase-space consisting of three spatial and two velocity-space dimensions. The boundary condition for each of these coordinates is a very important property of the numerical implementation, which determines the choice of discretization.

In GENE, the spatial dynamics are treated in a coordinate system which is aligned to the background magnetic field, taking advantage of the highly anisotropic particle mobility in a strongly magnetized plasma. This approach saves several orders of magnitude in terms of computing resources as compared to using a mesh which disregards the magnetic field structure. The spatial coordinates are labeled x , y , and z , which represent the radial, the binormal and the parallel direction, respectively. They are usually defined as

$$\begin{aligned} x &= \rho \\ y &= C_y [q(\rho) \theta - \zeta] \\ z &= \theta. \end{aligned} \tag{3.1}$$

Here, ρ is a flux surface label, θ is the straight field line angle, ζ is the toroidal angle and q is the safety factor, which is a flux function. C_y is defined to be a constant length factor, given by

$$C_y = \frac{\rho_0}{q_0},$$

where the subscript '0' indicates that the respective quantity is to be taken at the $x_0 = \rho_0$ position (usually the box center), which is used as the reference position in GENE.

3.2.2 PHYSICAL BOUNDARY CONDITIONS

Radial direction

In GENE, two different approaches are available to treat the radial direction and its boundary conditions. In the classical *flux-tube* approach [32], one assumes the simulation domain to model only a very thin annulus instead of the full plasma volume, in which the background profiles can be taken to be constant, enabling the usage of periodic boundary conditions and a spectral scheme.

In the *global* approach, the radial variation of the background profiles is taken into account and thus other boundary conditions, i.e. Dirichlet or Von-Neumann conditions have to be used. Here, the Dirichlet condition assumes the perturbed distribution function to be zero outside of the radial domain; the latter uses the same assumption, except that the flux-surface averaged distribution is allowed to have a finite value at the inner border, with its derivative constrained to be zero. Using this approach allows the simulation to adapt the profiles according the specified heat and particle sources. To reduce potential effects of the boundary

on turbulence, a Krook-type buffer zone (see Refs. [26, 33] for a more detailed description) is introduced, which damps fluctuations in the vicinity of Dirichlet boundaries.

Binormal direction

The boundary condition in the binormal direction is motivated directly by the physical condition of periodicity in the toroidal angle ζ , which can be expressed as

$$f(\rho, \zeta, \theta) = f(\rho, \zeta + 2\pi, \theta).$$

Translating this to the GENE coordinates, this corresponds to the condition

$$f(x, y, z) = f(x, y - C_y 2\pi, z).$$

Therefore, the standard size of the simulation domain in y direction which corresponds to one full toroidal turn is given by $L_y = 2\pi C_y = 2\pi x_0/q_0$. In many cases however, turbulent correlation lengths are much smaller than a full toroidal turn; then it is possible to allow for an additional degree of freedom by taking the toroidal box extent to be an integer fraction of a full toroidal turn while still assuming periodicity, so that we can write

$$\begin{aligned} L_y &= \frac{2\pi C_y}{n_0} = \frac{2\pi x_0}{n_0 q_0} \\ f(x, y, z) &= f(x, y - L_y, z) \end{aligned}$$

with n_0 as the lowest toroidal mode number. In both the local and the global version of GENE, the toroidal direction is represented in Fourier space, with toroidal mode numbers defined by

$$k_y = j k_{y,\min} = j \frac{2\pi}{L_y} = j \frac{n_0}{C_y}.$$

Evaluating the last expression for $j = 1, n_0 = 1$ gives the lowest possible wave number of the system considered.

Parallel direction

In the direction along the field line, which is usually labeled by $z = \theta$, the boundary condition is determined by the physical condition of poloidal periodicity

$$f(\rho, \zeta, \theta) = f(\rho, \zeta, \theta + 2\pi).$$

Due to the mixed definition of the y coordinate, this boundary condition leads to the shifted-periodic relation

$$f(x, y, z) = f(x, y + 2\pi q C_y, z + 2\pi) = f\left(x, y + 2\pi q \frac{n_0}{k_{y,\min}}, z + 2\pi\right).$$

When representing the y coordinate in Fourier space, we can write

$$f(x, y, z) = \sum_{k_y} f(x, k_y, z) e^{ik_y y} = \sum_{k_y} f(x, k_y, z + 2\pi) e^{ik_y(y+2\pi q C_y)},$$

which allows us to identify

$$f(x, k_y, z) = f(x, k_y, z + 2\pi) e^{i2\pi j n_0 q(x)}. \quad (3.2)$$

The last expression is the parallel boundary condition as it is enforced in the global code. In the local code, the radially dependent eikonal has to be recast in a form that does not conflict with the periodic radial boundary conditions. We expand

$$q(x) \approx q_0 + (x - x_0) \frac{\partial q}{\partial x} = q_0 \left(1 + \frac{x - x_0}{x_0} \hat{s}\right)$$

with the magnetic shear parameter $\hat{s} = (x_0/q_0)(\partial q/\partial x)$. Using the safety factor expansion and representing also the radial direction in Fourier space yields

$$f(x, k_y, z) = \sum_{k_x, k_y} f(k_x, k_y, z) e^{ik_x x} = \sum_{k_x, j} f(k_x, k_y, z + 2\pi) e^{ik_x x} e^{i2\pi j n_0 q_0} e^{i2\pi j n_0 \hat{s}(x - x_0)/C_y},$$

where we have used Eq. 3.2 and the safety factor expansion in the last step. In order to appropriately fulfill this condition, the radial grid has to be selected such that

$$k'_x = k_x + 2\pi \frac{j n_0}{C_y} \hat{s} = k_x + 2\pi \hat{s} k_y$$

is a wavenumber which is present in the system. Therefore, we have to choose the minimum radial mode number to be

$$k_{x,\min} = \frac{2\pi \hat{s} k_{y,\min}}{\mathcal{N}}$$

with an (in principle arbitrary) integer number $\mathcal{N} \geq 1$, which guarantees that mode numbers accessed through the parallel boundary condition are present in the system. For local simulations, this leads to a quantization for the perpendicular box dimensions, given by

$$\mathcal{N} = \frac{2\pi \hat{s} L_x}{L_y}.$$

Of course, one can only account for a finite number of k_x modes in numerical simulations, so the physical parallel boundary condition has to be replaced by a

numerical one at the end of the resolved grid. Two different options are available for this in GENE:

- Higher k_x components of fields and distributions are set to zero. This type of boundary condition conserves energy, but can in combination with finite-difference derivatives lead to artificial zig-zag structures in the parallel direction, requiring the addition of artificial hyperdiffusion terms [34].
- A dissipative ‘floating’ boundary condition is applied, which leads to slightly smoother parallel structures, but at the price of a slight nonphysical energy sink that is (in contrast to hyperdiffusion terms) not directly adjustable by the user.

Velocity space:

Within the delta- f approach, the perturbed distribution is assumed to retain an approximately Maxwellian structure (i.e., it has to decay exponentially towards large velocities); the largest velocities kept in the simulation then must be chosen such that all important contributions of the perturbed distribution are contained within the velocity domain. Under these assumptions, it is valid to assume Dirichlet boundary conditions with zero perturbation outside of the domain for derivatives with respect to the parallel velocity.

For the magnetic moment (μ) direction, usually no boundary condition is necessary, since no derivatives are computed. When taking into account a collision operator, the derivatives with respect to μ are computed in GENE using a finite volume scheme assuming vanishing fluxes across the outer domain boundaries.

3.2.3 REPRESENTATION OF DERIVATIVES

As laid out in the last subsection, periodic boundary conditions can only be applied in the binormal (y)—and in the local model also the radial (x)—direction, so that these directions can be treated by a Fourier decomposition, yielding numerical derivatives which are accurate up to machine precision. The parallel (z) and parallel velocity (v_{\parallel}) directions, on the other hand, have non-periodic boundaries and the derivatives in these directions are therefore represented as finite differences. The terms containing derivatives in these directions are written in Eq. 2.23 as

$$\left(\frac{\partial g_1}{\partial t} \right)_{z,v_{\parallel}} = -\frac{C}{JB} v_{\parallel} \Gamma_z + \frac{\mu}{m} \frac{C}{JB} \partial_z B \frac{\partial f_1}{\partial v_{\parallel}}.$$

Taking into account that

$$\Gamma_z = \partial_z f_1 + e \partial_z \bar{\psi}_1 \frac{F_0}{T_0},$$

we can define the non-adiabatic part of the distribution function

$$h_1 = f_1 + e \bar{\psi}_1 \frac{F_0}{T_0}$$

and recast the above expression as

$$\left(\frac{\partial g_1}{\partial t} \right)_{z,v_{\parallel}} = -\frac{C}{JB} v_{\parallel} \partial_z h_1 + \frac{\mu}{m} \frac{C}{JB} \partial_z B \frac{\partial h_1}{\partial v_{\parallel}}.$$

Noting furthermore that

$$v_{\parallel} = \frac{1}{m} \frac{\partial H_0}{\partial v_{\parallel}}$$

$$\text{and } \mu \partial_z B = \frac{\partial H_0}{\partial z}$$

with the zeroth-order Hamiltonian H_0 , we can combine the parallel advection and trapping term into the expression

$$\left(\frac{\partial g_1}{\partial t} \right)_{z,v_{\parallel}} = -\frac{C}{JB} \frac{1}{m} \frac{\partial H_0}{\partial v_{\parallel}} \partial_z h_1 + \frac{C}{JB} \frac{1}{m} \frac{\partial H_0}{\partial z} \frac{\partial h_1}{\partial v_{\parallel}} = \frac{1}{m} \frac{C}{JB} \{H_0, h_1\}_{z,v_{\parallel}},$$

where we have defined the two-dimensional Poisson bracket

$$\{F, G\}_{x,y} = \frac{\partial F}{\partial x} \frac{\partial G}{\partial y} - \frac{\partial F}{\partial y} \frac{\partial G}{\partial x}.$$

Some analytical conservation properties fulfilled by this bracket are given by

$$\int \{F, G\}_{x,y} dx dy = 0$$

$$\int F \{F, G\}_{x,y} dx dy = 0$$

$$\int G \{F, G\}_{x,y} dx dy = 0.$$

Traditionally, this parallel bracket has been discretized in GENE by using centered differences both for the parallel velocity and the parallel spatial direction. Such a treatment in general does not fulfill all the above properties of the Poisson bracket [35], so that the conservation of quantities such as the free energy can be violated¹⁵.

Currently, GENE offers the option to both use separate fourth-order discretizations of (z, v_{\parallel}) derivatives or the second-order version of the Arakawa scheme given in the above reference, which employs a nine-point stencil in the (z, v_{\parallel}) plane for a unified representation of the parallel Poisson bracket. Note that the

¹⁵ Comparing linear and nonlinear results with both discretization schemes does in general not exhibit significant differences in growth rates or transport quantities. Studies of turbulent energetics, however should only be performed with schemes preserving the analytical conservation properties.

derivatives of the equilibrium Hamiltonian H_0 are also computed numerically in this process to be consistent. By rewriting

$$\left(\frac{\partial g_1}{\partial t} \right)_{z,v_{\parallel}} = \frac{1}{m} \frac{\mathcal{C}}{JB} \{ H_0, h_1 \}_{z,v_{\parallel}} = \frac{TF_0}{m} \frac{\mathcal{C}}{JB} \left\{ \frac{1}{F_0}, h_1 \right\}_{z,v_{\parallel}},$$

the Arakawa term can be slightly modified to numerically conserve the local free energy, which is given by

$$\int \frac{h_1^*}{F_0} \left(\frac{\partial g_1}{\partial t} \right)_{z,v_{\parallel}} dz dv_{\parallel}.$$

This last version of the parallel bracket is implemented in **GENE**.

3.2.4 DISCRETIZATION OF THE NONLINEARITY

The nonlinear terms can, similar to the parallel advection and the trapping terms, be written in the form of a Poisson bracket. As in Eq. 2.23, the nonlinearity can be written as

$$\begin{aligned} \mathcal{N} = -\frac{c}{\mathcal{C}} \frac{B}{B_{\parallel}^*} (\partial_x \bar{\chi}_1 \Gamma_y - \partial_y \bar{\chi}_1 \Gamma_x) &= -\frac{c}{\mathcal{C}} \frac{B}{B_{\parallel}^*} (\partial_x \bar{\chi}_1 \partial_y g_1 - \partial_y \bar{\chi}_1 \partial_x g_1) \\ &= \frac{c}{\mathcal{C}} \frac{B}{B_{\parallel}^*} \{ g_1, \bar{\chi}_1 \}_{x,y}. \end{aligned}$$

In the local version of **GENE**, the conservation properties of the nonlinearity can be fulfilled to all orders by employing the decomposition in k_x and k_y Fourier modes together with the three-halves dealiasing described in Refs. [25, 36]. The derivatives of g and $\bar{\chi}_1$ are then computed in Fourier space, whereas their multiplication is performed in real space to avoid the computationally expensive convolution that would otherwise be required.

In the global version of **GENE**, on the other hand, the radial direction is treated in real space; two choices for the discretization of the nonlinearity are currently implemented: One scheme computes the radial derivatives using a fourth-order centered difference scheme and performs a real-space filtering procedure [33]; the other scheme (which is now the default setting) uses a mixed Fourier-space/real-space version of the Arakawa discretization described above, similar to Ref. [37]. The exact term computed is

$$\begin{aligned} \mathcal{N} &= \frac{1}{3} \{ (\partial_y \bar{\chi}_1 \partial_x g_1 - \partial_x \bar{\chi}_1 \partial_y g_1) + \partial_y (\bar{\chi}_1 \partial_x g_1 - g_1 \partial_x \bar{\chi}_1) \\ &\quad + \partial_x (g_1 \partial_y \bar{\chi}_1 - \bar{\chi}_1 \partial_y g_1) \}. \end{aligned}$$

As before, the derivatives are, if possible, computed still using the Fourier decomposition in k_y (using a fourth-order centered difference stencil for the radial

derivatives), but before performing the multiplications, the respective quantities are transformed to $x - y$ real space. Through the combination of the Fourier-space dealiasing and the Arakawa discretization, the conservation properties of the Poisson bracket are preserved up to machine accuracy.

3.2.5 PHASE-SHIFT DEALIASING

As an alternative to the three-halves dealiasing scheme usually employed in GENE [25], aliasing effects arising in the computation of the nonlinear terms can also be avoided via the so-called phase-shift dealiasing scheme [38, 39], which was implemented into the GENE code by F. Merz. This scheme avoids the computational expense of having to compute the nonlinear terms with 50% more modes (per Fourier dimension) than are actually advanced in the simulation.

The procedure can be understood (following Ref. [39]) by examining an aliased product of two Fourier-decomposed quantities. For simplicity, we examine only the one-dimensional problem

$$c_k = \sum_{\substack{m,n \\ m+n=k}} a_m b_n + \sum_{\substack{m,n \\ m+n=k \pm N}} a_m b_n. \quad (3.3)$$

Here, a_m and b_n denote the Fourier components of the two quantities to be multiplied and c_k the Fourier mode k of the product. In the Fourier decomposition of each quantity, N modes are kept. The first sum in Eq. 3.3 is the aliasing-free part of the result, since all combinations of m and n map back onto the mode k , which is in the resolved range. The second sum, on the other hand, contains those terms in which m and n combine into the wavenumbers $k \pm N$, but are misinterpreted as contributions to the mode k . The latter sum therefore consists of all aliased contributions to c_k .

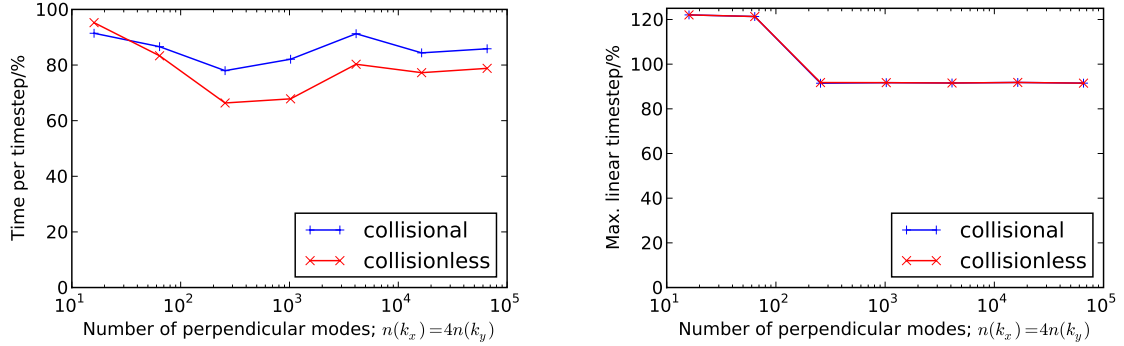
For the phase-shift dealiasing procedure, a phase factor $e^{ij\Delta}$ (j representing a mode number) is added to both a_m and b_n before multiplication, such that

$$\begin{aligned} a_m &\rightarrow a_m e^{im\Delta} \\ b_n &\rightarrow b_n e^{in\Delta}. \end{aligned}$$

Accordingly, the result c_k must be shifted back to yield

$$\begin{aligned} c_k &= e^{-ik\Delta} \left[\sum_{\substack{m,n \\ m+n=k}} a_m e^{im\Delta} b_n e^{in\Delta} + \sum_{\substack{m,n \\ m+n=k \pm N}} a_m e^{im\Delta} b_n e^{in\Delta} \right] \\ &= \sum_{\substack{m,n \\ m+n=k}} a_m b_n + e^{\mp iN\Delta} \sum_{\substack{m,n \\ m+n=k \pm N}} a_m b_n \end{aligned}$$

As can be seen from the last line, the alias-free part of the product is not affected by this procedure; but the aliased part is—due to the misinterpreted wavenumber—



(a) Relative CPU-time to compute a single timestep, comparing phase-shift with three-halves dealiasing for both collisionless and collisional simulations.

(b) Maximum linear timestep comparing the equally weighted Runge-Kutta scheme to the standard one.

Figure 5: Comparison of simulations employing the phase-shift dealiasing with ones using the three-halves dealiasing, scans over a large range of perpendicular resolutions are shown.

left with a phase factor. Defining the shift as a half grid spacing $\Delta = \pi/N$, the phase factor multiplying the aliased terms becomes

$$\exp(\mp iN\Delta) = -1.$$

This opens up the possibility to compute the product twice, using phase factors that differ by Δ (an obvious choice is taking $(+\Delta/2, -\Delta/2)$), and take the average of both results; since the aliased contributions have opposite phase factors, they drop out. Obviously, the price of this procedure is to carry out a second computation of the product; in d spatial dimensions this amounts to computing the product 2^d times, which would require significantly more operations than with the three-halves rule.

When using multi-stage timestepping schemes (e.g. Runge-Kutta) though, it is possible to perform the second evaluation of the product (with $-\Delta/2$) during the next stage of the scheme. Thus, only a single evaluation of the product per stage is required, however at the price of removing the aliasing error only approximately. Note, however, that the employed Runge-Kutta scheme has to use equally weighted stages, which leads to a slightly narrower stability region and reduces the timestep by a few percent.

To assess the overall efficiency of the scheme, a scan in perpendicular resolution was performed, starting from a regular ‘‘Cyclone Base Case’’ parameter set [40], but taking into account kinetic electrons and electromagnetic perturbations. The scan ranged from a radial resolution of $n(k_x) = 8$ up to $n(k_x) = 512$, while setting $n(k_y) = n(k_x)/4$. The other phase space resolutions were set to $24 \times 32 \times 8$ for the (z, v_{\parallel}, μ) directions, respectively. For each resolution, 100 timesteps were computed to provide sufficient statistics. Since the fraction of CPU time that is spent on computing the nonlinearity is crucial to the overall gain, both collisionless and

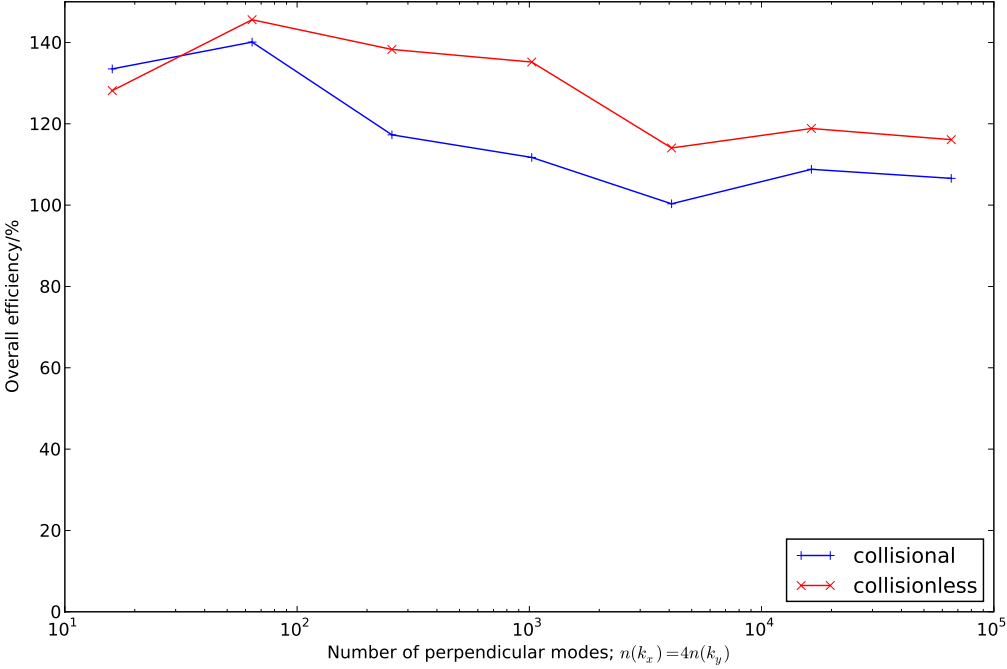


Figure 6: Overall efficiency of phase-shift dealiasing runs, compared to simulations using three-halves dealiasing. For collisionless runs, a gain of 15–20% can be expected, while for collisional ones, it is usually of the order of 10%.

collisional simulations were performed. In the latter, the computationally expensive collision operator reduces the fraction of total CPU time taken to compute the nonlinear term.

The results of the scan are shown in Figs. 5 and 6. As can be seen, the pure reduction of CPU time per timestep is of the order of at least 10% (20%) for collisional (collisionless) simulations. Due to the different timestepping scheme mentioned above, however, the maximum linear timestep is—for the practically relevant resolution range $10^3 < n(k_x)n(k_y) < 10^5$ —reduced by roughly 8%. In total (see Fig. 6), this amounts to an efficiency gain of up to 10% (10–20%) for collisional (collisionless) runs.

Note that we have assumed here that the reduction of the linear timestep carries over to nonlinear runs, which does not have to be fulfilled in general, since the timestep is adapted during nonlinear GENE simulations [25]. Especially for the better-resolved runs performed here, the timestep adaptation scheme became active already during the first 100 timesteps; in these cases, the adapted timesteps using the equal-weights Runge-Kutta scheme were indeed smaller than the standard ones by ∼5–10%, justifying the above analysis.

To demonstrate the preservation of physical accuracy when using the phase-shift dealiasing, the timetraces as well as the average values of the ion heat flux of a Cyclone Base Case simulation (using the corrected circular geometry instead of the $s\text{-}\alpha$ model, however) are shown in Figure 7 for comparison, yielding excellent statistical agreement.

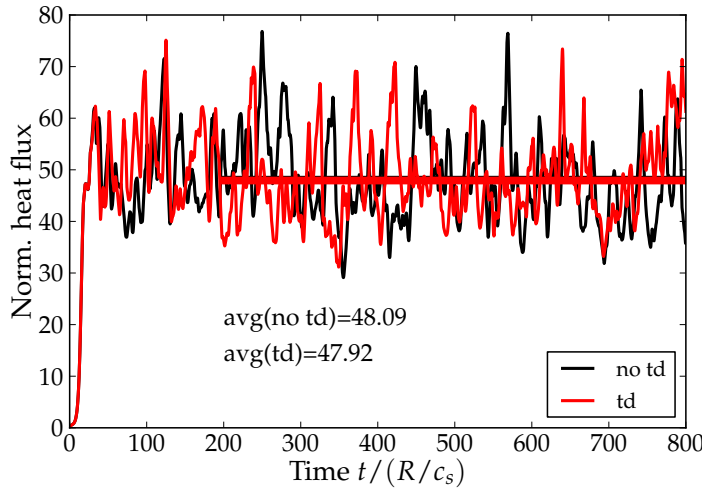


Figure 7: Comparison of heat flux timetraces for two simulations with ('td') and without ('no td') phase-shift dealiasing.

3.3 GYROPHASE AVERAGING

In the present section, the gyroaveraging operators that appear in both the Vlasov and the field equations are derived for application in the global version of GENE. In contrast to the local treatment, the gyroaveraging operator has to be distinguished with regard to where the affected quantities are evaluated. This distinction has been indicated in Sec. 2.5 by writing $\langle \dots \rangle$ or $\overline{\dots}$ in the field equations. The former version arises when taking velocity space moments of the distribution function, while the latter one—as a consequence of the gyrokinetic reduction—appears in the equations of motion and the pull-back operator.

3.3.1 IMPLEMENTATION OF THE GYROAVERAGING OPERATOR

In the global version of GENE, gyrophase averaging is carried out by means of a finite element interpolation, for which all considered quantities are expanded in terms of a set of basis functions, e.g.

$$\phi(x) = \sum_i \phi(x_i) \Lambda_i(x) = \sum_i \phi_i \Lambda_i(x).$$

The coefficients ϕ_i are the corresponding finite element coefficients and are defined to be the value of ϕ at the grid point x_i .

The present description will focus on the difference between the two kinds of gyroaverages discussed above. For more detail on the choice of the radial basis

functions $\Lambda_i(x)$ and the actual implementation, see Refs. [26, 33]. The gyrophase averages appearing in the Vlasov equation are defined by

$$\bar{\phi}_1(\mathbf{X}) = \frac{1}{2\pi} \int \phi_1(\mathbf{X} + \boldsymbol{\rho}) d\theta.$$

In the combined Fourier and finite element expansion, we can write

$$\bar{\phi}_1(X_k, Y, Z) = \frac{1}{2\pi} \int \sum_{i,k_y} e^{ik_y(Y+\rho^y)} \phi_i \Lambda_i(X_k + \rho^x) d\theta,$$

where we have chosen a specific radial grid point X_k . The parallel direction enters only as a parameter to determine the value of ϕ_i , since the gyroaveraging is a purely perpendicular operation. We can rearrange the last expression to find

$$\begin{aligned} \bar{\phi}_1(X_k, Y, Z) &= \frac{1}{2\pi} \sum_{i,k_y} e^{ik_y Y} \phi_i \int e^{ik_y \rho^y} \Lambda_i(X_k + \rho^x) d\theta \\ &= \sum_{i,k_y} e^{ik_y Y} \phi_i \mathcal{G}_{k,i} = \sum_{k_y} e^{ik_y Y} \mathcal{G} \cdot \boldsymbol{\phi}, \end{aligned}$$

where we have defined the gyroaveraging matrix

$$\mathcal{G}_{k,i}(k_y, z, \mu) = \frac{1}{2\pi} \int e^{ik_y \rho^y} \Lambda_i(X_k + \rho^x) d\theta \quad (3.4)$$

and the vector of the grid point values of ϕ

$$\boldsymbol{\phi} = (\phi(x_1), \dots, \phi(x_n))^T.$$

Note that the gyromatrix contains only equilibrium quantities like the size of the gyroradii and the basis functions, so that it need only be initialized once and can then be re-used throughout the simulation. The vector components of $\boldsymbol{\rho}$ are calculated from its definition

$$\boldsymbol{\rho} = \rho(x, \mu) \hat{\mathbf{a}} = \rho(\cos \theta \hat{\mathbf{e}}_1 - \sin \theta \hat{\mathbf{e}}_2),$$

but first the vectors $\hat{\mathbf{e}}_1$ and $\hat{\mathbf{e}}_2$ have to be related to the field aligned basis vectors of the GENE simulation domain. We take

$$\begin{aligned} \hat{\mathbf{e}}_1 &= \hat{\mathbf{e}}^x = \frac{\mathbf{e}^x}{\sqrt{g^{xx}}} \\ \hat{\mathbf{e}}_2 &= \widehat{\hat{\mathbf{b}} \times \hat{\mathbf{e}}_1} = \frac{1}{\sqrt{\gamma_1 g^{xx}}} (\mathbf{e}^y g^{xx} - \mathbf{e}^x g^{xy}) \end{aligned}$$

and arrive at

$$\begin{aligned}\rho^x &= \boldsymbol{\rho} \cdot \mathbf{e}^x = \rho \sqrt{g^{xx}} \cos \theta \\ \rho^y &= \boldsymbol{\rho} \cdot \mathbf{e}^y = \rho \frac{1}{\sqrt{g^{xx}}} [g^{xy} \cos \theta - \sqrt{\gamma_1} \sin \theta].\end{aligned}$$

Now we will consider the gyroaverages occurring in the field equations, which were denoted by $\langle \cdots \rangle$ in Sec. 2.5 and are defined as

$$\langle \phi_1 \rangle (\mathbf{x}) = \frac{1}{2\pi} \int \delta(\mathbf{X} - \mathbf{x} + \boldsymbol{\rho}) \phi_1(\mathbf{X}) d^3 X d\theta.$$

We apply again the expansion in Fourier and finite element coefficients to arrive at

$$\begin{aligned}\langle \phi_1 \rangle (x_k, y, z) &= \frac{1}{2\pi} \int \delta(\mathbf{X} - \mathbf{x}_k + \boldsymbol{\rho}) \sum_{i, k_y} e^{ik_y Y} \phi_i \Lambda_i(X) d^3 X d\theta \\ &= \frac{1}{2\pi} \int \sum_{i, k_y} e^{ik_y(y - \rho^y)} \phi_i \Lambda_i(x_k - \rho^x) d\theta \\ &= \frac{1}{2\pi} \sum_{i, k_y} e^{ik_y y} \phi_i \int e^{-ik_y \rho^y} \Lambda_i(x_k - \rho^x) d\theta.\end{aligned}$$

Exploiting the symmetry of the finite element basis functions, we can write

$$\Lambda_i(x_k - \rho^x) = \Lambda_0(x_k - \rho^x - x_i) = \Lambda_0(x_i + \rho^x - x_k) = \Lambda_k(x_i + \rho^x),$$

which allows us to recast the gyroaverage as

$$\begin{aligned}\langle \phi_1 \rangle (x_k, y, z) &= \frac{1}{2\pi} \sum_{i, k_y} e^{ik_y y} \phi_i \int e^{-ik_y \rho^y} \Lambda_k(x_i + \rho^x) d\theta \\ &= \sum_{i, k_y} e^{ik_y y} \phi_i \mathcal{G}_{i,k}^* = \sum_{k_y} e^{ik_y y} \mathcal{G}^\dagger \cdot \boldsymbol{\phi}.\end{aligned}$$

In this equation, we were able to re-use the gyromatrix defined in Eq. 3.4. Using the Fourier space representation for the binormal direction, we can write

$$\begin{aligned}\bar{\phi}_1(X, k_y, z) &= \mathcal{G} \cdot \boldsymbol{\phi}_1 \\ \langle \phi_1 \rangle (x, k_y, z) &= \mathcal{G}^\dagger \cdot \boldsymbol{\phi}_1.\end{aligned}$$

Note that the above derivation assumed that the metric coefficients do not vary over the course of a gyroradius. This assumption may not be well-justified close to the magnetic axis of a fusion device and in small devices. A possible alternate scheme which takes into account variations of the metric up to second order has been derived in Ref. [33]. When using the gyroaverage defined above, a similar approximation also has to be made to the Laplacian operator in the field equa-

tions in order to preserve the Hermiticity of the equations; in this case, only the (strongly dominant) Hermitian part of the Laplacian is retained by taking

$$\Delta \rightarrow \frac{1}{2} (\Delta + \Delta^\dagger).$$

3.3.2 CONSECUTIVE GYROAVERAGES

The field equations derived in Sec. 2.5 contain terms where gyroaveraged quantities are gyroaveraged a second time. Taking into account the results of the last paragraphs, these can be expressed in terms of the gyroaverage operator as

$$\langle \bar{\phi}_{1j} P_j \rangle (x, k_y, z) = \mathcal{G}^\dagger \cdot \{ P_j \mathcal{G} \cdot \phi_1 \},$$

where P_j is a symbol for the profile factors (represented by diagonal matrices in the discrete equations) appearing in the field equations. This 'sandwich' form of the double gyroaverage operator is necessary to preserve its analytical symmetry (or Hermiticity in the Fourier representation) as can be seen by writing

$$(\mathcal{G}^\dagger P \mathcal{G})^\dagger = \mathcal{G}^\dagger P^\dagger \mathcal{G} = \mathcal{G}^\dagger P \mathcal{G}.$$

Taking the profile factor out of the double gyroaverage—as is justified in case of weakly varying equilibrium—, we would get

$$(P \mathcal{G}^\dagger \mathcal{G})^\dagger = \mathcal{G}^\dagger \mathcal{G} P \neq P \mathcal{G}^\dagger \mathcal{G},$$

which would violate the symmetry property and potentially lead to numerical instabilities in simulations with kinetic electrons and low perpendicular wavenumbers.

3.4 NORMALIZATION

3.4.1 DEFINITION OF NORMALIZATION RULES

For easy comparison with characteristic physical quantities, all computations are carried out in normalized units, which can afterwards be reintroduced in the post-processing to allow for comparison with experimental cases. In GENE, the normalization is usually chosen such that all dimensionless quantities should be of order unity, avoiding the appearance of very large or very small numbers. The rules as detailed below have been used in similar setups from the outset of GENE development; the final version, however, has been developed and extended in Refs. [25, 26].

For the phase space coordinates, the anisotropic spatial structure of turbulence is taken into account by normalizing perpendicular distances to the small refer-

ence gyroradius ρ_{ref} , but keeping the dimensionless field line connection length (along z) to be $2\pi \sim \mathcal{O}(1)$. In contrast to this setup, the velocity space normalization must be species-dependent in order to account for potentially differing temperatures. The normalization does not consider the radial dependence of the temperature, however, so that the variation of the temperature has to be accounted for by choosing an appropriate velocity space width and resolution. Written explicitly, the phase space coordinates are normalized as

$$\begin{aligned} x &= \hat{x}\rho_{\text{ref}} & y &= \hat{y}\rho_{\text{ref}} & z &= \hat{z} \\ v_{\parallel} &= \hat{v}_{\parallel}\hat{v}_{Tj}|_{x_0}c_{\text{ref}} & \mu &= \hat{\mu}\hat{T}_{0j}|_{x_0}\frac{T_{\text{ref}}}{B_{\text{ref}}} & t &= \hat{t}\frac{L_{\text{ref}}}{c_{\text{ref}}}, \end{aligned}$$

where normalized quantities are indicated by a hat and the composed quantities

$$c_{\text{ref}} = \sqrt{\frac{T_{\text{ref}}}{m_{\text{ref}}}} \quad \rho_{\text{ref}} = \frac{m_{\text{ref}}c_{\text{ref}}c}{eB_{\text{ref}}} \quad \hat{v}_{Tj} = \sqrt{\frac{2\hat{T}_{0j}}{\hat{m}_j}}$$

have been introduced. The notation $|_{x_0}$ has been used to indicate evaluation at the position x_0 . Standard choices for the reference quantities are

$$T_{\text{ref}} = T_e \quad n_{\text{ref}} = n_e \quad m_{\text{ref}} = m_i,$$

such that $\rho_{\text{ref}} = \rho_s$ and $c_{\text{ref}} = c_s$. Furthermore, B_{ref} is chosen to be the toroidal magnetic field at the magnetic axis. L_{ref} , on the other hand, is usually taken to be the major (or minor) tokamak radius R (or a , ρ_{max} etc.). For the field fluctuations, the normalization is

$$\phi_1 = \hat{\phi}_1 \frac{T_{\text{ref}}}{e} \frac{\rho_{\text{ref}}}{L_{\text{ref}}} \quad A_{1\parallel} = \hat{A}_{1\parallel} \rho_{\text{ref}} B_{\text{ref}} \frac{\rho_{\text{ref}}}{L_{\text{ref}}} \quad B_{1\parallel} = \hat{B}_{1\parallel} B_{\text{ref}} \frac{\rho_{\text{ref}}}{L_{\text{ref}}},$$

where the factor $\rho_{\text{ref}}/L_{\text{ref}}$ accounts for the fact that the quantity being normalized is a (small) fluctuating quantity. In order to reflect the gyrokinetic ordering (Eq. 2.2) in the normalization, derivatives of fluctuating quantities are normalized according to

$$\frac{\partial}{\partial x} = \frac{1}{\rho_{\text{ref}}} \frac{\partial}{\partial \hat{x}} \quad \frac{\partial}{\partial y} = \frac{1}{\rho_{\text{ref}}} \frac{\partial}{\partial \hat{y}},$$

whereas derivatives of equilibrium quantities are normalized as

$$\frac{\partial}{\partial x} = \frac{1}{L_{\text{ref}}} \frac{\partial}{\partial \hat{x}} \quad \frac{\partial}{\partial y} = \frac{1}{L_{\text{ref}}} \frac{\partial}{\partial \hat{y}}.$$

By choosing this convention, the normalized versions of fluctuating quantities and their derivatives are of the same magnitude as those of equilibrium quantities.

Finally, the distribution functions¹⁶ appearing in the equations are normalized as

$$F_{0j} = \hat{F}_{0j} \frac{n_{\text{ref}}}{c_{\text{ref}}^3} \frac{\hat{n}_{0j}}{\hat{v}_{Tj}^3} \Big|_{x_0} \quad f_{1j} = \hat{f}_{1j} \frac{n_{\text{ref}}}{c_{\text{ref}}^3} \frac{\hat{n}_{0j}}{\hat{v}_{Tj}^3} \Big|_{x_0} \frac{\rho_{\text{ref}}}{L_{\text{ref}}}.$$

Note that using this normalization, the single-particle kinetic energy, which appears, e.g., in the background Maxwellian, is given by

$$E_{\text{kin}} = \frac{m_j}{2} v_{\parallel}^2 + \mu B = \left(\hat{v}_{\parallel}^2 + \hat{\mu} \hat{B} \right) T_{\text{ref}} \hat{T}_{0j} \Big|_{x_0} = \hat{E}_{\text{kin}} T_{\text{ref}} \hat{T}_{0j} \Big|_{x_0}.$$

The normalized equilibrium distribution therefore becomes

$$\hat{F}_{0j}(x, v_{\parallel}, \mu) = \frac{\hat{n}_{pj}(\hat{x})}{\pi^{3/2} \hat{T}_{pj}^{3/2}(x)} e^{-\hat{E}_{\text{kin}}(x, v_{\parallel}, \mu) / \hat{T}_{pj}(x)}.$$

Here we introduced the normalized temperature and density profiles $\hat{T}_{pj}(x)$ and $\hat{n}_{pj}(x)$. The profile quantities are hence taken to consist of three parts, e.g.

$$T_{0j}(x) = T_{\text{ref}} \hat{T}_{0j}(x_0) \hat{T}_{pj}(x).$$

The first part takes the dimension, the second part introduces the species dependence at a reference position x_0 (which is usually taken to be the box center), and the third part introduces the radial dependence of the profile.

3.4.2 DIMENSIONLESS EQUATIONS

Vlasov equation

Applying the above normalization to the gyrokinetic Vlasov equation derived in the last chapter (Eq. 2.23) yields the normalized equation

$$\begin{aligned} \frac{\partial \hat{g}}{\partial \hat{t}} &= + \frac{1}{\hat{\mathcal{C}} \hat{B}_{\parallel}^*} \partial_{\hat{y}} \hat{\chi}_1 \partial_{\hat{x}}^{n,T} \hat{F}_0 - \frac{1}{\hat{\mathcal{C}} \hat{B}_{\parallel}^*} (\partial_{\hat{x}} \hat{\chi}_1 \hat{\Gamma}_y - \partial_{\hat{y}} \hat{\chi}_1 \hat{\Gamma}_x) \\ &+ \frac{1}{\hat{\mathcal{C}} \hat{B}_{\parallel}^*} \frac{T_{0j}|_{x_0}}{q_j} \left[\frac{\hat{\mu} \hat{B} + 2 \hat{v}_{\parallel}^2}{\hat{B}} (\hat{K}_x \hat{\Gamma}_x - \hat{K}_y \hat{\Gamma}_y) - \hat{v}_{\parallel}^2 \frac{\beta_{\text{ref}}}{\hat{B}^2} \frac{\partial_{\hat{x}} \hat{p}}{\hat{p}} \hat{\Gamma}_y \right] \\ &- \frac{\hat{\mathcal{C}}}{\hat{J} \hat{B}} \hat{v}_{\parallel} \hat{v}_{Tj}|_{x_0} \hat{\Gamma}_z + \frac{\hat{\mu}}{2} \frac{\hat{\mathcal{C}}}{\hat{J} \hat{B}} \hat{v}_{Tj}|_{x_0} \partial_{\hat{z}} \hat{B} \frac{\partial \hat{f}_1}{\partial \hat{v}_{\parallel}} + \frac{1}{\hat{\mathcal{C}} \hat{B}_{\parallel}^*} \frac{\hat{\mu} \hat{B} + 2 \hat{v}_{\parallel}^2}{\hat{B}} \frac{T_{0j}|_{x_0}}{q_j} \hat{K}_x \partial_{\hat{x}}^{n,T} \hat{F}_0. \end{aligned}$$

The dimensionless quantity

$$\beta_{\text{ref}} = \frac{8\pi n_{\text{ref}} T_{\text{ref}}}{B_{\text{ref}}^2},$$

¹⁶ The modified distribution functions g_1 and h_1 follow the same rule as f_1 .

which indicates the ratio of thermal to magnetic pressure in the plasma, has been introduced.

Field equations

The normalized Poisson equation (derived from Eq. 2.32) is given by

$$\begin{aligned} & \hat{\lambda}_D^2 \hat{\nabla}_{\perp}^2 \hat{\phi}_1 - \sum_j \pi \hat{q}_j^2 \frac{\hat{n}_{0j}}{\hat{T}_{0j}} \Big|_{x_0} \int \left[\hat{\phi}_1 \hat{B} \frac{\hat{F}_{0j}}{\hat{T}_{pj}} - \left\langle \left\{ \hat{B} \hat{\phi}_{1j} \frac{\hat{F}_{0j}}{\hat{T}_{pj}} \right\} \Big|_{x-\rho} \right\rangle \right] d\hat{v}_{\parallel} d\hat{\mu} \\ &= - \sum_j \pi \hat{n}_{0j} \Big|_{x_0} \hat{q}_j \int \left[\left\langle \left\{ \hat{B} \hat{g}_{1j} \right\} \Big|_{x-\rho} \right\rangle + \left\langle \left\{ \hat{\mu} \hat{B} \hat{B}_{1\parallel j} \frac{\hat{F}_{0j}}{\hat{T}_{pj}} \right\} \Big|_{x-\rho} \right\rangle \right] d\hat{v}_{\parallel} d\hat{\mu}, \end{aligned}$$

where we have introduced the normalized Debye length

$$\hat{\lambda}_D = \frac{\lambda_D}{\rho_{\text{ref}}} = \sqrt{\frac{B_{\text{ref}}^2}{4\pi n_{\text{ref}} m_{\text{ref}} c^2}}.$$

For the parallel component of the Ampére equation, we get

$$\begin{aligned} & \hat{\nabla}_{\perp}^2 \hat{A}_{1\parallel} - \sum_j \pi \beta_{\text{ref}} \frac{\hat{q}_j^2}{\hat{m}_j} \hat{n}_{0j} \Big|_{x_0} \int \hat{v}_{\parallel}^2 \left\langle \left\{ \frac{\hat{F}_{0j}}{\hat{T}_{pj}} \hat{B} \hat{A}_{1\parallel j} \right\} \Big|_{x-\rho} \right\rangle d\hat{v}_{\parallel} d\hat{\mu} \\ &= - \sum_j \hat{q}_j \pi \frac{\beta_{\text{ref}}}{2} \left\langle \hat{n}_{0j} \hat{v}_{Tj} \right\rangle \Big|_{x_0} \int \hat{v}_{\parallel} \left\langle \left\{ \hat{B} \hat{g}_{1j} \right\} \Big|_{x-\rho} \right\rangle d\hat{v}_{\parallel} d\hat{\mu}. \end{aligned}$$

Finally, normalizing the perpendicular component of the Ampére equation yields

$$\begin{aligned} & \begin{pmatrix} \partial_y \hat{B}_{1\parallel} \\ -\partial_x \hat{B}_{1\parallel} \end{pmatrix} - \sum_j \pi \frac{\beta_{\text{ref}}}{2} \hat{q}_j \left\langle \hat{n}_{0j} \hat{v}_{Tj} \right\rangle \Big|_{x_0} \int \left\langle \left\{ \hat{e} \hat{B}^{3/2} \hat{B}_{1\parallel j} \frac{\hat{F}_{0j}}{\hat{T}_{pj}} \right\} \Big|_{x-\rho} \right\rangle \hat{\mu}^{\frac{3}{2}} d\hat{v}_{\parallel} d\hat{\mu} \\ &= \sum_j \pi \frac{\beta_{\text{ref}}}{2} \hat{q}_j \left\langle \hat{n}_{0j} \hat{v}_{Tj} \right\rangle \Big|_{x_0} \int \left\langle \left\{ \hat{e} \hat{B}^{3/2} \left[\hat{f}_{1j} - \hat{q}_j \hat{\phi}_{1j} \frac{\hat{F}_{0j}}{\hat{T}_{0j}|_{x_0} \hat{T}_{pj}} \right] \right\} \Big|_{x-\rho} \right\rangle \sqrt{\hat{\mu}} d\hat{v}_{\parallel} d\hat{\mu}. \end{aligned}$$

3.5 OBSERVABLES

For a meaningful analysis of gyrokinetic simulations, it is necessary to reduce the amount of information contained in the distribution function by taking appropriate moments over velocity space or the total phase space. The velocity space moments of the distribution function which had already been defined in Sec. 2.5 (see Eq. 2.28), are routinely computed in given intervals to provide the user with

information about the turbulence properties of the system. The moments M_{ab} are defined as (see also Sec. 2.5.2)

$$M_{ab}(\mathbf{x}) = \frac{1}{m} \int \delta(\mathbf{X} - \mathbf{x} + \boldsymbol{\rho}) \left[f_1 - \left(q\tilde{\phi}_1 - \mu \bar{B}_{1\parallel} \right) \frac{F_0}{T_0} \right] B v_{\parallel}^a v_{\perp}^b d^3 X dv_{\parallel} d\mu d\theta;$$

for the evaluation of fluxes caused by compressional magnetic fluctuations (only in the local model), additional moments N_{ab} are defined, in which the outer gyroaverage leads to a multiplication with μI_1 ¹⁷. These moments are given by

$$N_{ab}(\mathbf{x}) = \pi \left(\frac{2B}{m} \right)^{b/2+1} \int \left[f_1 + \left(q\bar{\phi}_1 + \mu \bar{B}_{1\parallel} \right) \frac{F_0}{T_0} \right] \mu I_1 v_{\parallel}^a \mu^{b/2} dv_{\parallel} d\mu$$

The normalized versions of both kinds of moments can be found in Ref. [41].

3.5.1 TRANSPORT QUANTITIES

The ultimate goal of turbulence simulations is to predict and optimize the transport of heat, particles and momentum in fusion-relevant plasmas, and measuring the turbulent fluxes of these quantities therefore is of prominent interest. The fluxes measured in GENE stem from the radial component of the fluctuating (generalized) $E \times B$ velocity v_{χ} defined in Eq. 2.14, giving rise to the radial flux components

$$\begin{aligned} \Gamma^x &= \left\langle \int v_{\chi}^x f_1(\mathbf{x}, \mathbf{v}) d^3 v \right\rangle \\ \Pi_{\parallel}^x &= m \left\langle \int v_{\chi}^x v_{\parallel} f_1(\mathbf{x}, \mathbf{v}) d^3 v \right\rangle \\ Q^x &= \frac{m}{2} \left\langle \int v_{\chi}^x (\mathbf{v} - \mathbf{u})^2 f_1(\mathbf{x}, \mathbf{v}) d^3 v \right\rangle \approx \frac{m}{2} \left\langle \int v_{\chi}^x v^2 f_1(\mathbf{x}, \mathbf{v}) d^3 v \right\rangle, \end{aligned}$$

where the brackets $\langle \dots \rangle$ denote the desired spatial averaging and $\Gamma, \Pi_{\parallel}, Q$ denote the flux of particles, parallel momentum and heat, respectively. Note that the parallel momentum flux can be used as an approximation to the toroidal momentum flux in usual tokamaks if $B_{\phi} \gg B_{\theta}$. The toroidal projection of this quantity can be calculated by multiplying with qRC/JB , neglecting smaller contributions due to curvature and grad- B drifts. Dividing v_{χ} into its field components

$$\mathbf{v}_{\chi} = \mathbf{v}_E + \mathbf{v}_A + \mathbf{v}_{B\parallel} = \frac{c}{B} \hat{\mathbf{b}} \times \nabla \left(\phi_1 - \frac{v_{\parallel}}{c} A_{1\parallel} - \frac{1}{c} \mathbf{v}_{\perp} \cdot \mathbf{A}_{1\perp} \right),$$

¹⁷ For the definition of I_1 , see Sec. 2.3.2.

we can separate the above definitions into transport driven by electrostatic and electromagnetic field fluctuations. Using the identity

$$\hat{\mathbf{b}} \times \nabla \xi \cdot \mathbf{e}^x = \mathbf{e}^x \times \hat{\mathbf{b}} \cdot \nabla \xi = -\sqrt{\gamma_1} \frac{\partial \xi}{\partial y} = -\frac{B}{C} \frac{\partial \xi}{\partial y},$$

we get

$$\begin{aligned} v_E^x &= -\frac{c}{C} \frac{\partial \phi_1}{\partial y} \\ v_A^x &= \frac{v_{||}}{C} \frac{\partial A_{1||}}{\partial y} \\ v_{B_{||}}^x &= \frac{1}{C} \mathbf{v}_{\perp} \cdot \frac{\partial \mathbf{A}_{1\perp}}{\partial y} \end{aligned}$$

As can be seen from the dependence on $v_{||}$ and \mathbf{v}_{\perp} , the fluxes generated by magnetic fluctuations depend on moments of the distribution function that are of higher order in these velocities. Considering this, the particle flux is given by

$$\Gamma^x = \left\langle -\frac{c}{C} \frac{\partial \phi_1}{\partial y} M_{00}(\mathbf{x}) + \frac{1}{C} \frac{\partial A_{1||}}{\partial y} M_{10}(\mathbf{x}) - \frac{c}{qC} \frac{\partial B_{1||}}{\partial y} N_{00}(\mathbf{x}) \right\rangle.$$

the radial flux of parallel momentum can be written as

$$\Pi_{||}^x = m \left\langle -\frac{c}{C} \frac{\partial \phi_1}{\partial y} M_{10}(\mathbf{x}) + \frac{1}{C} \frac{\partial A_{1||}}{\partial y} M_{20}(\mathbf{x}) - \frac{c}{qC} \frac{\partial B_{1||}}{\partial y} N_{10}(\mathbf{x}) \right\rangle,$$

and the heat flux is

$$\begin{aligned} Q^x &= \frac{m}{2} \left\langle -\frac{c}{C} \frac{\partial \phi_1}{\partial y} (M_{20}(\mathbf{x}) + M_{02}(\mathbf{x})) \right. \\ &\quad \left. + \frac{1}{C} \frac{\partial A_{1||}}{\partial y} (M_{30}(\mathbf{x}) + M_{12}(\mathbf{x})) - \frac{c}{qC} \frac{\partial B_{1||}}{\partial y} (N_{20}(\mathbf{x}) + N_{02}(\mathbf{x})) \right\rangle \end{aligned}$$

Applying the normalization rules of Sec. 3.4, we arrive at the dimensionless particle flux

$$\hat{\Gamma}_j^x = -\frac{\hat{n}_{0j}}{\hat{C}} \left\langle \frac{\partial \hat{\phi}_1}{\partial \hat{y}} \hat{M}_{00}(\hat{\mathbf{x}}) - \hat{v}_{Tj} \frac{\partial \hat{A}_{1||}}{\partial \hat{y}} \hat{M}_{10}(\hat{\mathbf{x}}) + \frac{\hat{T}_{0j}}{\hat{q}_j} \frac{\partial \hat{B}_{1||}}{\partial \hat{y}} \hat{N}_{00}(\hat{\mathbf{x}}) \right\rangle,$$

given in units of $\Gamma_{gB} = n_{\text{ref}} c_{\text{ref}} \rho_{\text{ref}}^2 / L_{\text{ref}}^2$. The normalized momentum flux can be calculated as

$$\hat{\Pi}_{||j}^x = -\frac{\hat{m}_j \hat{n}_{0j} \hat{v}_{Tj}}{\hat{C}} \left\langle \frac{\partial \hat{\phi}_1}{\partial \hat{y}} \hat{M}_{10}(\hat{\mathbf{x}}) - \hat{v}_{Tj} \frac{\partial \hat{A}_{1||}}{\partial \hat{y}} \hat{M}_{20}(\hat{\mathbf{x}}) + \frac{\hat{T}_{0j}}{\hat{q}_j} \frac{\partial \hat{B}_{1||}}{\partial \hat{y}} \hat{N}_{10}(\hat{\mathbf{x}}) \right\rangle,$$

the units being $\Pi_{gB} = n_{\text{ref}} m_{\text{ref}} c_{\text{ref}}^2 \rho_{\text{ref}}^2 / L_{\text{ref}}^2$. For the heat flux, we finally get

$$\begin{aligned}\hat{Q}_j^x &= -\frac{\hat{n}_{0j} \hat{T}_{0j}}{\hat{\mathcal{C}}} \left\langle \frac{\partial \hat{\phi}_1}{\partial \hat{y}} (\hat{M}_{20}(\hat{\mathbf{x}}) + \hat{M}_{02}(\hat{\mathbf{x}})) \right. \\ &\quad \left. - \hat{v}_{Tj} \frac{\partial \hat{A}_{1\parallel}}{\partial \hat{y}} (\hat{M}_{30}(\hat{\mathbf{x}}) + \hat{M}_{12}(\hat{\mathbf{x}})) + \frac{\hat{T}_{0j}}{\hat{q}_j} \frac{\partial \hat{B}_{1\parallel}}{\partial \hat{y}} (\hat{N}_{20}(\hat{\mathbf{x}}) + \hat{N}_{02}(\hat{\mathbf{x}})) \right\rangle\end{aligned}$$

in units of $Q_{gB} = p_{\text{ref}} c_{\text{ref}} \rho_{\text{ref}}^2 / L_{\text{ref}}^2$. Expanding the reference quantities, one can easily show that $Q_{gB} \propto T_{\text{ref}}^{5/2}$ and therefore depends, for fixed dimensionless quantities, very strongly on the reference temperature.

The derivation of the above quantities has so far concentrated on the contravariant radial component of the fluxes. In general geometry, however, these are not physically measurable quantities, since the length of the basis vector (see App. A) can vary, and it can even carry its own dimension. Therefore, to compare with experimental values, it is preferable to calculate the projection of the flux vectors onto a radial unit vector. The physical cross-field fluxes are then given by

$$A^r = \frac{A^x}{\sqrt{g^{xx}}},$$

and flux surface averaged diffusivities can then be calculated as

$$D = k \frac{\langle A^r \rangle}{\langle \sqrt{g^{xx}} \rangle}.$$

Here k is a prefactor that depends on whether the considered diffusivity concerns particles, momentum or heat.

3.6 HEAT AND PARTICLE SOURCES

GENE features a flexible set of sources and sinks, which allow for a variety of different investigations of global turbulence physics. There are two conceptually different approaches, the first of which allows to prescribe the plasma profiles, using adaptive sources in order to approximately keep the initial state. This is the so-called gradient-driven case, which is a global generalization of the local ansatz to turbulence simulations. The other approach is to prescribe particle and heat source profiles, and to allow the density and temperature profiles to freely evolve towards a steady state configuration, which is in turn determined by the specified sources. In this flux-driven case, the profiles may develop large enough fluctuations that the delta- f approximation is violated during the simulation; in that case, the background distribution can be adapted to accommodate the profile changes and allow an accurate continuation of the simulation. In the present thesis, however, we study only gradient-driven turbulence; therefore, we will focus on the sources that are applied in this type of examinations.

3.6.1 KROOK-TYPE HEAT AND PARTICLE SOURCES

In order to allow studies with approximately fixed plasma profiles, GENE provides adaptive sources, which force the flux-surface average distribution function towards the initial profiles. With the delta- f splitting employed in the GENE equations, this corresponds to forcing the perturbed distribution function towards zero. The implementation of the Krook-type heat source was originally inspired by Ref. [42]; its implementation, along with a slight modification due to GENE's different velocity space coordinates, was described in Ref. [33]. Here, another modification to that term is necessary, as we now focus on simulations which take into account kinetic electrons and, possibly, also impurities. We delay the discussion of this modification for the moment, since it is first necessary to introduce an entirely new term: In the case of adiabatic electrons, the transport of particles vanishes since the density and potential fluctuations are exactly in phase (see Sec. 2.5.5); as soon as kinetic electrons are taken into account, however, the particle transport will in general be finite, and therefore the density profiles will start to deviate from their initial state. If simulations with fixed profiles are to be performed, appropriate sources have to be introduced.

To achieve this, we introduce the particle source term

$$S_{P,j} = -\kappa_P \cdot \left(\langle f_j(X, |v_\parallel|, \mu) \rangle - \frac{\sum_i q_i \left\langle \int \langle f_i(X, |v_\parallel|, \mu) \rangle dv \right\rangle}{q_j n_{\text{spec}} \left\langle \int \langle F_{M,j}(X, |v_\parallel|, \mu) \rangle dv \right\rangle} \langle F_{M,j}(X, |v_\parallel|, \mu) \rangle \right) \quad (3.5)$$

to the right hand side of the Vlasov equation. Here, κ_P is a user-defined prefactor and $\langle \dots \rangle$ indicates a flux surface average. The gyrocenter distribution $f_j(X, |v_\parallel|, \mu)$ has been symmetrized with respect to v_\parallel , which guarantees that S_P introduces no overall parallel momentum to the Vlasov equation. Here, n_{spec} is the number of species taken into account in the simulation, and dv is the velocity space volume element. The second term in the brackets ensures that the overall charge density introduced by the particle source vanishes, so that quasineutrality is preserved and no artificial electrostatic potentials are introduced:

$$\sum_j q_j \left\langle \int S_{P,j} dv \right\rangle = 0$$

The heat source introduced in Ref. [33], on the other hand, is given by

$$\begin{aligned} S_{H,j} &= -\kappa_H \left(\left\langle f_j \left(X, |v_{\parallel}|, \mu \right) \right\rangle \right. \\ &\quad \left. - \frac{\left\langle \int \left\langle f_j \left(X, |v_{\parallel}|, \mu \right) \right\rangle dv \right\rangle}{\left\langle \int \left\langle F_{M,j} \left(X, |v_{\parallel}|, \mu \right) \right\rangle dv \right\rangle} \left\langle F_{M,j} \left(X, |v_{\parallel}|, \mu \right) \right\rangle \right), \end{aligned}$$

where the second term is added to ensure that S_H introduces no density perturbation. This can be verified by calculating

$$\left\langle \int S_{H,j} dv \right\rangle = 0.$$

To avoid cluttered notation in the following paragraphs, we set

$$\begin{aligned} f &= f_j \left(X, |v_{\parallel}|, \mu \right) \\ \text{and } F_M &= F_{M,j} \left(X, |v_{\parallel}|, \mu \right). \end{aligned}$$

When calculating the v^2 moment of the particle source term S_P , it becomes clear that this term will in general also add heat to the system. In order to compensate for this effect, we can redefine S_H with an adaptive coefficient κ_{mod} . The total heat introduced by the S_P operator is given by

$$Q_P = \kappa_P \left\langle \int v^2 \frac{S_P}{\kappa_P} dv \right\rangle,$$

where we expanded by κ_P to have it as a coefficient in front of the term. The total heat introduced by the S_H operator is in turn

$$Q_H = \kappa_H \left\langle \int v^2 \frac{S_H}{\kappa_H} dv \right\rangle.$$

In order to compensate for the heat contribution from the particle source, we modify the coefficient of the heat source such that

$$\begin{aligned} S_{H,\text{eff}} &= \frac{\kappa_{\text{eff}}}{\kappa_H} S_H \equiv \eta S_H \\ \text{with } Q_{H,\text{eff}} &= \eta Q_H = Q_H - Q_P \\ \text{and therefore } \eta &= \frac{Q_H - Q_P}{Q_H}. \end{aligned}$$

According to this rule, we have to choose the coefficient

$$\begin{aligned}\kappa_{\text{eff}} &= \kappa_H - \kappa_P \frac{\left\langle \int v^2 \frac{S_p}{\kappa_p} dv \right\rangle}{\left\langle \int v^2 \frac{S_H}{\kappa_H} dv \right\rangle} \\ &= \kappa_H - \kappa_P \left[\left(\langle \tilde{T} \rangle - \frac{\sum_i q_i \langle \tilde{n} \rangle}{q_j n_{\text{spec}} \langle n \rangle} \langle T \rangle \right) / \left(\langle \tilde{T} \rangle - \frac{\langle \tilde{n} \rangle}{\langle n \rangle} \langle T \rangle \right) \right].\end{aligned}\quad (3.6)$$

In the last step, we substituted the source operators and employed the notation

$$\begin{aligned}\langle n \rangle &= \left\langle \int \langle F_M \rangle dv \right\rangle = \langle n_j(X) \rangle \\ \langle T \rangle &= \left\langle \int v^2 \langle F_M \rangle dv \right\rangle = \langle T_j(X) \rangle \\ \langle \tilde{n} \rangle &= \left\langle \int \langle f \rangle dv \right\rangle = \langle \tilde{n}_j(X) \rangle \\ \langle \tilde{T} \rangle &= \left\langle \int v^2 \langle f \rangle dv \right\rangle = \langle \tilde{T}_j(X) \rangle.\end{aligned}$$

Note however, that these expressions differ from the actual definition of the fluid moments by taking additional flux surface averages and by using the symmetrized distribution function; furthermore no pull-back operation is employed, so that the moments are actually gyrocenter densities and temperatures. Reducing the last expression of Eq. 3.6 by $\langle T \rangle$ allows us to write

$$\kappa_{\text{eff},j}(X) = \kappa_H - \kappa_P \left[\left(\frac{\langle \tilde{T} \rangle}{\langle T \rangle} - \frac{\sum_j q_j \langle \tilde{n} \rangle}{q_j n_{\text{spec}} \langle n \rangle} \right) / \left(\frac{\langle \tilde{T} \rangle}{\langle T \rangle} - \frac{\langle \tilde{n} \rangle}{\langle n \rangle} \right) \right].\quad (3.7)$$

Using this expression (the same is true for Eq. 3.6) to define the heat source coefficient, however, has the drawback of being numerically unstable for cases in which the denominator in Eq. 3.7 becomes very small. In such cases, κ_{eff} will be set to very large values, introducing large amounts of heat to very narrow radial regions (often just one grid point). Therefore, we impose a lower limit on the denominator and choose $\kappa_{\text{eff},j}(X) = \kappa_H$ in case the limit is violated. As a result, only large heat contributions of the particle source will be compensated. The coefficients κ_P and κ_H are specified by the user, while κ_{eff} is adapted accordingly. It is therefore possible to set, e.g. $\kappa_H = 0$; in that case, κ_{eff} will adapt such that no heat is introduced to the system and $S_p + S_H$ is almost exclusively a particle source.

Another form of the particle source which has been suggested [43], is given by adding

$$S_{p,j} = -\kappa_P \frac{\langle F_{M,j} \rangle}{\sum_i \langle \int \langle F_{M,i} \rangle dv \rangle} \sum_i \left\langle \int \left\langle f_i \left(X, |v_{||}|, \mu \right) \right\rangle dv \right\rangle = -\kappa_P \frac{\langle F_M \rangle}{\sum_i \langle n_i \rangle} \sum_i \langle \tilde{n}_i \rangle\quad (3.8)$$

to the right hand side of the Vlasov equation. The latter form has the advantage of providing a quasineutral source automatically, if the equilibrium is quasineutral (which is always the case in GENE). Further, although the energy input may not be negligible, the influence on the total temperature is small, since the added particles have the same velocity distribution as the background Maxwellian. Therefore, it is not vital to compensate the energy contribution using the heat source, which avoids the complications of the above scheme.

3.6.2 LOCALIZED HEAT SOURCES

The most realistic way of treating heat sources in the GENE code is by prescribing a fixed heat source profile, which is designed to model the experimental source. This model is implemented by adding the term [29]

$$\hat{S}_{IH} = \hat{S}_0 \hat{S}_x \hat{S}_E$$

to the right hand side of the Vlasov equation. Here,

$$\begin{aligned}\hat{S}_E &= \frac{2}{3} \frac{1}{\hat{p}_{0j}(x)} \left(\frac{\hat{E}}{\hat{T}_p(x)} - \frac{3}{2} \right) \hat{F}_{0j} \\ \text{with } \hat{E} &= \hat{v}^2 = \hat{v}_{\parallel}^2 + \hat{\mu} \hat{B}\end{aligned}$$

is chosen such that no overall parallel momentum and no particles are introduced to the system. The component $\hat{S}_x(x)$ allows the user to specify an arbitrary¹⁸ profile, which is normalized such that

$$\int \hat{S}_x(x) \hat{j}(x, z) d\hat{V} = 1.$$

The factor \hat{S}_0 , finally, specifies the amplitude in units of $\hat{n}_{0j}(x_0) \rho_{\text{ref}} c_{\text{ref}} / \hat{v}_{Tj}^3(x_0) L_{\text{ref}}^2$, so that the total injected power is given by

$$P_{\text{add}} = S_0 \int d\hat{V} \int d\hat{v} \hat{E} \hat{S}_x \hat{S}_E = \hat{S}_0 n_{\text{ref}} T_{\text{ref}} \rho_{\text{ref}}^3 \frac{c_{\text{ref}}}{L_{\text{ref}}}.$$

This type of heat source has the advantage—compared to the Krook type sources shown in the previous section—that it does not unphysically remove heat in order to keep the profiles fixed; on the other hand, reaching true steady-state profiles is very expensive, since the simulations have to be run for transport times, which are several orders of magnitude larger than the turbulent timescales. Further, the accuracy of the presently available gyrokinetic equations in this limit has been questioned [45], and higher order equations as derived recently in Ref. [46] may be required to address these questions.

¹⁸ Actually, two specific choices are currently implemented in GENE, one being a Gaussian profile, the other one [44] yielding a broader peak width.

3.7 SHEARED EQUILIBRIUM FLOWS IN GENE

For many years it has been recognized that large-scale plasma flows can strongly influence turbulent transport. Since the flows we are concerned with in this chapter vary slowly in space and time, they are part of the equilibrium and can therefore be treated as input parameters, which do not vary over the course of a simulation. The interaction of flows and radial electric fields in the plasma is described by the radial force balance equation

$$E_r = \frac{\nabla p}{Z n_e} + v_\theta B_\zeta - v_\zeta B_\theta$$

As can be seen from this equation, radial electric fields can be caused by the pressure gradient as well as poloidal and toroidal plasma flows. The most important effect of flows on turbulence, however, is caused by their radial variation, termed ‘flow shear’, which reduces the turbulence correlation lengths and therefore the radial width over which heat and particles can be advected. To study this effect, there are currently two implementations available in GENE. One implementation (contributed by T. Görler) adds an externally imposed electrostatic potential of defined amplitude and profile¹⁹ to the nonlinear $E \times B$ advection term.

The second implementation models a radially constant $E \times B$ shearing rate by shearing the radial coordinate of the simulation domain in a time-dependent fashion, as described in Ref. [47]. This implementation is geared towards the case where the $E \times B$ flow is caused mostly by toroidal rotation, as is typically the case in the core of tokamaks. In transport barriers, modifications due to the strong pressure gradient can become important. To derive the Hammett $E \times B$ shear model, we define the toroidal angle in the co-moving frame

$$\zeta(x) = \zeta_0(x, t) - \Omega_{\text{tor}}(x)t,$$

with the radially dependent angular velocity $\Omega_{\text{tor}}(x)$ and the angle $\zeta_0(x, t)$ in the laboratory frame, which is now time-dependent due to the rotation. For the binormal coordinate, we obtain

$$y(x) = C_y \cdot (q(x)\theta - \zeta(x)) = y_0(x, t) + C_y \Omega_{\text{tor}}(x)t$$

in the co-moving frame. According to this equation, calculating the radial derivative in this frame will, through the chain rule, give

$$\frac{d}{dx} = \frac{\partial}{\partial x} + \frac{\partial y}{\partial x} \frac{\partial}{\partial y} = \frac{\partial}{\partial x} + \left(\frac{\partial y_0}{\partial x} + C_y t \Omega'_{\text{tor}} \right) \frac{\partial}{\partial y}.$$

The term $\partial y_0 / \partial x$ contains the magnetic shear, whereas the new term containing the radial derivative of Ω'_{tor} is due to the flow shear. As the y direction is treated

¹⁹ In the local code, only sinusoidal potential profiles are possible; in the global code, arbitrary profiles can in principle be defined.

in Fourier space in the global as well as in the local code, we can modify the usual radial derivatives by

$$\left(\frac{\partial}{\partial x} \right)' = \frac{\partial}{\partial x} + ik_y C_y t \Omega'_{\text{tor}},$$

for the global code, and

$$k'_x = k_x + k_y C_y t \Omega'_{\text{tor}}$$

for the local code. By changing to the rotating frame of reference, the time dependence of $y_0(x, t)$ itself drops out; only the effect of the flow shear Ω'_{tor} on the radial derivatives remains in the equations.

In the actual implementation, it is prohibitive to use a time-dependent radial coordinate grid, since many parts of the code would have to be re-initialized at every timestep instead of only once at the beginning of the run. Instead, the distribution and the electromagnetic fields are shifted on the stationary k_x grid periodically in time to achieve the same effect. In the local code, this has to be done in a discrete fashion as the available k_x grid points are discontinuous; therefore, on a grid with spacing Δk_x , the distribution function is shifted to the next available k_x once the accumulated shift $k_y C_y t \Omega'_{\text{tor}}$ exceeds $\Delta k_x / 2$. As can be seen, this operation occurs at different times for different k_y modes, so that small-scale modes experience more shifts per time unit.

Since only a finite number of k_x modes can be kept in a simulation, one has to choose an appropriate boundary condition for the effect of the flow shear. In GENE, the implementation is such that anything that is shifted beyond the available grid is discarded, while anything that is shifted into the grid from beyond the grid, is initially set to zero. Therefore, using the Hammett $E \times B$ model will introduce some artificial dissipation to the system.

Of course, this discrete variant of implementing a time-continuous process has limited accuracy, which is in this case determined by the k_x grid spacing, the k_y mode number and the magnitude of the flow shear. When performing linear simulations of large-scale modes at low flow shear, it can for instance happen that the linear growth rate fulfills GENE's convergence criterion before even experiencing the first shift in k_x . Convergence studies are therefore necessary, which can be done by increasing L_x (i.e. decreasing the k_x grid spacing) and at the same time increasing the number of k_x modes accordingly.

The normalized input parameter for the Hammett $E \times B$ shear model is

$$\hat{\gamma}_E = -C_y \frac{\partial \Omega_{\text{tor}}}{\partial x} \frac{L_{\text{ref}}}{c_{\text{ref}}} = -\frac{x_0}{q_0} \frac{\partial \Omega_{\text{tor}}}{\partial x} \frac{L_{\text{ref}}}{c_{\text{ref}}}.$$

Parallel flow shear

In addition to the perpendicular flow shear discussed in the last paragraph, we have to take into account that the Maxwellian equilibrium distribution now has to include a mean velocity, given by the toroidal rotation. In the laboratory frame

therefore, we enforce a Maxwellian distribution relative to the toroidal rotation velocity, given by

$$F'_0 = \frac{n_{0j}}{\pi^{3/2} v_{Tj}^3} \exp\left(-\frac{m_j (\mathbf{v} - R\Omega_{\text{tor}} \hat{\mathbf{e}}^\zeta)^2}{2T_{0j}}\right).$$

The expression $(\mathbf{v} - R\Omega_{\text{tor}} \hat{\mathbf{e}}^\zeta)^2$ can be expanded into

$$\mathbf{v}^2 - 2R\Omega_{\text{tor}} \mathbf{v} \cdot \hat{\mathbf{e}}^\zeta + R^2 \Omega_{\text{tor}}^2.$$

At this point, we introduce an additional ordering of the toroidal flow velocity in order to be able to drop the quadratic term. We define the toroidal Mach number M as

$$M = \frac{v_{\text{tor}}}{v_{th}} \ll 1,$$

which allows us to define the rotating Maxwellian as

$$F_0^{\text{rot}} = F_0 \exp\left(\frac{m_j R \Omega_{\text{tor}} \mathbf{v} \cdot \hat{\mathbf{e}}^\zeta}{T_{0j}}\right) \approx F_0 \left(1 + \frac{m_j R \Omega_{\text{tor}} \mathbf{v} \cdot \hat{\mathbf{e}}^\zeta}{T_{0j}}\right).$$

The toroidal component of the guiding center velocity is given by

$$v_{\text{tor}} = \mathbf{v} \cdot \hat{\mathbf{e}}^\zeta = (v_{\parallel} \hat{\mathbf{b}} + v_{\perp} \hat{\mathbf{c}}) \cdot \hat{\mathbf{e}}^\zeta \approx \frac{qv_{\parallel}}{|e_z| |\hat{\mathbf{e}}^\zeta|} = \frac{qRv_{\parallel}}{\sqrt{g_{zz}}},$$

where we dropped the perpendicular velocity term (which is oscillatory in the gyroangle) and employed the equality $e_z \cdot \nabla \zeta = q$ (see App. A). In the local description, we can change to the frame of reference rotating with Ω_{tor} , so that the above correction to F_0 drops out. In the linear drive term, however, an additional term arises due the parallel component of the flow shear Ω'_{tor} . Taking the radial derivative of the rotating Maxwellian gives the correction

$$\frac{\partial F_0^{\text{rot}}}{\partial x} = \frac{\partial F_0}{\partial x} + \frac{qR^2}{\sqrt{g_{zz}}} F_0 \frac{m_j v_{\parallel}}{T_{0j}} \frac{\partial \Omega_{\text{tor}}}{\partial x}.$$

In normalized GENE units, this corresponds to

$$\frac{\partial \hat{F}_0^{\text{rot}}}{\partial \hat{x}} = \frac{\partial \hat{F}_0}{\partial \hat{x}} - \hat{\gamma}_E \hat{F}_0 \frac{q \hat{R}^2}{\sqrt{\hat{g}_{zz}}} \frac{\hat{m}_j \hat{v}_{\parallel} \hat{v}_{Tj}}{\hat{T}_{0j} \hat{C}_y}.$$

The correction due to the additional term in the radial derivative of the equilibrium distribution constitutes an additional linear drive known as *parallel flow shear drive* and can, particularly for conventional tokamaks, overcome the effects of perpendicular flow shear and prevent turbulence quenching [48, 49]. Note that the quantity \hat{R} is not the major radius taken at the magnetic axis, but at the currently

considered position in the plasma. If \hat{R} is not readily available for a given geometry model, it can be calculated from the metric coefficients using the expression

$$\hat{R} = \sqrt{q^2 g^{zz} + \frac{1}{C_y^2} g^{yy} - \theta^2 \left(\frac{\partial q}{\partial x} \right)^2 g^{xx} - \frac{2q}{C_y} g^{yz}}^{-1} \quad (3.9)$$

for geometries using $z = \theta$, and using the expression

$$\hat{R} = \sqrt{q^2 g^{zz}}^{-1}$$

for TRACER geometry with $z = \zeta/q$. Note that for $s - \alpha$ geometry Eq. 3.9 is singular because of the inconsistencies in that model (see also Ref. [50]). In that case, the analytical expression for the normalized major Radius, given by

$$\hat{R} = (1 + \epsilon \cos \theta),$$

can be employed instead. The description of rotation effects given in this section is suitable only for local turbulence simulations. In a global model, no simplification can be achieved by transforming to a rotating frame of reference, and it is then preferable to choose a laboratory frame description. Further, the above derivation is only valid for low rotation; at higher angular velocities, Coriolis and centrifugal effects become increasingly important and the according drift terms should be retained.

3.8 SUMMARY

In this chapter, a description of the numerical methods employed in the GENE code was given. After introducing the field-aligned coordinate system, the boundary conditions applying to local and global simulations were discussed. The robustness of the global version of GENE was improved by treating the nonlinear terms with a mixed real-space/Fourier-space version of the Arakawa scheme, which provides a unified discretization of two-dimensional Poisson brackets, satisfying their basic conservation properties. By means of this scheme, nonlinear saturation is always found, even in absence of artificial small-scale dissipation. An option to treat the parallel advection and trapping terms in such a fashion is also available, enabling the local code to conserve the gyrokinetic free energy to machine precision.

The newly implemented phase-shift dealiasing scheme was described and tested for efficiency in both collisional and collisionless local simulations, showing that performance gains of up to 20% can be achieved. In global simulations with multiple particle species, it is necessary to employ both particle and heat sources to control the evolution of the background profiles during the simulation. Two new implementations of Krook-type particle sources in GENE were described, as well as

the existing localized and Krook-type heat sources. Finally, one section described the implementation of both parallel and perpendicular sheared background flows in the code, allowing for the investigation of shear-quenching of turbulence.

4

OPTIMIZED TREATMENTS OF MAGNETIC GEOMETRY

Over the past decade, plasma turbulence simulations have become increasingly complex, taking into account many new physics effects such as kinetic electrons, particle trapping, magnetic fluctuations, collisions and also the realistic geometry of the magnetic background field. Experimentally, it has been known for a long time that changing the shape of the plasma to a more elongated and/or triangular form can have a significant positive influence on the overall confinement. To enable quantitative predictions of microstability and turbulent transport, plasma turbulence codes therefore need to be able to take into account the effects of plasma shaping.

While turbulence codes historically often relied on the analytical $s - \alpha$ model [51], more realistic models including finite aspect ratio effects or even shaping [50, 52] have been devised. The GENE code is currently able to analytically model slab and $s - \alpha$ geometry, as well as the improved circular model. For more realistic geometries, the code includes interfaces to several established MHD codes²⁰, which can compute solutions to the magnetohydrodynamic equations based on measurements. These solutions can then be used as a background equilibrium for turbulence simulations with GENE. The following sections describe the implementation of a field line tracing module, as well as benchmarks validating its results.

In addition, a few methods will be described that are used to extend the limits of standard approaches when dealing with extreme geometries as they occur in strongly shaped plasmas. These methods include the shifted metric approach [57] for dealing with large shear, as well as a rescaling method of the parallel coordinate to compensate for the effect of strong shaping.

4.1 TRACER-EFIT INTERFACE

Most of the simulations performed for the present thesis take into account realistic numerical geometry. Initially, the geometric information was usually produced externally by the TRACER code and then read by GENE to set up a simulation. Over the course of this thesis, the core of the TRACER code has been integrated into GENE, along with an interface to the widely used EFIT G-EQDSK files. This section details some conversions that are performed on the output of the TRACER

²⁰ In particular, interfaces to CHEASE [53], EFIT [54], GIST [55], and TRACER [56] are supported.

module, as well as a benchmark of three simulations using the global circular geometry model, a circular equilibrium generated by `CHEASE`, and a circular EFIT equilibrium as processed by the `TRACER-EFIT` module. Close correspondence of all approaches is found, validating the implementation of the global `TRACER` module.

4.1.1 CONVERSION TO A RADIALLY INDEPENDENT BINORMAL COORDINATE

The field-line tracing procedure (FLT) as described in Ref. [56] generates, by construction, a coordinate system that is defined from the point of view of the local flux surface. These local coordinates are given as

$$\begin{aligned} x &= \rho \\ y &= C_y(\rho) (q\theta - \zeta) \\ z &= \frac{\zeta}{q}, \end{aligned}$$

where $C_y(\rho) = \rho/q$ with both q and ρ defined on the local flux surface, is radially dependent. The angles θ and ζ are the straight field line angle and the toroidal angle, respectively. Following Sec. 3.2.2, having C_y depend on the radius would correspond to a radially varying definition of the k_y grid. For convenience and comparability with the global circular geometry model described in [26, 33], we choose to transfer this radial dependence onto the prefactor C in the definition of the magnetic field (see Eq. 2.22). To achieve this, every geometric quantity that depends on y is transformed by means of the chain rule with

$$\frac{\partial y'}{\partial y} = \frac{C'_y}{C_y} = \frac{\rho_0 q}{q_0 \rho'}$$

where the subscript '0' denotes evaluation at the reference flux surface x_0 . The explicit transformation rules are

$$\begin{aligned} C' &= \frac{\rho q_0}{q \rho_0} \\ g^{xy'} &= g^{xy} \frac{\partial y'}{\partial y} \\ g^{y'z} &= g^{yz} \frac{\partial y'}{\partial y} \\ g^{y'y'} &= g^{yy} \left(\frac{\partial y'}{\partial y} \right)^2 \\ \frac{\partial B}{\partial y'} &= \frac{\partial B}{\partial y} \left(\frac{\partial y'}{\partial y} \right)^{-1}. \end{aligned}$$

A recalculation of the Jacobian determinant $J = (\det g)^{-1/2}$ is also performed. We immediately drop the primes on the new coordinates to prepare for the final step, which converts the parallel coordinate to the straight field line angle θ , giving the coordinate system

$$\begin{aligned} x' &= x \\ y' &= y \\ z' &= \theta. \end{aligned}$$

This modification affects the orientation of the covariant e_y basis vector, which is defined as (see also App. A)

$$e_y = \frac{\partial R}{\partial y}$$

with the position vector R . The reason for this is that the derivative with respect to y , keeping x and z constant, now leaves ζ as the only degree of freedom instead of θ . After this final change, the coordinate system is defined exactly as in the circular model, except for the more general radial coordinate. The rules for the final transformation are obtained from an explicit representation of the metric coefficients g^{ij} in terms of the coordinates ρ , θ and ζ . Thus,

$$\begin{aligned} g^{xz'} &= \nabla\rho \cdot \nabla\theta = \frac{1}{C_y q} g^{xy} - \theta \frac{1}{q} \frac{\partial q}{\partial \rho} g^{xx} \\ g^{z'z'} &= \nabla\theta \cdot \nabla\theta = \frac{1}{C_y^2 q^2} g^{yy} - \left(\theta \frac{1}{q} \frac{\partial q}{\partial \rho} \right) g^{xx} - g^{zz} - 2\theta \frac{1}{q} \frac{\partial q}{\partial \rho} g^{xz'} \\ g^{yz'} &= C_y \nabla(q\theta - \zeta) \cdot \nabla\theta = C_y q g^{z'z'} + C_y \theta \frac{\partial q}{\partial \rho} g^{xz'}. \end{aligned}$$

In these equations, we made use of the fact²¹ that $g^{\theta\zeta} \equiv 0$. For the components of ∇B , we obtain

$$\begin{aligned} \frac{\partial B}{\partial x'} &= \frac{\partial B}{\partial x} + \frac{\partial B}{\partial y} C_y \theta \frac{\partial q}{\partial \rho} \\ \frac{\partial B}{\partial y'} &= 0 \\ \frac{\partial B}{\partial z'} &= \frac{\partial B}{\partial z}. \end{aligned}$$

It would also have been possible to modify directly the differential equations in the FLT procedure [56], but we choose to perform the above conversion as a post-processing in order to have the original results readily available for comparison.

²¹ In the actual implementation, this is verified numerically by evaluating $g^{\theta\zeta}$ from the initial g^{yz} coefficient.

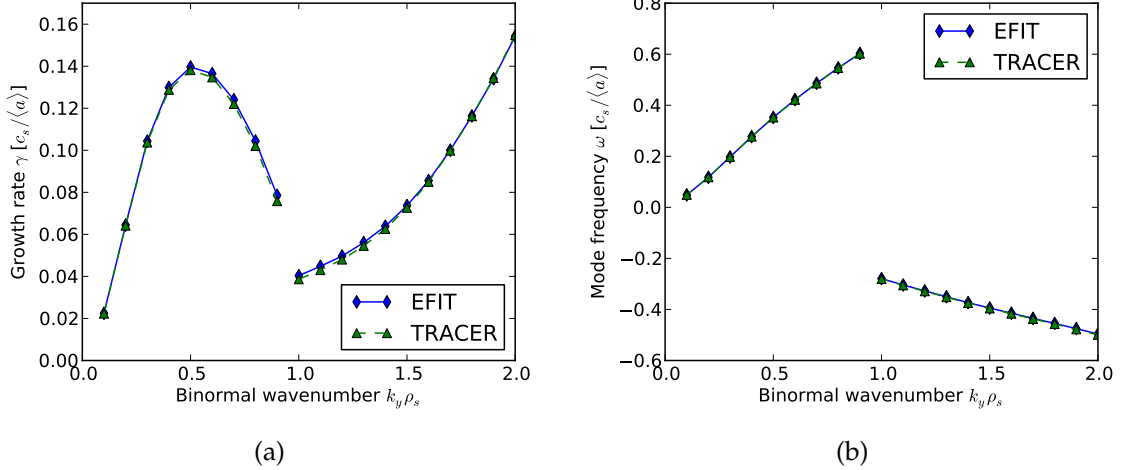


Figure 8: Benchmark of the GENE-internal FLT module using an ASDEX Upgrade EFIT file as input against the geometry provided by the standalone TRACER code. Shown are both the growth rates (a) and the real frequencies (b) for binormal wavenumbers between $k_y \rho_s = 0.1, \dots, 2.0$. At $k_y \rho_s = 1.0$, a mode transition from ITG to ETG is visible.

4.1.2 LOCAL BENCHMARK OF THE TRACER-EFIT INTERFACE

Comparison to the original TRACER code

To verify the validity of the above conversions, a parameter scan over the binormal mode number is performed in ASDEX Upgrade core geometry, retaining kinetic electrons, electromagnetic fluctuations, and collisions. As an input we take the MHD equilibrium from a high power ASDEX Upgrade discharge (#20431) and choose the radial position $\rho_{\text{tor}} = 0.59$ with the temperature and density gradients taken from a fit to the experimental profiles. The resolution taken for these linear simulations was $16 \times 1 \times 32 \times 32 \times 8$ in the $\{x, y, z, v_{\parallel}, \mu\}$ directions. The result of the comparison is displayed in Fig. 8, showing very good agreement between the two versions of the TRACER code. This is of course to be expected, since the numerical procedure used to compute the geometric coefficients is identical; there are, however, differences in the method used to find the flux surface to be traced, and in the setup of the initial condition for the computation, since the EFIT input file does not explicitly provide a grid in ρ_{tor} or the toroidal flux ϕ . Instead, the EFIT file provides, among other data, the poloidal flux ψ and the safety factor profile. The relation

$$\frac{d\phi}{d\psi} = q$$

is then used to obtain a $\rho_{\text{tor}}(R, Z)$ grid via spline interpolation.

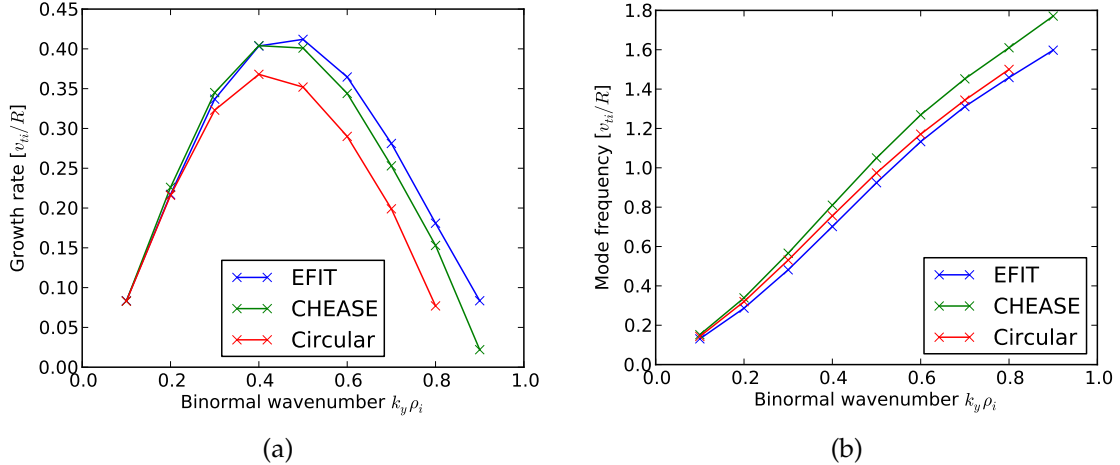


Figure 9: Comparison of linear growth rates and mode frequencies between the different geometry inputs.

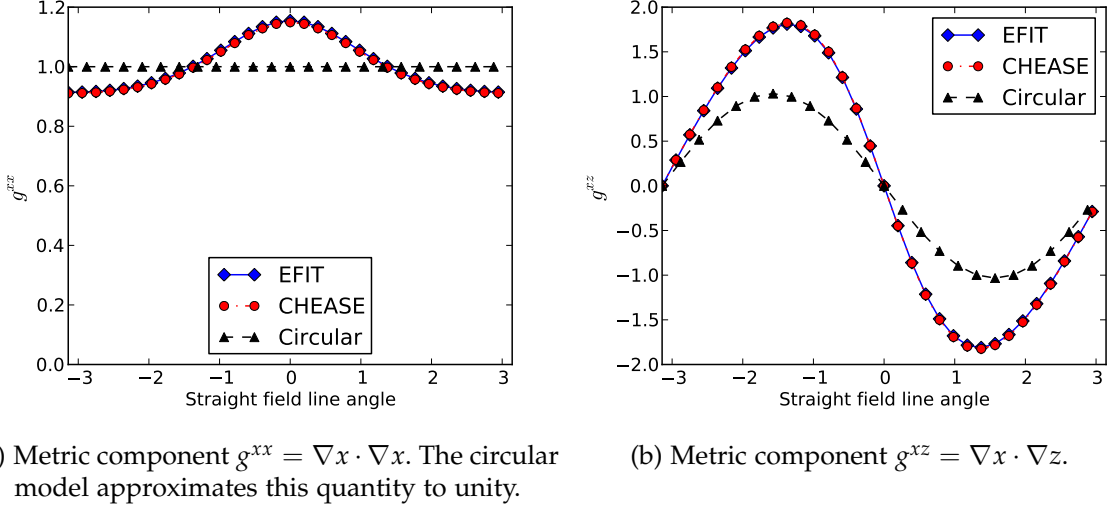
Comparison with CHEASE and the circular model

To further verify the accuracy of the EFIT interface and the implementation of the FLT module, linear and nonlinear simulations were compared to ones, in which the geometry was defined by the circular analytical model [50] or by input from the CHEASE [53] code. The latter input file is based on the simplest case from a recent gyrokinetic geometry benchmark [58]. The input files of that benchmark are publicly available as EFIT files under Ref. [59]; CHEASE format files can then be produced by processing the EFIT files with CHEASE itself. Using these three variants of input, linear growth rate scans, and nonlinear turbulence simulations are performed. We keep a simple adiabatic electron model for these runs and focus on possible deviations due to geometry.

We choose a mid-radius position with $x = 0.5$, $q = 1.41$ and $\hat{s} = 0.82$, setting the driving gradients to their Cyclone Base Case [40] values $R/L_{Ti} = 6.92$ and $R/L_n = 2.22$.

The linear simulations involve a scan in the binormal wavenumber k_y ranging over the typical ITG-unstable wavenumbers, $0.1 \leq k_y\rho_i \leq 1.0$. The results in terms of growth rates and mode frequencies are displayed in Fig. 9. As can be seen, for low k_y there is good agreement between all three inputs. For wavenumbers larger than $k_y\rho_i \sim 0.3$, the analytical model delivers a significantly smaller growth rate, while for $k_y\rho_i \gtrsim 0.5$ there is also some deviation between the CHEASE and EFIT growth rates.

A close examination of the metric coefficients derived from the various models reveals that the most likely reason for the strong deviation of the circular model is the neglect of the Shafranov shift that is present in the realistic MHD equilibrium. This is visible in Fig. 10, which shows that the metric component g^{xx} , which measures the distance between flux surfaces, is assumed to be unity while it varies by more than 20% in fact. More significantly, the maxima of the component g^{xz} differ



(a) Metric component $g^{xx} = \nabla x \cdot \nabla x$. The circular model approximates this quantity to unity.

(b) Metric component $g^{xz} = \nabla x \cdot \nabla z$.

Figure 10: Neglecting the Shafranov shift in the circular model leads to significant deviations in g^{xx} and g^{xz} from the realistic MHD equilibrium.

by almost 50% from the realistic value, showing that the angle between ∇x and $\nabla z = \nabla\theta$ deviates strongly. As a consequence of this, the parallel dependence of the local shear value is modified, which can be seen by calculating

$$g^{xy} = \nabla x \cdot \nabla y = C_y q g^{xz} + \hat{s}\theta g^{xx}.$$

Taking into account the definition of local shear,

$$\hat{s}_{\text{loc}} = \frac{\partial}{\partial\theta} \left(\frac{g^{xy}}{g^{xx}} \right),$$

we can see that the parallel variation of the magnetic shear comes about due to g^{xz} and g^{xx} , resulting in this case in a rather strong modification (see Fig. 11a). Especially at the outboard side ($z = 0$), where the microinstabilities typically peak, the shear value is significantly larger in the circular model, providing some (unrealistic) stabilization. Indeed, when reducing the global shear in the circular model simulation to match the realistic value of local shear at the outboard side, a much better agreement on the growth rates is achieved (Fig. 11b).

For the nonlinear runs, the unmodified shear value was taken, since for the low wavenumbers—which usually provide the largest transport—, there was reasonable agreement in the linear growth rates. In these simulations, a resolution of $128 \times 24 \times 24 \times 32 \times 8$ was chosen, which is, by experience, a well-converged resolution for this simple physical setting. We choose a square-sized box of $(125\rho_i)^2$ in the perpendicular direction, and the standard settings for velocity space. Since the particle flux vanishes with adiabatic electrons, the main quantity of interest is the heat flux. In addition, the volume-averaged fluctuation levels of density, parallel and perpendicular temperature, and fluid velocity were measured and time-averaged between $\hat{t} \in [70, 350]$. All these results are listed in Table 1.

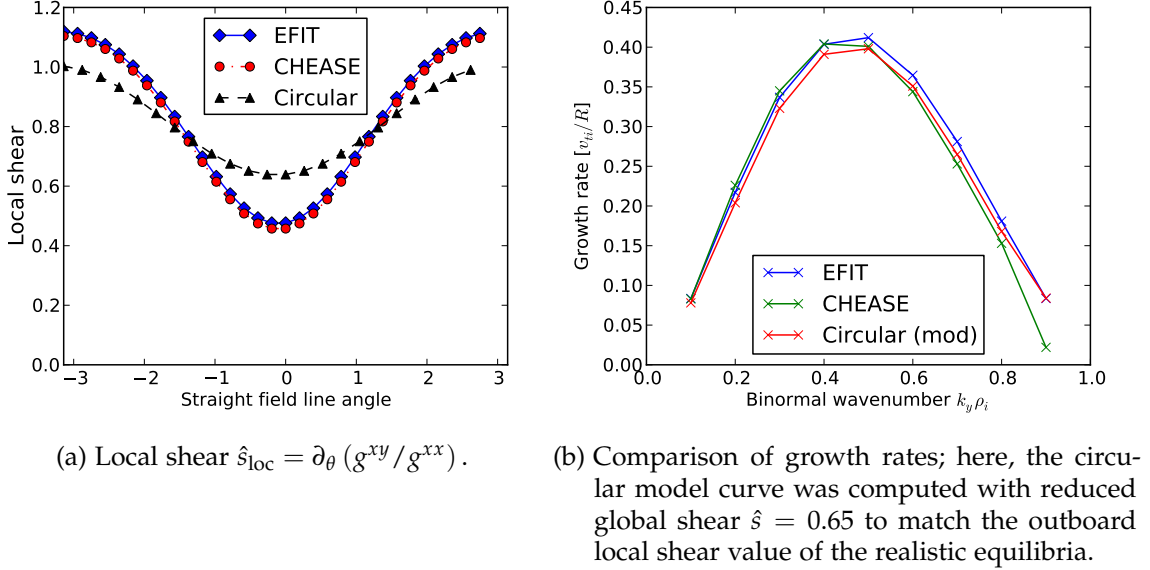


Figure 11: Parallel dependence of local shear (a); comparison of growth rates (b), taking a modified shear value in the circular model simulation.

Input	Q_{es}^i	$\langle \delta n / n \rangle_{rms}$	$\langle \delta T_{\parallel} / T \rangle_{rms}$	$\langle \delta T_{\perp} / T \rangle_{rms}$	$\langle \delta u_{\parallel} / v_{ti} \rangle_{rms}$
EFIT	50.6 ± 7.8	12.3	19.4	20.8	13.7
CHEASE	51.9 ± 7.2	13.3	20.2	21.2	12.9
Circular	47.8 ± 8.3	12.4	19.5	21.1	12.7

Table 1: Simulation results for the geometry comparison between the circular model, EFIT and CHEASE input. Note that all fluctuation levels in the above table are given in units of ρ_{ref} / L_{ref} .

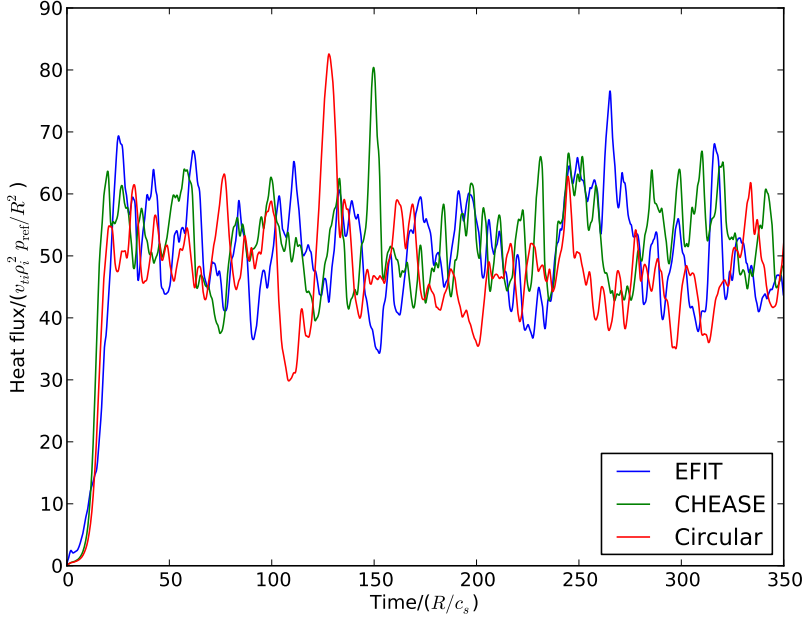


Figure 12: Comparison of turbulent heat flux with different geometry inputs, showing very good statistical agreement.

As is obvious from these values and also from the time traces shown in Fig. 12, the agreement between the different models is very good, the difference between the heat fluxes being less than half of the standard deviation of the time traces. As expected, the difference between the circular model and the realistic equilibria is much reduced compared to the linear spectra.

4.1.3 GLOBAL BENCHMARK OF THE TRACER-EFIT INTERFACE

The TRACER-EFIT interface includes the capability to set up global simulations in general tokamak geometry. To validate the output of the module for the global case (especially with respect to the coordinate transformations described above), a benchmark similar to the one discussed in the previous section was performed, but this time including radially dependent profiles and geometry. For this benchmark, three simple comparison runs were set up, using the circular geometry input files from Ref. [58]. Again, we restrict the simulations to the adiabatic electron model, using a resolution of $64 \times 24 \times 16 \times 48 \times 16$ in $\{x, y, z, v_{\parallel}, \mu\}$. The profiles were chosen to have a temperature gradient peak value²² of $a/L_T = 6.92$ and a density gradient peak of $a/L_n = 2.22$, with $\rho_i/a = 1/80$ and a radial box width of $L_x = 60\rho_i$. The full toroidal circumference of the torus is simulated, with a binormal wavenumber grid of $0.035 < k_y\rho_i < 0.805$. In Table 2 some spatially averaged

²² The gradients used in these simulations are motivated by the well-known Cyclone Base Case [40] values, but are normalized to the minor instead of the major radius, and therefore almost a factor of three larger than the Cyclone gradients.

Input	Q_{es}^i	$\langle \delta n / n \rangle_{\text{rms}}$	$\langle \delta T_{\parallel} / T \rangle_{\text{rms}}$	$\langle \delta T_{\perp} / T \rangle_{\text{rms}}$	$\langle \delta u_{\parallel} / v_{ti} \rangle_{\text{rms}}$
EFIT	37.4 ± 7.0	9.20	25.7	25.3	19.0
CHEASE	36.3 ± 6.3	9.34	24.5	24.8	18.1
Circular	35.3 ± 5.7	9.23	25.7	25.0	19.6

Table 2: Simulation results for the global comparison between the circular model, EFIT and CHEASE input. Again, all fluctuation levels in the above table are given in units of $\rho_{\text{ref}} / L_{\text{ref}}$ and averaged over the whole spatial domain.

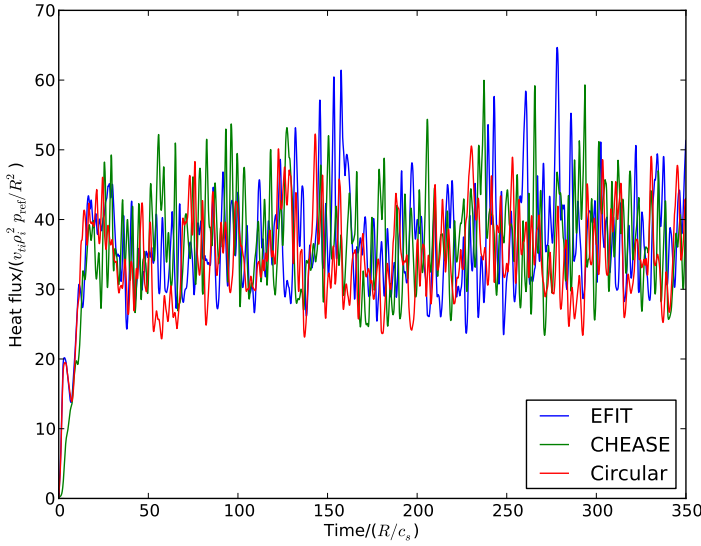


Figure 13: Comparison of heat flux time traces for global simulations using CHEASE, EFIT or the circular model equilibrium.

heat flux and fluctuation levels are displayed for comparison, showing excellent agreement between the various models. The same level of agreement is also obvious from Figs. 13, 14a, and 14b, which compare the heat flux time traces, radial profiles, and binormal spectra, respectively. The applicability of the TRACER-EFIT module for global simulations can therefore be considered proven.

4.2 GEOMETRY TREATMENT IN STRONGLY SHEARED PLASMA REGIONS

In the present thesis, turbulence simulations focus on transport barrier regions, taking into account realistic magnetic geometry. While this is both an important and a physically interesting research topic, it is also very challenging from a numerical point of view: In both core (Ch. 5) and edge transport barriers (Ch. 6), strong variations in the background current profile can occur, resulting in a strongly sheared magnetic field. In this section, we will examine two established types of

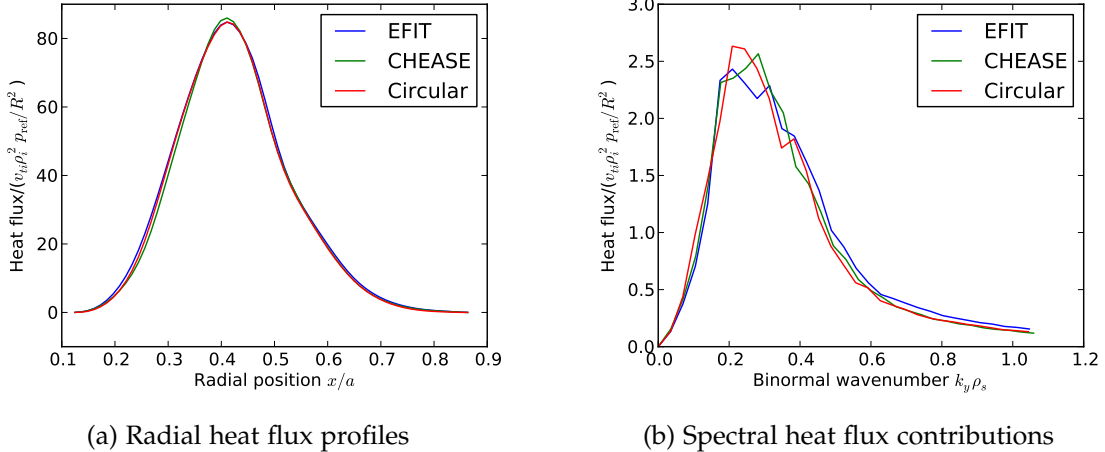


Figure 14: Comparison of spatial heat flux dependencies with different geometry input in a global simulation.

field-aligned coordinate systems, their applicability to different types of turbulence codes and their behavior in complex geometries. The main contents of this section have been published in Ref. [60].

4.2.1 PROPERTIES OF FIELD-ALIGNED COORDINATE SYSTEMS

As was already explained, it is common for plasma turbulence codes to employ a spatial coordinate system which is aligned to the magnetic field, taking advantage of the fact that in strongly magnetized plasmas all particles experience the Lorentz force and their dynamics therefore become strongly anisotropic. In the literature, numerous derivations of field-aligned coordinates (see, e.g. Refs. [24, 32, 57, 61]) can be found, which we will not repeat here. Instead we will give a description of some properties of these coordinate systems. In addition to the standard field-aligning approach, one of the aforementioned works [57] also defined a ‘shifted-metric’ approach, which differs from the former one in several aspects that will be examined here.

Magnetic shear in straight and shifted metric

In the usual transformation from cylindrical to field-aligned coordinates, one defines a set of three coordinates x, y, z , which represent the radial, binormal, and parallel direction, respectively. For convenience, one often chooses the reference position to be where the contravariant $e^x = \nabla x$ vector is parallel to the cylindrical $e^r = \nabla r$, i.e. where the flux surface is perpendicular to the (cylindrical) radial direction. For up-down symmetric geometries, this is the outboard midplane. The e^y vector, on the other hand, lies in the flux surface, perpendicular to the field line direction. However, the x and y coordinate vectors are only orthogonal at the aforementioned reference position, which can be seen as follows: Since the safety

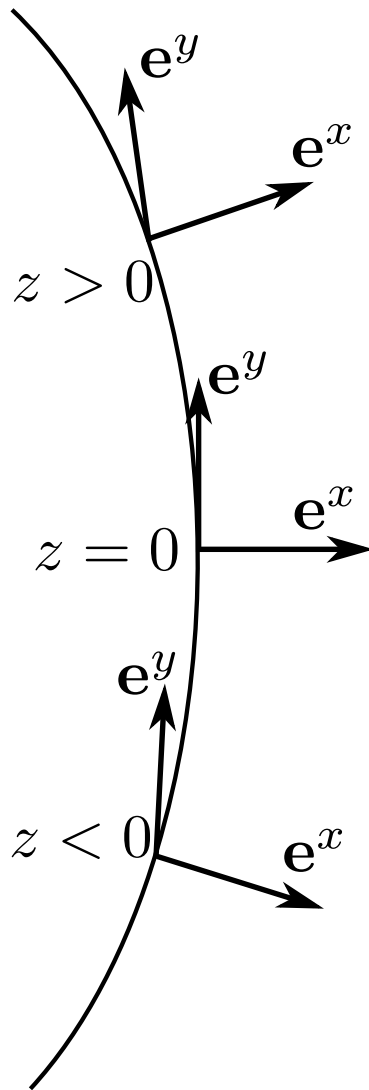


Figure 15: Orientation of contravariant basis vectors relative to a flux surface for different parallel positions.

factor is not constant across the minor plasma radius, the pitch of the magnetic field changes between different radii. At the reference position, where y (the field line label) can be defined to be zero for all radial positions, a small step in direction of e^x changes only the x coordinate. At a different parallel position, however, a small step in x direction will in general be accompanied by a change of the y coordinate, since the field lines with $y = 0$ that we started with are now at different poloidal angles due to the differing safety factor. This means that $e^y = \nabla y$ now has a radial component, so that $g^{xy} = \nabla x \cdot \nabla y \neq 0$ when departing from the outboard midplane. Therefore, the perpendicular grid is only orthogonal at the reference position where y is defined to be zero for all radial positions. As one follows the field line, the angle between the e^x and e^y vectors increases according to magnetic shear (or local shear, if its parallel dependence is taken into account, see, e.g., Ref. [62, 63]). This situation is depicted in Fig. 15.

The shifted-metric approach, which was first described in Ref. [57], avoids these complications by introducing a different coordinate y_k for every position z_k along the field line. y_k is defined such that $g^{xy_k} = 0$ everywhere, which requires the definition

$$y_k = y - \frac{g^{xy}}{g^{xx}}|_k x, \quad (4.1)$$

where the metric coefficient g^{xy} is to be calculated with the unshifted y coordinate, at position z_k . Note that the above relation must be generalized in case of radially dependent metric, which will be done here only after the local properties of the shifted metric have been studied. The same transformation as above is also applied in simulations employing the standard Clebsch approach, but only at the parallel ends of the simulation domain, and then with the integrated coefficient $g^{xy}/g^{xx}|_\pi - g^{xy}/g^{xx}|_{-\pi} = 2\pi\hat{s}$. In the shifted metric case, on the other hand, the shift of the y coordinate is split into as many pieces as there are parallel points in the simulation.

Adaptation of parallel derivatives for shifted metric

Since each parallel position now has a different y coordinate, the calculation of parallel derivatives must be adapted to account for the shifts, as has also been shown in Ref. [57]. As various gyrokinetic codes like GS2 [64, 65], GKW [66], and local GENE compute the perpendicular dynamics in Fourier space, a short repetition of the calculation for such cases is given. If the parallel derivatives are computed via fourth-order centered finite differences, then the function values from two neighboring points in each direction enter the computation. In the shifted metric case, the coordinate system changes from point to point, so that in order to calculate the derivative of $f(z)$ at parallel position k , one has to perform the following operation on data from position $k+i$: First execute an inverse shifted metric transformation $y_{k+i} \rightarrow y$ (changing from the coordinate system at point $k+i$ to the field-aligned reference system), then transform $y \rightarrow y_k$ (back to the shifted coordinate at position k). The complete transformation is therefore

$$y_k = y_{k+i} + \left(\frac{g^{xy}}{g^{xx}}|_{k+i} - \frac{g^{xy}}{g^{xx}}|_k \right) \cdot x \equiv y_{k+i} + \chi_{ki} \cdot x. \quad (4.2)$$

Thus, when using a value of f from a parallel point $k+i$, we have to apply a shift when calculating the derivative in terms of the coordinates at point k , given by

$$f(x, y_{k+i}, z_{k+i})|_{y_{k+i}} \rightarrow f(x, y_k - \chi_{ki} \cdot x, z_{k+i})|_{y_k}. \quad (4.3)$$

Here, the label $|_{y_{k+i}}$ is used to indicate that the value has been calculated in the coordinate system y_{k+i} . Due to the discretization, in a real-space treatment an interpolation will in general be required (especially in complicated geometries, where χ_{ki} can take arbitrary values) to evaluate the function values at the actual

spatial grid points. Performing a Fourier transform only in the y direction on the right hand side of the above condition yields

$$f(x, k_y, z_{k+i})|_{y_k} = \int_{-\chi_{ki} \cdot x}^{L_y - \chi_{ki} \cdot x} f(x, y_k - \chi_{ki} \cdot x, z_{k+i}) e^{-ik_y y_k} dy_k. \quad (4.4)$$

Now we shift the y_k coordinate to y_{k+i} ,

$$\int_0^{L_y} f(x, y_{k+i}, z_{k+i}) e^{-ik_y(y_{k+i} + \chi_{ki} \cdot x)} dy_{k+i} = f(x, k_y, z_{k+i})|_{y_{k+i}} e^{-ik_y \chi_{ki} \cdot x}. \quad (4.5)$$

This equation implies that, when using function values from neighboring parallel positions, these values have to be multiplied by a phase factor

$$f(x, k_y, z_{k+i})|_{y_k} = f(x, k_y, z_{k+i})|_{y_{k+i}} e^{-ik_y \chi_{ki} \cdot x}. \quad (4.6)$$

If the x direction is treated in Fourier space as well, the transformation reads

$$f(k_x, k_y, z_{k+i})|_{y_k} = f(k_x + k_y \chi_{ki}, k_y, z_{k+i})|_{y_{k+i}}. \quad (4.7)$$

Radial boundary conditions

According to Eq. 4.7, the shift in y is associated (in Fourier space) to a mode shift in k_x (see also Ref. [32]). Applying the shifted metric to a code which computes both perpendicular directions in Fourier space is therefore only possible if all k_x modes that can occur due to the shifts are present in the system. While in the standard field-aligned approach, the only k_x shifts occur at the parallel ends of the box, the shifts are much smaller in the shifted metric case. To ensure the same radial resolution, a much larger number of k_x modes would be necessary to allow for the shifts. Furthermore, the shifts can be arbitrary in general geometry, so that no straightforward implementation for local Fourier codes is possible.

If, on the other hand, only the y direction is treated in Fourier space, the shifts in that direction become a multiplication with a phase factor (see Eq. 4.6), so that in principle arbitrary shifts become possible. If one wants to emulate flux-tube simulations with such an implementation, however, one has to take into account that the phase shifts in general violate the radial periodic boundary condition that is used in the flux-tube model [32, 57]. Since the phase factor depends on k_y , periodicity can only be fulfilled if the radial box extension L_x is chosen such that the phase factor becomes a multiple of $\exp(i\pi)$ at the radial boundary for each k_y mode. This can, depending on the shear value, enforce very large radial box sizes (corresponding to the small k_x shifts from above) in order to fulfill the periodic boundary condition for every k_y mode—in that case one would face the same problem as in a fully spectral code. Note, however, that global simulations

can anyway only be performed with non-periodic boundaries, e.g. of Dirichlet or von-Neumann type, for which the shifted metric does not cause any problem.

4.2.2 NUMERICAL TESTS OF STANDARD AND SHIFTED METRIC

Since we intend to focus on very basic features of the numerical treatment, the physical complexity in this study is kept low by using only one species (ions) and considering the electrons to be adiabatic, neglecting effects like magnetic fluctuations, collisions, and nonlocal effects. As discussed in Sec. 4.2.1, a straightforward implementation of the shifted metric is only possible for the latter operation mode. Therefore, all simulations with shifted metric have been carried out with the global version of GENE, emulating, however, the local simulations without profile variation.

Effect of radial boundary conditions

To compare the convergence of both shifted and straight (standard) metric with Dirichlet and periodic boundary conditions, linear simulations using a Cyclone Base Case [40] parameter set were performed, choosing $k_y \rho_i = 0.3$ and increasing the radial box size L_x and the number of radial points simultaneously in order to keep the resolution constant. Fig. 16a shows the convergence behavior for periodic boundary conditions. With this approximation, the flux tube simulation always gives the same result, while the shifted metric simulation converges to within 10% of the flux tube result for $L_x \gtrsim 50\rho_i$. At a value of $L_x \approx 67\rho_i$, the shifted metric result is identical to the flux tube one, since with this L_x the periodic boundary condition is exactly fulfilled. The same would also be visible at $L_x \approx 2 \cdot 67\rho_i = 134\rho_i$, but this setting is not included in the scan. For Dirichlet boundaries, on the other hand (see Fig. 16b), the speed of convergence is almost identical for both shifted and straight metric, reaching an accuracy of 10% as soon as $L_x \gtrsim 50\rho_i$. Thus, for global simulations, the impact of the radial boundary condition on the simulation is the same for both the straight and shifted metric approach.

Nonlinear simulations with straight and shifted metric

In Ref. [57], it was shown that turbulence simulations employing standard field-aligned coordinates become inaccurate when studying conditions with large (global) magnetic shear: Although a sheared slab geometry was used, in which, due to the absence of curvature effects, the heat flux at all parallel points should be equal, it was found that parallel transport profiles yielded a ‘ballooned’ structure, i.e. the transport value decreased from the center towards the ends of the flux tube. As a remedy, the shifted-metric approach was put forward, which was able to eliminate the artificial structure. As we have seen above, however, for a flux tube code with periodic boundaries (like the local GENE version), the shifted metric approach cannot be easily implemented. Therefore, we will now study if the standard approach leads to similar problems in a Fourier treatment, and if there is a

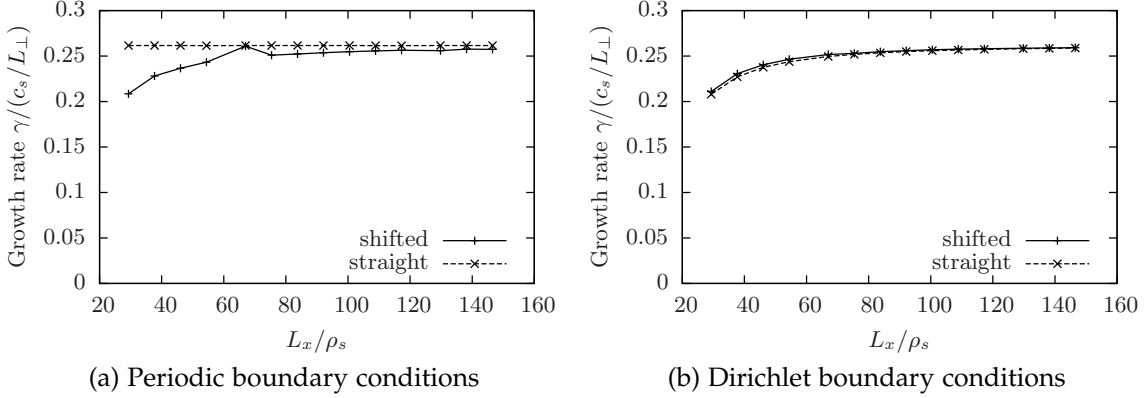


Figure 16: Convergence of linear growth rates with increasing radial box size, keeping the resolution constant.

possibility to overcome them. In Ref. [57], a four-field model was employed that described the nonlinear electron dynamics while assuming cold ions. The physical model thus differs clearly from the kinetic ion/adiabatic electron model that we employ in our study; as we will see, however, both models yield very comparable results with respect to the geometric properties discussed here. For the first simulation, we choose a grid of $60\rho_i \times 20\pi\rho_i$ in the perpendicular plane, with a resolution of $32 \times 32 \times 16 \times 32 \times 8$ grid points in the x, y, z, v_{\parallel} and μ directions, respectively, keeping the same resolution as in the original simulations (but using a smaller box in y direction). The gradients are selected such that ion temperature gradient modes are unstable ($L_{\parallel}/L_T = 10, L_{\parallel}/L_n = 2.2$), and global shear is set to unity to match the metric from Ref. [57]. In Fig. 17a, the parallel heat flux profile obtained from this simulation is depicted. Near the parallel boundaries, zig-zag structures appear which indicate insufficient resolution. This result differs from the one in Ref. [57] in that it can be clearly recognized as a numerical deficiency, while in the original work, there was a smooth reduction in transport towards the parallel boundaries, which is more difficult to be distinguished from the natural ballooning effect one would expect in a toroidal geometry.

As will be illuminated in more detail in the following sections, increasing the magnetic shear value will require an according increase in the radial resolution. Indeed, as it turns out, the zig-zag structures found in the parallel heat flux profiles vanish only when using four times the resolution compared to the initial setup, yielding a completely flat profile (see Fig. 17b) then. For a shear value of $\hat{s} = 2$, this is achieved at a resolution of $n_x = 192$ (Fig. 18).

Influence of numerical schemes

To illuminate the origin of the numerical problems that arise at high magnetic shear, we will first compare the numerical treatments of the perpendicular direction that were used in the original and our simulations: In the original work, a second-order upwind scheme was employed [67], whereas the local GENE simu-

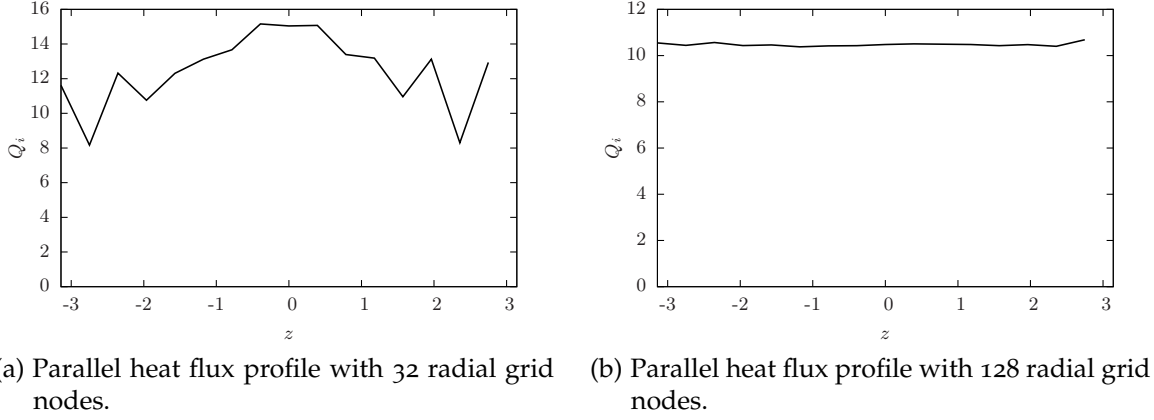


Figure 17: Parallel heat flux profiles obtained from nonlinear slab simulation with global shear $\hat{s} = 1$ at two different resolutions.

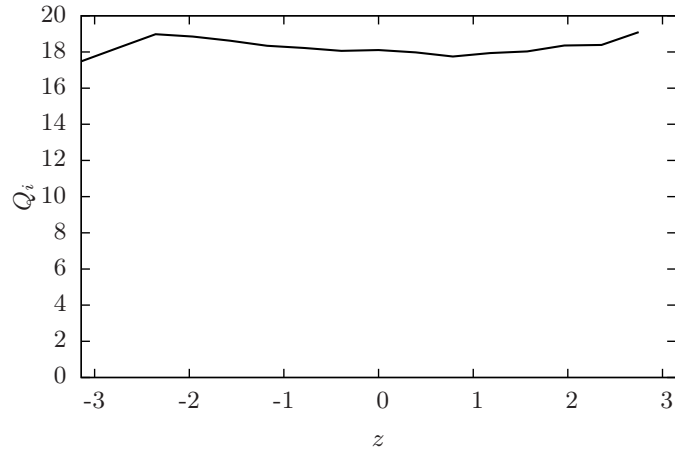


Figure 18: Parallel heat flux profile with global shear $\hat{s} = 2$ and $n_x = 192$. Note that the temperature scale length has been increased to $L_{\parallel}/L_T = 15$ to compensate for the stabilization due to the larger shear value.

lation uses a Fourier treatment, which yields exact derivatives (limited only by machine accuracy). The upwind scheme is intrinsically dissipative, which on the one hand serves to eliminate detrimental aliasing effects by damping small-scale structures. On the other hand, we will see that in combination with the field-aligned coordinates, the dissipation of the scheme facilitates the appearance of the observed spurious ballooning, while at the same time masking its numerical origin.

As has been explained in Sec. 3.2.4, when using a Fourier space treatment of the perpendicular plane, it is possible to perform a clean dealiasing of the nonlinear terms. In contrast to this, the real-space treatment used in [57] requires—and intrinsically contains—dissipation to avoid aliasing effects. To emulate the conditions of these simulations with the GENE code, we add a fourth-order radial hyperdiffusion term, which is available, but not normally used in the local version of GENE. The term added to the right hand side of the Vlasov equation is given by

$$D_x = -\epsilon_x \left(\frac{1}{2} \Delta x k_x \right)^4 f_1, \quad (4.8)$$

where f_1 is the distribution function. The expression in parentheses is chosen such that the prefactor ϵ_x does not have to be adjusted when changing resolution, since $\Delta x = L_x/n_x$ with the number of radial modes n_x . Nonlinear simulations with finite ϵ_x do indeed show smooth ballooning in the transport profile as well as in the temperature, density, and potential fluctuation amplitudes, similar to the simulation from Ref. [57]. In Fig. 19, a nonlinear scan over ϵ_x is shown, which demonstrates a clear dependence of the magnitude of ballooning on the hyperdiffusion coefficient ϵ_x .

As these results show, although turbulence codes with a completely spectral perpendicular treatment cannot employ the shifted metric, correct simulation results can be achieved even for highly sheared flux tubes, provided that a non-diffusive dealiasing scheme, along with the necessary resolution, is employed. A lack of resolution, on the other hand, can be recognized rather easily in the parallel profiles.

Studies with real space treatment of the radial direction

In a global turbulence code, only the y direction can be computed in Fourier space, so that the Orszag scheme cannot be applied to the radial direction anymore, and different dealiasing mechanisms have to be employed. We study such a setup with the global version of GENE, which computes radial derivatives using fourth-order centered differences.

When emulating the Orszag dealiasing scheme in real space through Lagrange interpolation to a finer grid, it achieves, unlike in Fourier space, only a partial elimination of aliasing effects [68], but still it allows the use of a smaller coefficient for the hyperdiffusive term. A saturated nonlinear simulation without such a term was not achieved, however. This difference in behavior can be attributed

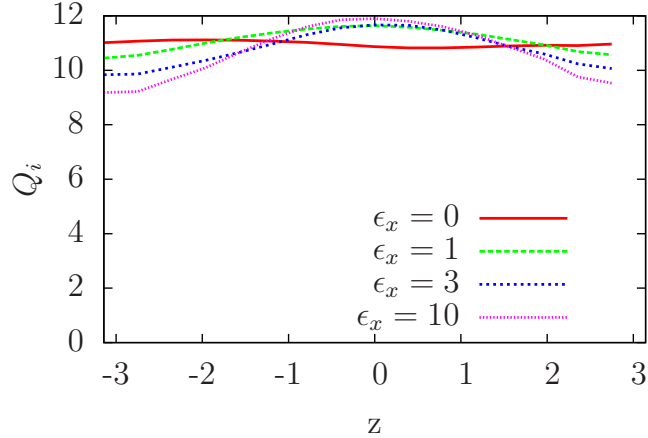


Figure 19: With increasing radial hyperdiffusion coefficient ϵ_x , the parallel heat flux profile exhibits an increasing amount of unphysical ballooning.

to the local nature of the finite-difference scheme, which yields only finite-order accuracy while the spectral derivatives are given through an expansion in global basis functions, achieving arbitrary accuracy. In analogy to the Fourier version, the real space hyperdiffusion term is given by

$$D_x = \epsilon_x \Delta x^4 \left(\frac{d^4 f_1}{dx^4} \right). \quad (4.9)$$

To quantify the amount of spurious ballooning found in a real-space simulation with standard metric, a resolution scan was conducted. For simplicity, we chose again a sheared slab geometry with a global shear value of $\hat{s} = 2$ and a radial box length of $L_x = 80\rho_i$. This specific value of L_x was chosen to allow for the use of periodic radial boundary conditions for comparison with the shifted metric. For each chosen resolution, a scan in ϵ_x was performed to find the lowest possible value of hyperdiffusion with which a saturated simulation could be achieved. Figure 20 shows the results of the resolution scans with and without shifted metric. The curves labeled only by n_x are runs which use the nonlocal version of GENE with standard metric, emulating the local code setup. As can be seen, increasing the radial resolution increases the accuracy with which slab modes are represented, but completely flat heat flux profiles can, for this shear value and box length, not even be achieved for 256 radial grid nodes, making converged simulations very expensive. A sixth-order centered difference scheme was also tested in conjunction with a sixth-order hyperdiffusion term, but this yielded only marginally better results than the corresponding fourth-order runs.

With shifted metric, even for relatively low resolution an accurate representation of the slab heat flux profile is obtained, shown here for three different radial resolutions.

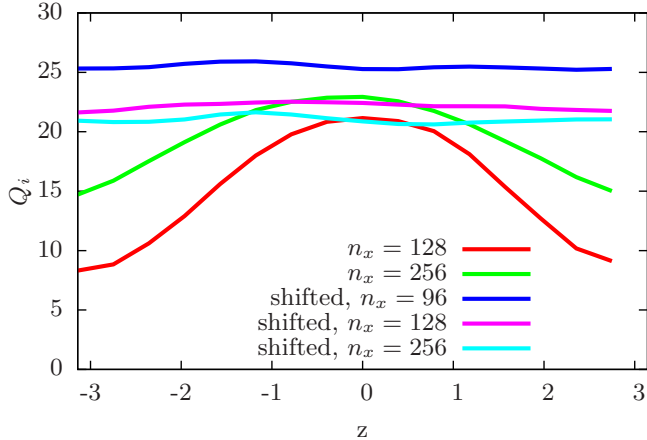


Figure 20: Parallel heat flux profiles with and without shifted metric in the nonlocal code version.

Influence of the nonlinearity implementation

Another test involved the implementation of the Arakawa-type nonlinearity described in Sec. 3.2.4, which allows for stable nonlinear saturation even when running without an additional radial hyperdiffusion term, yielding very robust code operation. However, in such simulations some spurious oscillations occur at the smallest scales, which should be prevented by a small hyperdiffusion contribution to yield more physical results.

The same resolution scan as mentioned above was done with the Arakawa-type nonlinearity in order to find out whether this yields improvement over the standard treatment. The parallel heat flux profiles for different radial resolutions are shown in Fig. 21. As can be seen, the spurious ballooning effect is not completely avoided, but clearly reduced when compared to the standard implementation. In addition, the transport values of the runs with the Arakawa representation are somewhat closer to the converged values. Also shown in the figure is the comparison between the converged local (Fourier) simulation and the shifted metric simulation at the same resolution, which coincide very well.

4.2.3 DISCUSSION OF THE NUMERICAL RESULTS

Understanding the origin of artificial ballooning

To shed some light on what causes the spurious ballooning induced by radial hyperdiffusion, we will now examine a nonlinear slab run without radial hyperdiffusion (conducted with the local GENE version)—i.e. a run where the transport profiles found in our simulations are flat, as they should be. In the GENE post-processing tool, one can produce z -profiles not only of transport quantities, but also of the fields and various moments of the distribution function. Adding all contributions, one arrives at flat profiles as expected; however, when fixing k_y to a single value and examining specific k_x modes of the electrostatic potential, these

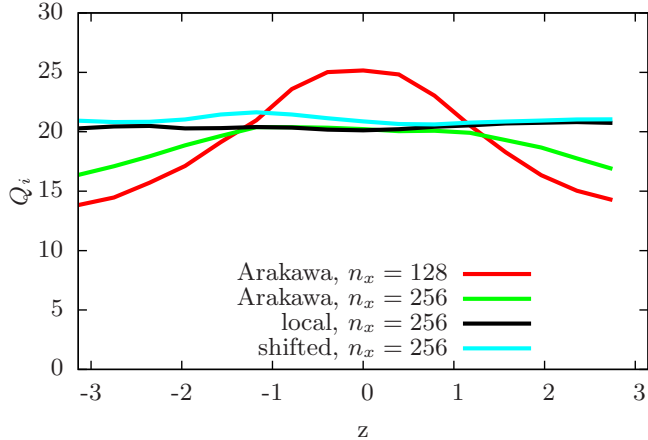


Figure 21: Parallel heat flux profiles with an Arakawa-type nonlinearity, the Fourier-space code version and the nonlocal version with shifted metric.

can be found to exhibit peaked parallel profiles with a relatively short parallel correlation length. The peak position depends on the value of k_x one is studying (see examples in Figures 22a and 22b).

The peaked behavior of each perpendicular mode (k_x, k_y) is directly linked to the drive that each of these mode pairs is subjected to: In Fourier space, the gyroaveraged potentials, which determine the strength of the gradient drive, are calculated by just multiplying the potential with a Bessel function $J_0(k_\perp^2 \rho^2)$. Here, ρ is the gyroradius and k_\perp^2 is given by

$$k_\perp^2 = g^{xx} k_x^2 + 2g^{xy} k_x k_y + g^{yy} k_y^2. \quad (4.10)$$

Since $g^{xx} = 1$, $g^{xy} = \hat{s}z$, and $g^{yy} = 1 + \hat{s}^2 z^2$ in a straight metric slab, k_\perp^2 is a parabola. When varying k_x , the position of the parabola's apex at $z_0 = -k_x / (\hat{s}k_y)$ —where the mode experiences the strongest drive—is shifted along the field line. Thus, the ballooning caused by radial hyperdiffusion becomes understandable: While the $k_x = 0$ mode peaks at the center of the flux tube, the higher k_x modes that peak off the center are increasingly damped and the total profile becomes peaked. As the shear is increased, modes which peak at a specific position z_0 have an ever higher k_x and therefore experience stronger damping, explaining the stronger spurious ballooning effect.

Let us now examine Figures 22a and 22b more closely: Fig. 22a was done with the local version of GENE and with a rather large value of hyperdiffusion, while Fig. 22b was done with zero radial hyperdiffusion, as is standard in the code. Both figures show, for $k_y \rho_i = 0.75$, the same k_x modes with the values $k_x \rho_i = 0, \pm 0.942, \pm 1.885$, where the mode with central peak is the $k_x = 0$ mode and the other peaks depart from the center with increasing $|k_x|$. As is clearly visible, in Fig. 22a, with activated hyperdiffusion, the modes that peak off the center are rather strongly damped and their peak positions altered, coinciding with a peaked transport profile (solid line in the Figure). On the other hand, in Fig. 22b, where

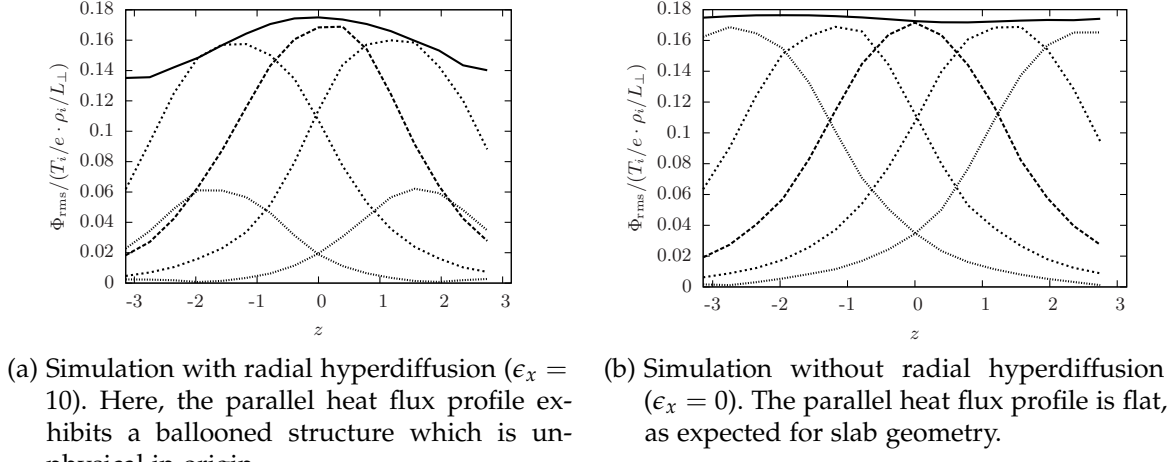


Figure 22: Time-averaged electrostatic potential for $k_y \rho_i = 0.75$ and $k_x \rho_i = 0$ (dashed), $k_x \rho_i = \pm 0.942$ (shorter dashes) and $k_x \rho_i = \pm 1.885$ (dotted) for simulations with different hyperdiffusion coefficients, demonstrating their influence on the parallel heat flux profile (solid lines).

hyperdiffusion is turned off, there is no damping of finite- k_x modes and therefore the resulting transport profile is flat.

Considering the impact hyperdiffusion has on modes with finite k_x , one can expect a strong impact also on the heat flux spectra. Indeed, Figs. 23a and 23b show some qualitative differences. While the k_x spectra look very similar for $k_x \lesssim 1$, there is a significant change of behavior for $k_x \gtrsim 1$: Whereas the undamped spectrum decays in a roughly straight line, the fall-off of the damped spectrum is strongly curved, so that the difference quickly becomes several orders of magnitude. This stronger fall-off is what disturbs the slab character of turbulence.

In the k_y spectrum, although not directly affected by radial hyperdiffusion, there are still some differences to be found: While the deviation of the x -damped spectrum from the undamped case is much weaker than in the k_x spectra, the difference between both cases is still an order of magnitude at the high- k end of the spectrum. On the other hand, the coincidence of the curves for lower k_y values is not as good as in the radial spectra. The transport peak is slightly shifted toward lower k_y , while the spectral heat flux density differs by up to a factor of two for the lowest k_y . The overall heat flux, however, is barely affected by these deviations: For the 'clean', unbalanced case, we find an ion heat flux of 11.0 ± 1.0 in units of $v_{ti} \rho_i^2 / (n_i T_i L_\perp)$, while in the balanced case the value is 10.7 ± 1.2 .

Applying these results to the situation of the local Fourier code, it is easy to understand the origin of the zig-zag structures observed in Fig. 17a: Although there is no explicit k_x -dependent damping in the code, all unresolved modes are set to zero. At too low radial resolution, as is the case in our first simulation, these modes will couple strongly to the modes that are taken into account, affecting the computation of parallel derivatives near the parallel boundaries.

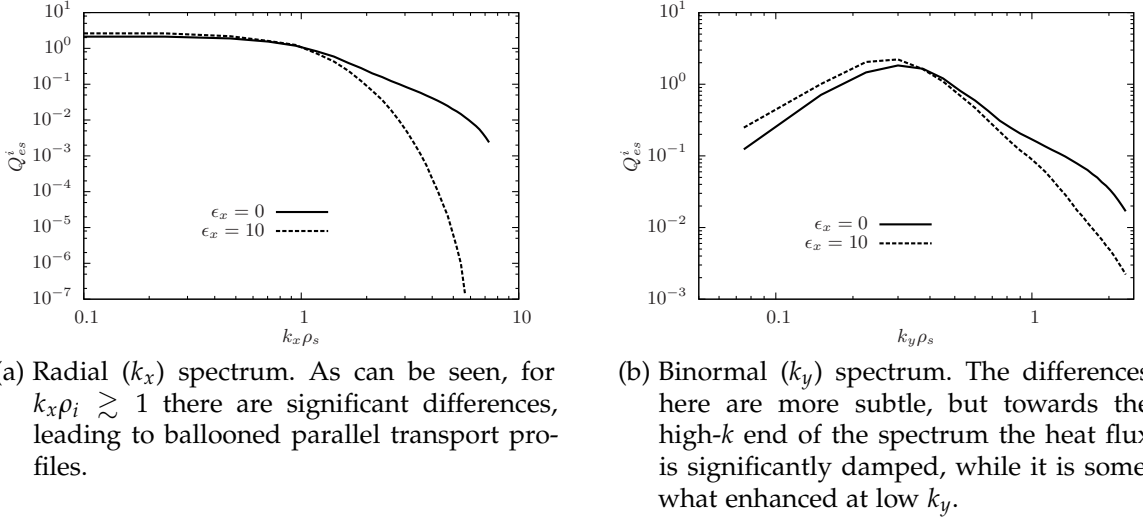


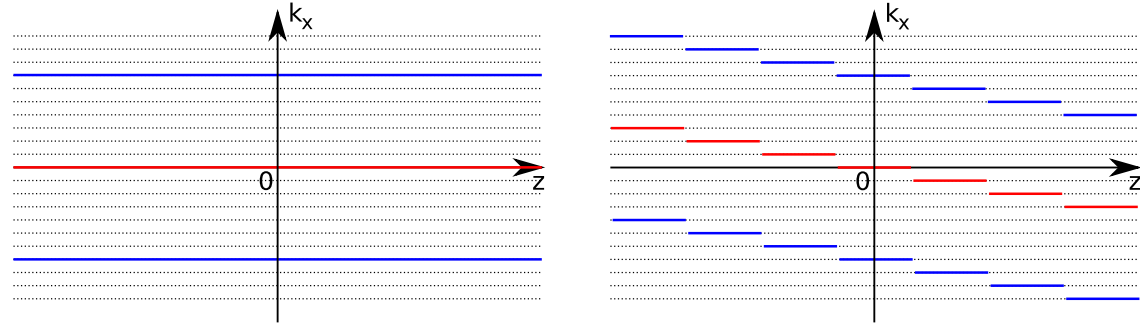
Figure 23: Heat flux spectra obtained from simulations with ($\epsilon = 10$) and without ($\epsilon = 0$) radial hyperdiffusion.

Understanding the correction via the shifted metric

Having discussed the effect which radial hyperdiffusion has on turbulence simulations in slab geometry, it is now straightforward to see how the shifted metric approach can avoid peaked profiles even with a dissipative numerical scheme. For easier understanding, we provide an explanation in terms of k_x and k_y modes instead of viewing the problem in real space.

With the straight metric approach, magnetic shearing is taken into account via the shape of the flux tube, i.e. the flux tube is twisted when following the field line. Thus, when calculating parallel derivatives, one can use the values from the same k_x mode, since the shearing is automatically included. In the shifted metric approach, however, the flux tube is not deformed, but the shearing must ‘manually’ be taken into account by applying the k_x shifts discussed above (see Figures 24a and 24b for an illustration). The radial (hyper-)diffusion term, on the other hand, is proportional to some (even-numbered) power of k_x , regardless of whether the straight or shifted metric is used. When using straight metric, the dissipation for a particular k_x mode, is equally strong over the entire parallel length of the flux tube. With shifted metric, the same is true, but the k_x value used to refer to one sheared eddy depends on the parallel position, and thus the damping of that mode also varies.

As shown above, the parallel transport profile in slab geometry consists of many single peaks that are added up. With straight metric and hyperdiffusion, modes with finite k_x are damped, so that the transport profile is affected only off the center position (since this is where the $k_x = 0$ mode peaks). With shifted metric, on the other hand, the metric is changed such that the modes which have a constant finite k_x in straight metric, pass through $k_x = 0$ exactly where they peak. This



(a) With straight metric, parallel derivatives follow the sheared magnetic field automatically when using the same k_x mode, and a large shift has to be applied at the ends of the z domain in order to connect to beyond the flux tube end.

(b) With shifted metric, a small k_x shift has to be applied from each parallel position to the next in order to follow the sheared magnetic field, and periodic boundary conditions suffice to connect to the next flux tube. In straight metric, the mode drawn in the picture would correspond to $k_x = 0$ all along the flux tube.

Figure 24: Illustration of parallel derivatives and boundary conditions with straight and shifted metric.

way, the peak of one mode is always undamped; instead only its tails are damped, resulting in a flat overall transport profile.

Another way to put it is that while with straight metric hyperdiffusion is aligned with the modes (since the grid on which hyperdiffusion is applied is sheared along with the eddies), with shifted metric, the hyperdiffusion is (as is the grid) dealigned from the sheared modes and thus procures equal damping to each mode and does not ‘prefer’ particular ones.

A possibility to avoid introducing dependencies that are not present in the original system is the usage of a dissipation term proportional to k_{\perp}^{2n} ($n = 1, 2, \dots$), since k_{\perp} is a physical wavenumber, independent of the coordinates used to describe the system. Furthermore, if only a radial dissipation is desired, one can employ a term proportional to $k_r^{2n} = (k_x + k_y g^{xy}/g^{xx})^{2n}$.

4.2.4 INVARIANCE OF PHYSICS

Finally, it should be noted that shifting the y coordinate does not change the physics contained in the simulation. This can be seen when inserting the coordinate transformation $y_k = y - x \cdot g^{xy}/g^{xx}$ and the shifted $k'_x = k_x + k_y \cdot g^{xy}/g^{xx}$ into Eq. 4.10, which gives k_{\perp}^2 , the Fourier space counterpart to the perpendicular Laplacian which enters the Poisson and Ampère equations. Considering that $g^{\rho\sigma} = \nabla\rho \cdot \nabla\sigma$ for $\rho, \sigma \in x, y, z$, the shifts all cancel to yield the original dependence. The same is true for the $E \times B$ nonlinearity and the perpendicular Jacobian $J^{-1} = g^{xx}g^{yy} - (g^{12})^2 = |\nabla x|^2|\nabla y|^2 - (\nabla x \cdot \nabla y)^2$: One merely transfers part of the z dependence from the metric coefficients to a new z dependence of the radial derivative (giving the shifts in k_x).

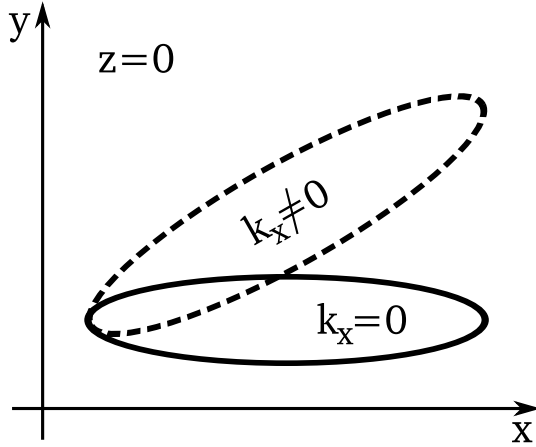
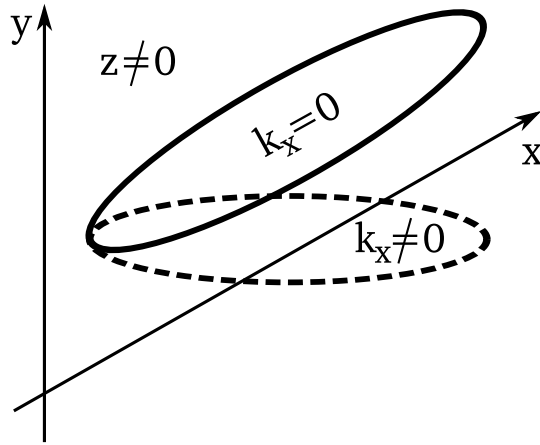


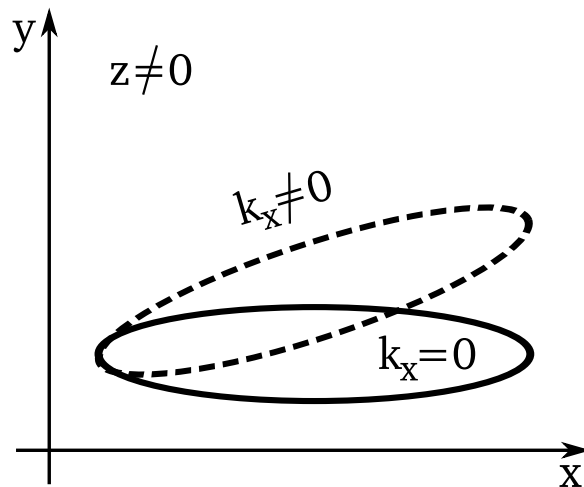
Figure 25: Perpendicular plane at the reference position $z = 0$, where $e_x \perp e_y$ both for shifted and straight metric.

However, simulations using either of the two approaches differ in the set of modes which make up the perpendicular plane. While with shifted metric, each parallel position has a mode that points radially outward, with straight metric this mode is in general only present at the reference position, where the grid is perpendicular (Fig. 25). At all other positions, the mode labeled $k_x = 0$ is tilted away from the outward direction and the grid has a rhomboid shape (Fig. 26a). The direction radially outward is in general only approximately contained in the simulation, and if radial hyperdiffusion were used, this direction would be damped since it is labeled with finite k_x values. In an undamped simulation, on the other hand, modes which follow the sheared field are *not* preferred and a correct treatment of perpendicular dynamics is ensured. Note, however, that such simulations may still require large radial resolutions to take into account all modes which generate relevant transport.

With shifted metric, the situation is inverted: At the reference position, there is no difference with respect to the standard metric, but when going to $z \neq 0$ the grid remains perpendicular. Therefore, in a simulation with dissipation (which is a likely setup for a shifted-metric simulation), the modes which point radially outward are now preferred over the damped $k_x \neq 0$ modes (Fig. 26b). Therefore the parallel correlation length of structures which follow the sheared field will suffer some artificial reduction. This is particularly important for small-scale eddies, since the k_x shifts (given by Eq. 4.7) are proportional to the k_y wavenumber. A small eddy in a heavily sheared magnetic field thus quickly connects to k_x modes which are not resolved anymore, and is damped to avoid aliasing. Therefore, in situations with large local shear, it must be ensured via convergence tests that the radial resolution is sufficient to represent the evolution of turbulent structures along the field lines correctly.



(a) Straight metric: Here, e_x and e_y are no longer orthogonal. Radial hyperdiffusion acts on modes with finite k_x , which are tilted with respect to e_x .



(b) Shifted metric: e_x and e_y are still orthogonal, so that radial hyperdiffusion now acts only on modes which do not point radially outward.

Figure 26: Illustration of radial basis vector alignment at a finite parallel position $z \neq 0$, for both straight and shifted metric.

4.2.5 IMPLICATIONS FOR TURBULENCE SIMULATIONS

In this section, the properties of two different variants of field-aligned coordinate systems for numerical simulations of turbulence have been examined. The first approach, which is the well-known field-aligning transformation, generates a coordinate system whose perpendicular coordinates are nonorthogonal in the case of sheared magnetic fields. The other approach is the shifted metric ansatz, which yields a whole set of coordinate systems, one for each position along the field line, each of which has orthogonal basis vectors in the perpendicular plane.

As was known from earlier work, turbulence simulations employing standard field-aligned coordinates can exhibit spurious parallel dependencies when studying highly sheared magnetic geometries. This effect was found to arise from a lack of radial resolution, and can be amplified by the use of a radial hyperdiffusion term (or a dissipative numerical scheme), which is often used to prevent aliasing effects caused by energy transfer to smaller scales than described by the grid. It was studied how the creation of artificial parallel structures can be prevented in different numerical treatments. Since flux-tube codes which compute the perpendicular dynamics in Fourier space need to use periodic radial boundary conditions, they cannot implement the shifted metric approach. However, such codes may be run without hyperdiffusion, if an appropriate dealiasing scheme, e.g. the three-halves rule, is used. Simulations performed in this way do not exhibit the spurious ballooning observed in damped simulations, provided that the radial resolution is high enough. A lack of resolution, on the other hand, leads to zig-zag structures in the parallel profiles and is thus easily identifiable, a property that can be important when there is also physical ballooning, e.g. in toroidal geometry.

In global codes, on the other hand, the radial boundary conditions can not be periodic, excluding the use of Fourier schemes. Therefore, to avoid aliasing effects, one has to resort to a numerical diffusion term, which can, as shown above, lead to the creation of artificial parallel structure. Although this situation can again be improved by increasing the radial resolution, while at the same time keeping hyperdiffusion as low as possible (possibly using a nonlinearity scheme with low dissipation like the Arakawa discretization), reaching a converged simulation proves more expensive than with a Fourier code.

These codes, on the other hand, offer the possibility to implement the shifted metric approach, which avoids the creation of spurious parallel structures. Still, large local or global shear will lead to strong twisting of the simulated eddies with respect to the box, resulting again in the need to perform convergence checks to ensure sufficient radial resolution.

4.2.6 GENERALIZATION TO GLOBAL SIMULATIONS

In the previous sections, all simulations used local geometry, i.e. no radial variation of the metric coefficients was considered when applying the shifted metric transformation. Its generalization is given by

$$y_k = y - \int_{x_0}^x \frac{g^{xy}}{g^{xx}} \Big|_{x', z_k} dx',$$

satisfying the above requirement. When calculating parallel derivatives (Sec. 4.2.1), again one has to consider shifts in the coordinate system. The transformation from the y_{k+i} to the y_k coordinate reads in its global version

$$y_k = y_{k+i} + \int_{x_0}^x \left(\frac{\frac{g^{xy}}{g^{xx}} \Big|_{x', k+i} - \frac{g^{xy}}{g^{xx}} \Big|_{x', k}}{g^{xx}} \right) dx' \equiv y_{k+i} + \chi_{ki}.$$

Note that under these circumstances, it is no longer possible to write the shift as $\chi_{ki}x$, but the radial integration element is now contained in the above definition of χ_{ki} . Function values from neighboring parallel positions therefore are transformed as

$$f(x, y_{k+i}, z_{k+i}) = f(x, y_k - \chi_{ki}, z_{k+i}),$$

or

$$f(x, k_y, z_{k+i}) \Big|_{y_k} = f(x, k_y, z_{k+i}) \Big|_{y_{k+i}} e^{-ik_y \chi_{ki}},$$

when using a Fourier decomposition in k_y , which is the expression that is implemented in GENE and will be used in Chapters 5 and 6.

4.3 TREATMENT OF STRONGLY SHAPED PLASMAS

After having discussed the numerical impact of strongly sheared magnetic fields, we now turn to the numerical implications of plasma shaping. In many modern tokamaks, additional external coils are used to deform the plasma in an elliptical and/or triangular fashion, yielding better confinement than the simple circular cross-section of earlier devices. The strongest effects of these additional coils can be expected in the plasma edge, since their fields have to penetrate the plasma from outside. Furthermore, the edge is often characterized by very steep pressure gradients, which lead to the Shafranov shift that had already been discussed in Sec. 4.1.2, resulting in a compression of flux surfaces on the low field side.

For such a magnetic field geometry, when setting up the spatial grid using the coordinate system as defined in the previous sections (specifically, using $z = \theta$ or $z = \zeta/q$ as parametrization for the parallel coordinate), one effect that can be observed is that the number of parallel grid points on the low-field side of the plasma decreases significantly as one approaches the plasma edge. Due to the fact that the turbulence 'balloons', i.e. is most intense on the outboard side, this

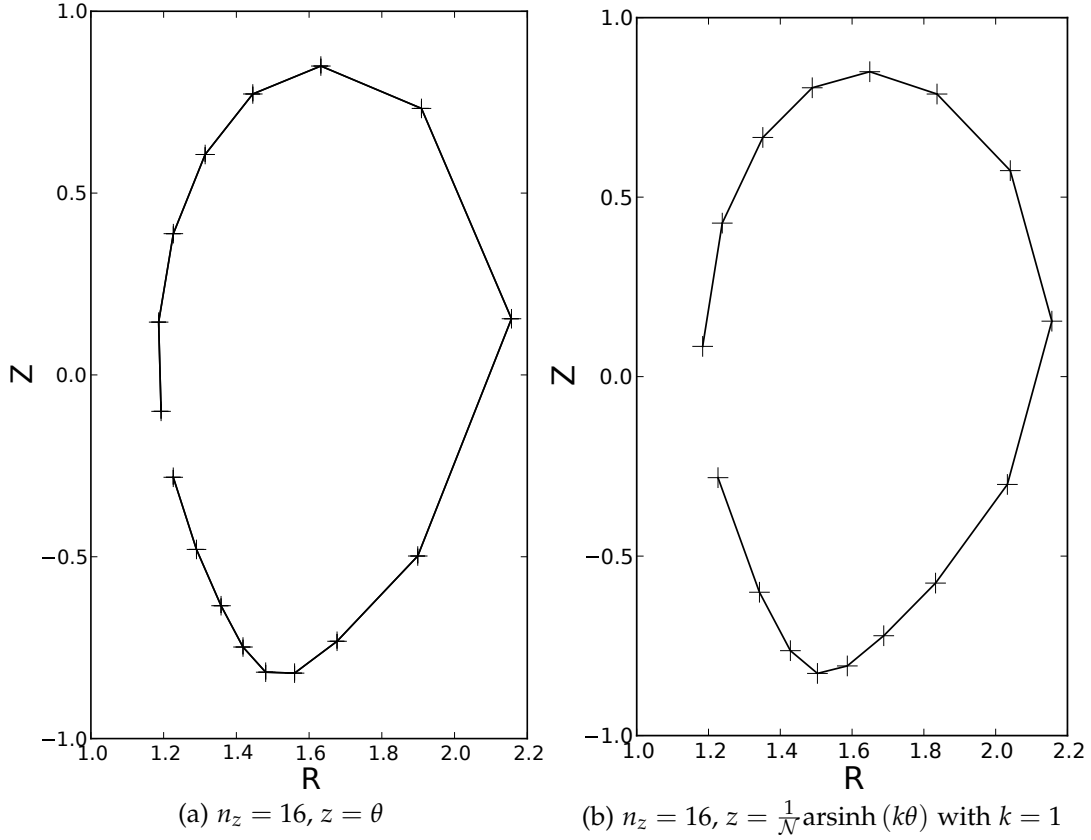


Figure 27: Distribution of parallel grid points using the standard parametrization and an optimized parametrization of the parallel coordinate.

leads to strongly increased requirements in parallel resolution. The distribution of the grid points is unfavorable, however, and a large number of grid points is required to appropriately resolve the important dynamics. To counter this effect, an alternative definition of the parallel coordinate may be used, leading to a more favorable grid point arrangement (for illustration, see Figure 27).

For the new parallel coordinate, we choose

$$z' = \frac{1}{N} \operatorname{arsinh}(kz),$$

where k is an arbitrary factor influencing the coordinate scale. N is a normalization factor which ensures that $z' \in [-\pi, \pi]$ and is given by

$$\frac{1}{N} = \frac{\pi}{\operatorname{arsinh}(k\pi)}.$$

Using these definitions, it is straightforward to show that the parallel boundary condition remains unchanged.

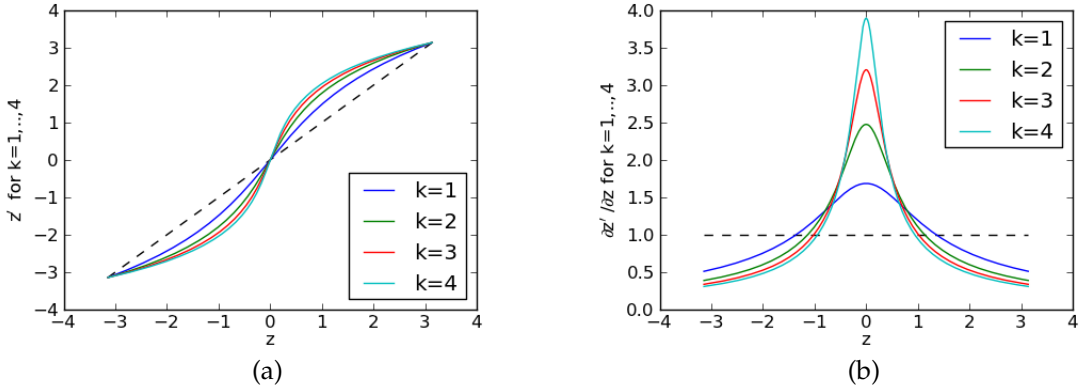


Figure 28: Dependence of z' (a) and its derivative (b) on the original z coordinate. For reference, the latter is also drawn as a black dashed line. The plots demonstrate how the outboard resolution is increased at the expense of the inboard side resolution.

The transformation to the z' coordinate is achieved by applying the chain rule to all metric coefficients involving the z' coordinate, e.g.

$$g^{yz'} = \nabla y \cdot \nabla z' = \nabla y \cdot \nabla z \frac{\partial z'}{\partial z} = g^{yz} \frac{\partial z'}{\partial z} = g^{yz} \frac{k}{\mathcal{N} \sqrt{(kz)^2 + 1}}.$$

The coefficients to be transformed are g^{xz} , g^{yz} , g^{zz} , the Jacobian determinant J and $\partial B / \partial z$. Afterwards, all geometry coefficients are interpolated onto a grid that is equidistant in z' in order to suit the finite difference derivative schemes employed in the parallel direction. To ensure an accurate interpolation, the geometry coefficients are generated on a very fine grid (using 1024 parallel grid nodes by default) and then interpolated onto the comparatively coarse grid used for the simulation. Note that using this procedure, the resolution on the low-field side is increased at the expense of the resolution on the high-field side, which might not be desirable in some cases (e.g. in the plasma core, where the grid points are already adequately distributed). For illustration, Fig. 29 shows a scan over the parallel resolution for typical ASDEX Upgrade core parameters, using the above coordinate redefinition for $k = 0, 2, 4$, where the label ' $k = 0$ ' indicates that no optimization is performed, and the original $z = \theta$ coordinate is used. Obviously, with increasing parallel resolution the same result is achieved in all cases, but for these parameters, there is little gain from using the optimized coordinate. Demonstration of a case with significant improvement is deferred to Sec. 6.4.2.

Note that there exists also another approach detailed in Ref. [69], which uses conformal coordinates to avoid the stretch-squeeze behavior of the considered simulation domain, while at the same time employing a reduced form²³ of the shifted metric approach. As a drawback, due to the form of the coordinate def-

²³ Only the global shear dependence is removed from the metrics, while the local shear dependence—which can be very strong in edge plasmas—persists.

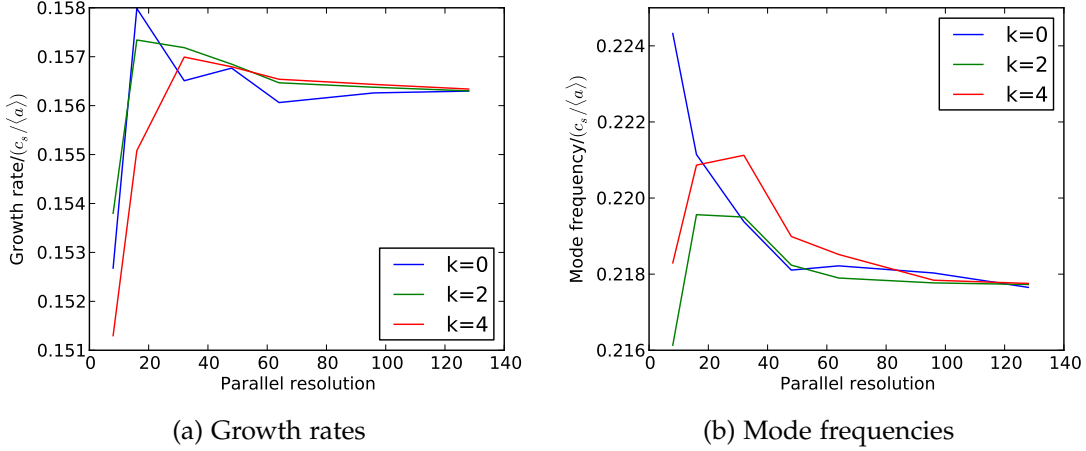


Figure 29: Demonstration of convergence for the standard parallel coordinate θ (blue) and the optimized coordinate, using $k = 2$ and 4.

initiation, simulations must always keep the full flux surface and no truncation of the toroidal domain is allowed. Simulations of hyperfine ETG turbulence as presented in this thesis would in general not be feasible with that constraint, which is why we choose to perform all simulations using standard field-aligned or (fully) shifted metric coordinates. Resolution requirements due to strong shaping are—at least for the parallel direction—dealt with by employing the simple remapping procedure outlined above.

4.4 SUMMARY

In this chapter, details of a newly implemented geometry interface to the widely used EFIT file format were described. In order to adapt the field line tracing procedure of the TRACER code to global simulations, a simple coordinate transformation was applied to both the binormal (y) and parallel (z) coordinate. Benchmarks of the new interface were performed, comparing local simulations with shaped geometry to the results obtained with the stand-alone version of TRACER. Furthermore, both local and global circular geometry simulations were compared using the analytical circular model, a CHEASE input file, and an EFIT input file, finding good statistical agreement. Generally, it was found that nonlinear heat fluxes tend to exhibit better agreement than linear growth rates and mode frequencies, since small deviations between the various input methods appear less prominently at the relatively low k_y wavenumber driving the strongest transport.

In conclusion, the TRACER-EFIT interface can be expected to deliver reliable results in both local and global cases. In addition, it is more convenient to use than the interface to the stand-alone TRACER code, since it allows scans in the radial position or radial/parallel resolutions without having to provide new input files, facilitating parameter studies and convergence tests.

In Sec. 4.2, the properties of the standard field aligned coordinate system were compared to the shifted metric approach. For highly sheared geometries, it was found that the shifted metric approach can relax the resolution requirements somewhat. In addition, the simulations showed that in the case of a lack of resolution, the combination of a perpendicular Fourier space treatment with zero-boundary conditions allows a clear distinction between simulations suffering from a lack of resolution, or simulations exhibiting a naturally occurring ballooned mode structure. For this study, the shifted metric has been implemented into GENE in its global version, and will be used for a number of simulations in both of the following chapters.

In the last part of this chapter, a method for optimizing the distribution of grid points in the parallel direction was described. As will be shown in Chapter 6, this method yields significant savings in the parallel resolution required for the accurate simulation of ETG turbulence in the plasma edge.

5

GLOBAL SIMULATIONS OF INTERNAL TRANSPORT BARRIERS

5.1 OVERVIEW

The recent addition of global capabilities to the GENE code [26, 29, 33] opens up the possibility to study plasma conditions in which the local approximation, which had been the standard in earlier code versions, is no longer valid. Commonly, the transition from global to local turbulence is measured by the quantity ρ^* , which denotes the ratio of a thermal ion gyroradius to the minor radius a of the considered device,

$$\rho^* = \frac{\rho_i}{a}.$$

Scans in this parameter usually find (see Fig. 30) that the heat diffusivities obtained from global and local turbulence simulations agree well for $\rho^{*-1} \gtrsim 300$ [70, 71, 72], and that the heat diffusivity in this regime scales like the so-called gyro-Bohm diffusivity, i.e.

$$\chi \propto \chi_{\text{GB}} = \rho^* \chi_B = \rho^* \rho_i v_{ti}.$$

For smaller devices²⁴, on the other hand, the diffusivity scales like the Bohm diffusivity χ_B defined in the above equation. The impact of the diffusivity on the energy confinement time can be estimated by (see, e.g., Ref. [75])

$$\tau_E \propto a^2 / \langle \chi \rangle.$$

Therefore, the difference between gyro-Bohm and Bohm-like transport has a direct impact on the scaling of the energy confinement with the device size. In the more favorable gyro-Bohm case, we obtain $\tau_E \propto 1/\rho^*$, i.e. improved confinement in a larger machine. Being able to evaluate the effects of the system size on turbulent transport on a first-principles basis is therefore one of the primary benefits of global gyrokinetic simulations.

²⁴ The turnover point at $1/\rho^* \sim 300$ corresponds to a tokamak with a size roughly between ASDEX Upgrade [73] and JET [74].

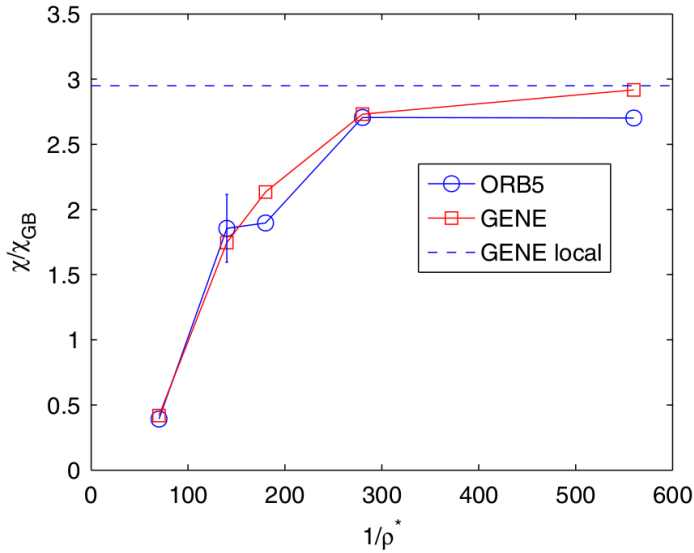


Figure 30: Scaling of the heat diffusivity with the system size parameter ρ^* . At about $1/\rho^* \sim 300$, the transition from Bohm scaling to gyro-Bohm scaling can be observed. Source: Ref. [72]

Of special interest with regard to the physics of transport barriers is a recent study ([72], see also the discussion in Sec. 5.7), which has demonstrated that it is actually the modified parameter

$$\rho_{\text{eff}}^* = \frac{\rho_{\text{ref}}}{\Delta_r}$$

to which the turbulent diffusivity is sensitive rather than to ρ^* . Here, Δ_r represents the width of the region where turbulence is driven, i.e. the characteristic width of the (temperature/density) gradient profile. The diffusivity scaling with ρ^* is, of course, still valid if one is interested in the effect of transferring given input profiles to a larger device (i.e. $\Delta_r \propto a$).

As a consequence of the ρ_{eff}^* scaling, even in large devices such as ITER, which have small ρ^* , the local approximation will fail in regions of steep profile gradients such as core and edge transport barriers, where ρ_{eff}^* is large. Achieving a consistent physical picture of such barriers is a highly important subject, as transport barriers are crucial to the efficient operation of a future fusion reactor.

In the present chapter, comprehensive global simulations of internal transport barrier discharges are performed in order to gain insight into the properties of turbulent transport under such conditions. In Sec. 5.2, the experimental properties of the relevant discharges are described, and a short overview on previous theoretical results on this topic is provided. Sec. 5.3 details the setup of the simulations and the input profiles and magnetic equilibria. In Sec. 5.4, the results obtained from global simulations using the nominal parameters are presented. Sec. 5.5 is dedicated to a sensitivity study assessing the robustness of the results from the preceding section, and in Sec. 5.7, we provide some scaling arguments to explain the simulation results. In Sec. 5.8, the results are summarized.

5.2 EXPERIMENTAL SITUATION AND PREVIOUS FINDINGS

5.2.1 ELECTRON INTERNAL TRANSPORT BARRIERS IN TCV

In the present work, we study so-called “electron internal transport barriers” (eITB) obtained at the Tokamak à Configuration Variable (TCV) [76], which is located in Lausanne, Switzerland. The TCV tokamak was constructed with the aim to examine the effect of plasma shaping on the confinement quality and was therefore designed with a flexible shaping system, allowing it to achieve plasmas of very variable elongation and triangularity without requiring changes to the hardware. In the beginning of the last decade, successful steady-state plasma discharges were reported [77], in which the entire plasma current could be driven solely by electron cyclotron current drive (ECCD), requiring no additional inductive current drive by the central solenoid. Later, it was shown [78] that by imposing hollow current profiles, transport barriers in the electron temperature and density could be triggered, drastically improving the energy confinement time (characterized by a confinement improvement over TCV L-modes of a factor²⁵ $H_{RLW} \sim 3 - 6$). In the present chapter, we study a set of discharges, which differ solely by the addition of a small ohmic current in the very core of the plasma [81]. Depending on whether this current subtracts from or adds to the combined bootstrap and EC-driven current, this slight modification allows a substantial improvement or degradation of the ITB quality.

In this chapter, we will examine two discharges, 29863 and 29866, which were presented in Ref. [82] and were intended to study whether the presence of flux surfaces with low-order rational safety factors had a significant impact on the formation of the barrier. This was done by changing the total plasma current and thereby varying the minimum of the q -profile. In the reference discharge 29867 (not separately simulated here), the current was fully non-inductive starting from $t = 0.5$ s, from when the ohmic transformer current, which induces the plasma current, is held constant (see Fig. 31 for the relevant timetraces). In contrast to this, in discharge 29863 a loop voltage of +90 mV was induced (visible in the slow decay of the transformer current), which enhanced the core plasma current and led to a confinement degradation. Discharge 29866, on the other hand, had a negative induced loop voltage of -30 mV, driving a counter-current which resulted in improved confinement.

Due to the relation between current and safety factor profile²⁶, a hollow current profile corresponds to negative magnetic shear values. The experimental results therefore point to the conclusion that stronger negative shear in the core facilitates the occurrence and enhances the strength of an internal transport barrier. In this chapter, we will use the MHD equilibria and plasma profiles from two of the afore-

²⁵ The factor $H_{RLW} = \tau_E / \tau_{E,RLW}$ gives the improvement of the confinement time over the empirical Rebut-Lallia-Watkins scaling [79, 80] for the electron heat transport.

²⁶ The poloidal magnetic field is determined by the enclosed plasma current and in turn, via $\int B^\zeta / B^\theta d\theta = q$, defines the safety factor.

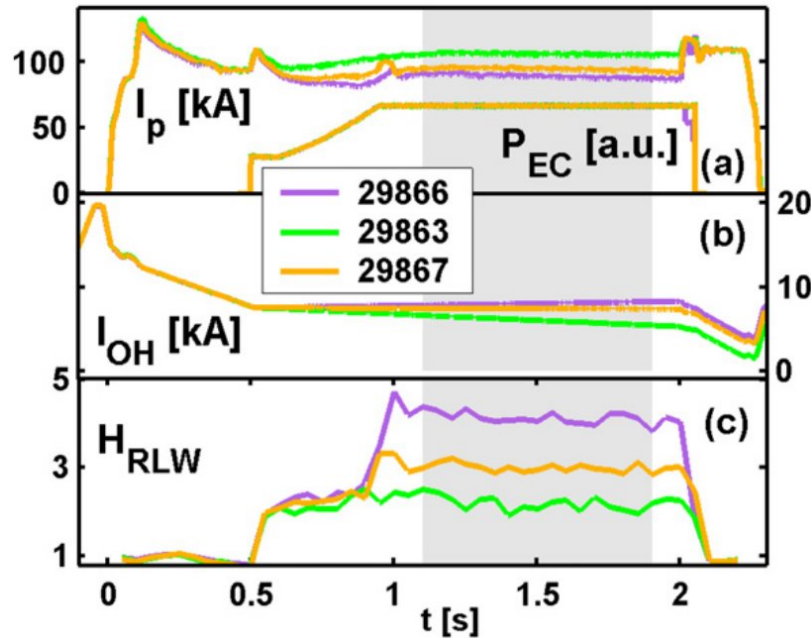


Figure 31: Timetraces [82] of the plasma current I_p , the ohmic transformer current I_{OH} and the confinement scaling factor H_{RLW} in the discharges studied here. See text for more information.

mentioned discharges and verify the effect of this shear reversal on the turbulence. In addition, the precise mechanisms determining the shape of the barrier will be investigated.

In the above experiments, there is no external momentum source in the experiment as the discharges have no neutral beam heating, and the electron momentum associated with the EC-driven current is negligible. Plasma rotation does therefore not appear to have a significant role in influencing the barrier steepness, and we will initialize the simulations with zero rotation. The particle and heat sources used in the present simulations (see Sec. 3.6) do not impose a torque, allowing a free development of the rotation profile. The majority of our simulations will describe one ion species and electrons, thereby assuming a pure deuterium plasma. The effect of the impurity content on turbulence is investigated in dedicated simulations.

5.2.2 PREVIOUS THEORETICAL RESULTS

In addition to the experimental investigations, several theoretical studies have been conducted in the past to shed light on the physics of the electron ITB. The first gyrokinetic study [83] of this type of discharge was performed using the linear global code LORB²⁷. Employing a hybrid model composed of a drift-kinetic treatment of the trapped electrons, and an adiabatic approximation for the passing

²⁷ LORB5 has meanwhile been replaced by the nonlinear electromagnetic code ORB5/NEMORB, which features similar capabilities as GENE, using however a particle-in-cell (PIC) approach as opposed to the grid-based GENE code. See Refs. [72, 84] for benchmark results of both codes.

electrons, it was shown that the most unstable modes in TCV eITBs are trapped electron modes (TEMs). It should be noted that this model, due to the simplified treatment of passing electrons, is unable to describe electron-scale instabilities such as ETG modes.

A particularly striking experimental feature, namely the stationarity of the density barrier despite the absence of a core particle source, was later examined in local quasilinear gyrokinetic studies [85, 86]. Therein, it was found that when ion temperature gradient driven (ITG) modes and TEMs coexist, the particle flux vanishes due to a thermo-diffusive pinch²⁸, so that the experimental ratio $\eta_e = L_n / L_{Te}$ reaches a value of 2–3. The requirement of coexisting TE and ITG modes places a constraint on the ion temperature profile, allowing also more precise theoretical studies of the heat flux. Nonlinear local studies under these conditions using GENE were conducted in Refs. [33, 89] and confirmed the particle flux cancellation found in the quasilinear studies. However, it was also found that—even for weaker profile gradients—the local results for the heat flux substantially exceed the expectation, implying the necessity of a global model.

Such an approach is pursued in the present work. As a consequence of the fact that full radial profiles are considered, it is more difficult to achieve the condition of zero particle flux, since a coexistence of TE and ITG modes would have to be achieved not only at a single radial position, but with radially varying profiles. This would either require appropriate input profiles which already fulfill this condition (and which could have been determined, e.g. from a local quasilinear optimization) or a flux-driven simulation with freely evolving profiles that is allowed to relax into such a state. For the discharges studied in the present work, no measurement of the ion temperature profiles was available, giving rise to considerable uncertainty in the profile shape. At present, we will thus focus on the global description of the main actors driving the heat flux, and leave global particle flux studies to future work.

5.3 SETUP OF THE SIMULATIONS

5.3.1 SOME GENERAL REMARKS

When performing global simulations, the background temperature and density profiles have to be specified in order to define the equilibrium Maxwellian which serves as the zeroth-order solution to the system. While in Refs. [26, 33, 90], these profiles were based on analytical formulae, GENE also supports an interface to experimental profile data, which allows the user to specify the latter using an input file. Optionally, this information can also be used to automatically calculate the dimensionless parameters β_{ref} , ν_{ref} and $\lambda_{D,\text{ref}}$ and to extract the reference temperatures and densities.

²⁸ See Ref. [87] for a nonlinear scan in such a regime, and Ref. [88] for an introduction to particle transport physics.

Velocity space requirements

An important aspect that requires more consideration in global than in local simulations is the definition of the velocity space grid. Currently, GENE uses a radially independent velocity space grid which is normalized with respect to the reference position x_0 (see also Sec. 3.4). As a consequence, the radial dependence of the temperature must be taken into account when defining the extent and resolution of the velocity space grid. In local simulations, a usually sufficient choice is $L_{v\parallel} = 3.0 \hat{v}_{Tj}|_{x_0} c_{\text{ref}}$ and $L_\mu = 9.0 \hat{T}_{0j}|_{x_0} T_{\text{ref}}/B_{\text{ref}}$ for the extent of the $v\parallel$ and μ grids, respectively. In a global simulation, on the other hand, this choice will be only valid at the reference position x_0 ; regions with higher temperatures will contain particles with larger velocities, while regions with low temperature will require a larger number of grid nodes in order to properly resolve the local velocity space dynamics.

In concrete numbers, this means that for the discharge with the strongest eITB—and therefore the steepest temperature profile—we require a velocity space resolution of $n_{v\parallel} \times n_\mu = 96 \times 64$, while the exact values of $L_{v\parallel}$ and L_μ depend on the temperature at x_0 . Since this position is generally not at the maximal temperature, the velocity grid extent is usually larger in normalized units than its local counterpart (e.g. $\hat{L}_{v\parallel} = 4.1$, $\hat{L}_\mu = 17.2$). Comparing these settings with the standard velocity space resolution of 32×8 used in local runs, it is clear that the CPU-time requirements for these simulations will be more than 20 times as high (even neglecting the according reduction of the timestep due to Courant-Friedrichs-Lowy-type restrictions²⁹).

Computational requirements

With these constraints, an average, well-converged global nonlinear simulation can consume of the order of 100,000 CPU-hours. An exemplary timetrace of such a run is depicted in Fig. 32. Nonlinear saturation occurs in all cases at times $t < 10 R/c_s$, and the simulations are usually taken well beyond $50 R/c_s$ to ensure stationary results. Fluxes are then averaged over a time window containing a significant fraction of the total simulation time, up to the end of the simulation.

Heat flux profiles

In this chapter, radial profiles of the heat flux generated by the turbulence will be evaluated. For this purpose, at each radius the physical heat flux components—the projections of \mathbf{Q} on the radial unit vector (see Sec. 3.5)—, are summed over all

²⁹ To ensure the accuracy and even the stability of the timestepping scheme, the timestep should be small compared to the characteristic rate of change of the distribution function. As a crude estimate, the timestep has to be much smaller than the time it takes a particle to cross a given phase-space cell.

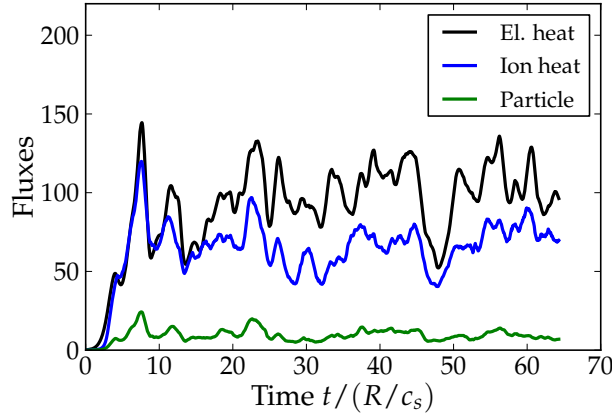


Figure 32: Time trace of a nonlinear global run with TCV parameters (for Case III, see Sec. 5.3.2).

k_y contributions, and averaged also in the parallel direction. The heat flux profile is therefore given by

$$Q^r(x) = \left\langle \sum_{k_y} \frac{Q^x}{\sqrt{g^{xx}}} \right\rangle_z.$$

Multiplying this heat flux profile by the flux surface area A_{FS} , defined as

$$A_{FS} = \int \sqrt{g^{xx}} J dy dz,$$

gives the total heat transport rate through a given flux surface

$$P(x) = Q^r(x) A_{FS}(x).$$

This can be compared to the experimental input power, which is, for the examined discharges, $P_{ext} = 2.25$ MW of EC-power. Of course, it should be considered that the heat deposition is also a function of the radius, and $P(x)$ therefore will, in steady state, be an integral over the source profile. Assuming that all heat sources have been deposited inside of a given flux surface, the heat flux at outer radii should then be inversely proportional to the minor radius, $Q^r \propto 1/r$ as the flux surface area in a torus is $A_{FS} \propto r$.

It should be noted that in the gradient-driven approach to global simulations, the radial profiles of the heat flux will not necessarily fulfill this condition. Due to experimental uncertainty, the input profiles may differ from the profiles that would develop in a self-consistent equilibrium of heat input and turbulent transport. In a flux-driven simulation, the profiles would be free to adapt accordingly—in the present case, on the other hand, the profiles are kept fixed and heat and particles can also be removed from the system for this purpose, which does not occur in the actual experiment. The resulting heat flux profile will therefore pro-

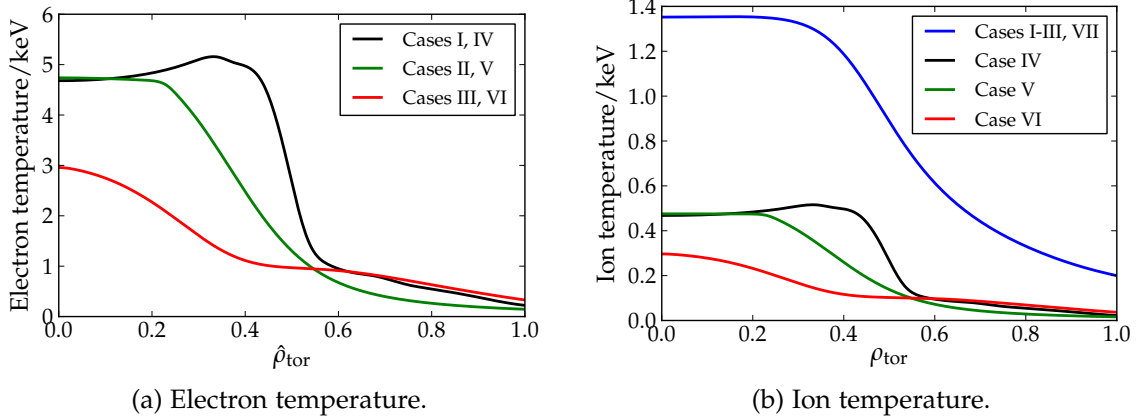


Figure 33: Comparison of the temperature profiles used in the different input datasets.

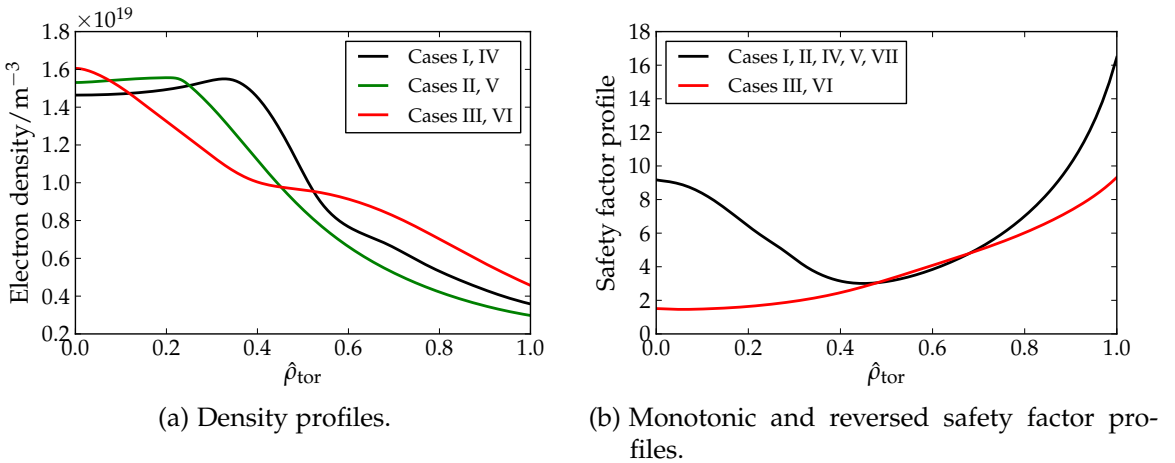


Figure 34: Density and safety factor profiles for the studies of the present chapter.

vide insight not only on turbulence properties, but also about the accuracy of the input profiles.

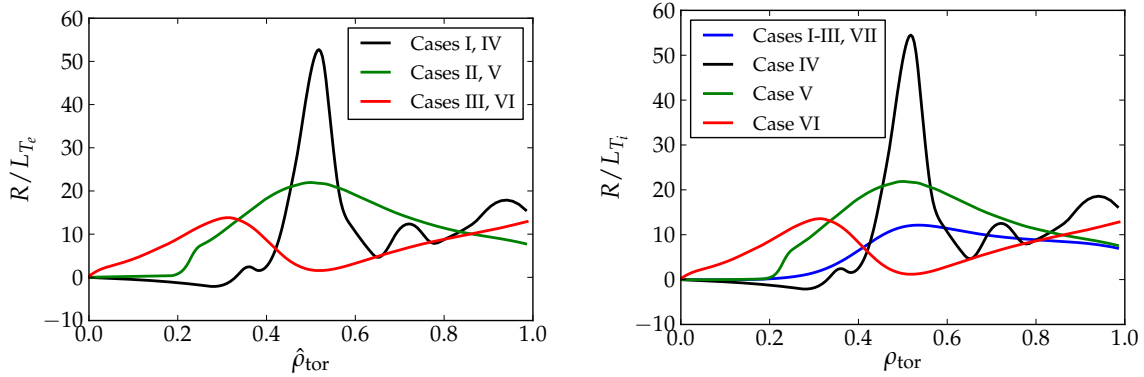
5.3.2 INPUT PARAMETERS

In the present chapter, several different electron profiles are studied and combined with different ion profiles. To increase the clarity of the text, we assign each of the cases a unique number. Table 3 contains all examined cases along with a description of their properties.

In Fig. 33, both the T_e and T_i profiles are shown. Note that in Fig. 33a, only the black and red curves are taken from experimental measurements; these profiles were generated from data measured during discharges 29866 and 29863, respectively. The green curve, on the other hand, is an ad-hoc profile chosen to provide an intermediate step between the two extreme cases. This profile will be used in combination with the reversed-shear MHD-equilibrium from discharge 29866.

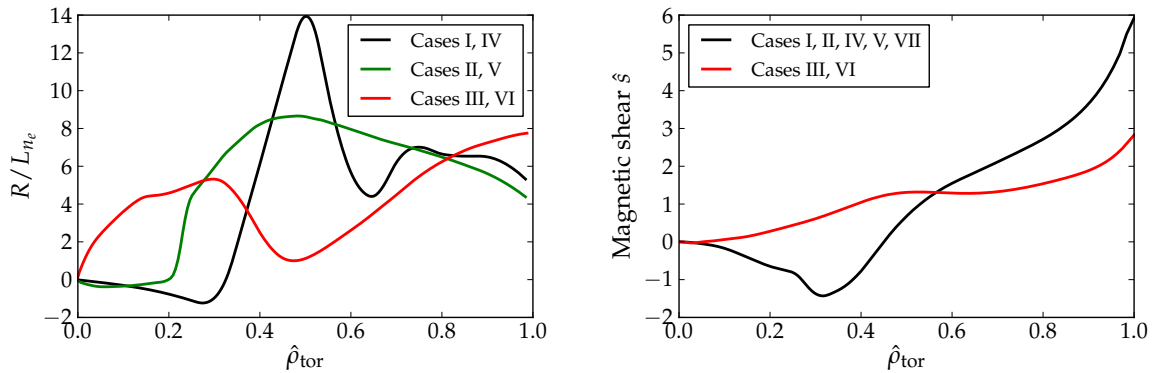
Case	Discharge	T_e	T_i	q -profile	Figure
I	29866	steep	high	reversed	T_e/T_i : 33a, 33b, n_e : 34a, q : 34b
II	29866	intermediate	high	reversed	
III	29863	shallow	high	monotonic	
IV	29866	steep	low	reversed	
V	29866	intermediate	low	reversed	
VI	29863	shallow	low	monotonic	
VII	29866	steep (relaxed)	high	reversed	T_e, n_e : 45, T_i : 33b, q : 34b

Table 3: List of all studied input profiles and their properties.



(a) Logarithmic gradients of the electron temperature. (b) Logarithmic gradients of the ion temperature.

Figure 35: Comparison of the electron and ion logarithmic temperature gradients.



(a) Comparison of logarithmic density gradients.

(b) Magnetic shear profiles for both the monotonic and the reversed q -profile.

Figure 36: Comparison of gradient profiles and magnetic shear for the different eITB cases.

Due to the absence of neutral beam injection, no spectroscopic ion temperature measurement is available for the eITB discharges studied here. However, the CNPA diagnostic (Compact Neutral Particle Analyzer [91]) provides a measurement for the central ion temperature which lies at about 1.4 keV in the present cases. Since the ions are not directly heated and have—due to the relatively low density—only a weak thermal coupling to the electrons, the standard ion temperature is assumed to be the same in all examined discharges, regardless of the electron profiles. The corresponding profile is shown as a blue line in Fig. 33b. To examine the sensitivity of the results with respect to the ion temperature, simulations will also be performed for a lower ion temperature given by $T_e/T_i \approx 10$ (Fig. 33b), similar to what has been studied in earlier work [83].

Figures 35 and 36 shows a comparison of the temperature and density gradients, and of the shear profiles for the cases studied here. It is noteworthy that even in the weak barrier discharge 29863, there is still a region of increased gradients, but it is much less pronounced and shifted to considerably smaller radii, so that a much smaller plasma volume is affected. In the figures, the depicted logarithmic gradients of a quantity x are defined as

$$\frac{R}{L_x} = -\frac{1}{x} \frac{\partial x}{\partial \hat{\rho}_{\text{tor}}} \frac{R}{\rho_{\max}},$$

where $\rho_{\text{tor}} = \sqrt{\Phi_{\text{tor}}/\pi B_{\text{edge}}}$, $\hat{\rho}_{\text{tor}} = \rho_{\text{tor}}/\rho_{\max}$, and $\rho_{\max} = \sqrt{\Phi_{\text{edge}}/\pi B_{\text{edge}}}$. Furthermore, B_{edge} is the magnetic field at the geometric major radius of the last closed flux surface, Φ_{tor} is the toroidal flux, and ρ_{\max} can be regarded as a measure of the minor radius.

For all simulations in the present chapter, we use the realistic plasma shape of the TCV discharges, which is imported into GENE using the interface to the CHEASE equilibrium code, which was discussed and benchmarked already in Chapter 4. Fig. 37 shows that the flux surfaces in the examined discharges are elongated and have also a finite triangularity. All simulations in the present chapter are performed using the shifted metric approach (see Sec. 4.2) to avoid resolution problems due to the large negative and positive magnetic shear values occurring within the simulation domain.

5.4 SIMULATION RESULTS

5.4.1 LINEAR SIMULATIONS

For the initial studies, the nonlinear term in the gyrokinetic Vlasov equation (Eq. 2.23) will be neglected, enabling a study of the linear eigenmodes present in the system. Here, these simulations are initialized with a small perturbation in the distribution function g_1 , and the time evolution of the equation system

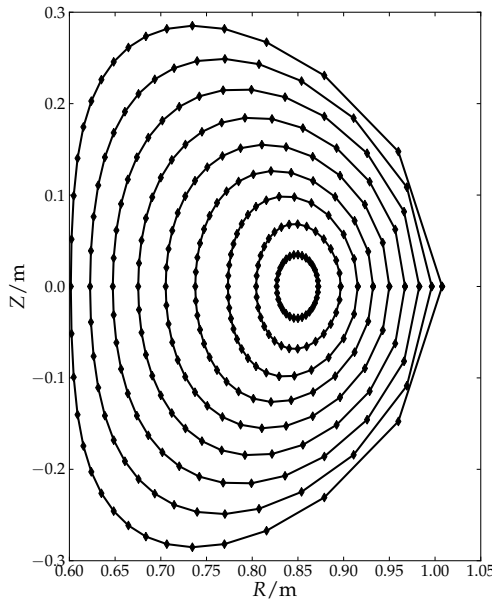


Figure 37: Flux surface shape in TCV discharge 29866. (32 points per flux surface, equidistant in $\rho_{\text{tor}} \leq 0.9$)

is solved³⁰. All unstable eigenmodes will then grow exponentially; at late times, when the amplitude of the most unstable mode dominates, its growth rate and frequency can be accurately measured. The spectra of these quantities will be the focus in the present section.

The linear simulations conducted in this chapter are both global and electromagnetic, i.e. the fluctuations of the magnetic field due to the finite thermal pressure of the plasma are taken into account. Realistic values are taken for the plasma parameter β_e (the ratio of thermal electron pressure to magnetic pressure), which can reach up to 1.4 % at the position of largest pressure of the Case I/IV profiles.

Although the full turbulent simulation is characterized by a complex interplay of both unstable *and* stable modes, there is often a close relation between the physics of the dominant instability and the characteristics of the turbulent system (see, e.g., Ref. [28]), allowing the development of quasi-linear models for the turbulent transport. The numerical parameters used for the present linear simulations are listed in Table 4.

First, the cases I-III are examined, considering the standard ion temperature profile, which matches the experimentally obtained value from the CNPA diagnostic ($T_i(0) \approx 1.4$ keV). For this first study, the influence of impurities is neglected, and only a single deuterium ion species is considered, along with a fully kinetic electron species. In Fig. 38a and 38b, the obtained growth rates and mode frequencies

³⁰ GENE also offers the possibility to study the full eigenmode spectrum by solving for the eigenvectors and eigenvalues of the linear gyrokinetic operator instead of solving its time evolution. Studies using this method have been published, e.g., in Refs. [87, 92, 93].

Case	n_x	n_{ky}	n_z	n_v	n_μ	L_x	L_v	L_μ	ϵ_z	$\epsilon_{v\parallel}$
I	128/256	1	24	96	64	25.588	3.2	10.5	2.0	0.2
II	128/256	1	24	96	64	40	5.2	27.0	2.0	0.2
III	128/256	1	24	80	48	67.54	5	25	2.0	0.2

Table 4: Numerical parameters for linear simulations.

are plotted versus the toroidal mode number. A conversion of toroidal mode numbers to binormal wavenumbers can be obtained by using the relations

$$\begin{aligned} \text{Case I, IV: } k_y \rho_s &= 0.114n \\ \text{Case II, V: } k_y \rho_s &= 0.080n \\ \text{Case III, VI: } k_y \rho_s &= 0.076n. \end{aligned}$$

Electron temperature gradient driven modes

An immediate observation is the presence of instabilities with fast growth rates at high wavenumbers. In all three cases, these instabilities exhibit negative mode frequency, i.e. the wave propagates in the electron-diamagnetic direction. Both this feature and the large wavenumber are characteristics of an ETG instability, which is primarily fed by the electron temperature gradient (ETG). The presence of such modes is already a new feature which was not found in earlier studies, either because of a simplified electron model (Ref. [83] used an adiabatic passing electron model, which excludes ETG physics) or because ETG modes were stable for the chosen parameters [89]. It will therefore be a primary concern of this chapter to investigate whether the observed ETG instabilities play an important role also in nonlinear simulations, and to examine their sensitivity with respect to parameter changes.

Instabilities at low wavenumbers

Turning towards the large-scale modes, we obtain different results for all three cases:

- In Case I, a rather pronounced instability exists, which dominates all mode numbers up to $n = 20$, and which exhibits a positive mode frequency, i.e. the mode rotates in the direction of the ion diamagnetic drift. This would be a feature of ITG instabilities, which were predicted to be significant in earlier studies [85, 89]; however, scanning the electromagnetic parameter β_e about its experimental value³¹, we find (for $n = 6$, see Fig. 39) a threshold behavior typical of a kinetic ballooning mode (KBM), showing that the experimental β_e is roughly 20% beyond its critical value.

³¹ This scan is performed as a mere parameter variation, i.e. without considering the corresponding change to the magnetic geometry.

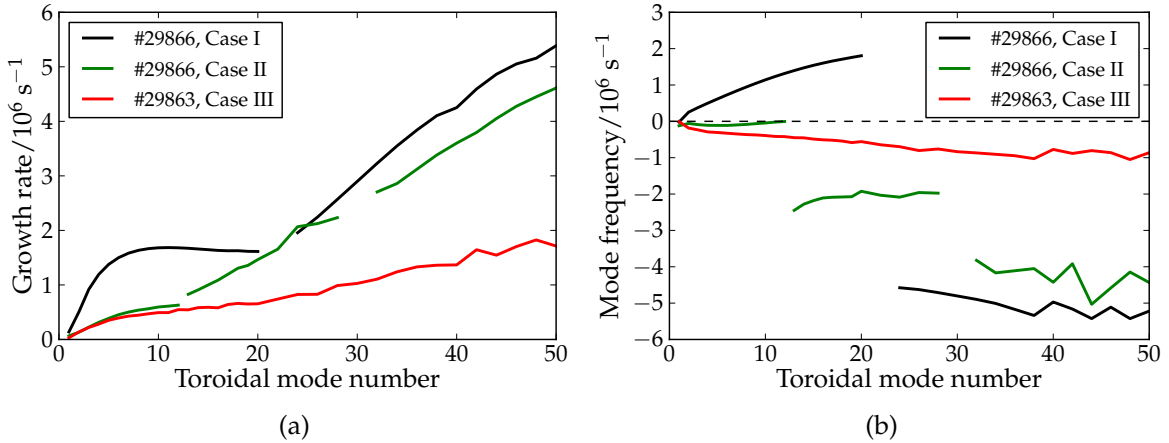


Figure 38: Linear growth rates and frequencies for high ion temperature, exhibiting prominent ETG instabilities for all three cases.

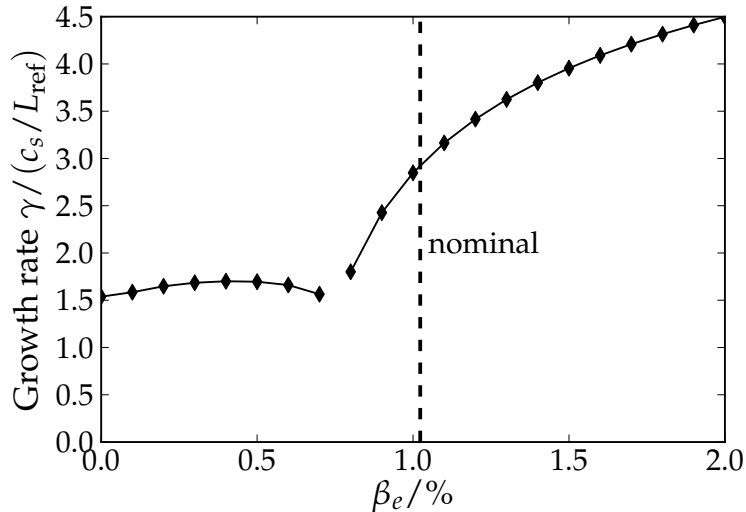


Figure 39: Global scan over the reference electron beta $\beta_e = \beta_e(x_0 = 0.45)$ with $L_{\text{ref}} = R$.

- In Case II, the reduced steepness of the profiles, while keeping the magnetic geometry constant, results in substantially smaller growth rates both in the large and small scales. At low wavenumbers, the KBM is replaced by a TEM, which dominates the spectrum up to $n = 12$, above which an ETG instability again takes over. The latter then dominates up to the highest wavenumbers studied.
- With Case III, we turn to both flatter temperature and density profiles as well as to the monotonic safety factor profile. Interestingly, although there is still an ETG branch at large wavenumbers, the spectra show no prominent discontinuities in the frequency or growth rate. Instead, the ETG instability is smoothly connected to the TEM dominating the low mode numbers.

Summarizing the results obtained so far, it can be noted that the observed instabilities are in all cases driven dominantly by the free energy in the electron temperature profile—with the exception of the KBM, which feeds from the total pressure gradient and is therefore driven by all profile gradients. These results therefore agree well with the experimental situation of pure electron heating.

The observation of an unstable KBM in the steep barrier case (I) deserves some additional discussion: In common scenarios³², these modes are associated with a rather violent outflux of heat and particles, and it appears therefore unlikely that the experiment should, for these parameters, be found clearly beyond the onset threshold for these modes. A linear sensitivity study of the KBM indicates that it is most sensitive to the magnetic shear and the ω_{Te} parameter, and that small shifts between the profiles and the magnetic equilibrium (still within the experimental uncertainty) can stabilize it. Case I is therefore close to the KBM threshold, but probably not beyond it. This observation agrees also with the experimental fact that, when the confinement is still more improved by making the magnetic shear even more negative, the gradients become so steep that the discharge disrupts [81].

5.4.2 TURBULENCE SIMULATIONS

As a first approach to the nonlinear simulations, we use an electrostatic, collisionless approximation. The former assumption is used in order to focus on the electrostatic instabilities present for our nominal parameters, excluding the KBM mode. Comparing the resulting transport levels with the experimental ones, one can then assess the profile behavior, and conclude whether the KBM threshold could be reached at all.

The collisionless assumption, on the other hand, is justified by the low density of the eITB discharges, which, in combination with the relatively high temperatures leads to collision frequencies of $\nu_{ee} \sim \nu_{ei} \lesssim 10^4$ Hz, which is more than two orders of magnitude³³ below the electron bounce frequency $\omega_{be} \approx \sqrt{\epsilon}v_{th,e}/qR \sim 3 \cdot 10^6$ Hz and at least one order of magnitude below the relevant mode frequencies, and can therefore be expected to exert only weak damping on TEMs. Linear scans and a nonlinear comparison run have been performed to validate this assumption.

In this section, we again study the Cases I-III from above, considering as before a single deuterium ion species. The code parameters used for the nonlinear simulations of these discharges are listed in Table 5. The coefficients to the Krook-type sources (Sec. 3.6) were set to $0.5 c_{\text{ref}}/L_{\text{ref}}$, which is a factor of four (or more) below the maximum linear growth rates. The values of the coefficients determine to which degree profile relaxation is allowed and thus have some influence on the resulting transport levels. For the present simulations, no qualitative changes in

³² See, e.g., literature [94] on the linear drive for edge-localized modes (ELMs), which periodically thrust out a large fraction of the energy content of the edge pedestal.

³³ Here, a temperature of 1 keV was assumed for both ions and electrons, and particles at thermal velocity were considered.

Case	n_x	n_{ky}	n_z	n_v	n_μ	L_x	L_y	L_v	L_μ	ϵ_x	ϵ_z	$\epsilon_{v\parallel}$
I	128	64	24	96	64	25.588	40.14	3.2	10.5	1.0	2.0	0.2
II	128	48	24	80	60	40	80.574	5.2	27.0	1.0	2.0	0.2
III	128	32	24	80	48	67.54	82.51	5	25	1.0	2.0	0.2

Table 5: Typical numerical parameters for nonlinear simulations.

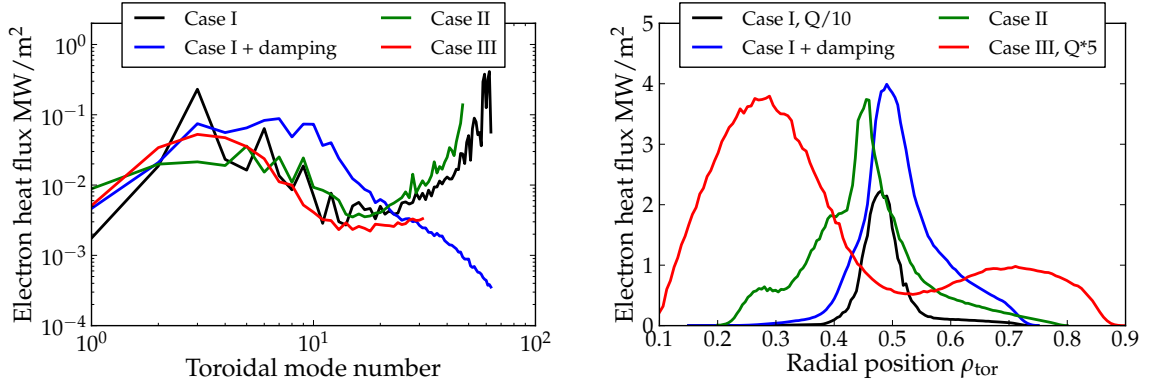
the results were observed when varying the source coefficients between 0.1 and 1.0. At lower values, however, the profile relaxation can become strong enough to cause violations of the delta- f ordering, which should be avoided.

The (radially averaged) binormal electron heat flux spectra obtained from the nonlinear simulations are plotted in Fig. 40a, and Fig. 40b shows the radial heat flux profiles. In the latter figure, both Case I and II show clear stabilization in the low/negative shear region within $\rho_{\text{tor}} \leq 0.45$, demonstrating that the essential physics is correctly captured by the simulations. Note that the heat flux curve for the steep barrier case has been divided by 10 in order to fit all graphs into the same diagram.

In the linear simulations of Sec. 5.4.1, it was observed that in all three cases, ETG modes were unstable. The nonlinear simulations presented here confirm their significance:

- In Case I, the ETG destabilization due to the steep electron temperature profile is strong enough that the majority of the electron heat flux is produced at the smallest scales present in the simulation. Unfortunately, it was not possible with the available computer resources to extend the perpendicular resolution enough to completely encompass both ion and electron scales. Such a study is therefore left for future work. It is, however, possible to apply artificial hyperdiffusion to the smallest scales³⁴ and thus suppress the ETG contributions (blue curve in Fig. 40a). In such a simulation, the heat flux exhibits a rather broad peak at $n = 3 - 10$, driven by TEMs. The radial heat flux profile for this simulation peaks preferentially around $\rho_{\text{tor}} = 0.5$, where the drive of R/L_{Te} is maximal, and shows a relatively strong decay towards outer radii. The peak heat flux is 4 MW/m^2 , which corresponds (using $A_{FS} = 4.65 \text{ m}^2$) to a total heat transport rate of 18.6 MW , which is in significant excess of the experimental value, despite the artificial damping.
- In Case II, the overall picture is similar as in Case I: The electron heat flux is mostly generated at the smallest scales, which are not sufficiently resolved to treat the ETG modes adequately. On the other hand, this observation indicates already that ETGs should be important even for this less-steep version of the transport barrier.

³⁴ In the present example, we set $\epsilon_x = \epsilon_y = 3$. See Section 4.2.2 for a description of the employed hyperdiffusion terms.



(a) Electron heat flux spectrum (radial average). The steeper profiles with reversed shear show a strong build-up of amplitudes at small scales due to ETG instabilities, which are not sufficiently resolved in the present simulations.

(b) Radial electron heat flux profiles. Note that the profiles for Case I (without damping) and Case III have been scaled down by a factor 10 and up by a factor of 5, respectively.

Figure 40: Heat flux properties for the simulations with high ion temperature.

- In Case III, even though the heat flux contribution at large mode numbers is clearly subdominant, there is a small amount of ‘spectral blocking’ (a pile-up at the smallest scales), indicating a weak contribution due to the unstable ETGs observed in Sec. 5.4.1. Indeed, when doubling the binormal resolution to $n_y = 64$ modes, the heat flux peak around $\rho_{\text{tor}} = 0.25$ increases by $\sim 50\%$ due to the increased high- k contribution. The heat flux at this position, taken from the profile depicted in Fig. 40b, is $Q_e = 0.75 \text{ MW/m}^2$, giving a total heat transport rate (with $A_{\text{FS}} = 2.0 \text{ m}^2$) through the flux surface of 1.5 MW , which is close to the experimental input power of 2.25 MW . Interestingly, the gap visible around $\rho_{\text{tor}} = 0.5$ in the electron heat flux profile is, for these parameters, almost exactly filled by the ion heat flux, which dominates in this region. For these parameters, turbulent transport in this discharge is therefore dominated by TEM around $\rho_{\text{tor}} = 0.25$, by ITG around $\rho_{\text{tor}} = 0.5$, and by TEM again towards the edge.

Obviously, *all* of the cases studied so far exhibit substantial transport contributions from ETG modes for the present parameters. A sensitivity study is however required to assess the robustness of this result. Summarizing the observations from the nonlinear simulations obtained so far, there are several possibilities which could lead to an overestimation of the heat flux contribution due to ETGs and will therefore be investigated in the following:

- In a fully saturated state (which is difficult to reach once high-amplitude ETG turbulence has developed, due to the accompanying timestep reduction), ETG turbulence might be suppressed to some extent by interaction with the larger scales through $E \times B$ shearing of ETG streamers—if they are present. A first attempt at investigating this issue is shown in Sec. 5.5.4,

but ultimately, a fully self-consistent multi-scale simulation will be required, which is left for future work.

- The contribution of ETG turbulence may be smaller when it is fully resolved. As mentioned above, in the present simulations it was not possible to capture the ETG spectra adequately. However, it is possible to conduct single-scale simulations which include *only* electron scales, in order to answer this question—neglecting, of course, the interaction with ion scales. This is done in Sec. 5.5.3.
- Even when suppressing the ETG contribution in Case I, the heat flux at $\rho_{\text{tor}} = 0.5$ is overestimated. Sec. 5.5.5 deals with the question, to which degree this could be caused by a too steep input profile.
- The contribution of ETG turbulence might be reduced when taking into account the presence of impurities in the plasma. This question will be addressed in the framework of global adiabatic ion simulations (see Sec. 5.5.3), considering only electron-scale turbulence.
- As noted before, the exact ion temperature profile is unknown for the examined discharges, leaving some degree of freedom in the question of ETG stability (see also Sec. 6.4.4). This question will be addressed both by the above mentioned ETG simulations in Sec. 5.5.3, as well as by repeating the simulations shown up to now, but with a substantially reduced ion temperature. This point will be tested in the following section.

5.5 SENSITIVITY STUDY OF ETG STABILITY

The present section is dedicated to investigating the robustness of the ETG contributions found in Sec. 5.4.2. As a first step, we repeat the linear and nonlinear studies from before, this time imposing low ion temperature profiles (Fig. 33b) given in each case by $T_i/T_e = 1/10$.

5.5.1 LINEAR SIMULATIONS AT LOW ION TEMPERATURE

We begin, as before, with a linear study of the Cases IV-VI described in Table 3. These are identical to Cases I-III, except that they are all performed with low ion temperature. The mode number spectra of growth rates and frequencies are plotted in Fig. 41a and 41b, respectively.

- The small mode numbers for the Case IV parameters are still KBM unstable, as were those of Case I. As the T_i/T_e ratio was already low to begin with, and the ion contribution to the pressure gradient is therefore small anyway, this is not too surprising. At the high wavenumbers, it becomes obvious that the plasma is still clearly ETG-unstable, in spite of the stabilizing effect of low ion temperature.

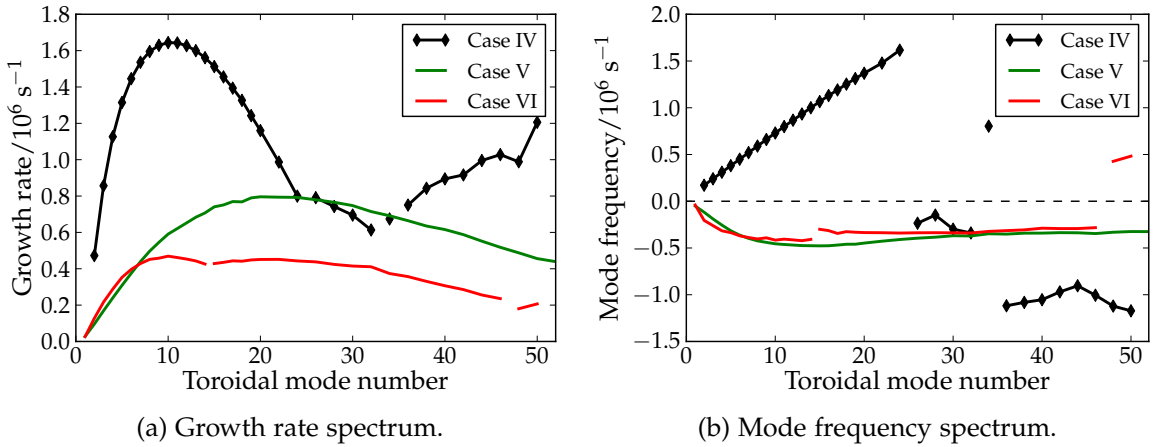


Figure 41: Linear spectra for Cases IV-VI, conducted with the low ion temperature assumption.

- In Case V, at least for the studied wavenumbers, the ETG instability appears to be stabilized by the low ion temperature, and only a TEM remains at the largest scales. Its growth rate peaks at $n = 22$, but does not decay completely until $n = 50$, which is as far as the linear study extends.
 - In Case VI, as could be expected due to the weak gradients, the ETG instability is also completely stabilized under the low T_i assumption. Similarly as for Case V, a broadly peaked TEM dominates the spectrum, which exhibits its maximum growth rate at $n = 10$. Up to $n = 14$, the dominant instability peaks at $\rho_{\text{tor}} = 0.3$, where also the heat flux maximum in Sec. 5.4.2 was found; above $n = 15$, another TEM becomes dominant, which peaks at $\rho_{\text{tor}} = 0.8$, where another maximum in the density and temperature gradients can be found.

5.5.2 NONLINEAR SIMULATIONS AT LOW ION TEMPERATURE

We now turn to nonlinear simulations of the low- T_i cases IV-VI. These were performed using the same typical numerical parameters as given in Table 5. Figure 42a shows the radially averaged electron heat flux spectra for all three profiles versus the toroidal mode number.

In Fig. 42b, the radial heat flux profiles are plotted. For the heat flux peaks in the present cases, we can again evaluate the heat transport rates as shown in Table 6.

- For the steep barrier case (IV), although there was some hint of unstable ETG modes in the linear results, we find no substantial high- k contributions to the electron heat flux. Only at the highest wavenumbers, a slight knee in the flux spectrum can be observed, which indicates the presence of ETG contributes at high k . At lower wavenumbers, we find the same broad transport spectrum as for the damped Case I simulations, which was essentially flat

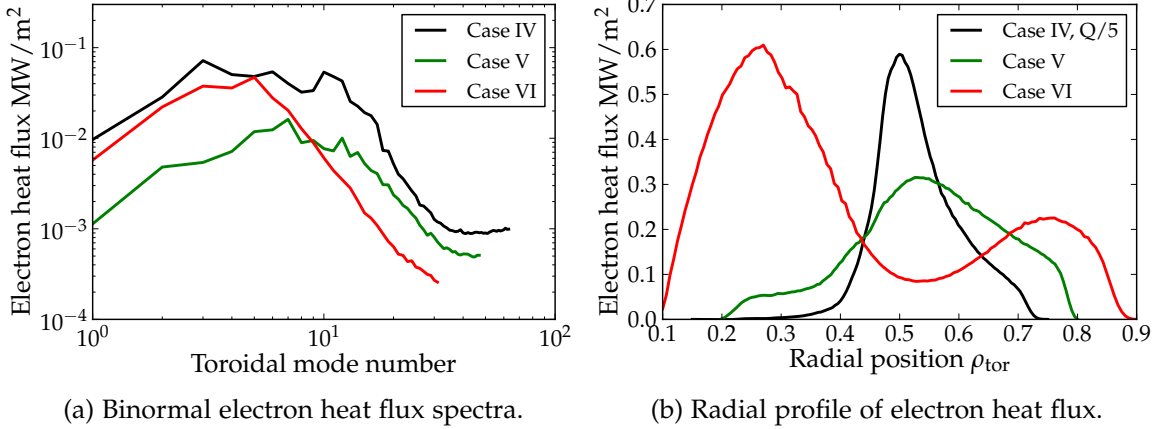


Figure 42: Nonlinear results for electron heat flux for Cases IV-VI.

Case	ρ_{tor}	$Q_e / (\text{MW}/\text{m}^2)$	Area/ m^2	P / MW	P / P_{exp}
IV	0.5	2.91	4.65	13.5	6.01
V	0.52	0.31	4.75	1.50	0.67
VI	0.25	0.61	2.0	1.22	0.54

Table 6: Heat flux evaluations for the heat flux peaks found in three TCV simulations at low ion temperature. For P_{exp} , the experimental input power of 2.25 MW was assumed.

from $n = 3$ up to $n = 10$, though at a slightly lower level than in Case I. Despite the missing ETG contribution, the heat flux concentrates in the mid-radius region and still amounts to 2.91 MW/m^2 , roughly six times as much as expected in the actual discharge.

- For Case V, we also find no ETG contribution left at small scales, but only a heat flux peak due to TEMs around $n = 5$. The heat transport rate at mid-radius is found to be 1.50 MW. This value is below the experimental expectation—of course, the input profile is not directly based on experimental measurements, and has weaker gradients than those of the actual profiles.
- For the monotonic q case VI, the heat transport rate at the heat flux peak at $\rho_{\text{tor}} = 0.25$ is $P_{\text{out}} \approx 1.22 \text{ MW}$, corresponding to 54% of the experimental input power. This result, including the radial heat flux profile, is very similar to that of Case III, except that the ETG contribution at large wavenumbers has disappeared.

5.5.3 PURE ETG TURBULENCE SIMULATIONS

In the previous sections, it was not possible to encompass electron gyroradius scales in the simulations. In the present section, electron-scale simulations are per-

formed in order to assess the transport generated by pure ETG turbulence. These simulations make use of the adiabatic ion approximation introduced in Sec. 2.5.5, which—while not explicitly evolving the ion distribution functions—allows to take into account the effects of impurities and the ion/electron temperature ratio on ETG turbulence.

The simulations are global, but take into account only a small radial region centered around $x_0 = 0.48$, where the ETG heat flux peak was found in Sec. 5.4.2. We vary the adiabatic ion parameter $\tau = Z_{\text{eff}}T_e/T_i$ and examine the ETG-driven turbulent transport for $\tau = 1, 3, 10$. To fully cover the ETG-unstable part of the spectrum, we restrict to the range above $k_y\rho_e \geq 0.08$ (corresponding to multiples of $n = 40$), taking 24 toroidal modes. The electron temperature varies by a factor 1.5 over the radial box width $L_x = 200\rho_e \approx 3.3\rho_s$. Since this is a rather weak variation compared to the full-radius case, we keep the standard local velocity space resolution 32×8 in (v_{\parallel}, μ) , while using 128 points in the radial direction. In Fig. 43, the decrease of the ETG generated electron heat flux with increasing impurity content and decreasing ion temperature is shown. As can be inferred from Fig. 33, the ratio between electron and ion temperature is roughly 3 in the relevant radial region. In combination with an effective ion charge $Z_{\text{eff}} \sim 3$ (similar to what is used in Refs. [86, 89]), the experiment is situated in the far right of Fig. 43, where the ETG-driven heat flux is lowest. At $\tau = 10$, the flux still amounts to 1.7 MW/m^2 , corresponding to a power of $\sim 8.5 \text{ MW}$ passing through the entire flux surface. Therefore, even when considering the effect of impurities *and* low ion temperature, ETG turbulence is capable of driving four times the experimental heat flux.

On the scale of Fig. 43, the simulations of Sec. 5.4.2 would be situated roughly at $\tau = 3$, since the temperature ratio was taken into account, but not the impurity content of the plasma. According to the results of the present section, this corresponds to a difference in the resulting heat fluxes of a factor 2.

An interesting comparison is also possible with the ion-scale simulation of Case IV, which did not exhibit ETG contributions at large wavenumbers. That simulation corresponds to the $\tau = 10$ run of this section, which *does* show finite heat flux due to ETGs. This apparent contradiction can be solved by examining the spectra of both simulations. Indeed, the $\tau = 10$ run has its heat flux peak at $k_y\rho_s \approx 18$, well beyond the resolution maximum of the Case IV simulation. This is therefore an example where ion and electron scales are clearly separated.

5.5.4 INTERACTION WITH LARGE-SCALE TURBULENCE

One factor which could be able to reduce the ETG-driven transport beyond temperature ratio or impurity effects is the quenching of the small-scale ETGs by large-scale turbulence, which imposes a fluctuating perpendicular velocity shear on ETG eddies, reducing their correlation length and therefore their radial transport efficiency. Such an effect cannot be considered in the adiabatic ion simulations of the previous section, as the large-scale turbulence is missing.

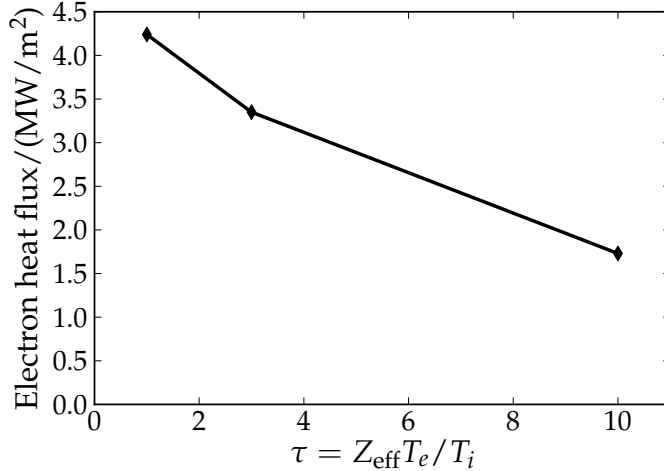


Figure 43: Effect of impurities and temperature ratio on ETG-generated heat flux.

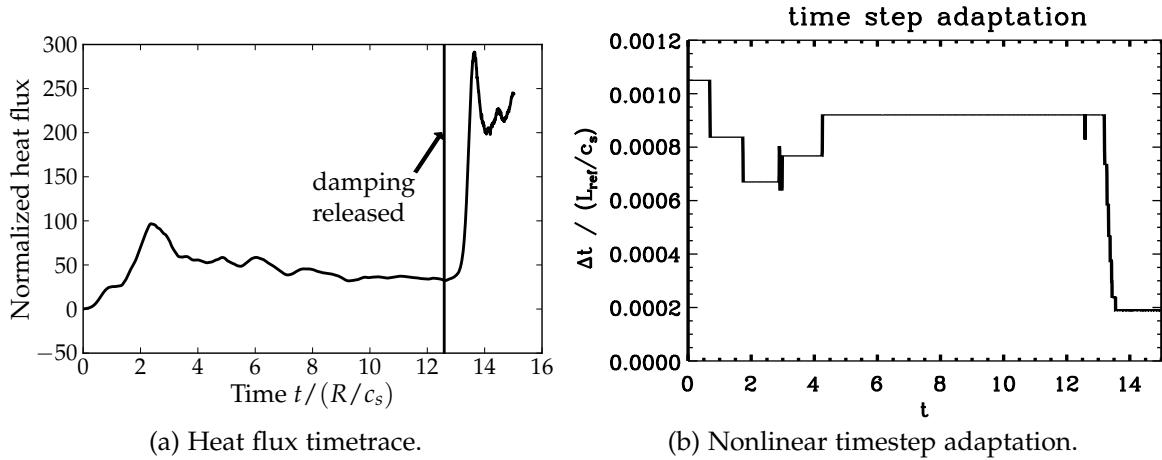


Figure 44: Timetraces of a nonlinear global simulation, which was started up with artificial damping terms. At $t = 12.5 R/c_s$, these terms are switched off, and explosive ETG growth sets in.

In order to test this conjecture, a simulation of the steep barrier case described above was set up, using both kinetic ions and electrons, but starting with artificial damping terms. After saturation of the remaining large-scale turbulence, the damping was released, the idea being that the already established low- k turbulence would suppress the growth of ETG instabilities.

However, such a behavior was not observed in the simulation (see Fig. 44a). Instead, after releasing the damping, an apparently unhampered ETG growth set in, resulting in a more than tenfold increase of the electron heat flux until saturation of the ETG flux occurred. It is also possible that a quenching of ETG turbulence would occur only after a longer time, when an equilibrium between the large and small scale turbulence has developed. However, as the ETG-driven fluctuations develop large amplitudes, the timestep must be adapted to very low values (Fig. 44b), making a continuation of the simulation computationally expen-

sive. Such a study is outside the scope of the current work, and is left for future multi-scale simulations.

5.5.5 EFFECT OF EXPERIMENTAL UNCERTAINTY

Like all measurements, the profiles of temperatures and densities obtained from the experimental diagnostics have a given error margin. Turbulence is especially sensitive to these uncertainties, as it delicately depends on the profile *gradients*, and also on the derivative of the safety factor. In the previous sections, independently of the ion temperature, all heat fluxes—TEM or ETG—obtained for the steep barrier profile (Case I/IV) were above the experimental values.

In order to test the sensitivity of both large- and small-scale turbulence, we repeat some of the above studies with modified electron temperature and density profiles, which will be designated as Case VII (see Table 3). These are obtained by applying a transformation to the radial coordinate, which stretches the region around the barrier somewhat and compresses the radii outside this region for compensation, resulting in the profiles depicted in Fig. 45. As can be seen, the profiles are slightly³⁵ shifted towards inner radii, so that the steepest gradient is at a position with lower magnetic shear. In addition, the steep gradient region is wider than in the original profile, and the maximum gradient is accordingly reduced from $R/L_{Te} = 52$ to $R/L_{Te} = 33$. The maximum and minimum values of temperature and density are unchanged, and the ion temperature profile (we use the standard T_i with $T_i(0) = 1.4$ keV) is also not modified.

The linear growth rate and frequency spectra obtained with these profiles are shown in Figs. 46a and 46b in comparison to the original scans. As can be seen, a clear stabilization of both the low- k KBM and the ETG mode can be obtained by a rather small change to the input profiles which is within the experimental error bars, emphasizing the delicacy of microinstability physics under transport barrier conditions.

Repeating the adiabatic ion ETG simulations from Sec. 5.5.3 with the relaxed profile, it is found that indeed the electron heat flux generated by ETG turbulence is reduced by roughly a factor 2 throughout the studied range of the τ parameter—see Fig. 47. At the relevant range of $\tau \sim 9$, the heat flux is now roughly a factor 2 above what would be expected in the experiment, showing that even for a relaxed profile and including impurity stabilization, a significant ETG contribution to the experimental heat flux is to be expected.

Next, we study the influence of the relaxed profile on the TEM-generated heat flux. For this, we restrict the simulation again to ion scales. In order to suppress the significant ETG contributions, it is again necessary to apply artificial dissipation to the smaller perpendicular scales. We set $\epsilon_x = 2$ and $\epsilon_y = 2$, which proves to be sufficient in this case. Using these settings, we obtain the heat flux spectrum and profile shown in Figures 48a and 48b. The maximum heat flux, measured at

³⁵ The shift is approximately $\Delta\rho_{\text{tor}} = 0.03$. This corresponds to less than one centimeter in real space, and is just below the resolution of the Thomson scattering system used to obtain the profiles.

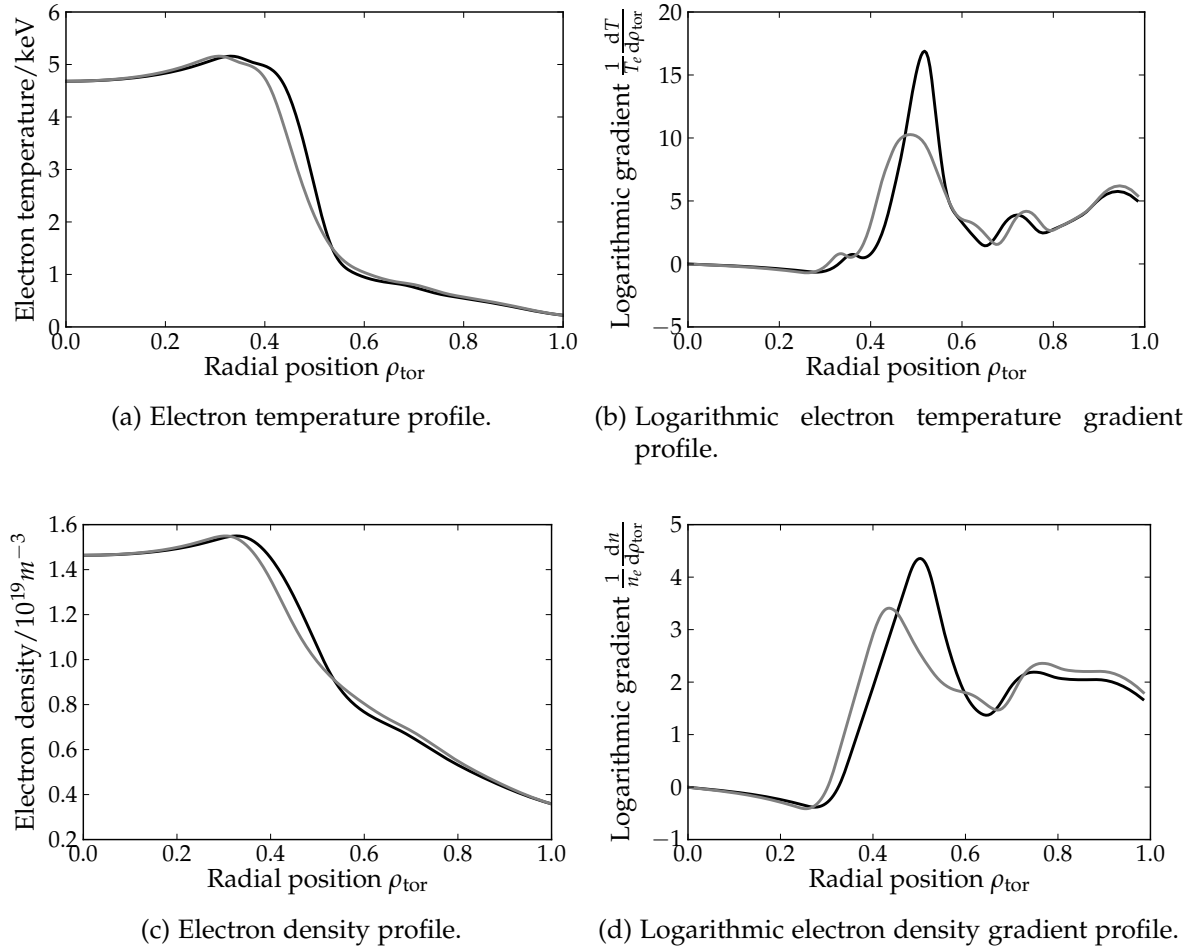


Figure 45: Comparison of original and slightly relaxed profiles. The black and gray curves give the original and modified profiles, respectively.

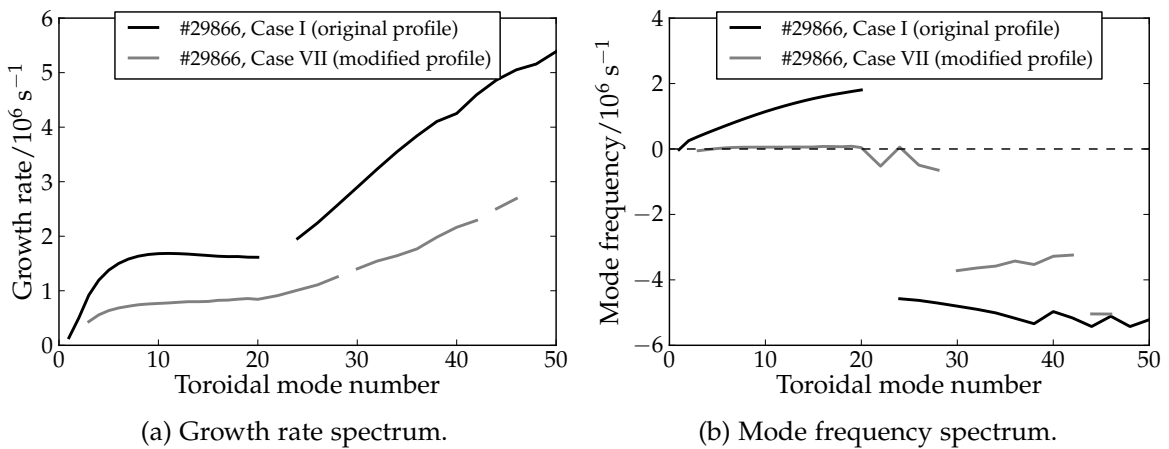


Figure 46: Comparison of the growth rate and frequency spectra of the original and the modified profile.

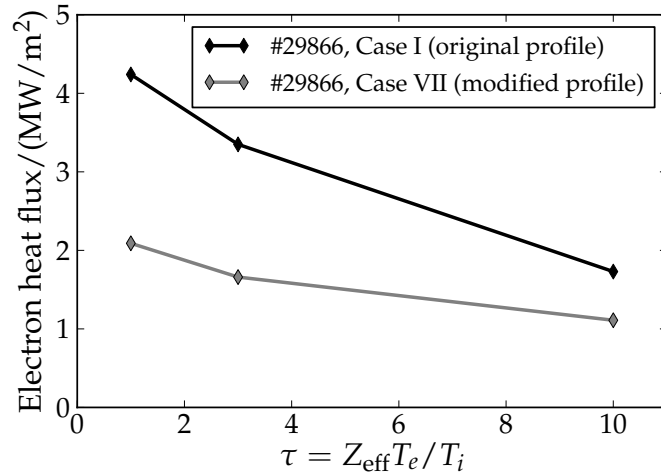


Figure 47: Comparison of the electron heat flux generated by ETG turbulence in a global simulation of the barrier region for the original profile (black line), as well as for the modified profile (gray line).

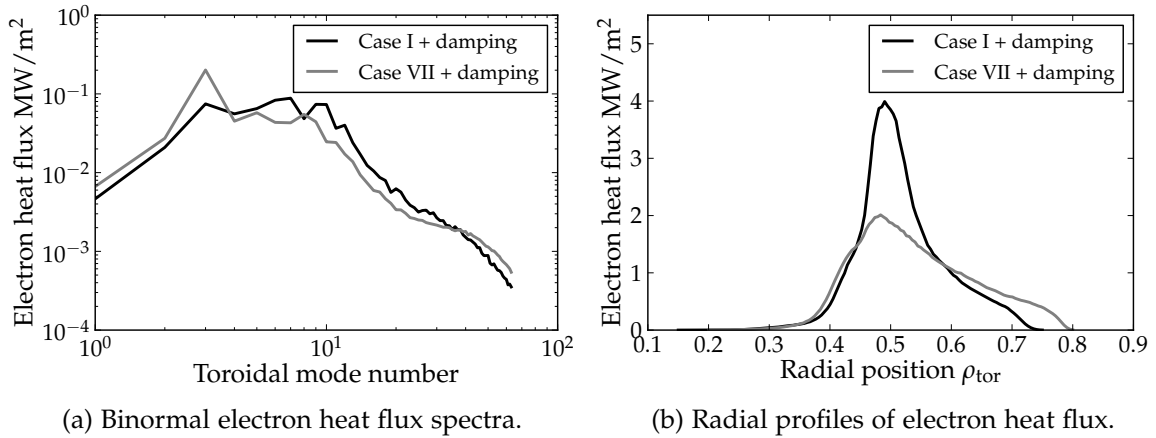


Figure 48: Comparison of heat flux results for the profiles of Case I and Case VII.

$\rho_{\text{tor}} = 0.5$, amounts to $Q_e = 1.87 \text{ MW/m}^2$, which is—like the ETG result—still above the experimental value, but reduced by a factor two from the Case I result. At the present parameters, neglecting the electron/ion scale interaction, the TEM-generated heat flux is roughly 50 % larger than the ETG contribution. Adding both parts, the overall heat transport rate is, at $\sim 13.8 \text{ MW}$, still above the experimental value, providing further evidence that ETG and TEM turbulence will limit the barrier steepness before the KBM threshold is exceeded.

While the discrepancy between the simulated and experimental heat fluxes is still substantial, this is already a significantly better agreement than is often obtained in local gyrokinetic studies. In the next section, it is demonstrated that the use of a global model is crucial to even obtain heat fluxes of a similar order of magnitude as the experiment.

Case:	I	V	VI
\hat{Q}_e/\hat{Q}_i local	17.2	11.8	8.55
$\hat{Q}_e/\hat{\Gamma}$ local	13.4	8.2	6.6
\hat{Q}_e/\hat{Q}_i global	22.0	10.0	9.33
$\hat{Q}_e/\hat{\Gamma}$ global	8.8	10.8	6.02
$P_{\text{local}}/\text{MW}$	299	13.3	4.98
$P_{\text{local}}/P_{\text{global}}$	15	9	4.1

Table 7: Comparison of fluxes obtained in local and global simulations.

5.6 COMPARISON TO LOCAL SIMULATIONS

In the present section, we examine the capability of the local version of GENE to model the ITB discharges studied in the present chapter. We run simulations for Case I, Case V, and Case VI, using again the electrostatic assumption. The obtained heat fluxes are compared, but as a measure of qualitative agreement, we examine also the ratios between heat and particle fluxes for both ions and electrons, as these indicate the type of turbulence dominating the system. All values are given in Table 7.

- In Case I, the local simulation (restricted to the large scales, as in the global run, and using also $\epsilon_x = \epsilon_y = 3$) obtains a heat flux of 63 MW/m^2 at $\rho_{\text{tor}} = 0.5$, corresponding to 299 MW of power passing through that flux surface, which is more than two orders of magnitude above the experimental value, and roughly a factor 15 above the global result. The ratios between the obtained fluxes agree with those of the global simulation to within $\sim 30\%$. When run without perpendicular hyperdiffusion, the local simulation, like the global one, finds substantial heat flux at the smallest scales, implying the necessity of electron-scale resolution.
- For Case V, the overall heat flux is found to be $Q_e = 2.79 \text{ MW/m}^2$. This corresponds to a heat transport rate of 13.3 MW, exceeding the experimental input power by a factor ~ 6 (but using a weaker profile than measured). In addition, the global heat flux result at that position is exceeded by a factor ~ 9 even in this ‘flat barrier’ case. The ratios between the fluxes agree with their global counterparts to within 20%.
- Case VI was compared at $\rho_{\text{tor}} = 0.25$, where the heat flux peaked in the global simulation. At this position, the heat flux amounts to $Q_e = 2.49 \text{ MW}$. In combination with the flux surface area $A_{\text{FS}} = 2.0 \text{ m}^2$, we arrive at a heat transport rate of 4.98 MW. Again, this result is significantly higher than both the global result, as well as the experimental input power. The flux ratios, are accurate to 10%, for this parameter set.

Case	ρ_{tor}	q	\hat{s}	ω_{Te}	ω_{Ti}	ω_n	T_i/T_e
I	0.5	3.11	0.66	48.0	11.70	14.0	0.333
V	0.5	3.11	0.66	22.25	21.87	8.68	0.106
VI	0.25	1.77	0.44	11.75	11.38	5.02	0.103

Table 8: Physical parameters for local TCV simulations.

Case	n_{kx}	n_{ky}	n_z	n_v	n_μ	L_x	L_y	L_v	L_μ	$\epsilon_x = \epsilon_y$	ϵ_z	$\epsilon_{v\parallel}$
I	128	64	32	32	8	120.37	62.83	3.0	9.0	3	0.5	0.2
V	128	48	32	32	8	120.37	62.83	3.0	9.0	0	5	0.2
VI	128	48	32	32	8	136.97	125.66	3.0	9.0	0	2	0.2

Table 9: Numerical parameters for local TCV simulations.

The parameters of the local simulations used for this comparison are shown in Tables 8 and 9. Summarizing the results of the present section, we observe that the local simulations do not match the heat fluxes of the global runs well, even for the case without an ITB. A clear improvement of the situation towards decreasing gradients can be observed, however. The qualitative agreement of the results regarding the ratios between ion/electron heat and particle fluxes is quite reasonable, providing a validation of earlier local studies on the particle flux properties of eITB plasmas (see also Sec. 5.2).

5.7 DISCUSSION OF THE SIMULATION RESULTS

In this section, a theoretical explanation is proposed for the prominent role of ETG instabilities under the eITB conditions. Studying the existing literature, one can find scalings of the heat diffusivity versus the driving gradient R/L_T (for brevity denoted here as κ). Examples of such scalings are plotted in Fig. 49 for heat diffusivities due to ITG, TEM, and ETG turbulence.

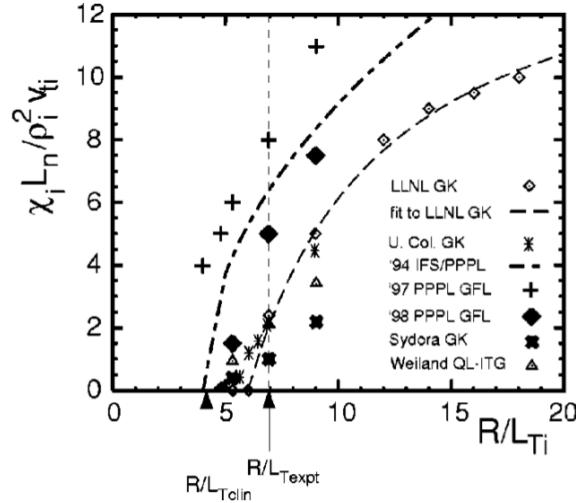
As can be observed in these figures, both for ITG and TEM turbulence, the effective heat diffusivity χ_{eff} , defined by

$$\chi_{\text{eff}} = -\frac{Q}{n |\nabla T|} = Q \frac{R}{n T \kappa},$$

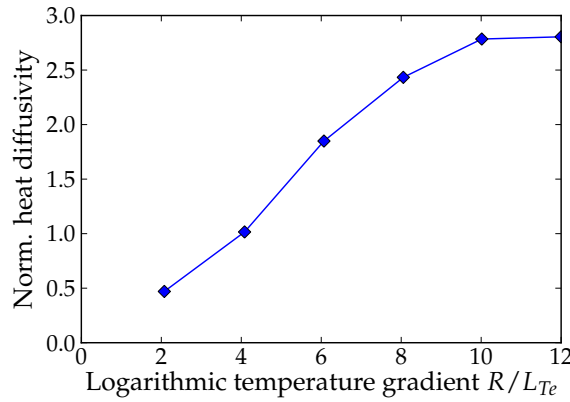
starts with the value 0 at the nonlinear critical gradient κ_c . It then rises steeply and exhibits a rollover towards larger values of κ . This is consistent with an offset-linear $Q(\kappa)$ dependence, which can phenomenologically be written as

$$Q(\kappa) = m (\kappa - \kappa_c) H(\kappa - \kappa_c).$$

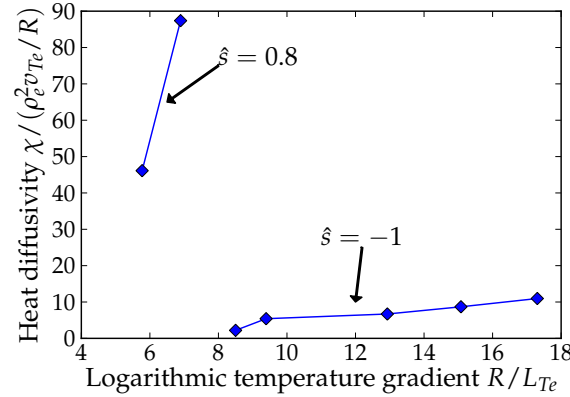
Here, m is the slope or the *stiffness* of the heat flux above the critical gradient. It is a measure of the amount of heat input that is required to achieve a given profile



(a) Scaling for ITG turbulence [40].



(b) Scaling for TEM turbulence (adapted from Ref. [95]).



(c) Scaling for ETG turbulence at different magnetic shear (adapted from Ref. [96]).

Figure 49: Scaling of the heat diffusivity in gyro-Bohm units versus the driving gradient for different turbulence types.

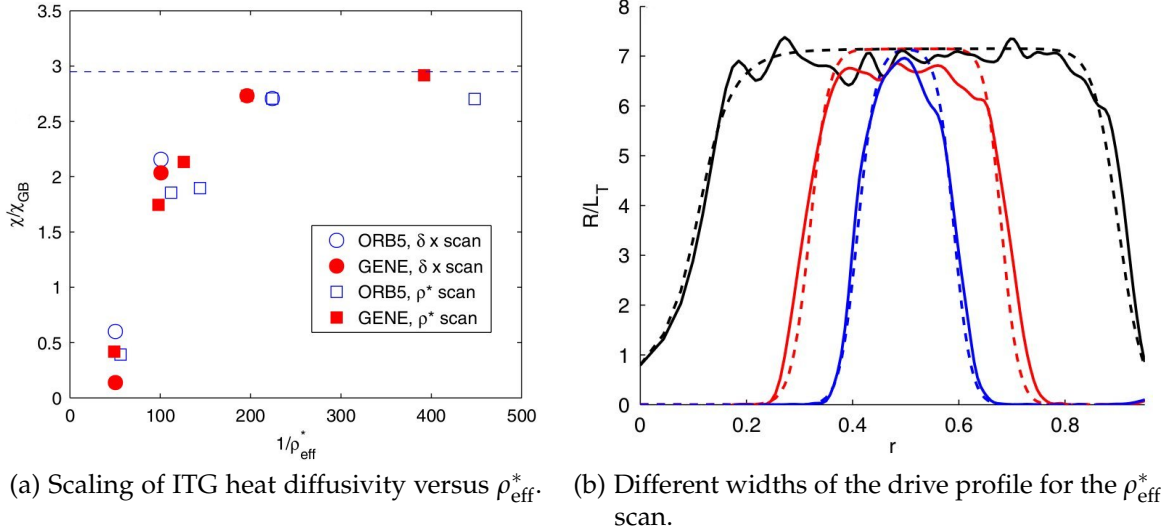


Figure 50: Heat diffusivities and input profiles of a nonlinear scan over the ρ_{eff}^* parameter. As the width of the driving profile approaches the gyroradius scale, the diffusivity decreases strongly. Source: Ref. [72]

gradient. $H(x)$ is the Heaviside step function, which is 1 for positive argument, and zero otherwise.

In the diffusivity scalings given in Fig. 49c for ETG turbulence, two distinct regimes are visible: For positive shear, ETG turbulence exhibits a large diffusivity (due to radially elongated streamers), which quickly rises with the gradient. For negative shear, on the other hand, the diffusivity appears to increase weakly with the gradient, at rather low values. For the present considerations, we will regard this behavior as a constant diffusivity. Translating the above observations to heat fluxes, one obtains for large κ

$$\begin{aligned} Q_{ITG} &\propto \kappa - \kappa_c \\ Q_{TEM} &\propto \kappa - \kappa_c \\ Q_{ETG}(\hat{s} = -1) &\propto \kappa - \kappa_c \\ Q_{ETG}(\hat{s} = 0.8) &\propto (\kappa - \kappa_c)^2. \end{aligned}$$

One would therefore expect that towards large gradients, the heat flux due to ETG turbulence increases at least as strongly as that of ITG or TEM. Another effect that must be considered, is given by global effects, which become important more quickly at steeper gradients. Considering the ρ_{eff}^* scaling from Ref. [72] (see Fig. 50), it is obvious that, as the width of the driving profile approaches the gyroradius scale, the generated diffusivity decreases accordingly. In a transport barrier situation, the width Δ_r of the driving profile can be considered to be proportional to the scale length of this profile, i.e. $\Delta_r \propto L_T \propto \kappa^{-1}$. With this reasoning, global effects can be assumed to reduce the $\chi_{eff}(\kappa)$ scaling by a factor κ^{-1} .

If we now consider again the situation for large-scale turbulence like ITG/TEM and small-scale ETG turbulence, there is a crucial difference in that the gyroradius scale of the latter is smaller by a factor $\sqrt{m_e/m_i}$, which is—for deuterium ions—a factor of 1/60. The diffusivity reduction due to finite profile width is therefore only relevant for large-scale turbulence, but not for ETGs, as these are, in the plot of Fig. 50a, located at very large values of $1/\rho_{\text{eff}}^*$. Applying the simple reasoning from above and examining the scaling at large κ , one then arrives at

$$\begin{aligned} Q_{\text{ITG}} &\propto 1 \\ Q_{\text{TEM}} &\propto 1 \\ Q_{\text{ETG}}(\hat{s} = -1) &\propto \kappa - \kappa_c \\ Q_{\text{ETG}}(\hat{s} = 0.8) &\propto (\kappa - \kappa_c)^2. \end{aligned}$$

Therefore, at steeper gradients, the heat fluxes of ITG and TEM are limited despite the increasing gradient, while those of ETG turbulence would keep increasing³⁶ and thus be the limiting factor in the steepness of a barrier.

The above considerations are crude, of course, and the situation in a real transport barrier is not exactly the same as in the scan depicted in Fig. 50. In reality, the gradient outside the barrier will not be zero, since the injected heat flux must be transported outward by some kind of turbulence. The latter is therefore not exclusively active in the region of the steepest gradient. As an example of a realistic barrier profile, consider that of Case I in Fig. 33a, which has a rather narrow Δ_r , but a finite gradient at outer radii.

Also, the above estimates are valid in the large κ limit. On the other hand, when κ approaches the critical value κ_c , the ETG contributions (especially when no streamers are present) can be small, and at a given heat flux, the rise of the profile gradient may already be limited by large-scale turbulence before the contribution due to ETGs grows to significant values.

Still, the present discussion offers some insight why ETG turbulence is expected to become important in the regimes studied here. It is also well supported by the simulation results of the present chapter, which showed the most dominant appearances of ETG turbulence exactly in the regions of steepest gradients. In addition, the discrepancy between the heat fluxes obtained from local and global runs is understandable in light of the ρ_{eff}^* scaling, since all cases studied in this chapter are—due to the small size of TCV—in a range where ρ_{eff}^* is substantially larger than 1/100.

5.8 SUMMARY

In the present chapter, the global GENE code was applied for the first time to discharges exhibiting an electron internal transport barrier, performing the most

³⁶ Of course, at sufficiently steep gradients, global effects would start to affect also ETG turbulence. This would happen earlier for streamer-dominated ETGs at positive shear; but due to their rather large heat flux, it is questionable whether the gradient could even rise to a sufficiently high level.

comprehensive simulations to date of such a scenario. The discharges studied were fully non-inductive, but with minor imposed current perturbations to tweak the magnetic shear profile, with implications on the barrier strength. Two such discharges from the TCV tokamak were examined here, and an additional set of profiles was used as an intermediate case.

As expected, the simulations found a turbulence-free region in the core plasma of the reversed-shear cases. Unlike in previous studies, unstable ETG modes were found in the linear simulations for both the reversed-shear parameters with an eITB, as well as for the monotonic q parameters without an ITB. In the nonlinear runs, these ETG instabilities persisted, and enforced the usage of artificial damping of small-scale modes in order to achieve converged simulations. While this is unsatisfactory from a physical point of view, it also demonstrates that ETGs apparently can contribute a large fraction of the electron heat flux.

To substantiate this result, a comprehensive sensitivity study was carried out. Using a significantly lower ion temperature, the ETG contributions could be stabilized in all cases *except* the eITB case (IV), where linearly unstable ETGs persisted. In the nonlinear regime, it was found that even at this lower ion temperature, the transport driven by ETG turbulence was large enough to explain the experimental electron heat flux. It was also shown that while the presence of impurities reduces the ETG-driven heat flux, it remains large enough to surpass the experimental fluxes. The most realistic heat flux levels for the steep eITB, which were obtained with slightly relaxed electron profiles, had a contribution of 40 % driven at ETG scales, underscoring their importance.

Due to restrictions of the computational resources, it was not possible in the present work to study the interplay of large-scale and small-scale turbulence in a simulation encompassing both ion and electron scales. Such a study is thus left for future work. From the presently available evidence, and also theoretical scaling arguments, we conclude that ETG turbulence is a key player in eITB physics.

6

ELECTRON TEMPERATURE GRADIENT DRIVEN TURBULENCE IN THE PLASMA EDGE

6.1 OVERVIEW

In the present chapter, the GENE code is used to study instabilities and turbulence for plasma conditions found in the edge of ASDEX Upgrade. As input, we use profile and equilibrium data from a particular ASDEX Upgrade discharge, which is described in Sec. 6.2. As will be shown in Sec. 6.3, the linear growth rate spectra exhibit ETG instabilities, which dominate over a large part of the spectrum. Considering the common notion that large-scale turbulence is suppressed by $E \times B$ shear flows in the edge, ETG turbulence could play an important role in driving the residual electron heat transport in the H-mode pedestal, since it exists at very small spatial scales and is therefore not affected much by equilibrium flows.

Section 6.4 gives a detailed account of the numerical setup employed in the present ETG studies, as well as extensive nonlinear convergence studies, demonstrating the accuracy of the obtained results. Issues regarding the initialization of such simulations, as well as the application of different numerical and physical dissipation mechanisms are discussed. Furthermore, an improvement of the parallel resolution through the optimized coordinate definition (Sec. 4.3) is demonstrated, and the validity of the adiabatic ion approximation is examined. By comparison against simulations using the shifted metric (Sec. 4.2), it is shown that the strong variation of the local magnetic shear at the edge is accurately described also in the standard local simulations.

In Section 6.5, nonlinear simulations of ETG turbulence for realistic ASDEX Upgrade edge parameters are shown. The physical effects studied in the present chapter include the radial dependence of the heat flux and heat diffusivity generated by the ETG turbulence. It is observed that ETG turbulence in the edge is very strongly localized around the outboard midplane, where the magnetic shear is low or even negative. This, together with the strong Shafranov shift, suppresses the generation of streamers and leads to isotropic eddy structures at all examined radial positions. Beyond the standard parameter set, another important question related to edge plasmas is the influence of impurities and varying temperature ratios on the heat flux. This issue, although related to ion physics, can be accommodated within the adiabatic ion framework used for the majority of the ETG simulations presented here. Some of the linear results reported in the present

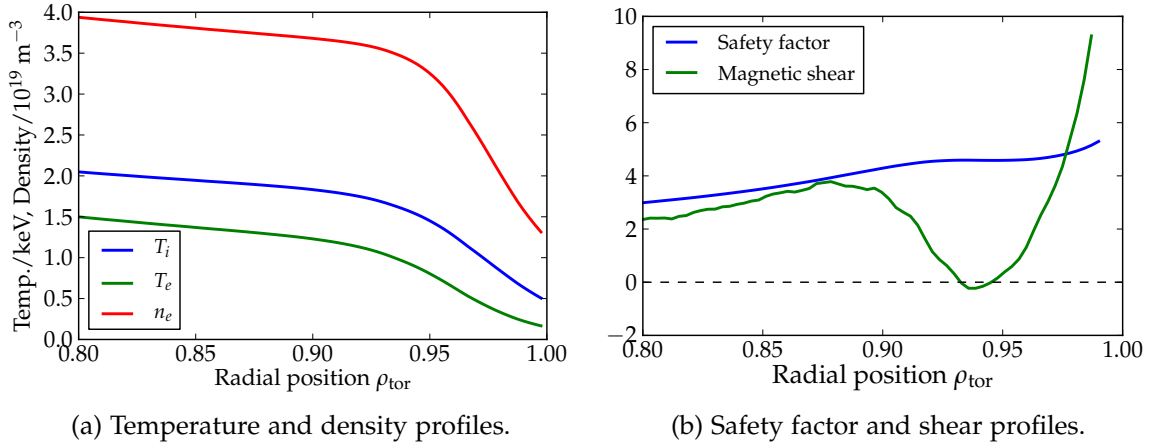


Figure 51: Profiles for ASDEX Upgrade discharge #20431.

chapter have been published in Ref. [97], and first nonlinear simulations of edge ETG turbulence for these conditions were reported in Ref. [98].

6.2 DISCHARGE 20431

The plasma discharge primarily studied in the present chapter is a Type-I ELM_y H-mode discharge with a plasma current of 1.0 MA and a toroidal magnetic field of 2.4 T. In this discharge, a scan over the input power delivered by neutral beam injection (NBI) was performed, increasing from 5.0 to 10.0 MW in three phases, while a constant ICRH power of 3.4 MW was applied throughout the discharge. The studies in this chapter focus on the first phase with 5.0 MW of NBI heating.

The ion and electron temperature and density profiles (assuming a pure Deuterium plasma) are plotted in Fig. 51a, showing the pedestal shoulder roughly at $\rho_{\text{tor}} = 0.94$ (corresponding to $\rho_{\text{pol}} \sim 0.97$). The MHD equilibrium for this discharge was reprocessed in CLISTE [99], taking into account the additional bootstrap current generated by the steep profile gradients at the edge. This leads to a local flattening of the safety factor profile (Fig. 51b) and even a slight shear reversal in the top half of the pedestal.

6.3 INSTABILITIES IN THE PLASMA EDGE

To get a first impression of the relevant physics under specific plasma conditions, it is generally advisable to study the linear properties of the system, as in many cases observations from such simulations help to understand the characteristics of the fully developed turbulence. The studies shown in this section have partly been published in Ref. [97], but are revisited and more thoroughly investigated here. In particular, some findings that appear unusual when compared to core plasma results can be explained when taking into account edge geometry effects.

6.3.1 LINEAR SIMULATION RESULTS

In the present chapter, we study instabilities and turbulence properties in the edge of an H-mode discharge, which exhibits a very steep pedestal in the density as well as the ion and electron temperatures. Extensive linear studies for this case have already been published in Ref. [97]; here, we focus only on the key results regarding the role of ETG instabilities and turbulence in the edge. In Fig. 52a, the growth rate and mode frequency spectrum obtained for the flux surface $\rho_{\text{pol}} = 0.98$ ($\rho_{\text{tor}} = 0.957$) is displayed, showing a prominent kinetic ballooning mode (KBM) peak at wavenumbers between $0.01/\rho_s$ and $0.1/\rho_s$, followed by a rather weak microtearing instability between $0.1/\rho_s$ and $0.2/\rho_s$. Note, that in Ref. [97] the KBM peak was mislabeled as an „ITG-like” instability; a scan over β_e (see Fig. 52b) shows, however, a clear dependence on this parameter. The results for such very low wavenumbers should, however, be considered with some caution, since all the simulations in this chapter were carried out using the local approximation.

A striking feature of the growth rate spectrum in Fig. 52a is the observation that an ETG mode becomes the dominant instability at rather low wavenumbers around $k_y\rho_s \sim 0.25$. A closer examination of the ETG modes with such low wavenumbers reveals furthermore that they do not peak at $k_x = 0$, as is usually the case for core simulations, but at some finite radial wavenumber. This translates, in the parallel direction, to a peak at the top or bottom of the plasma (Fig. 53), depending on the sign of the radial wavenumber. For both positive and negative radial wavenumber, separate peaks at the same k_y can be found, leading to the two branches of ETG growth rate spectra displayed in Fig. 52a.

The strong parallel localization of the ETG modes observed here allows for linear scans in two dimensions, varying both k_x and k_y while examining only a single k_x mode at a time, instead of the usual procedure of having several parallel connections. Such a scan leads to a growth rate spectrum as displayed in Fig. 54a, which exhibits two branches of ETG modes for each k_y , one of which peaks at the top, the other at the bottom of the plasma. Such a scan was first shown in Ref. [98].

As it will turn out, however, the heat flux generated by ETG turbulence, peaks at $k_x \sim 0$, in apparent contradiction of the linear results. Performing again a 2D linear scan (see Fig. 54b), but for the k_y wavenumbers that dominate nonlinearly ($k_y\rho_s \gtrsim 50$), reveals that for these larger k_y the ETG modes again tend to peak closer to the outboard midplane, and around $k_x = 0$, in close agreement with the nonlinear results that will be shown below.

6.3.2 GEOMETRIC CONSIDERATIONS

As explained previously, the effect of plasma shaping affects the edge region most strongly, and it is therefore worth taking a closer look at the changes to the field geometry occurring there. For this analysis, we will study the geometric coefficients of a flux surface situated in the edge pedestal of discharge #20431. The

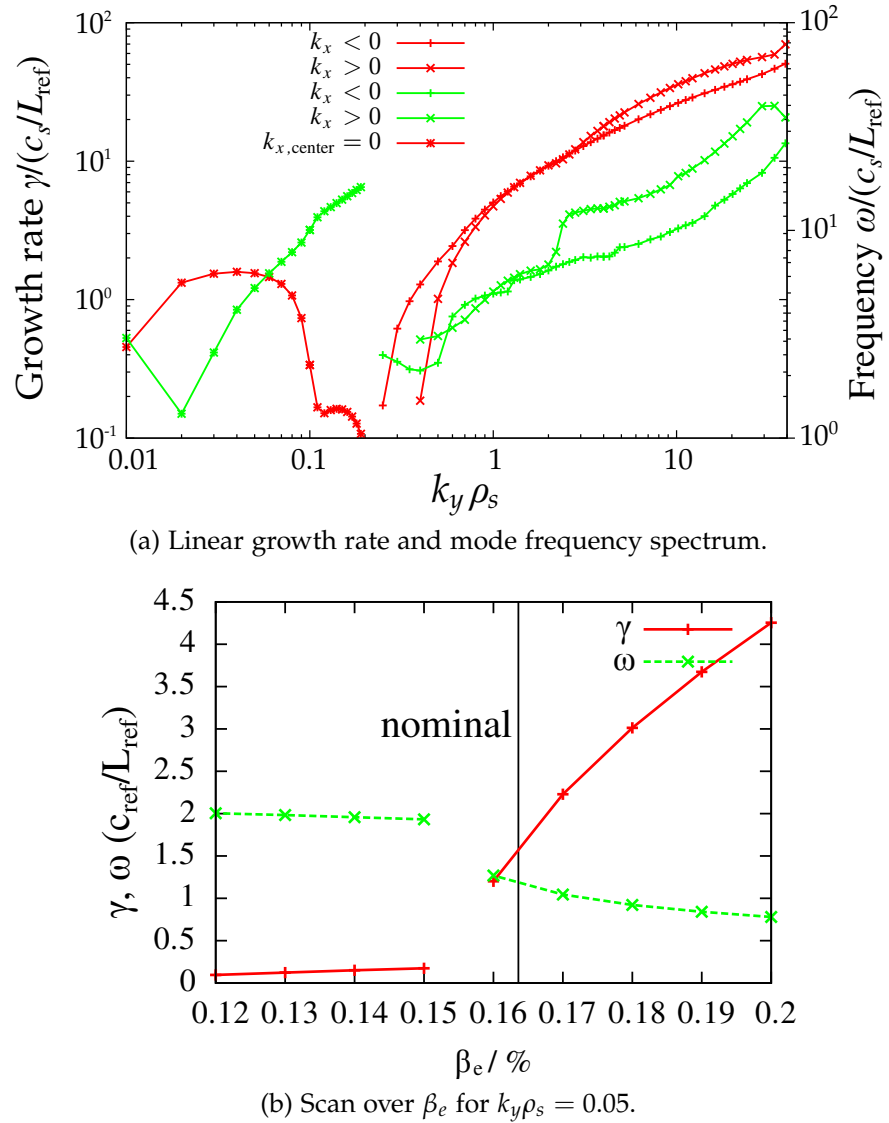


Figure 52: Linear simulation results for $\rho_{\text{pol}} = 0.98$.

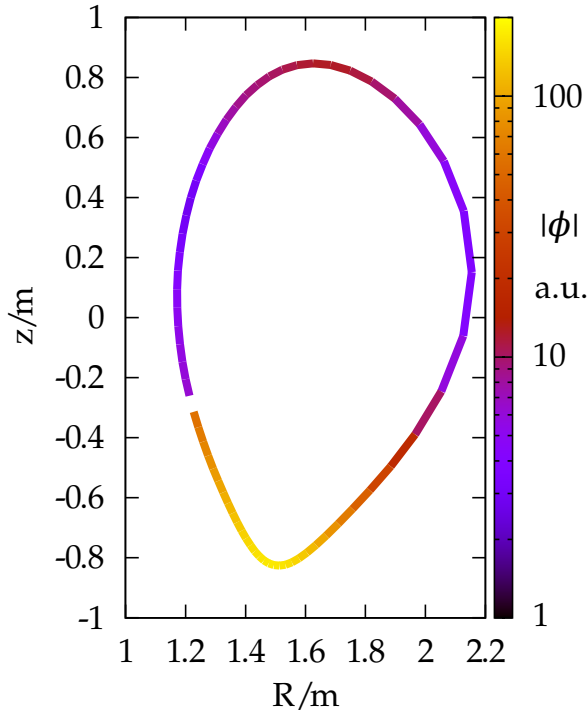


Figure 53: Peak of the electrostatic potential amplitude at the bottom of the plasma for negative k_x .

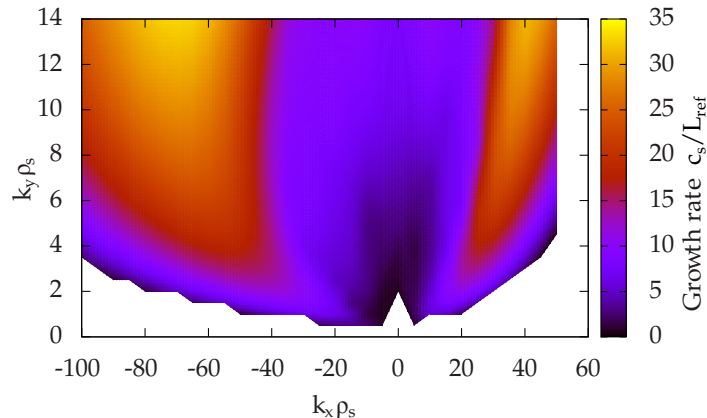
geometric coefficients were generated using the TRACER-EFIT interface described in Chapter 4, based on a CLISTE MHD equilibrium.

As explained before, the Shafranov shift and the elongation of the plasma lead to a stretch-squeeze deformation of the flux tube, which is especially pronounced in the plasma edge. This behavior is shown in Fig. 55: The blue line shows the radial compression of the flux surfaces, while the green line shows the compression of the flux tube in the direction perpendicular to the field and to the radial direction (labeled by \hat{e}_2 in Sec. 3.3). These two factors are given by (see App. A)

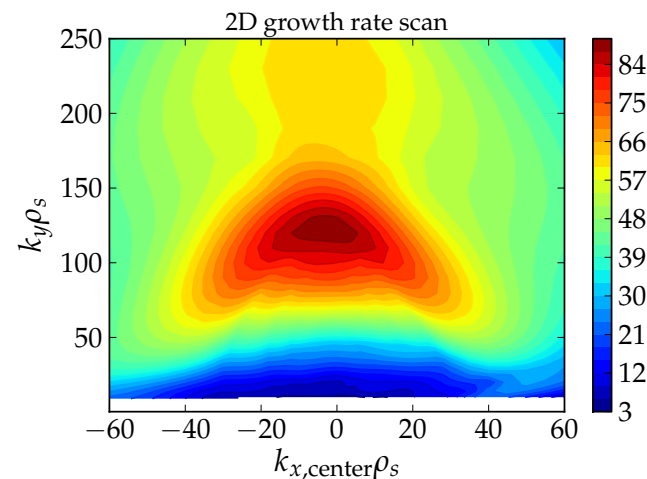
$$\begin{aligned} c_x &= \frac{k_x(k_y = 0)}{k_1} = \frac{1}{\sqrt{g^{xx}}}, \\ c_y &= \frac{k_y}{k_2} = \sqrt{\frac{g^{xx}}{\gamma_1}} = \sqrt{\frac{g^{xx}}{g^{xx}g^{yy} - (g^{xy})^2}}. \end{aligned}$$

Note that the product of these two compression factors is proportional to the magnetic field strength (red line in the figure) and therefore varies slowly along the field line, but each direction by itself can experience a rather strong compression. The curves in Fig. 55 can serve as a direct translation from physical wavenumbers in the radial or binormal direction (k_1 or k_2 , respectively) to the wavenumbers³⁷ in the field-aligned coordinate (k_x and k_y). Considering this effect,

³⁷ The expression for the physical radial wavenumber contains, due to magnetic shear, an additional term proportional to k_y (see App. A), so that c_x should best be regarded as the factor modifying the distance between the flux surfaces.



(a) 2D linear scan for low k_y wavenumbers. The ETG instability peaks at finite k_x values (off the outboard midplane).



(b) 2D linear scan. For higher k_y modes, the ETG instability peaks again around $k_x = 0$ (close to the outboard midplane).

Figure 54: 2D linear scans over k_x and k_y , considering only a single k_x in each simulation.

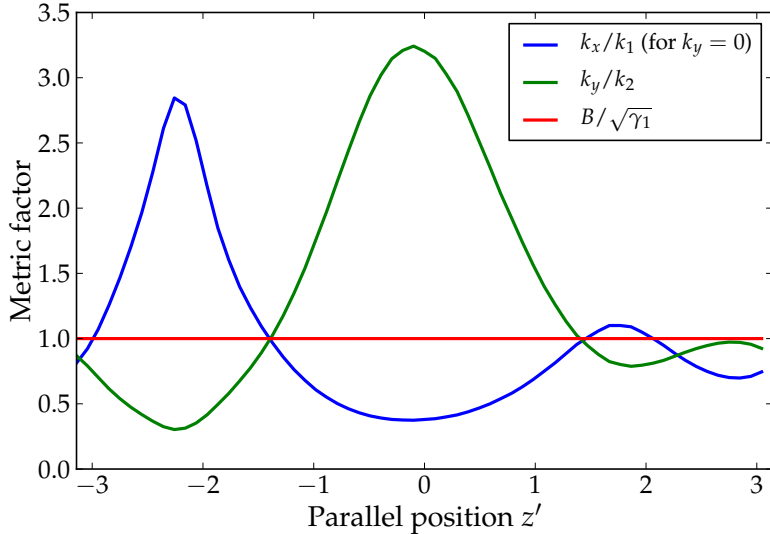


Figure 55: Illustration of the deformation due to shaping of a typical ASDEX Upgrade flux tube at $\rho_{\text{pol}} = 0.98$, versus the (optimized) parallel coordinate z' . See text for description.

binormal wavenumbers appear to be much larger at the outboard side, while radial wavenumbers appear to be smaller. Conversely, at the bottom of the plasma, radial wavenumbers are scaled to larger values, and the binormal wavenumbers to smaller ones. This largely explains why ETG modes at the bottom of the plasma appear for very small k_y , and why they can at the same time peak at very large k_x .

Taking into account these factors, ETG modes at the bottom of the plasma appear at $k_2 \rho_s \sim 0.75$, and the growth rate peak at the outboard side (at $k_y \rho_s \sim 120$) moves down to $k_2 \rho_s \sim 35$. As is obvious from the figure, at the top of the plasma the modification of the wavenumber is small, so that ETG modes there indeed appear for $k_2 \rho_s \sim 0.5$. Some reduction of the low- k_y cutoff can, however, also be expected due to the very steep gradients in the edge; an estimate for the cutoff wavenumber of toroidal ETG modes is given roughly [100] by the wavenumber at which the transit frequency and the diamagnetic frequency are equal,

$$k_{y,\text{cutoff}} \rho_e = \sqrt{\frac{T_e}{T_i} \frac{L_{Te}}{qR}}.$$

Using edge values (see Table 10), this leads to an estimated $k_{y,\text{cutoff}} \rho_s \sim 0.15$.

As can be seen from the linear simulation results (Figure 52a), ETG-type instabilities dominate large parts of the growth rate spectrum, indicating their possible importance under these conditions. The small-scale nature of ETG turbulence facilitates a local description even in the edge transport barrier, despite the narrow radial extent of the latter. We will therefore perform local nonlinear simulations to study the transport properties of ETG turbulence in the edge. Note, however, that this can only be done in a single-scale fashion, excluding the physics of low wave numbers. The reason for this restriction is the extreme spread of the edge

growth rate spectrum, which exhibits unstable modes from the very lowest possible (see Sec. 3.2.2) wave numbers around $k_y \rho_s \sim 0.01$ to extremely large wave numbers of $k_y \rho_s \gtrsim 100$, which would require extremely large simulations in order to involve both ion and electron scales³⁸. Furthermore, for most of the simulations we are going to employ the adiabatic ion approximation, whose validity will be examined in several dedicated simulations. Careful numerical convergence tests will be performed in order to verify that the grid resolution is sufficient. Before we elaborate on the results of these simulations, however, a short historical overview on ETG turbulence properties will be given.

6.3.3 BRIEF HISTORY OF ETG TURBULENCE

From the early descriptions of electron temperature gradient modes [102, 103] until the late 1990s, the prevalent opinion on ETG modes was that their contribution to turbulent transport should be negligibly small, and that the latter should be determined by ion temperature gradient-driven turbulence (ITG) and trapped electron mode turbulence (TEM). This opinion was based on the well-known mixing length estimate, which states that the heat diffusivity caused by temperature gradient driven turbulence is roughly given by $\chi_{j,\text{ml}} = \rho_j^2 v_{Tj} / L_{Tj}$, where the species index j stands for either ions or electrons. This estimate is based on assumptions about the eddy sizes and eddy turnover times relevant to the respective turbulence. Inserting the numbers, one can easily see that the ion heat diffusivity exceeds its electron counterpart by a factor of $\sqrt{m_i/m_e} \approx 60$. Another theory [104] suggested that ETG transport should be dominantly electromagnetic, leading to a heat diffusivity scaling like $\chi_e \sim \chi_{e,\text{ml}} / \beta$, or that radially elongated streamers could raise the effective heat diffusivity to experimentally relevant levels [61, 105].

In 2000, nonlinear gyrokinetic simulations showed [27, 65, 96] that ETG turbulence in toroidal geometry (as opposed to a curvature-free slab) indeed exhibited pronounced streamers, generating an electron heat flux close to experimentally observed levels. This result was later challenged by further nonlinear gyrokinetic simulations [106] conducted with a particle-in-cell (PIC) code, which did not find the same large transport levels and suggested that streamers could—even if present—not affect the overall transport. As was subsequently shown [107, 108, 109, 110], however, these simulations were dominated by noise, invalidating their results. Improved noise handling in modern PIC codes allowed to resolve these issues. A recent theoretical investigation [111], on the other hand, examined the dynamics of particle motion in radial streamers, reinforcing again the result that streamers can cause a significant transport enhancement.

A particularly interesting development in the context of ETG physics is the advent of multi-scale simulations (see Refs. [26, 101, 112]), allowing for investigations of the coupling between ITG- and ETG-scale turbulence. Therein it was, among

³⁸ Of the order of 10,000 binormal modes would be required, and roughly the same number of radial modes. For comparison consider the multi-scale runs presented in Ref. [101] for core parameters, with a perpendicular resolution of 768×384 modes.

other things, found that ETG streamers persist also in the presence of large-scale turbulence. It was shown that they can provide a significant or even dominant contribution to the electron heat flux; in the case of strongly driven low- k turbulence, ETG-driven transport can be limited due to shearing of the streamers by the large-scale turbulence.

As we will see in the following sections, however, in the plasma edge, ETG turbulence does not exhibit streamers due to the properties of the background geometry, making them more robust against the background modulation due to large-scale turbulence. The absence of streamers in this case does not imply negligible transport: Due to the large gradients in the edge, even the electron mixing length estimate is already comparable to the diffusivities of $\chi \lesssim 1 \text{ m}^2/\text{s}$ observed in the edge.

6.4 NUMERICAL SETUP AND CONVERGENCE

6.4.1 INITIALIZING A NONLINEAR ETG SIMULATION

When performing ETG runs for edge conditions, it has proven advantageous to choose a slightly different initialization for nonlinear simulations. The standard scheme in GENE is to start from a g_1 distribution which has all perpendicular modes initialized, with their amplitudes proportional to $k_x^{-1}k_y^{-1}J^2$, where J is the Jacobian determinant. When using the optimized parallel coordinate detailed in Sec. 4.3, it proves to be more advantageous to choose the parallel dependence of the initial distribution proportional to a Gaussian, since this is closer to the resulting fluctuation profiles.

Furthermore, when initializing with powers of -1 in perpendicular Fourier space, the nonlinear timestep adaptation of GENE [25], which accounts for timestep restrictions due to nonlinear $E \times B$ drift velocities, immediately reduces the timestep to a small fraction of the linear timestep limit upon startup, making the initial phase of the simulation very slow. When initializing the simulation with powers of -2 in both k_x and k_y , on the other hand, the timestep remains at the linear timestep limit for a much longer time, so that the saturated state is reached faster (in wall-clock time). These modifications of the initial condition can be achieved in the GENE parameters by setting `init_cond='ppg'`, `init_aux_x=2`, and `init_aux_y=2`.

In Fig. 56, nonlinear time traces of the lowest-order moments as well as the transport quantities are shown for a nonlinear simulation with adiabatic ions. Note that by definition, the particle fluxes are zero, as for adiabatic ions the cross-correlation between density and potential fluctuations vanishes. Furthermore, the electromagnetic contribution to the heat flux is roughly three orders of magnitude below the electrostatic one; we still keep electromagnetic fluctuations in all simulations, since there is little computational gain in neglecting them.

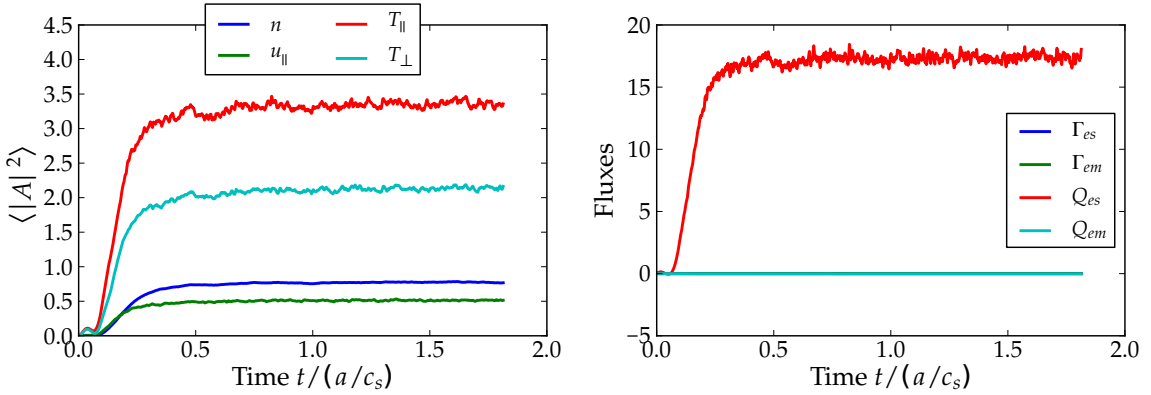


Figure 56: Time traces of normalized RMS amplitudes and normalized fluxes for a typical nonlinear ETG simulation under edge conditions.

6.4.2 OPTIMIZED PARALLEL COORDINATE

In Sec. 4.3, an optimized parallel coordinate was introduced in order to counter the decreasing grid point density on the outboard side as one approaches the edge. Agreement with the standard coordinate was shown in that section, but a demonstration of a case with significant resolution savings is still missing. In the present section, we study the effect of the optimization on linear edge ETG modes, setting $k_y \rho_s = 50$, which is roughly where the most nonlinearly relevant modes are situated. The optimization parameter k , which determines the degree of optimization, is set to 0 (i.e. the standard parallel coordinate is used), 2, and 4, and resolution scans in the parallel resolution are performed.

Figure 57 shows the results of this scan for a parallel grid point number of 64 points. Clearly, without optimization of the parallel coordinate, this resolution is insufficient³⁹ to correctly represent the parallel mode structure. For this case, the correct mode structure is achieved only with 256 parallel points. With $k = 2$, the result is for 64 points already close to the converged result⁴⁰, although the profiles are somewhat jagged—this effect disappears for 96 parallel points. With $k = 4$, on the other hand, smooth parallel profiles are achieved already with 64 parallel grid points.

The growth rate and frequency convergence with increasing parallel grid point number, on the other hand, is demonstrated in Fig. 58. Here, it is visible that the convergence is much smoother with $k = 2$ and $k = 4$ than without any optimization of the parallel coordinate.

For the nonlinear runs performed in this chapter, we choose to set $k = 2$, and we usually run with a parallel resolution of 64 grid points. A resolution scan in the parallel grid point number will be performed below to show that this is adequate.

³⁹ The jaggedness of the parallel mode structure at insufficient resolution is an effect of the finite difference scheme used to compute parallel derivatives.

⁴⁰ Note that the apparent stretching of the mode structures is not caused by insufficient resolution, but by the different definitions of the z' coordinate at given k .

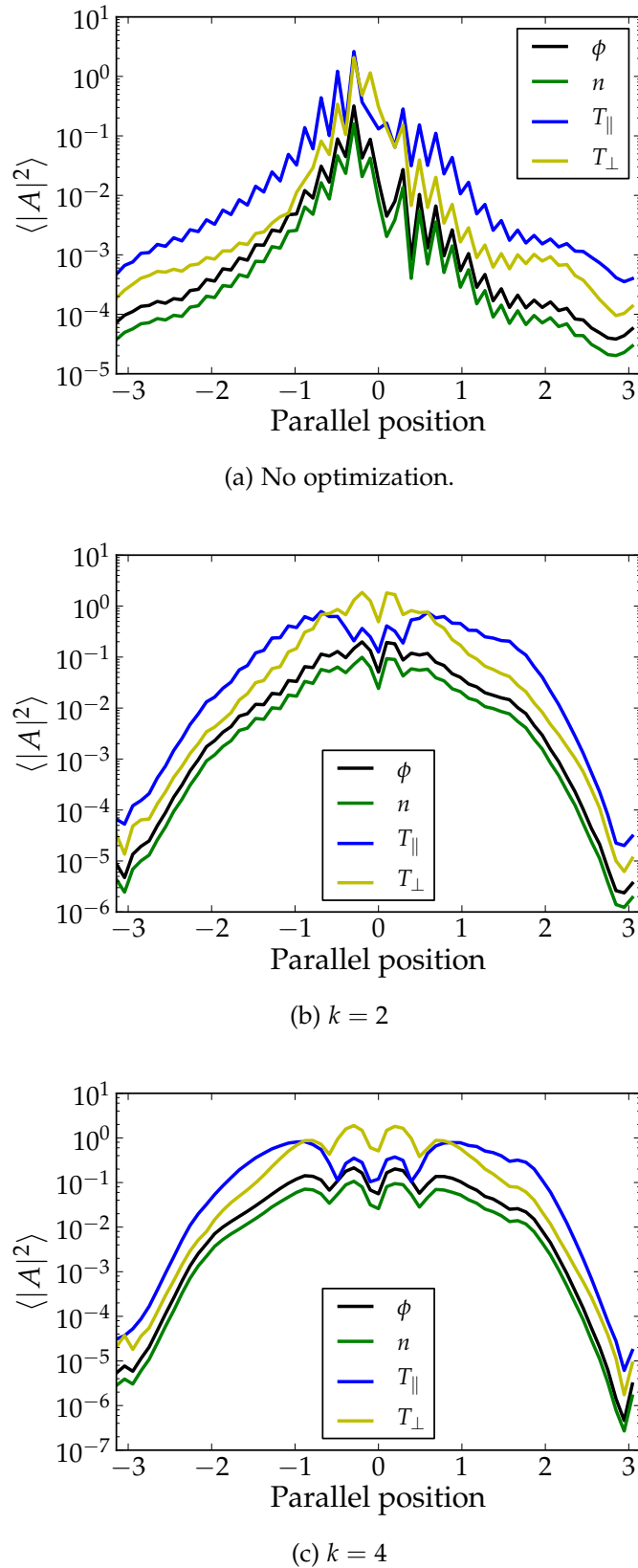


Figure 57: Parallel amplitude profiles versus z' for $k = 0', 2, 4$ with 64 parallel grid points.

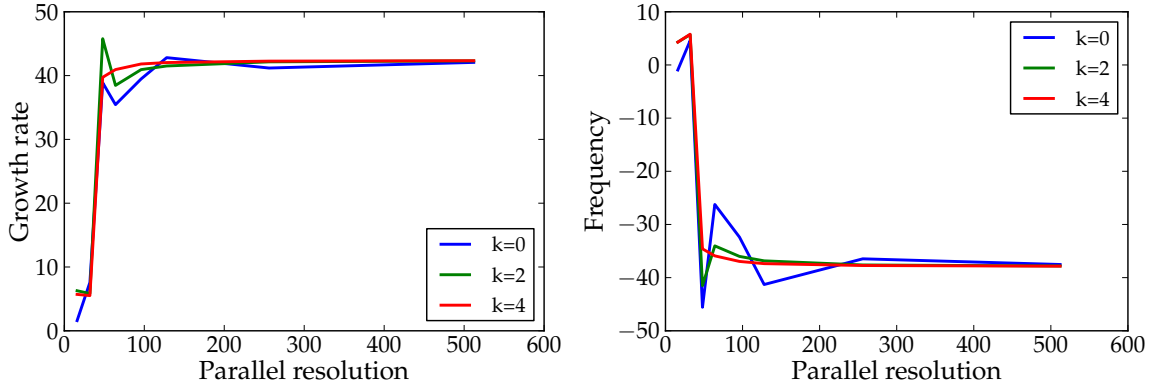


Figure 58: Growth rate and frequency convergence for increasing parallel resolution

6.4.3 ROLE OF DISSIPATION

Although the effect of collisions on ETG turbulence is usually considered to be weak, most of the simulations presented in this chapter will nevertheless be performed with realistic collisions in order to provide a sink for the free energy injected into the system. Usually, in collisionless GENE simulations, hyperdiffusion terms [34] take this role. In particular, the parallel velocity and parallel spatial derivative terms are supplemented by a dissipative part, which is usually of fourth order, i.e. the damping rate scales with the wavenumber k_{\parallel} or $k_{v\parallel}$, respectively, to the fourth power. Similar terms are also available for the other phase space coordinates, with the general form

$$D_{\lambda}^n f = -\epsilon_{\lambda} \left(\frac{\Delta \lambda}{2} \right)^n \frac{\partial^n f}{\partial \lambda^n},$$

where n is the (even) order of the derivative and ϵ_{λ} is the coefficient to the dissipation term of the coordinate λ . The prefactor $\Delta \lambda^n$ is introduced in order to make the coefficient independent of the resolution.

When computing linear growth rates for varying damping coefficient, a plateau regime is usually found, in which the introduction of the hyperdiffusion operator remedies deficiencies of the numerical scheme (e.g. spurious zig-zag structures on the grid scale) but does not significantly alter the physical system. This property is, at least for parallel hyperdiffusion, not well fulfilled for the ETG turbulence cases here due to the strong parallel localization of the underlying linear instabilities. Instead, when varying the parallel hyperdiffusion coefficient ϵ_z , it is found that the resulting nonlinear heat flux can differ greatly: For too low values ($\epsilon_z = 2$ in ion units) no saturated turbulence level is found; in this case, the sinks are too weak to balance the free energy input from the drive terms. For larger coefficients ($5 < \epsilon_z < 20$), saturation is consistently found, but the resulting heat fluxes vary by almost an order of magnitude.

To resolve this unsatisfactory situation, other types of dissipation, including perpendicular hyperdiffusion terms, as well as electron self-collisions at realistic col-

lisionality were examined. In these tests, it was found that when using collisions and a low parallel hyperdiffusion of $\epsilon_z = 2$, saturation was found (in contrast to the collisionless runs), and a similar transport level as for $\epsilon_z = 10$ was reached. Also, for radial hyperdiffusion with $\epsilon_x = 10$, good agreement was found, giving confidence in the validity of the nonlinear fluxes for collisionless runs with moderate hyperdiffusion coefficients. For the convergence tests detailed below, the approach with collisions and $\epsilon_z = 2$ is used to exclude possible resolution effects on the hyperdiffusion terms.

6.4.4 NUMERICAL CONVERGENCE CRITERIA

As mentioned already in Sec. 4.3, due to the extreme shaping and magnetic shear in the plasma edge one has to ascertain numerical convergence of the simulations. In this section, we will describe the criteria that have been used for the present study of edge ETG turbulence.

For our convergence studies, we can deduce several implications from Fig. 55:

- The radial box size is most critical at the outboard midplane ($z = 0$), as the flux tube is most strongly compressed there. To ensure sufficient radial box size with periodic radial boundary conditions, we will measure the turbulence correlation lengths at the outboard midplane and verify that the autocorrelation of the electrostatic potential ϕ decays to zero within the radial box. A scan in radial box size shows that this condition is well satisfied for $L_x \sim 3\rho_s$, and a converged correlation length is achieved for this choice.
- The binormal (y) direction is most strongly stretched at the outboard midplane, therefore at this position the k_y spectra will be shifted to the highest values. An appropriate resolution can then be ensured by verifying that the k_y spectra of all quantities decay sufficiently well at the outboard midplane. In practice, this turns out to be the case for k_y grids extending up to $k_y\rho_s \sim 250$, which will be used as a constraint for the following simulations.

Using the above two constraints (and some experience from earlier simulations of the same case), we can set up a reference simulation with sufficient perpendicular resolution at the outboard midplane, where turbulence usually is strongest. From this initial setup, we will perform convergence tests to find whether this resolution is sufficient also for other parallel positions; for this scan, we have to increase the radial resolution and extend the binormal box size to account for the deformation of the flux tube at positions other than the outboard midplane.

Note that the aforementioned procedure does not explicitly deal with the implications of large magnetic shear. However, the latter automatically enters into any radial resolution test, and can ultimately be dealt with by verifying the standard simulations against shifted metric runs.

ρ_{tor}	ρ_{pol}	q	\hat{s}	ω_{Te}	ω_n	$\beta_e/\%$	$\lambda_{D,\text{ref}}/10^{-3}$	$\nu_{\text{ref}}/10^{-2}$
0.957	0.98	4.599	0.745	24.79	11.17	0.164	4.50	1.47

Table 10: Physical parameters for the ETG convergence test.

n_{kx}	n_{ky}	n_z	n_v	n_μ	L_x	L_y	L_v	L_μ	ϵ_z
128	128	64	32	8	3.35	3.14	3.0	9.0	2.0

Table 11: Numerical parameters for the ETG convergence test. The spatial resolutions n_{kx} , n_{ky} and n_z printed in this table are the converged values that are used for all following physics scans at $\rho_{\text{pol}} = 0.98$. For other positions, the parameters are slightly varied from this setup.

Basic parameter set

All convergence studies shown here are performed with the physical parameters taken from the H-mode (low power) phase of ASDEX Upgrade discharge #20431, the profiles having been averaged over the time window from $t \in [1.65 \text{ s}, 2.0 \text{ s}]$. The electron temperature and density diagnostics were sufficiently well resolved in time to select only values from before the onset of ELMs. The physical and numerical parameters for the convergence tests are summarized in Tables 10 and 11, respectively.

Radial resolution

We start from a baseline case with 64×32 modes in the perpendicular plane and increase the number of radial modes sequentially by factors of two, keeping the radial box size $L_x = 2.85$ constant.

Figures 59a and 59b show the radial and binormal spectra of various fluctuating quantities with increasing resolution. Plotted are the electrostatic potential, density, and parallel/perpendicular temperature fluctuations in black, green, blue, and yellow color, respectively, with solid, dashed and dash-dotted linestyles denoting the different resolution levels in increasing order.

In the radial spectra, all of the aforementioned quantities show—as could be expected—changes mainly in the smallest radial scales; namely, the contributions at small-scales decrease significantly when increasing the resolution. In the binormal spectra, the same effect can be observed at the smaller scales. In both directions, the difference between 64 and 128 modes is much larger than the difference between 128 and 256, indicating more satisfactory convergence for the 128-mode case. The same is also visible in Figs. 59c and 59d, which display the radial and binormal heat flux spectra. The spectra for 64 modes differ—in their level, not so much in their shape—significantly from the other two resolution cases.

Finally, the parallel heat flux profile is shown in Fig. 60a, and the overall flux levels in Fig. 60b. Again, the parallel profile shape is similar for all radial resolutions, but the overall heat flux level is $\sim 30\%$ higher when comparing lowest

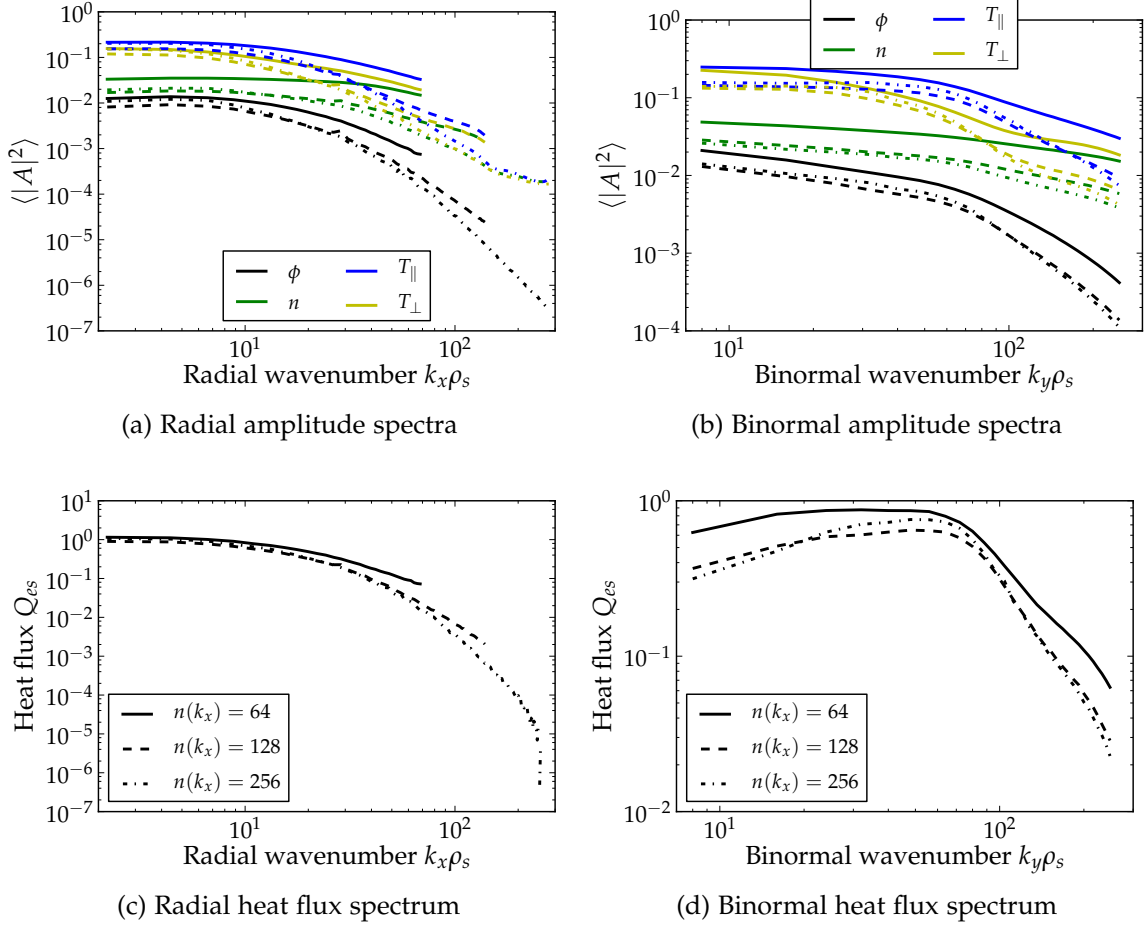


Figure 59: Amplitude and heat flux spectra for increasing radial resolution. The solid, dashed and dash-dotted lines represent radial resolutions of 64, 128 and 256 modes, respectively.

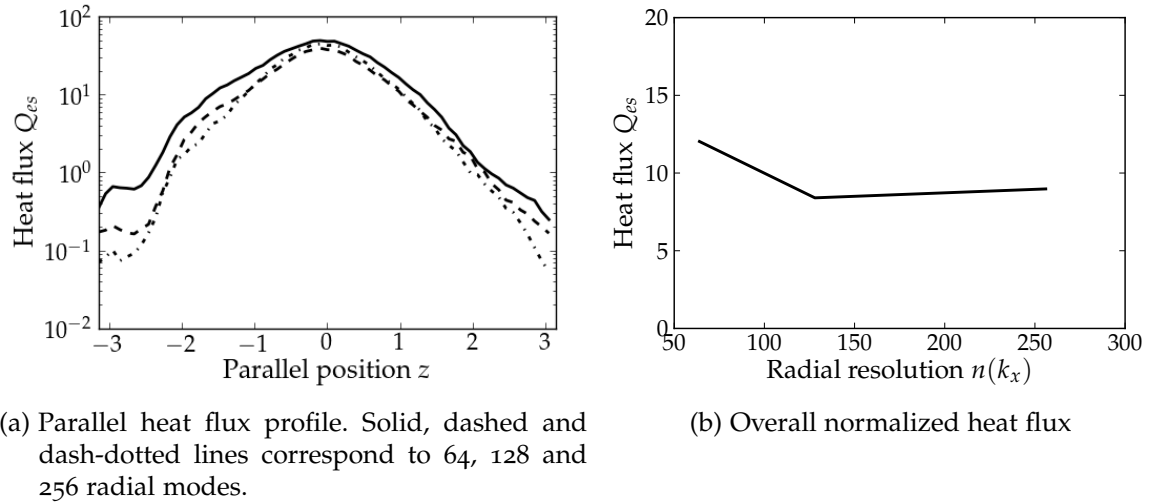


Figure 60: Parallel heat flux profile and total heat flux dependence on radial resolution.

and highest resolutions. From the results of this section, we can conclude that 128 radial modes should suffice to resolve the features of edge ETG turbulence.

Binormal resolution

In the present section, we study the effect of the binormal box size, setting the radial resolution to $n_x = 64$ modes. As has been stated in Sec. 6.4.4, the outboard midplane position is most challenging for the binormal resolution, since the flux tube is—due to the edge geometry—stretched significantly, reducing the effective wavenumbers contained in the grid. By earlier experience, the baseline parameter set is chosen such that the maximum wavenumber is $k_{y,\max}\rho_s \sim 250$ (corresponding to a physical wavenumber of $k_2\rho_s \sim 80$). As was shown in the linear studies of Sec. 6.3, for lower k_y edge ETG modes tend to peak at the top or bottom of the plasma. To study their influence, we increase the binormal box size by lowering the minimum k_y limit sequentially, starting from $k_{y,\min}\rho_s = 8$, and decreasing it in factor-2 steps. In order to keep the resolution constant, at the same time the binormal mode number is increased from 32 (baseline) to 64 and 128 modes, respectively. The radial box size in this case is chosen slightly differently, $L_x = 3.35\rho_s$, in order to fulfill the radial periodic boundary condition for the lowest $k_{y,\min}$ value.

Note that in this convergence study, when displaying binormal spectra, we multiply the spectral contributions by a factor of 2 (4) for the case with 64 (128) modes. This is necessary due the fact that, in our definition, the spectra are actually the contributions of specific modes to the overall value [113], given by the form

$$A_{\text{tot}} = \sum_{k_y} A_{k_y}.$$

Therefore, when we increase the binormal box size, the spacing between the modes is reduced by a factor of 2, keeping A_{tot} constant. The relative contribution of each A_{k_y} is therefore also reduced by a factor of 2, which we choose to compensate in the plots for better comparability of the spectra.

Figures 61a and 61b then show, as before, the root-mean-squared spectra of ϕ , n , T_{\parallel} and T_{\perp} fluctuations for the three different resolutions. The radial amplitude spectra show remarkable agreement for all three resolutions, indicating that all significant contributions are already included at the lowest resolution. Also the binormal spectra overlap very well, except that the cases with larger box size have additional contributions at the largest scales. It is noteworthy that at these scales, the heat flux decreases although the fluctuation amplitudes do not; therefore the decrease in heat flux must be attributed to less favorable cross-correlation of the fluctuating quantities.

Also, the parallel profiles (Fig. 62a) show no significant dependence on the binormal box size. Accordingly, the overall heat flux levels barely change between the different cases. From the results of this section, we can conclude that quantitatively, the case with 32 modes and a minimum wavenumber of $k_y\rho_s = 8$ seems to be sufficiently well-resolved. However, the subsequent simulations will still be

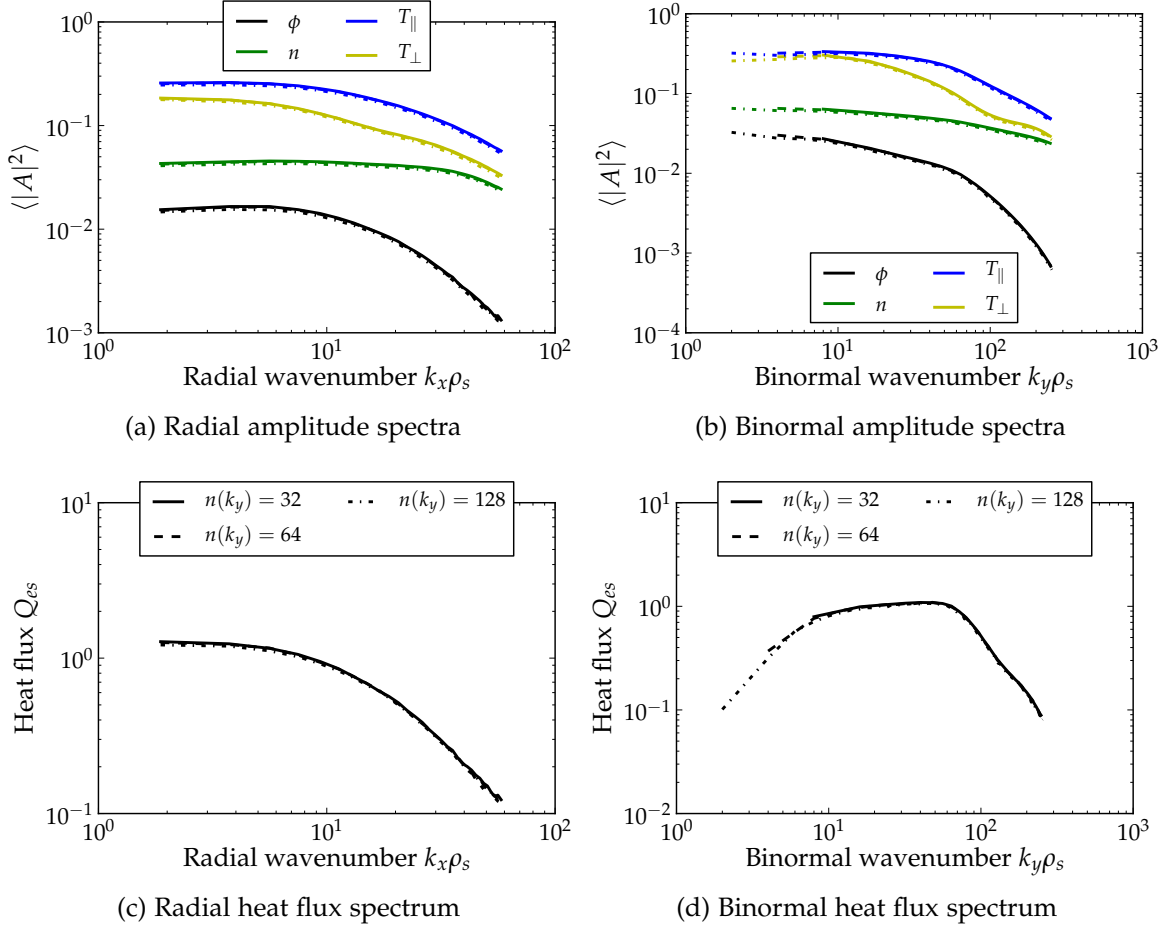


Figure 61: Amplitude and heat flux spectra for increasing binormal box size. The solid, dashed and dash-dotted lines represent resolutions of 32, 64 and 128 modes, respectively, with proportionally increasing box size L_y . In the binormal spectra, the relative contributions of the modes have been scaled for better comparability of the curves (see text).

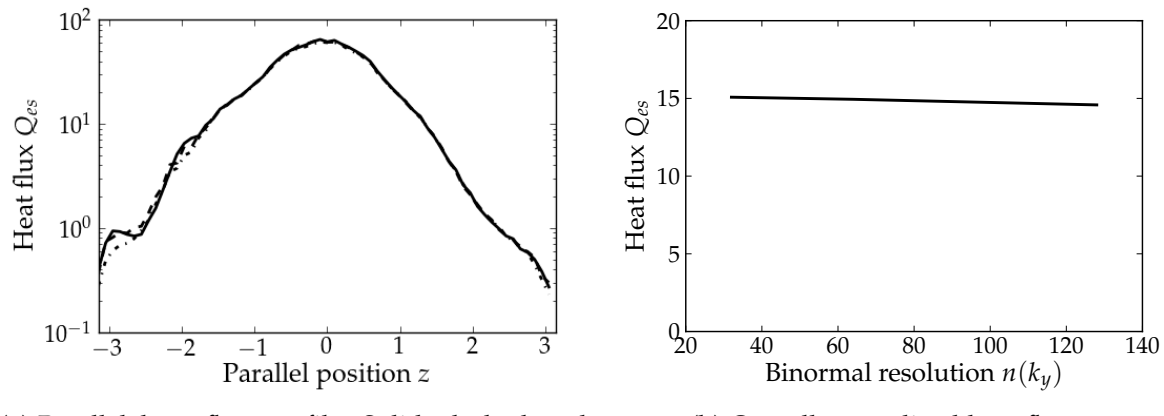


Figure 62: Parallel heat flux profile and total heat flux dependence on binormal box size.

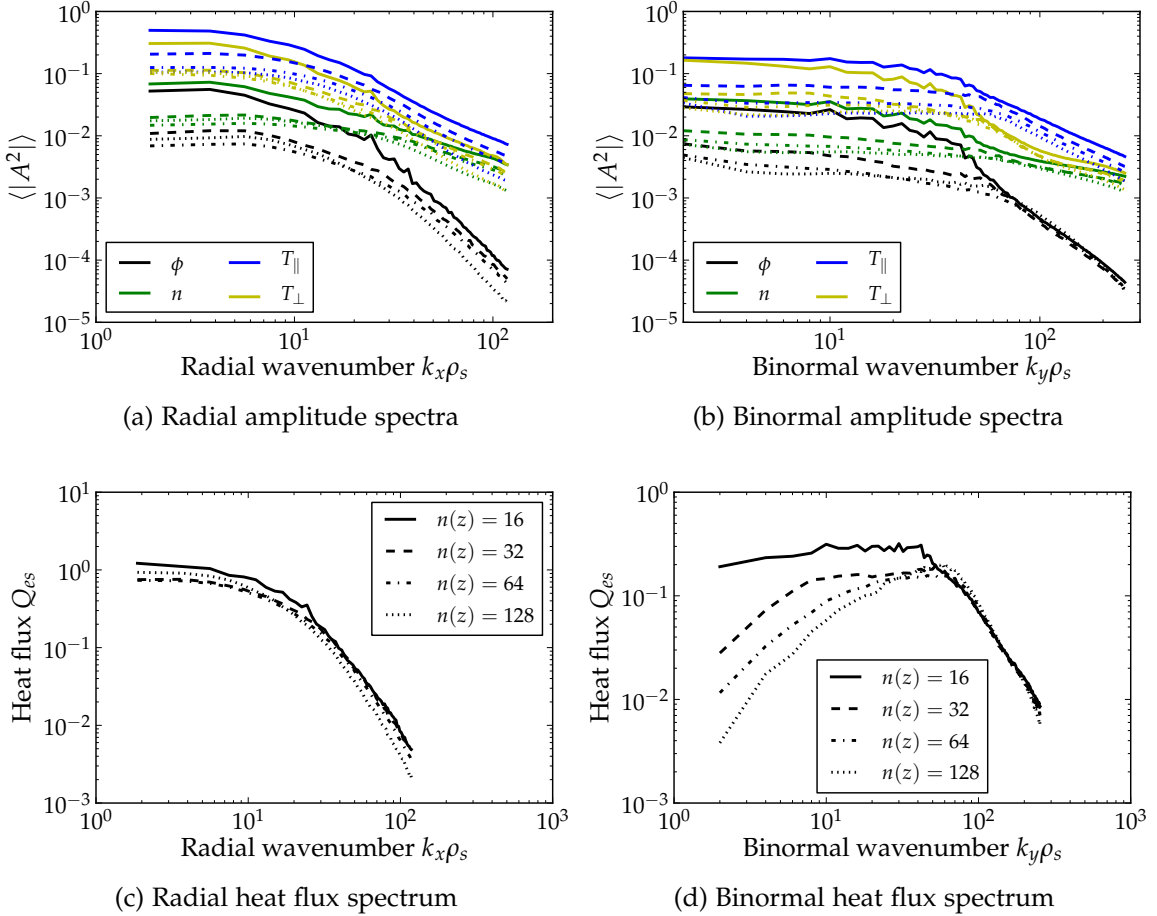


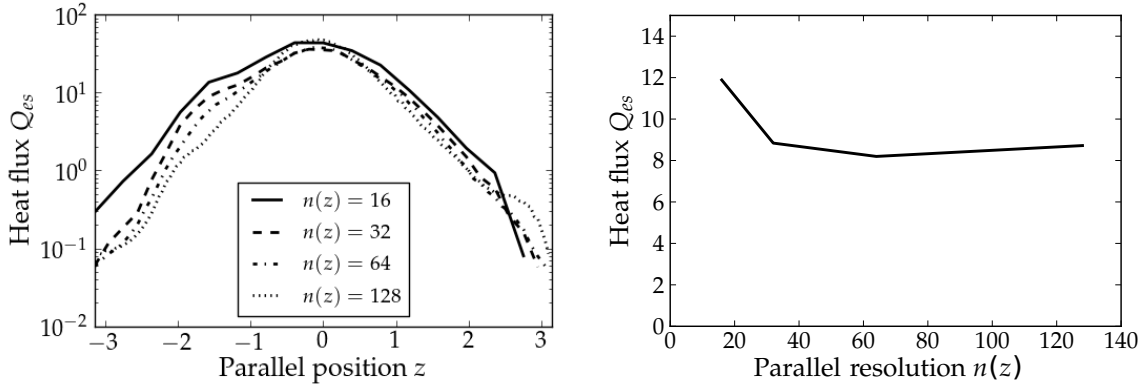
Figure 63: Amplitude and heat flux spectra for increasing parallel resolution. The solid, dashed, dash-dotted, and dotted lines represent resolutions of 16, 32, 64, and 128 grid points, respectively.

performed with 64 or 128 modes, in order to catch the decrease of the heat flux levels towards large scales.

Note also that the present studies have been conducted using the adiabatic ion approximation. Dropping the latter, more significant changes can be expected to occur when considering larger scales in the computation; see below for a discussion of this topic.

Parallel resolution

In this section, we check for convergence in the parallel resolution, taking $k = 2$ for the degree of optimization in the parallel coordinate. The perpendicular grid is kept fixed at 128×128 modes in $\{x, y\}$ during the scan, and in the parallel direction we examine simulations with 16, 32, 64, and 128 grid points, which are again distinguished in the figures by the linestyle; solid, dashed, dash-dotted, and dotted curves correspond to 16, 32, 64, and 128 points, respectively.



(a) Parallel heat flux profile. Solid, dashed, dash-dotted, and dotted lines correspond to 16, 32, 64 and 128 parallel grid points.

(b) Overall normalized heat flux

Figure 64: Parallel heat flux profile and total heat flux dependence on parallel grid resolution.

In this scan, the parallel hyperdiffusion coefficient is kept fixed at $\epsilon_z = 2$. As described in Refs. [114, 34], the coefficient is defined such that the maximum damping rate applied remains unchanged with the resolution scan, but the affected parallel scales become ever smaller with increasing resolution.

As can be seen in Figures 63a and 63b, the fluctuation amplitudes decrease significantly with parallel resolution, only at 64 points the results can be considered well-converged. The same is true for the heat flux spectra depicted in Figs. 63c and 63d: For low parallel resolution, especially the low- k_y contributions to the heat flux are overestimated. Beyond the heat flux maximum, on the other hand, the agreement is good for all resolutions. The overall heat flux levels are overestimated by 30% at $n_z = 16$, but from 32 points onwards, the agreement with the converged result is better than 10%. All subsequent simulations are performed with 64 parallel points to achieve good convergence not only in the heat flux levels, but also in the fluctuation spectra.

Velocity space resolution

In contrast to the global simulations of the previous chapter, the local nonlinear runs of the present chapter do not require a significantly increased velocity space extent or resolution. Simple convergence tests have shown that the standard GENE settings for the normalized velocity grid size, $L_{v\parallel} = 3.0$ and $L_\mu = 9.0$, are sufficient for the presently studied ETG cases, as well as the standard resolutions of $n(v\parallel) = 32$ and $n(\mu) = 8$.

Adiabatic ion approximation

In this section, the validity of the adiabatic ion approximation for the present edge ETG simulations is discussed. For comparison, we examine simulations with ki-

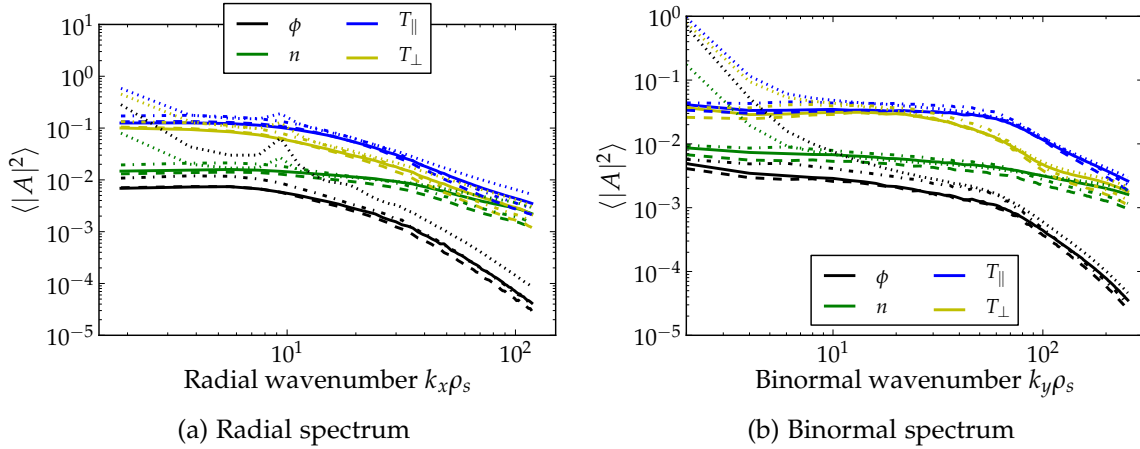


Figure 65: Comparison of amplitude spectra with different degrees of kinetic ion treatments. The solid, dashed, dash-dotted and dotted lines correspond to adiabatic ions, kinetic ions with zero gradients, kinetic ions with only the density gradient, and kinetic ions with all gradients and the realistic temperature ratio.

netic ions with different settings. Figure 65 depicts the radial and binormal fluctuation amplitude spectra for adiabatic ions, kinetic ions with zero gradients, kinetic ions with only the density gradient, and full kinetic ions. As can be seen, the spectra do not change a lot for the first three cases; but when including the ion temperature gradient and the realistic temperature ratio, significant destabilization occurs at the lowest wavenumbers of the system, indicating turbulent activity also at large scales. It should, however, be kept in mind that the large-scale dynamics would be incompletely described even if its scales were completely included in the present simulations, since the effects of profile variation and the $E \times B$ background flow are not taken into account. In the radial spectra (Fig. 65a), upon adding the ion temperature gradient, peaks appear at $k_x \rho_s \sim 9$, which is due to the fact that this mode is the first parallel connection of the $(k_x = 0, k_{y,\min})$ mode, which leads to a coupling of these wavenumbers.

The heat flux spectra do not react to the inclusion of „undriven” ions, but upon adding the ion density gradient, there is an increased flux over a large part of the spectrum. When adding also the ion temperature gradient and the realistic temperature ratio, the flux is still increased, but some more emphasis is on the largest scales of the system. With respect to what generates the residual turbulent transport found in the edge, it is also interesting to examine the particle flux generated by ETG turbulence in a two-species simulation. In the simulations performed in this section, this contribution was negligible, providing only a particle diffusivity of $D \sim 0.007 \text{ m}^2/\text{s}$ with only the density gradient, and $D \sim 0.002 \text{ m}^2/\text{s}$ when adding the ion temperature gradient and the temperature ratio. This is a further indication that ETG turbulence at the scales studied here is probably not the only contributor to edge transport.

Fig. 67 depicts the changes in overall heat flux when going from the adiabatic ion model to increasingly realistic ion treatments. Similar to what could be ob-

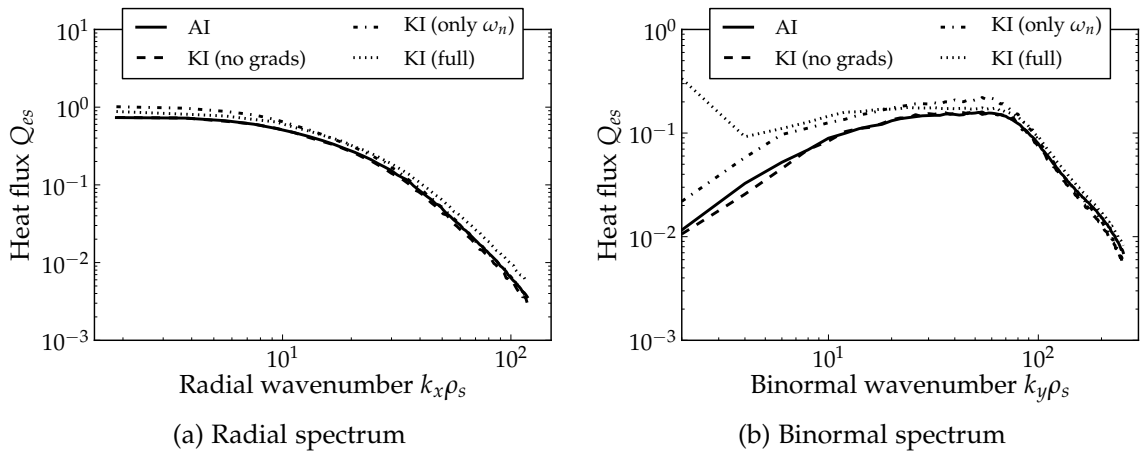


Figure 66: Comparison of heat flux spectra with different ion treatments.

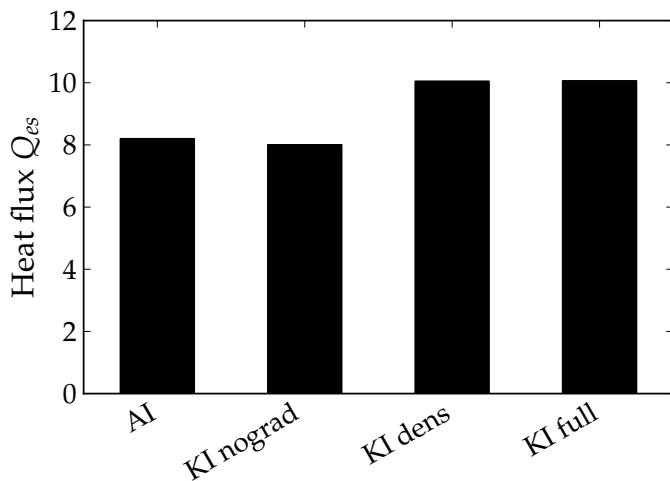


Figure 67: Heat flux varying with increasingly realistic ion models. The label 'AI' refers to adiabatic ions, while 'KI nograd', 'KI dens' and 'KI full' refer to kinetic ions with no drive, only the density gradient, and full kinetic ions, respectively.

served already in the spectra, there is no change when introducing „passive” ions with no drive. Upon adding the density gradient, the overall heat flux increases by $\sim 25\%$. This is not changed when adding also the temperature gradient and temperature ratio, but the added heat flux is then driven at larger scales.

6.4.5 VERIFICATION AGAINST SHIFTED METRIC SIMULATIONS

One striking observation from the nonlinear ETG simulations is the pronounced localization of the heat flux on the outboard midplane. Considering the discussion of the shifted metric in Sec. 4.2, the suspicion arises that this ballooning might not be a natural property of the turbulent system, but rather a numerical artifact due to insufficient resolution. In that respect, it is rather comforting that this should have become obvious in the radial convergence tests performed in Sec. 6.4.4; but

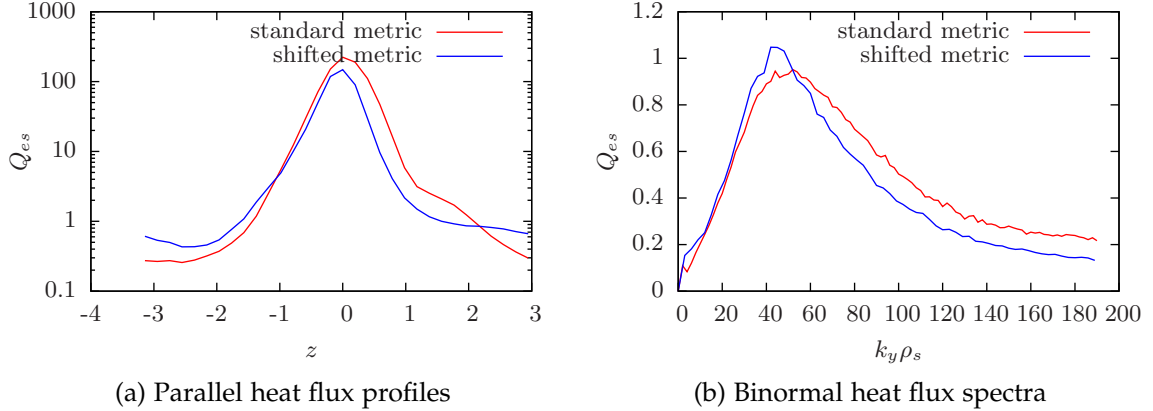


Figure 68: Comparison between shifted metric and standard metric simulations of edge ETG turbulence.

an even better way to validate this result is to compare these simulations to ones using the shifted metric.

As was discussed in Sec. 4.2, the shifted metric can not be straightforwardly implemented in local GENE, since it would in general violate the periodic radial boundary condition. One possibility, however, is to run the global version of GENE, using all the assumptions of the local code, including radially constant geometry and profiles, but with Dirichlet boundary conditions (plus the radial buffer zones). The results of such a simulation are displayed in Fig. 68. Both the parallel heat flux⁴¹ profiles as well as the heat flux spectra show good agreement between the local and shifted metric simulations, confirming that the pronounced ballooning of ETG turbulence is accurate. There is, however, a 20% decrease in the transport level, which can be attributed to the fact that the averaging procedure used to obtain this value included also the buffer zones, which by definition have strongly reduced flux levels.

6.5 PHYSICAL PROPERTIES OF EDGE ETG TURBULENCE

6.5.1 RADIAL DEPENDENCE OF THE ELECTRON HEAT FLUX

This section is devoted to the question of how the electron heat flux caused by ETG modes in the plasma edge depends on the radial position. As can be seen in Fig. 69a, the nominal input profiles show a systematic decrease of the ratio between the density and temperature length scales, defined as

$$\eta_e = \frac{L_n}{L_{Te}} = \frac{R/L_{Te}}{R/L_n} = \frac{\partial \ln T_e}{\partial \ln n}.$$

⁴¹ The curves in Fig. 68 show the contravariant radial component of the heat flux (instead of the physical value); the comparison between the two simulations is, however, not affected.

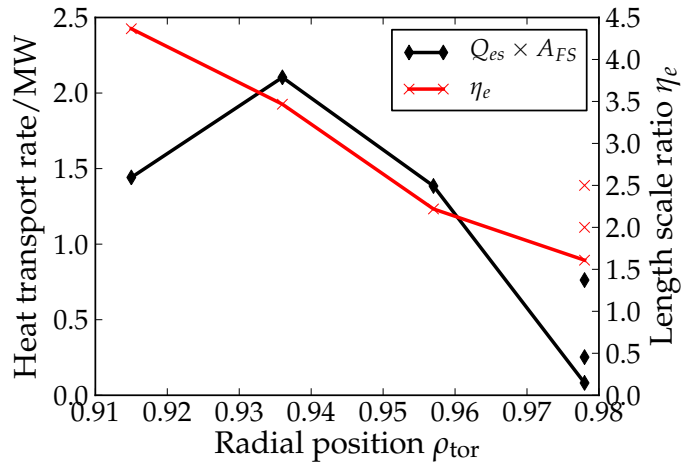
Starting from $\rho_{\text{tor}} = 0.915$, which corresponds to $\rho_{\text{pol}} = 0.96$ (the pedestal shoulder), this ratio decreases from a value of 4.37 to 1.61 for $\rho_{\text{tor}} = 0.978$ ($\rho_{\text{pol}} = 0.99$). The total power passing a given flux surface, on the other hand, increases at first, finds a maximum of ~ 2.2 MW at the $\rho_{\text{tor}} = 0.936$ ($\rho_{\text{pol}} = 0.97$) flux surface, and starts to decrease again towards the lower half of the pedestal. For our standard flux surface at $\rho_{\text{pol}} = 0.98$, we find a heat transport rate of 1.38 MW. Therefore, ETG turbulence transports about 20 – 40 % of the total input power (of which a large part heats the ions) in the region $0.91 \leq \rho_{\text{tor}} \leq 0.96$.

For $\rho_{\text{pol}} = 0.99$ and the nominal profiles, we find a heat transport rate of only 0.1 MW. Considering, however, that there is significant uncertainty regarding the exact values of η_e , a scan over that parameter was also performed to examine whether the observed decrease is just due to the parameters being closer to marginality. Indeed, the scan reveals that even for this radial position, when increasing η_e to 2.5 (roughly the nominal value for $\rho_{\text{pol}} = 0.98$) by raising the electron temperature gradient, the heat transport rate reaches again a value of about 0.76 MW, indicating that even at lower temperatures ETG turbulence can still contribute a relevant fraction of total transport. Nevertheless, a decrease of the heat flux level towards the separatrix is visible. This could be an indication that at the foot of the barrier, another turbulence type—possibly situated at lower wavenumbers—becomes an important contributor.

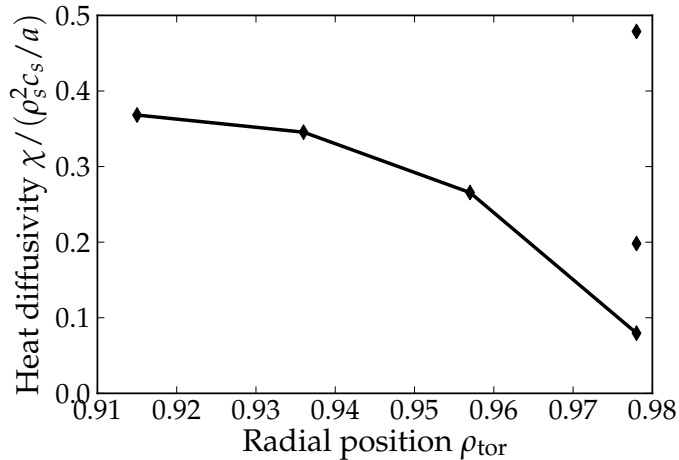
A transport modeling study, focusing on heat and particle transport in the pedestal of the DIII-D tokamak can be found in Ref. [115]. In that study, interpretive transport codes were used to deduce the transport coefficients required to explain the experimental profiles. In addition, predictive transport codes, which employ analytical estimates for various turbulence types, neoclassics, as well as the paleoclassical transport mechanism (which is theoretically disputed, see Ref. [116] and comments), were used to match the experimental profiles. In these analyses, it was found that a combination of ETG transport in the top part of the pedestal, and paleoclassical transport in the lower part of the pedestal was able to achieve the best agreement. While it is beyond the scope of this thesis to discuss the paleoclassical transport mechanism, we can compare the ETG estimates of Ref. [115] to the present results. In Fig. 69b, the radial dependence of the electron heat diffusivity is shown in units of the gyro-Bohm diffusivity $\chi_{gB} = \rho_s^2 c_s / a$. In the upper part of the pedestal, i.e. up to $\rho_{\text{tor}} = 0.96$, χ / χ_{gB} is roughly constant. The physical meaning of this proportionality becomes obvious when noticing that $\chi_{gB} \propto T_e^{3/2}$, i.e. the turbulent diffusivity decreases strongly towards the separatrix. For the heat flux, this leads to

$$Q = -n\chi\nabla T_e \propto n_e T_e^{5/2} \frac{\chi}{\chi_{gB}} \frac{1}{L_T}.$$

Therefore, at constant χ / χ_{gB} and constant temperature scale length L_T , the heat flux would decrease like $T_e^{5/2}$ towards the separatrix. In Ref. [115], it is argued that due to this behavior, ETG turbulence is unlikely to contribute strongly to the transport in the lower pedestal. As can be seen in Fig. 69a, however, this is not necessarily true— T_e changes by more than a factor 2 from $\rho_{\text{tor}} = 0.91$ to $\rho_{\text{tor}} = 0.96$,



(a) Radial dependence of heat transport rate $Q_{es} \cdot A_{FS}$ (total power passing a given flux surface) and length scale ratio η_e .



(b) Heat diffusivity in Gyro-Bohm units.

Figure 69: ETG turbulence results for different radial positions.

while the heat flux remains at roughly the same levels. The reason for this is the strong reduction of the profile scale length towards the edge, which thus competes with the decreasing diffusivity. In addition, the ratio $\eta_e = L_n/L_T$ is found to have a strong effect on the precise value of χ/χ_{gB} (even at the outermost position examined, see Fig. 69b), making a general statement concerning the significance of ETG turbulence at the bottom of the pedestal difficult, given the very sensitive dependence on the background profiles.

6.5.2 ABSENCE OF STREAMERS

In Figure 70, a contour plot of the electrostatic potential fluctuations in the perpendicular plane is shown. Interestingly, there are no clear streamer-like structures, and the eddies appear rather isotropic. As described in Sec. 6.3.3, it is usually assumed that streamers are a necessary ingredient to raise ETG heat fluxes to experimentally relevant levels; in contrast to this, the present simulations show that in the edge, isotropic ETG turbulence prevails, and is able to deliver experimentally relevant transport levels.

A more analytical way of measuring the degree of anisotropy is to compare the turbulence autocorrelation lengths in the perpendicular plane. Figure 71 shows the perpendicular correlation lengths of the electrostatic potential deduced from simulations at the same radial positions as in the previous section. Note that here the output from the GENE DIAGNOSTICS TOOL (GDT) had to be post-processed, as it contains the correlation lengths in the field-aligned coordinates. In order to compare the physical lengths, the obtained radial correlation length has to be divided by $\sqrt{g^{xx}}$, while the binormal correlation length must be divided by⁴² $\sqrt{g^{yy}}$ —see App. A for a more detailed description of the reasons for this step. As is obvious from Figure 71, the radial and binormal correlation lengths are almost identical for every radial position examined, and lie between 4 – 6 ρ_e .

A likely explanation for the absence of streamers is the magnetic field geometry at the edge: In an earlier study [27], it was shown that the appearance of streamers is determined by the interplay of magnetic shear \hat{s} and the Shafranov shift parameter $\alpha = -q^2 R \beta'$, such that no streamers appear for large α and low shear, resulting in lower heat flux. While α is indeed large in the edge due to the strong pressure gradients, the role of magnetic shear is less clear, since it can take very large values due to the proximity of the separatrix. This issue can be resolved, however, by examining the details of the simulation results: As is obvious from the parallel heat flux spectra (e.g., 64a), the vast majority of the overall flux is generated in a rather narrow parallel region close to the outboard midplane. In turn, we examine the parallel dependence of the *local* shear⁴³, given by $\hat{s}_{loc} = \partial_\theta(g^{xy}/g^{xx})$. Figure 72 shows this quantity for the examined radial positions. One can observe that the

⁴² Note that the division by $\sqrt{g^{yy}}$ is only valid at the $z = 0$ position, where the perpendicular coordinate vectors are orthogonal.

⁴³ The local shear is plotted here in terms of the straight field line angle instead of the optimized parallel coordinate.

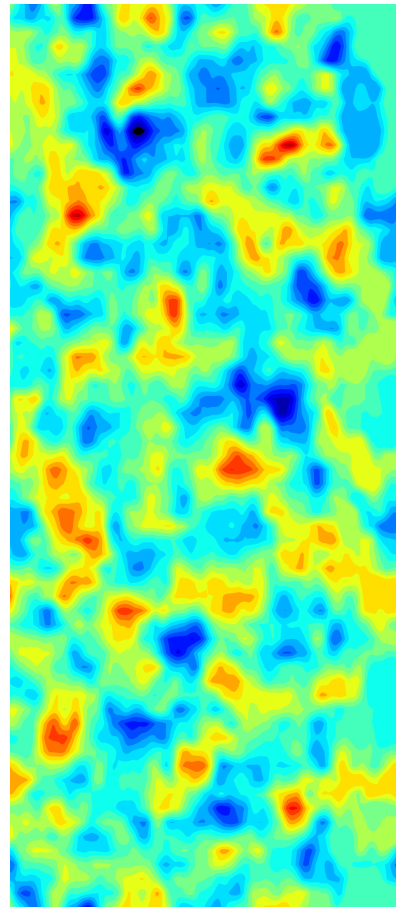


Figure 70: Contour plot of the electrostatic potential fluctuations generated by ETG turbulence in the perpendicular plane $z = 0$. The axes are plotted to physical scale, so that the eddy shapes are realistic—the radial size of the box is, however, only $1.1\rho_s$ or 1.8 mm.

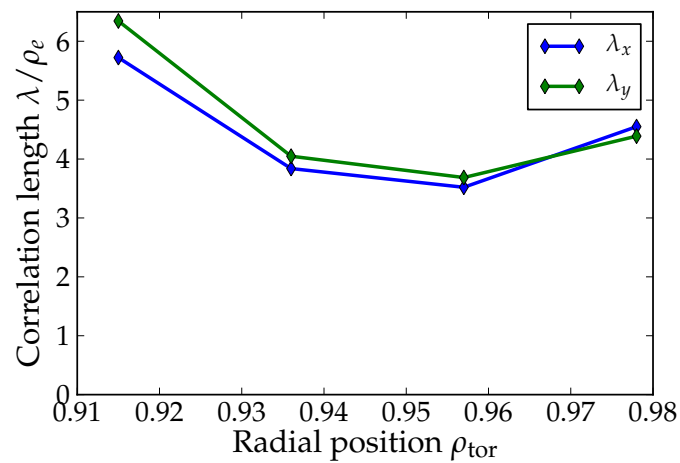


Figure 71: Radial dependence of the radial and binormal turbulence correlation lengths in physical units, showing statistical isotropy in the perpendicular plane.

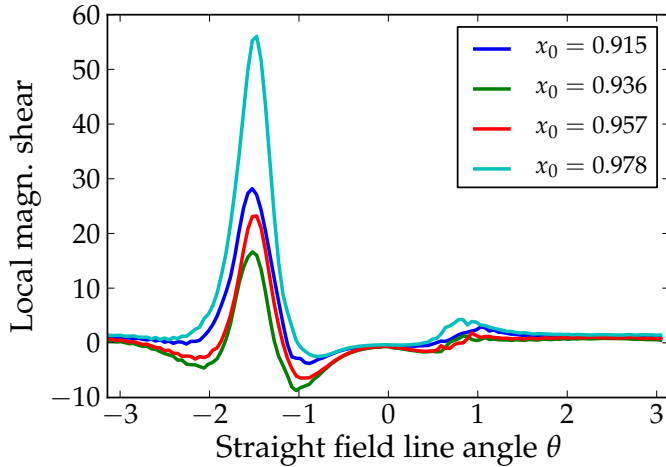


Figure 72: Parallel dependence of local magnetic shear for four radial positions close to the separatrix. The edge divergence of the magnetic shear is localized around the X-point.

edge divergence of the magnetic shear is mainly caused by the peak appearing at the bottom of the plasma, in the vicinity of the X-point. The outboard side, on the other hand, where the heat flux peak is found, is characterized by low or even negative shear. This, together with the large Shafranov shift, provides a viable explanation for the absence of streamers in the plasma edge.

6.5.3 INFLUENCE OF IMPURITIES AND TEMPERATURE RATIO

Due to the proximity to the material walls, the concentration of impurities is usually significantly larger in the plasma edge than in the plasma core. As had been shown in Sec. 2.5, in the adiabatic ion approximation the influence of the ions only enters in the Poisson equation. For equal ion temperatures, this reduces to the adiabatic ion parameter $\tau = Z_{\text{eff}}T_e/T_i$, which is unity for a pure hydrogen plasma with equilibrated electron and ion temperatures. In the local framework, the normalized adiabatic ion Poisson equation (solved for ϕ , and neglecting B_{\parallel} fluctuations) can be written [25] as

$$\phi_1 = \frac{\pi q_e n_{0e} \int J_0 \left(\frac{v_{Te}}{\Omega_e} k_{\perp} \sqrt{\mu B} \right) g_{1e} dv_{\parallel} d\mu}{k_{\perp}^2 \lambda_D^2 + \frac{n_{0e}}{T_{0e}} \left[1 + \tau - \Gamma_0 \left(\frac{T_e m_e k_{\perp}^2}{B^2} \right) \right]}.$$

As can be seen from this form of the equation, the τ parameter directly taps into the feedback loop of the instability, as it decreases the fields resulting from a given density perturbation. One can therefore expect a weakening of ETG instabilities and the corresponding turbulence by impurities and also by a large temperature ratio T_e/T_i .

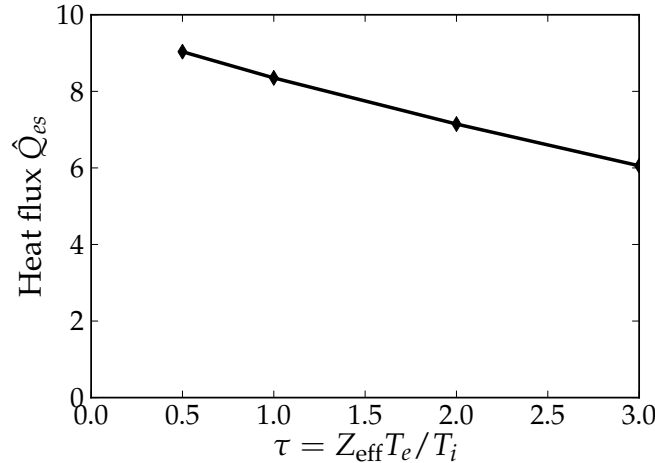


Figure 73: Dependence of electron heat flux on the adiabatic ion parameter τ . The normalized heat fluxes in the graph correspond to power flows of about 1–1.5 MW through the entire flux surface.

In the present section, the parameter τ is varied, which can be considered a combined study of the influence of impurities and the electron/ion temperature ratio. As a reference, we use the converged result for the $\rho_{\text{pol}} = 0.98$ flux surface with $\tau = 1$. In ASDEX Upgrade, the edge values of Z_{eff} can range from 1.5–4 [117], and the temperature ratio tends to be close to unity. For the nominal profiles of the discharge studied here (#20431), the ion temperature at ρ_{pol} is almost a factor of two larger than the electron temperature, pushing the τ parameter back towards unity. Fig. 73 depicts the spatio-temporally averaged heat flux determined from several nonlinear simulations with varying τ , exhibiting a rather weak dependence on the adiabatic ion parameter.

Fig. 74 shows the radial and binormal spectra of density, electrostatic potential fluctuations and the heat flux, where the curves for increasing τ are plotted with an increasingly sparse linestyle. As can be seen in the figures, with increasing τ the density fluctuations are enhanced, especially at the larger scales. The potential fluctuation level, on the hand, decreases in the whole spectral range, which in combination leads to a heat flux reduction mostly at larger scales. Overall, this picture corresponds well to the simple picture drawn from the Poisson equation, with the nonlinear modification that *both* density and potential fluctuation levels change, rather than one staying fixed with varying τ .

6.6 SUMMARY

In the present chapter, microinstabilities and turbulence in the edge of an actual ASDEX Upgrade discharge have been analyzed. In linear simulations, it was found that an ETG instability dominates a large part of the spectrum, while the largest scales are close to the threshold of kinetic ballooning modes. Studying further the properties of the linear ETG instabilities, it turned out that, especially for

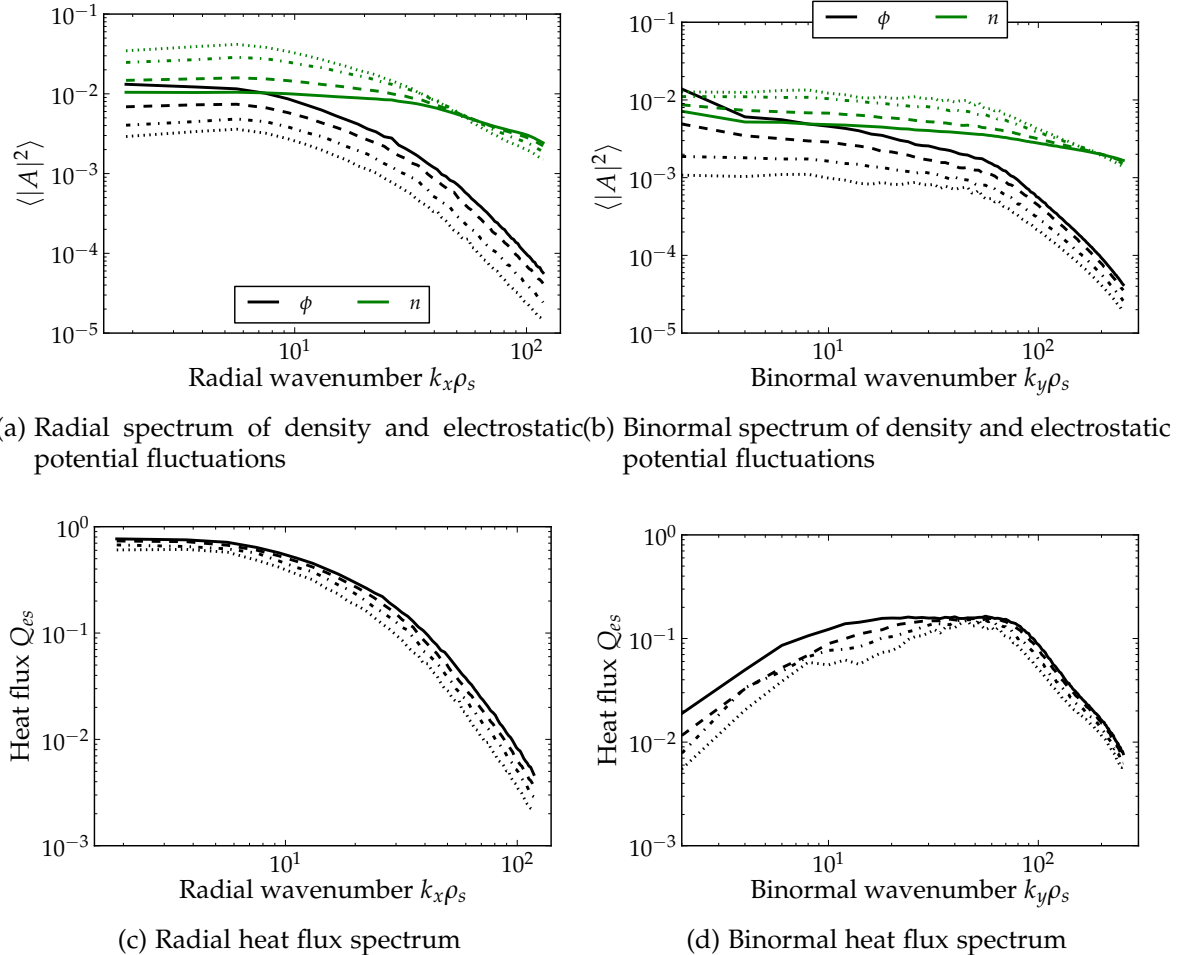


Figure 74: Amplitude and heat flux spectra for varying adiabatic ion parameter τ . Solid, dashed, dash-dotted and dotted lines correspond to $\tau = 0.5, 1, 2$, and 3 , respectively.

low k_y , the modes can peak away from the outboard midplane, and even at the top or bottom of plasma. For higher wavenumbers ($k_y \rho_s \gtrsim 50$), the modes are again more unstable at the outboard midplane than at other positions, and are so strongly localized there that they can still exist in spite of the negative shear. This strong parallel localization is reflected also in the nonlinearly generated transport, and encouraged the use of the optimized parallel coordinate introduced in Sec. 4.3. Extensive numerical convergence tests were performed to ensure an accurate treatment of the turbulent system. These tests involved the radial, binormal, and parallel resolution.

Varying the radial position about the initially studied flux surface, it was found that ETG turbulence can generate a significant fraction of the electron heat transport across the entire edge region. Towards the lower part of the pedestal, some decrease in the heat flux was found, indicating the possibility that other turbulence mechanisms take over towards the scrape-off layer. The stabilizing influence of impurities and low ion temperature was found to be rather weak for edge ETG turbulence.

A striking feature of edge ETG turbulence is that relatively high transport levels were found even in absence of radially elongated streamers, which were so far assumed to be a necessary ingredient for relevant ETG turbulence. In the edge, however, ETGs peak preferentially around the outboard midplane, where—due to the strong shaping—the local magnetic shear is very low, or even negative, even though the global shear may reach large values. At the same time, the Shafranov shift is strong in the edge due to the large pressure gradient. The combination of both low shear and large Shafranov shift is likely to be the reason for the suppression of streamers in the edge. While this reduces the ETG transport levels, the smaller radial extent of the ETG structures makes this kind of turbulence more robust with respect to global effects due to background profile variation or drive modulation due to coexisting large-scale turbulence.

CONCLUSIONS

The primary goal of the studies presented in this thesis was to examine the physics of plasma turbulence in transport barriers, which provide substantial improvements to both energy and particle confinement in modern fusion experiments. The description and control of transport barriers is thus a key physics problem on the way to the efficient operation of future fusion power plants. In the present thesis, transport barrier discharges of two different experiments were examined in detail in the framework of gyrokinetics, which is regarded as the most complete physics model of low-frequency dynamics in magnetized plasmas. The gyrokinetic equations were derived and discussed, and their implementation in the plasma microturbulence code GENE was described in detail. This code was then applied to discharges of the TCV tokamak exhibiting a core transport barrier, as well as to a discharge of the ASDEX Upgrade tokamak featuring an edge transport barrier. The main aspects of this work are described in the following.

7.1 SUMMARY

CODE DEVELOPMENT

During the present thesis work, the plasma microturbulence code GENE was enhanced with several features, greatly improving the ability of the code to describe plasma turbulence in transport barriers. The nonlinear terms in the global version of the code are now discretized using a conservative Arakawa scheme, enabling stable nonlinear saturation even without artificial dissipation in the plane perpendicular to the magnetic field. In simulations which take into account kinetic electrons, the particle transport due to $E \times B$ advection becomes finite, requiring the inclusion of a particle source in order to maintain the initial density profile. Therefore, two different types of Krook-type particle sources have been implemented. The first one is coupled to the Krook-type heat source, so that the energy introduced by the particle source is removed again by the heat source. This approach thus provides separate knobs to adjust particle and heat sources. The second type of particle source is simpler, but introduces finite energy to the plasma. Both of these sources are constructed such that the introduction of artificial fields is avoided and that the overall parallel momentum is conserved.

A significant improvement to both local and global simulations was achieved by including an interface to the widely-used EFIT G-EQDSK files. These contain a spatially resolved grid of the poloidal flux, along with profiles of the current and the safety factor. From this information, the metric coefficients which enter the gyrokinetic equations are generated via a field-line tracing approach. This approach, which is implemented in both the TRACER [56] and GIST [55] codes, was integrated directly into GENE, making the user interface very convenient and enabling at the same time also global simulations with realistic tokamak geometry.

As the physics of transport barriers is intimately related to the shape and the current profile of the plasma, measures were taken to overcome the challenges arising from the geometry of the background field. In order to deal with strongly sheared fields, the shifted metric approach was implemented for use in the global code. This scheme employs an alternative definition of the binormal coordinate, which results in an orthogonalization of the perpendicular grid, yielding resolution savings in the case of strong magnetic shear. For strongly shaped plasmas, an optimized definition of the parallel coordinate was devised, which provides a more even grid point distribution at the plasma edge and thus provides significant resolution savings for the turbulence studies in the present thesis.

A further important feature required for many studies of realistic experimental cases is the consideration of sheared flows of the background plasma. These terms, which use a low-Mach-number ordering and consider both the perpendicular and parallel components of a sheared toroidal rotation of the plasma in a co-moving frame, were included into GENE during this work.

GLOBAL SIMULATIONS OF ELECTRON ITB PLASMAS

Using these improvements, the GENE code was employed to perform the most comprehensive simulations to date of electron internal transport barriers (eITB), which exhibit steep gradients in both the electron temperature and density, yielding improved confinement properties in a significant part of the plasma volume. Two separate discharges were studied, which differed in the character of their plasma current profile. The first discharge had pronounced negative magnetic shear in the plasma core, and a very steep eITB, while the second one had a monotonic q -profile (with positive magnetic shear) and reduced confinement.

At the nominal parameters, all examined cases exhibited linearly unstable ETG instabilities at the smallest scales, which were found to persist also in nonlinear simulations. For the dataset with the steepest profiles, due to the presence of the ETGs it was impossible to achieve a converged simulation of ion-scale turbulence, unless an artificial damping term was applied to suppress the small scale turbulence, indicating that ETGs are not negligible. Simulations of pure ETG turbulence then revealed that when sufficiently resolved, ETG turbulence can generate enough heat flux to easily explain the experimental values present in the barrier. In all examined cases, the large-scale TEM turbulence remained important, but 40 % of the electron heat flux obtained for the most realistic dataset stemmed from

ETG turbulence. This situation was found to be robust with respect to changes in the profiles and the impurity content, leading to the conclusion that electron-scale turbulence is a crucial component of turbulence in internal transport barriers.

ETG TURBULENCE IN THE PLASMA EDGE

These studies were then extended to edge transport barriers, focusing on a local description of instabilities and turbulence in the edge of an ASDEX Upgrade H-mode discharge. In linear simulations, it was again found that an ETG instability dominates a large part of the spectrum, while the largest scales are close to the threshold of kinetic ballooning modes, in agreement with common models for edge localized modes (ELMs). The strong shaping of the plasma, in concert with the steep background gradients, leads to a strong parallel localization of the linear instabilities, allowing for unusual spatial mode structures and placing high resolution requirements on numerical simulations. These requirements were subsequently examined in a detailed nonlinear convergence study, proving the validity of the numerical description.

Low ion temperature and the presence of impurities provide, as in the ITB simulations, a stabilizing influence on ETG turbulence, which was examined in the framework of adiabatic ion simulations. For experimentally relevant impurity concentrations and ion temperatures, the ETG-driven transport remained at significant levels.

Varying the radial position about the initially studied flux surface, it was found that, even though radially elongated streamers are absent, ETG turbulence can generate a significant fraction of the electron heat transport across the entire edge region. Towards the lower part of the pedestal, some decrease in the heat flux was found, indicating the possibility that other turbulence mechanisms take over at the foot of the edge transport barrier, where the transition to 'open' field lines intersecting with material plates occurs.

7.2 OUTLOOK

The prominent role of ETG turbulence in both edge and core transport barriers raises the question of how the ion and electron scales interact in such situations. This question can, in principle, be answered by means of simulations involving both spatial scales at the same time, but these are very challenging computationally and beyond the scope of the present thesis. To further increase the accuracy of transport predictions for eITBs, ion temperature profile and rotation measurements (which were not available for the discharges studied here) should be included in future studies. With this additional information, it would also be feasible to conduct a global study of particle flux properties in eITB plasmas, which could provide an important verification of the existing local quasilinear picture of the density barrier.

With regard to edge transport barriers, global studies are required to clarify the role of large-scale turbulence in the pedestal. In the present thesis, ETG turbulence was shown to be a viable candidate for explaining the electron thermal transport in the edge, but the particle fluxes generated by this kind of turbulence were much smaller than the experimental observations, indicating the presence of residual large-scale transport. Such a study could provide further insight into the turbulence mechanisms in the edge, and yield a valuable contribution to the predictions of pedestal heights and widths of future large fusion experiments like ITER and DEMO.

Such applications of GENE to transport barriers would also benefit from the inclusion of induced rotation effects and a momentum source into the global equations. To this aim, it would be advantageous to remain in the laboratory frame, as there is no preferred co-moving frame in the global case. The equilibrium electrostatic potential must then be retained in the equations, and modifications to the equations would arise in the case of large angular velocities.

Apart from the tokamak studies in this thesis, GENE is also being applied successfully to stellarator experiments. In order to treat the intrinsic non-axisymmetry of these devices, the code has been extended (partially as a spin-off of this thesis project) with the capability to treat the variation of the magnetic geometry on a flux surface, while remaining local in the radial direction. By making the radial and binormal directions interchangeable in the source code, this '*y*-global' version of the code uses the same numerical schemes as its radially global counterpart used in the present thesis.

A

REMARKS ON CURVILINEAR GEOMETRY

The purpose of the present appendix is to give the reader an overview about some subtleties that arise when describing physics in a curvilinear coordinate system. In such a system, the length as well as the orientation of the basis vectors are allowed to vary spatially, which has to be taken into account when expanding the vector operators appearing in physical equations. A detailed introduction to curvilinear coordinates including applications to fusion research can be found in Ref. [24].

In orthonormal coordinates, a vector v can be decomposed in terms of the coordinate basis vectors as

$$v = v_i \hat{i} + v_j \hat{j} + v_k \hat{k},$$

where i, j, k are the coordinate directions of the three-dimensional physical space we consider here. In contrast to this well-known case, the basis vectors of a curvilinear coordinate system are in general neither orthogonal nor unit vectors, and every vector v can be expanded in two different sets of basis vectors known as co- and contravariant basis vectors. These expansions are given by

$$\begin{aligned} v &= v_i e^i + v_j e^j + v_k e^k \\ v &= v^i e_i + v^j e_j + v^k e_k. \end{aligned}$$

Here, quantities with subscripts are referred to as *covariant* components or basis vectors, and quantities with superscripts are their *contravariant* counterparts. The two kinds of basis vectors are defined as

$$\begin{aligned} e^\mu &= \nabla u^\mu & (\mu = i, j, k) \\ e_\mu &= \frac{\partial \mathbf{R}}{\partial u^\mu} \end{aligned} \tag{A.1}$$

with the position vector \mathbf{R} and the coordinates u^μ , and they fulfill the relationship

$$e^\mu \cdot e_\nu = \delta_\nu^\mu, \tag{A.2}$$

where δ_ν^μ is the Kronecker delta. The co- and contravariant *metric coefficients* of the coordinate system are defined by the scalar products of the basis vectors

$$g^{\mu\nu} = e^\mu \cdot e^\nu, \quad g_{\mu\nu} = e_\mu \cdot e_\nu.$$

The covariant elements can be obtained via inversion of the contravariant metric tensor

$$(g_{\mu\nu}) = J^2 \begin{pmatrix} g^{yy}g^{zz} - (g^{yz})^2 & g^{xz}g^{yz} - g^{xy}g^{zz} & g^{xy}g^{yz} - g^{xz}g^{yy} \\ g^{xz}g^{yz} - g^{xy}g^{zz} & g^{xx}g^{zz} - (g^{xz})^2 & g^{xy}g^{xz} - g^{xx}g^{yz} \\ g^{xy}g^{yz} - g^{xz}g^{yy} & g^{xy}g^{xz} - g^{xx}g^{yz} & g^{xx}g^{yy} - (g^{xy})^2 \end{pmatrix}.$$

In the last equation, we have introduced the Jacobian determinant, which is defined as

$$J = [\det(g^{\mu\nu})]^{-1/2} = [\det(g_{\mu\nu})]^{1/2}.$$

The elements of the covariant metric tensor are also the source of the abbreviations γ_1 , γ_2 and γ_3 which appear as a result of vector analytical operators in the gyrokinetic equation. These expressions are given by

$$\begin{aligned} \gamma_1 &= J^{-2}g_{zz} \\ \gamma_2 &= -J^{-2}g_{yz} \\ \gamma_3 &= J^{-2}g_{xz}. \end{aligned}$$

By expressing any vector relations appearing in the physical equations using the above introduced formalism, the computation can be carried out in any coordinate system, provided that its metric tensor is given.

A.1 FIELD-ALIGNED COORDINATES

For our purposes, we employ a set of coordinates constructed such that one of the coordinates is aligned with the background magnetic field, while the other two describe the physics governing the perpendicular dynamics. Usually, a Clebsch-coordinate setup is chosen, where the magnetic field can be written as

$$\mathbf{B} = \mathcal{C} \nabla x \times \nabla y,$$

where \mathcal{C} is radially dependent and x and y are the perpendicular coordinates. In GENE, these coordinates are usually defined as

$$\begin{aligned} x &= \rho \\ y &= C_y (q(\rho)\theta - \zeta) \\ z &= \theta, \end{aligned} \tag{A.3}$$

where ρ is a flux surface label, θ the straight field line angle, ζ the toroidal angle and $C_y = \rho_0/q_0$ is a constant length, so that \mathcal{C} has the dimension of a magnetic field. Several types of geometry are available in GENE:

- Slab geometry (i.e. with a homogeneous background field) is used for astrophysical applications and for comparisons to analytical results.

- The $s\text{-}\alpha$ model [51] is used for basic turbulence studies in a toroidal plasma with circular cross-section and Shafranov shift.
- The *circular* model, also used for basic turbulence studies, corrects the $\mathcal{O}(r/R)$ inconsistencies present in $s\text{-}\alpha$ geometry [50], neglects, however, Shafranov shift effects.
- Interfaces to the CHEASE, EFIT, GIST and TRACER codes allow studies with numerically generated MHD equilibria, which are themselves derived from experimental measurements.

For each of these geometry types, ρ can represent different radial coordinates. For the circular geometries, the minor radius r is used, while for the numerical interfaces $\rho = \rho_{\text{tor}}$ is the usual choice (while others are possible). In the $s\text{-}\alpha$ model, the straight field line angle is approximated with the elementary poloidal angle, and in the interface to TRACER, a different parallel coordinate $z = \zeta/q_0$ is used.

A.2 VISUALIZING CURVILINEAR GEOMETRY

As has been discussed in the last section, there are two sets of basis vectors in curvilinear coordinates, which have very different meanings. In the present section, we will try to give a clear and simple picture of this distinction, as well as its application to magnetic field geometry.

From Eq. A.1, we can see that a contravariant basis vector e^μ is defined as the gradient of the coordinate u^μ . By definition of the gradient vector, this basis vector points into the direction of most strongly increasing u^μ , i.e. it is perpendicular on the surface $u^\mu = \text{const}$. On the other hand, the covariant basis vector e_μ is defined by a derivative with respect to u^μ , keeping the other coordinates fixed. Therefore, e_μ defines the coordinate line of u^μ .

In Fig. 75, the surfaces where $\rho_{\text{tor}} = \text{const}$ (corresponding to the flux surfaces that make up the radial grid in GENE) and the coordinate lines of the same coordinate are shown. The covariant basis vector e_ρ thus follows the black dashed lines, while the contravariant one e^ρ is perpendicular to the flux surfaces. As the figure shows, in general these vectors do not point in the same direction, underlining the necessity to carefully distinguish both kinds of vectors. Taking the above statements into account, a vector describing a displacement in field-aligned coordinates is locally (at a position x_0) decomposed in terms of the *covariant* basis as

$$\Delta x = \Delta x e_x + \Delta y e_y + \Delta z e_z.$$

When covering larger distances (e.g. in the radial direction for global simulations), the variation of the basis vectors must be considered.

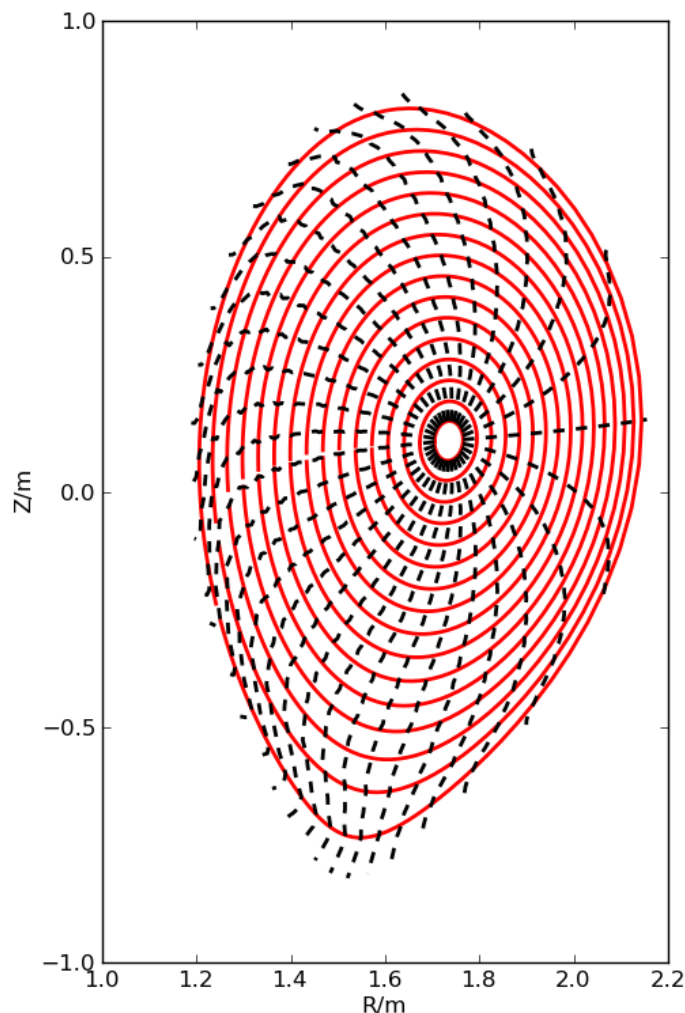


Figure 75: Poloidal projection of $\rho_{\text{tor}} = \text{const}$ surfaces (solid red lines) and ρ_{tor} coordinate lines (dashed black lines) for various parallel positions in an ASDEX Upgrade discharge.

A.3 DEFINITION OF WAVENUMBERS

In the turbulence literature, terms referring to spatial quantities extracted from numerical codes are sometimes used in a rather confusing way. For instance, the wavenumber k_y is referred to as poloidal, toroidal or perpendicular wavenumber. Strictly speaking, all of these terms are imprecise, since the physical wavenumber represented by a certain k_y value depends on the spatial position. While this is usually no problem in simple analytical geometry models, the situation becomes more complex when introducing realistic geometry. In this section, an attempt is made to clarify the relationship in general geometry.

We start from the mathematical origin of wavenumbers, the gradient vector, which is given in three-dimensional curvilinear coordinates by

$$\nabla = e^x \frac{\partial}{\partial x} + e^y \frac{\partial}{\partial y} + e^z \frac{\partial}{\partial z}.$$

When representing the perpendicular plane in Fourier space, the perpendicular part of the gradient operator is replaced by the respective wavenumber vector, which is given by

$$\mathbf{k}_\perp = e^x k_x + e^y k_y.$$

The *perpendicular wavenumber* is therefore $k_\perp = |\mathbf{k}_\perp|$ and contains contributions of both perpendicular directions. Note also that the position vector is defined in terms of the coordinates and the *covariant* basis vectors, whereas the wavenumber vector is defined in terms of the wavenumbers and the *contravariant* basis vectors. It is, of course, possible to expand both vectors in both sets of basis vectors, but the above expansions are the natural ones.

For analysis of the turbulent wavenumber spectra, it is useful to be able to separate the radial and binormal contributions to k_\perp . In order to derive the physically measurable wavenumbers in these directions, we can calculate the projections of \mathbf{k}_\perp onto the orthonormal perpendicular basis vectors \hat{e}_1 and \hat{e}_2 (see also Sec. 3.3)

$$\begin{aligned}\hat{e}_1 &= \hat{e}^x = \frac{e^x}{\sqrt{g^{xx}}} \\ \hat{e}_2 &= \widehat{\hat{b} \times \hat{e}_1} = \frac{1}{\sqrt{\gamma_1 g^{xx}}} (\hat{e}^y g^{xx} - \hat{e}^x g^{xy}),\end{aligned}$$

with $\gamma_1 = g^{xx} g^{yy} - (g^{xy})^2$. The projections of \mathbf{k}_\perp onto these vectors are then given by

$$\begin{aligned}k_1 &= \mathbf{k}_\perp \cdot \hat{e}_1 = \frac{1}{\sqrt{g^{xx}}} (k_x g^{xx} + k_y g^{xy}) \\ k_2 &= \mathbf{k}_\perp \cdot \hat{e}_2 = \sqrt{\frac{\gamma_1}{g^{xx}}} k_y = \sqrt{\frac{g^{xx} g^{yy} - (g^{xy})^2}{g^{xx}}} k_y.\end{aligned}$$

The above equations demonstrate that when a specific k_y wavenumber is prescribed for a simulation, depending on the position in the plasma, the wavenumber k_2 *actually* studied is modified by the magnetic field geometry. For traditional $s - \alpha$ geometry, this metric prefactor reduces to 1, and k_y remains unmodified.

On the other hand, the value of k_1 —which is the physical radial wavenumber—is determined by *both* wavenumber components of \mathbf{k}_\perp , which can turn out to be a rather undesirable property: In a sheared magnetic field, g^{xy} has a secular parallel dependence, and the radial wavenumbers k_1 that are actually represented by a set of (k_x, k_y) modes therefore also depend secularly on the parallel position. For strongly sheared magnetic fields as they are encountered in the plasma edge, this behavior can under certain circumstances lead to resolution problems. In such cases, the shifted metric treatment can be introduced, removing the secular metric dependence (see Ref. [57], and also Sec. 4.2).

To find the poloidal and toroidal wavenumbers, we calculate the projections of the gradient operator onto the poloidal and toroidal unit vectors. The unnormalized versions of the latter are given by

$$\begin{aligned}\mathbf{e}_\zeta &= -C_y \mathbf{e}_y \\ \mathbf{e}_\theta &= qC_y \mathbf{e}_y + \mathbf{e}_z,\end{aligned}$$

which can be found by taking

$$\mathbf{R} = R\mathbf{e}_R + Z\mathbf{e}_Z + x\mathbf{e}_x + y\mathbf{e}_y + z\mathbf{e}_z$$

as the position vector. Here, the first two terms define a point of interest in the plasma in cylindrical coordinates (R, Z) (see also Figure. 75), while the last three terms describe small displacements from (R, Z) in the directions of the local basis vectors. Taking derivatives of \mathbf{R} with respect to ζ and θ (keeping the cylindrical terms and the basis vectors fixed, and using Eq. A.3) gives the above toroidal and poloidal basis vectors. Projecting their normalized versions onto the gradient operator, we arrive at

$$\begin{aligned}\hat{\mathbf{e}}_\zeta \cdot \nabla &= -\hat{\mathbf{e}}_y \cdot \nabla = -\frac{1}{\sqrt{g_{yy}}} \frac{\partial}{\partial y} \\ \hat{\mathbf{e}}_\theta \cdot \nabla &= \frac{1}{|\mathbf{e}_\theta|} \left(qC_y \frac{\partial}{\partial y} + \frac{\partial}{\partial z} \right) \approx \frac{qC_y}{|\mathbf{e}_\theta|} \frac{\partial}{\partial y}.\end{aligned}$$

In the last step, the parallel derivative was dropped due to the parallel wavenumber ordering. Using $g_{yy}^{-1/2} = C_y/R$, the conversion of wavenumbers is given by

$$\begin{aligned}k_\zeta &= -\frac{C_y}{R} k_y \\ k_\theta &= \frac{qC_y}{|\mathbf{e}_\theta|} k_y = \frac{qC_y}{\sqrt{q^2 C_y^2 g_{yy} + 2qC_y g_{yz} + g_{zz}}} k_y,\end{aligned}$$

with the norm of e_θ given explicitly in the last equation. Obviously, the toroidal wavenumber has a rather direct relation to the binormal one, as it is only scaled by a constant factor and the major radius. The conversion from k_y to the poloidal wavenumber, on the other hand, contains the more complex variation of the basis vector along the straight field line angle direction, which is affected by shaping. In summary, since there are also shaping terms in the conversion to k_2 (the physical binormal wavenumber), the most direct relationship of k_y is to the toroidal wavenumber. Their actual values can still differ significantly, as $C_y/R = \rho_0/Rq_0 \approx \epsilon/q_0$, with the inverse aspect ratio ϵ . Therefore, in the very core, C_y/R is small due to the small inverse aspect ratio, while towards the edge, the safety factor can take rather large values.

B

GENE LAUNCHER TOOL

Besides the aim to use and improve the physical capabilities of the GENE code, considerable effort was also dedicated during this thesis work to making the code more easily accessible to the user. While GENE is readily portable to many platforms, its increasing physical capabilities also make the user access increasingly complex, so that there are many pitfalls in setting up the input parameters, which GENE itself can only detect when it is executed. Therefore, errors in the parameters are often only noticed after hours or even days of waiting in a queue. To improve this situation, a graphical launcher tool (which can be found in the GENE root directory under the name '`GENE-GUI.py`') has been created, which can be used to set up the input parameters for GENE and perform plausibility checks to ensure robust operation.

The tool itself is written in the PYTHON 2.x language [118], which is a portable script language that is available on many high-performance computers and otherwise can be easily installed by the user. The graphical interface is implemented using the TKINTER toolkit, which is of limited optical appeal, but also readily available since it is contained in the standard PYTHON distribution.

The launcher tool includes many hard-wired parameter options (and plausibility checks for these), but also allows the user to define custom parameters. Up to five (in the default Launcher setup) GENE runs can be managed at the same time, and one-click-submission of the runs to the batch queue is possible on all machines, using a template submit script. Figs. 76 and 77 show screenshots of the standard launcher window and the profile setup window that is available for global simulations. Further information on the usage of the launcher tool can be found in the GENE documentation [119].

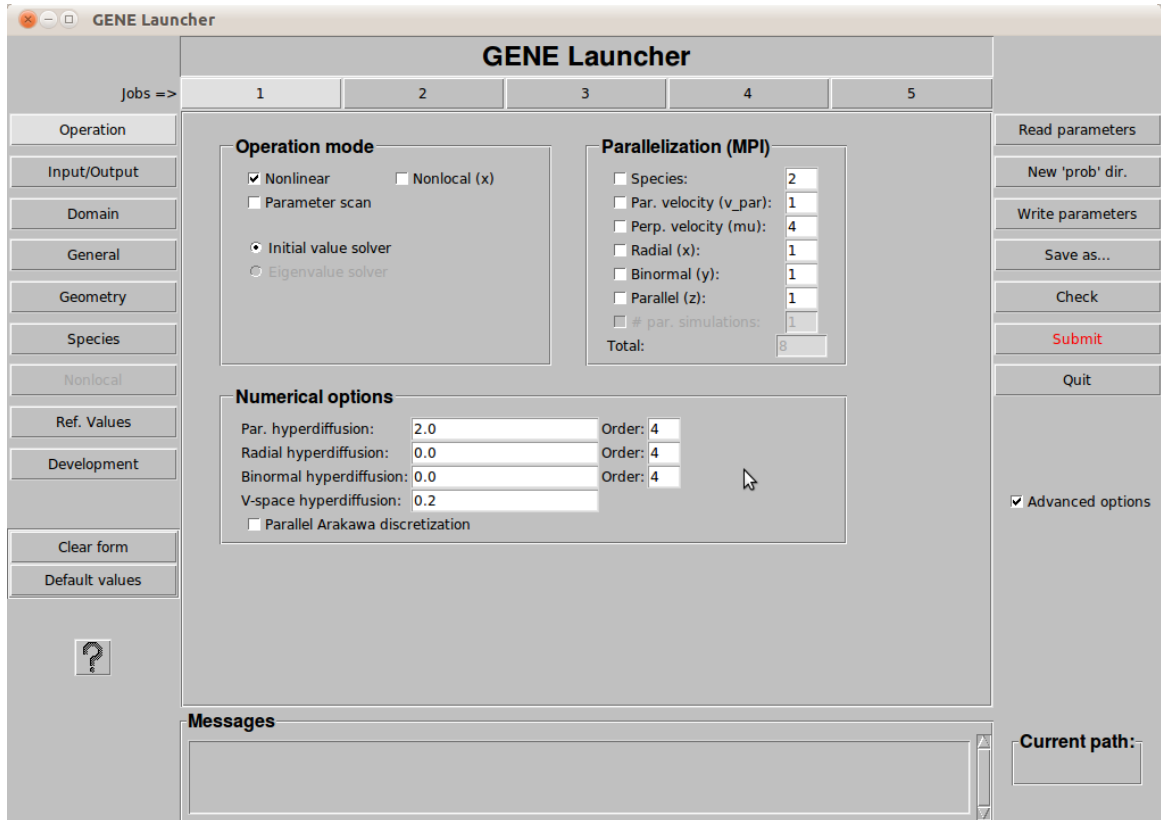


Figure 76: Screenshot of the GENE launcher tool.

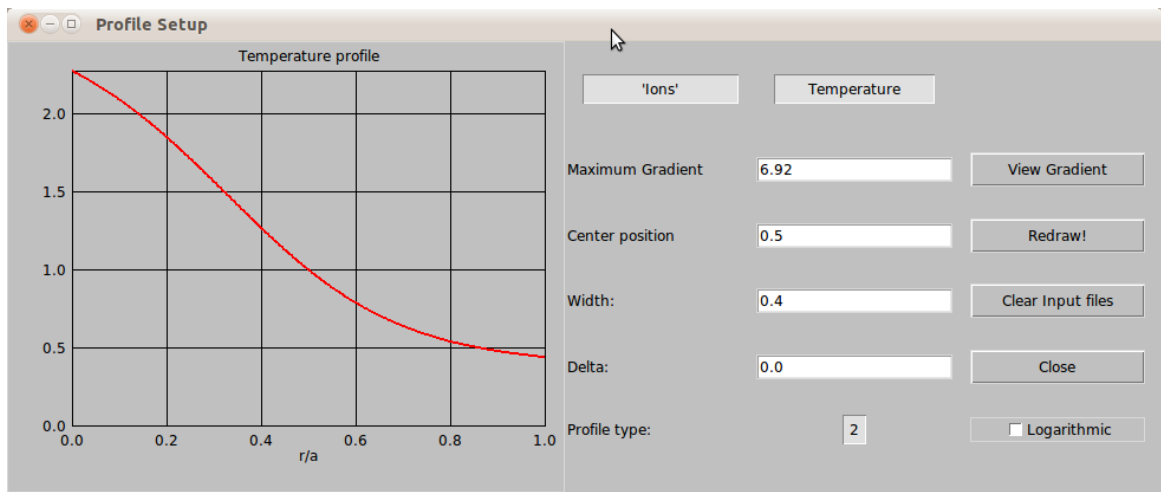


Figure 77: Setup of temperature and density profiles for global simulations in the GENE launcher.

BIBLIOGRAPHY

- [1] G. Audi, O. Bersillon, J. Blachot, and A. H. Wapstra. The Nubase evaluation of nuclear and decay properties. *Nuclear Physics A*, 729:3–128, December 2003. doi: [10.1016/j.nuclphysa.2003.11.001](https://doi.org/10.1016/j.nuclphysa.2003.11.001). (Cited on page 2.)
- [2] A. M. Bradshaw, T. Hamacher, and U. Fischer. Is nuclear fusion a sustainable energy form? *Fusion Engineering and Design*, 86(9-11):2770 – 2773, 2011. doi: [10.1016/j.fusengdes.2010.11.040](https://doi.org/10.1016/j.fusengdes.2010.11.040). (Cited on page 2.)
- [3] David Maisonnier, Iau Cook, Sardain Pierre, Boccaccini Lorenzo, Di Pace Luigi, Giancarli Luciano, Norajitra Prachai, and Pizzuto Aldo. Demo and fusion power plant conceptual studies in europe. *Fusion Engineering and Design*, 81(8-14):1123 – 1130, 2006. doi: [10.1016/j.fusengdes.2005.08.055](https://doi.org/10.1016/j.fusengdes.2005.08.055). (Cited on page 3.)
- [4] F. Wagner, G. Becker, K. Behringer, D. Campbell, A. Eberhagen, W. Engelhardt, G. Fussmann, O. Gehre, J. Gernhardt, G. V. Gierke, G. Haas, M. Huang, F. Karger, M. Keilhacker, O. Klüber, M. Kornherr, K. Lackner, G. Lisitano, G. G. Lister, H. M. Mayer, D. Meisel, E. R. Müller, H. Murmann, H. Niedermeyer, W. Poschenrieder, H. Rapp, H. Röhr, F. Schneider, G. Siller, E. Speth, A. Stäbler, K. H. Steuer, G. Venus, O. Vollmer, and Z. Yü. Regime of Improved Confinement and High Beta in Neutral-Beam-Heated Divertor Discharges of the ASDEX Tokamak. *Physical Review Letters*, 49:1408–1412, November 1982. doi: [10.1103/PhysRevLett.49.1408](https://doi.org/10.1103/PhysRevLett.49.1408). (Cited on page 5.)
- [5] F. Wagner. A quarter-century of H-mode studies. *Plasma Physics and Controlled Fusion*, 49:1, December 2007. doi: [10.1088/0741-3335/49/12B/S01](https://doi.org/10.1088/0741-3335/49/12B/S01). (Cited on page 5.)
- [6] R. C. Wolf. Topical Review: Internal transport barriers in tokamak plasmas. *Plasma Physics and Controlled Fusion*, 45:1, January 2003. doi: [10.1088/0741-3335/45/1/201](https://doi.org/10.1088/0741-3335/45/1/201). (Cited on page 6.)
- [7] F. L. Hinton and R. D. Hazeltine. Theory of plasma transport in toroidal confinement systems. *Reviews of Modern Physics*, 48:239–308, April 1976. doi: [10.1103/RevModPhys.48.239](https://doi.org/10.1103/RevModPhys.48.239). (Cited on page 6.)
- [8] Martin Gardner. Mathematical games the fantastic combinations of john conway's new solitaire game "life". *Scientific American*, 223:120–123, 10 1970. URL http://ddi.cs.uni-potsdam.de/HyFISCH/Produzieren/lis_projekt/proj_gamelife/ConwayScientificAmerican.htm. (Cited on page 7.)

- [9] F. F. Chen. *Introduction to Plasma Physics and Controlled Fusion*. Plenum Publishing Corporation, 1984. (Cited on page 9.)
- [10] R. J. Goldston and P. H. Rutherford. *Introduction to plasma physics*. Plasma Physics Series. Institute of Physics Pub., 1995. (Cited on page 9.)
- [11] T. J. M. Boyd and J. J. Sanderson. *The physics of plasmas*. Cambridge University Press, 2003. (Cited on pages 9 and 26.)
- [12] A. J. Brizard. *Nonlinear gyrokinetic Tokamak physics*. PhD thesis, Princeton University, 1990. (Cited on page 10.)
- [13] A. J. Brizard and T. S. Hahm. Foundations of nonlinear gyrokinetic theory. *Reviews of Modern Physics*, 79(2):421, 2007. doi: 10.1103/RevModPhys.79.421. (Cited on pages 10, 17, and 19.)
- [14] H. Goldstein. *Classical mechanics*. Addison-Wesley series in physics. Addison-Wesley Pub. Co., 1980. (Cited on pages 12 and 14.)
- [15] Robert G. Littlejohn. Variational principles of guiding centre motion. *Journal of Plasma Physics*, 29(01):111–125, 1983. doi: 10.1017/S002237780000060X. (Cited on page 14.)
- [16] A. J. Brizard. Nonlinear gyrokinetic Vlasov equation for toroidally rotating axisymmetric tokamaks. *Physics of Plasmas*, 2:459–471, February 1995. doi: 10.1063/1.871465. (Cited on page 14.)
- [17] John R. Cary and Robert G. Littlejohn. Noncanonical hamiltonian mechanics and its application to magnetic field line flow. *Annals of Physics*, 151(1):1 – 34, 1983. doi: DOI:10.1016/0003-4916(83)90313-5. (Cited on page 15.)
- [18] T. S. Hahm, W. W. Lee, and A. Brizard. Nonlinear gyrokinetic theory for finite-beta plasmas. *Physics of Fluids*, 31(7):1940–1948, 1988. doi: 10.1063/1.866641. (Cited on page 16.)
- [19] T. S. Hahm. Nonlinear gyrokinetic equations for tokamak microturbulence. *Physics of Fluids*, 31(9):2670–2673, 1988. doi: 10.1063/1.866544. (Cited on page 16.)
- [20] T. Dannert. *Gyrokinetische Simulation von Plasmaturbulenz mit gefangenen Teilchen und elektromagnetischen Effekten*. PhD thesis, Technische Universität München, 2005. (Cited on pages 17 and 18.)
- [21] F. Jenko. Gyrokinetic theory. Draft, 2005. (Cited on page 18.)
- [22] J. Candy, R. E. Waltz, S. E. Parker, and Y. Chen. Relevance of the parallel nonlinearity in gyrokinetic simulations of tokamak plasmas. *Physics of Plasmas*, 13(7):074501, July 2006. doi: 10.1063/1.2220536. (Cited on page 23.)

- [23] S. Jollet. *Gyrokinetic particle-in-cell global simulations of ion-temperature-gradient and collisionless-trapped-electron-mode turbulence in tokamaks*, PhD Thesis No. 4326. PhD thesis, Ecole Polytechnique Fédérale de Lausanne, 2009. (Cited on page 23.)
- [24] W. D. D'Haeseleer. *Flux Coordinates and Magnetic Field Structure: A Guide to a Fundamental Tool of Plasma Theory*. Springer Verlag, 1991. (Cited on pages 24, 76, and 163.)
- [25] Florian Merz. *Gyrokinetic Simulation of Multimode Plasma Turbulence*. PhD thesis, Universität Münster, 2008. (Cited on pages 26, 32, 33, 37, 43, 44, 46, 50, 137, and 155.)
- [26] T. Görler. *Multiscale Effects in Plasma Microturbulence*. PhD thesis, Universität Ulm, 2009. (Cited on pages 33, 39, 48, 50, 68, 99, 103, and 136.)
- [27] F. Jenko, W. Dorland, M. Kotschenreuther, and B. N. Rogers. Electron temperature gradient driven turbulence. *Physics of Plasmas*, 7:1904–1910, May 2000. doi: 10.1063/1.874014. (Cited on pages 34, 37, 136, and 153.)
- [28] T. Dannert and F. Jenko. Gyrokinetic simulation of collisionless trapped-electron mode turbulence. *Physics of Plasmas*, 12(7):072309, July 2005. doi: 10.1063/1.1947447. (Cited on pages 37 and 109.)
- [29] T. Görler, X. Lapillonne, S. Brunner, T. Dannert, F. Jenko, F. Merz, and D. Told. The global version of the gyrokinetic turbulence code GENE. *Journal of Computational Physics*, 230:7053–7071, August 2011. doi: 10.1016/j.jcp.2011.05.034. (Cited on pages 37, 60, and 99.)
- [30] H. Lederer, R. Hatzky, R. Tisma, A. Bottino, and F. Jenko. Hyperscaling of plasma turbulence simulations in deisa. In *Proceedings of the 5th IEEE workshop on Challenges of large applications in distributed Environments*. ACM Press, New York (2007), 2007. (Cited on page 37.)
- [31] H. Lederer, R. Tisma, R. Hatzky, A. Bottino, and F. Jenko. *Parallel Computing: Architectures, Algorithms and Applications*, volume 15 of *Advances in Parallel Computing*, chapter Application Enabling in DEISA: Petascaling of Plasma Turbulence Codes, page 713. IOS press, 2008. (Cited on page 37.)
- [32] M. A. Beer, S. C. Cowley, and G. W. Hammett. Field-aligned coordinates for nonlinear simulations of tokamak turbulence. *Physics of Plasmas*, 2:2687–2700, July 1995. doi: 10.1063/1.871232. (Cited on pages 38, 76, and 79.)
- [33] X. Lapillonne. *Local and Global Eulerian Gyrokinetic Simulations of Microturbulence in Realistic Geometry with Applications to the TCV Tokamak*. PhD thesis, École Polytechnique Fédérale de Lausanne, 2010. (Cited on pages 39, 43, 48, 49, 57, 58, 68, 99, and 103.)

- [34] M. J. Pueschel, T. Dannert, and F. Jenko. On the role of numerical dissipation in gyrokinetic Vlasov simulations of plasma microturbulence. *Computer Physics Communications*, 181:1428–1437, August 2010. doi: 10.1016/j.cpc.2010.04.010. (Cited on pages 41, 140, and 147.)
- [35] A. Arakawa. Computational Design for Long-Term Numerical Integration of the Equations of Fluid Motion: Two-Dimensional Incompressible Flow. Part I. *Journal of Computational Physics*, 1:119, August 1966. doi: 10.1016/0021-9991(66)90015-5. (Cited on page 42.)
- [36] S. A. Orszag. On the Elimination of Aliasing in Finite-Difference Schemes by Filtering High-Wavenumber Components. *Journal of Atmospheric Sciences*, 28:1074–1074, September 1971. doi: 10.1175/1520-0469(1971)028<1074:OTEAOAI>2.0.CO;2. (Cited on page 43.)
- [37] J. Candy and R. E. Waltz. An Eulerian gyrokinetic-Maxwell solver. *Journal of Computational Physics*, 186:545–581, April 2003. doi: 10.1016/S0021-9991(03)00079-2. (Cited on page 43.)
- [38] G. S. Patterson, Jr. and S. A. Orszag. Spectral Calculations of Isotropic Turbulence: Efficient Removal of Aliasing Interactions. *Physics of Fluids*, 14:2538–2541, November 1971. doi: 10.1063/1.1693365. (Cited on page 44.)
- [39] R. S. Rogallo. Numerical experiments in homogeneous turbulence. *NASA STI/Recon Technical Report N*, 813:31508–+, September 1981. (Cited on page 44.)
- [40] A. M. Dimits, G. Bateman, M. A. Beer, B. I. Cohen, W. Dorland, G. W. Hammett, C. Kim, J. E. Kinsey, M. Kotschenreuther, A. H. Kritz, L. L. Lao, J. Mandrekas, W. M. Nevins, S. E. Parker, A. J. Redd, D. E. Shumaker, R. Sydora, and J. Weiland. Comparisons and physics basis of tokamak transport models and turbulence simulations. *Physics of Plasmas*, 7(3):969–983, 2000. doi: 10.1063/1.873896. (Cited on pages 45, 71, 74, 80, and 125.)
- [41] T. Görler. *Local code observables, GENE documentation*. Max-Planck-Institut für Plasmaphysik, April 2011. (Cited on page 54.)
- [42] B. F. McMillan, S. Jolliet, T. M. Tran, L. Villard, A. Bottino, and P. Angelino. Long global gyrokinetic simulations: Source terms and particle noise control. *Physics of Plasmas*, 15(5):052308, 2008. doi: 10.1063/1.2921792. (Cited on page 57.)
- [43] B. F. McMillan. Private communication. (Cited on page 59.)
- [44] Y. Sarazin, V. Grandgirard, J. Abiteboul, S. Allfrey, X. Garbet, P. Ghendrih, G. Latu, A. Strugarek, and G. Dif-Pradalier. Large scale dynamics in flux driven gyrokinetic turbulence. *Nuclear Fusion*, 50(5):054004–+, May 2010. doi: 10.1088/0029-5515/50/5/054004. (Cited on page 60.)

- [45] F. I. Parra and P. J. Catto. Limitations of gyrokinetics on transport time scales. *Plasma Physics and Controlled Fusion*, 50(6):065014–+, June 2008. doi: 10.1088/0741-3335/50/6/065014. (Cited on page 60.)
- [46] F. I. Parra and I. Calvo. Phase-space Lagrangian derivation of electrostatic gyrokinetics in general geometry. *Plasma Physics and Controlled Fusion*, 53(4):045001–+, April 2011. doi: 10.1088/0741-3335/53/4/045001. (Cited on page 60.)
- [47] G. W. Hammett, W. Dorland, N. F. Loureiro, and T. Tatsuno. Implementation of Large Scale $E \times B$ Shear Flow in the GS2 Gyrokinetic Turbulence Code. *APS Meeting Abstracts*, pages 1136P–+, October 2006. (Cited on page 61.)
- [48] J. E. Kinsey, R. E. Waltz, and J. Candy. Nonlinear gyrokinetic turbulence simulations of $E \times B$ shear quenching of transport. *Physics of Plasmas*, 12(6):062302, 2005. doi: 10.1063/1.1920327. (Cited on page 63.)
- [49] F. J. Casson, A. G. Peeters, Y. Camenen, W. A. Hornsby, A. P. Snodin, D. Strintzi, and G. Szepesi. Anomalous parallel momentum transport due to $E \times B$ flow shear in a tokamak plasma. *Physics of Plasmas*, 16(9):092303–+, September 2009. doi: 10.1063/1.3227650. (Cited on page 63.)
- [50] X. Lapillonne, S. Brunner, T. Dannert, S. Jollet, A. Marinoni, L. Villard, T. Görler, F. Jenko, and F. Merz. Clarifications to the limitations of the s-alpha equilibrium model for gyrokinetic computations of turbulence. *Physics of Plasmas*, 16(3):032308, 2009. doi: 10.1063/1.3096710. (Cited on pages 64, 67, 71, and 165.)
- [51] J. W. Connor, R. J. Hastie, and J. B. Taylor. Shear, periodicity, and plasma ballooning modes. *Phys. Rev. Lett.*, 40(6):396–399, Feb 1978. doi: 10.1103/PhysRevLett.40.396. (Cited on pages 67 and 165.)
- [52] R. L. Miller, M. S. Chu, J. M. Greene, Y. R. Lin-Liu, and R. E. Waltz. Non-circular, finite aspect ratio, local equilibrium model. *Physics of Plasmas*, 5(4):973–978, 1998. doi: 10.1063/1.872666. (Cited on page 67.)
- [53] H. Lütjens, A. Bondeson, and O. Sauter. The chease code for toroidal mhd equilibria. *Computer Physics Communications*, 97(3):219 – 260, 1996. doi: DOI: 10.1016/0010-4655(96)00046-X. (Cited on pages 67 and 71.)
- [54] L. L. Lao, H. St. John, R. D. Stambaugh, A. G. Kellman, and W. Pfeiffer. Reconstruction of current profile parameters and plasma shapes in tokamaks. *Nuclear Fusion*, 25(11):1611, 1985. (Cited on page 67.)
- [55] P. Xanthopoulos, W. A. Cooper, F. Jenko, Yu. Turkin, A. Runov, and J. Geiger. A geometry interface for gyrokinetic microturbulence investigations in toroidal configurations. *Physics of Plasmas*, 16(8):082303, 2009. doi: 10.1063/1.3187907. (Cited on pages 67 and 160.)

- [56] P. Xanthopoulos and F. Jenko. Clebsch-type coordinates for nonlinear gyrokinetics in generic toroidal configurations. *Physics of Plasmas*, 13(9):092301, 2006. doi: 10.1063/1.2338818. (Cited on pages 67, 68, 69, and 160.)
- [57] B. Scott. Shifted metric procedure for flux tube treatments of toroidal geometry: Avoiding grid deformation. *Physics of Plasmas*, 8(2):447–458, 2001. doi: 10.1063/1.1335832. (Cited on pages 67, 76, 78, 79, 80, 81, 83, and 168.)
- [58] A. Burckel, O. Sauter, C. Angioni, J. Candy, E. Fable, and X. Lapillonne. On the effects of the equilibrium model in gyrokinetic simulations: from $s-\alpha$ to diverted MHD equilibrium. *Journal of Physics Conference Series*, 260(1): 012006–+, November 2010. doi: 10.1088/1742-6596/260/1/012006. (Cited on pages 71 and 74.)
- [59] O. Sauter. Benchmark for gyrokinetic codes with kinetic electrons and mhd equilibrium, August 2011. URL <https://crppwww.epfl.ch/~sauter/benchmark/>. (Cited on page 71.)
- [60] D. Told and F. Jenko. Applicability of different geometry approaches to simulations of turbulence in highly sheared magnetic fields. *Physics of Plasmas*, 17(4):042302, April 2010. doi: 10.1063/1.3365549. (Cited on page 76.)
- [61] S. C. Cowley, R. M. Kulsrud, and R. Sudan. Considerations of ion-temperature-gradient-driven turbulence. *Physics of Fluids B: Plasma Physics*, 3(10):2767–2782, 1991. doi: 10.1063/1.859913. (Cited on pages 76 and 136.)
- [62] A. Kendl, B. D. Scott, and H. Wobig. LETTER TO THE EDITOR: Transition from tokamak to stellarator turbulence. *Plasma Physics and Controlled Fusion*, 42:L23–L29, November 2000. doi: 10.1088/0741-3335/42/11/101. (Cited on page 77.)
- [63] A. Kendl and B. D. Scott. Magnetic Shear Damping of Dissipative Drift Wave Turbulence. *Physical Review Letters*, 90(3):035006–+, January 2003. doi: 10.1103/PhysRevLett.90.035006. (Cited on page 77.)
- [64] M. Kotschenreuther, G. Rewoldt, and W. M. Tang. Comparison of initial value and eigenvalue codes for kinetic toroidal plasma instabilities. *Computer Physics Communications*, 88:128–140, August 1995. doi: 10.1016/0010-4655(95)00035-E. (Cited on page 78.)
- [65] W. Dorland, F. Jenko, M. Kotschenreuther, and B. N. Rogers. Electron temperature gradient turbulence. *Phys. Rev. Lett.*, 85(26):5579–5582, Dec 2000. doi: 10.1103/PhysRevLett.85.5579. (Cited on pages 78 and 136.)
- [66] A. G. Peeters, Y. Camenen, F. J. Casson, W. A. Hornsby, A. P. Snodin, D. Strintzi, and G. Szepesi. The nonlinear gyro-kinetic flux tube code GKW. *Computer Physics Communications*, 180:2650–2672, December 2009. doi: 10.1016/j.cpc.2009.07.001. (Cited on page 78.)

- [67] P. Colella. Multidimensional upwind methods for hyperbolic conservation laws. *Journal of Computational Physics*, 87:171–200, March 1990. doi: 10.1016/0021-9991(90)90233-Q. (Cited on page 81.)
- [68] X. Lapillonne, T. Dannert, S. Brunner, A. Marinoni, S. Jolliet, L. Villard, F. Jenko, T. Goerler, and F. Merz. Effects of geometry on linear and non-linear gyrokinetic simulations, and development of a global version of the GENE code. In O. Sauter, X. Garbet, & E. Sindoni, editor, *American Institute of Physics Conference Series*, volume 1069 of *American Institute of Physics Conference Series*, pages 289–294, November 2008. doi: 10.1063/1.3033716. (Cited on page 83.)
- [69] T. T. Ribeiro and B. D. Scott. Conformal tokamak geometry for turbulence computations. *Plasma Science, IEEE Transactions on*, 38(9):2159 –2168, sept. 2010. ISSN 0093-3813. doi: 10.1109/TPS.2010.2056935. (Cited on page 95.)
- [70] Z. Lin, S. Ethier, T. S. Hahm, and W. M. Tang. Size Scaling of Turbulent Transport in Magnetically Confined Plasmas. *Physical Review Letters*, 88(19):195004–+, May 2002. doi: 10.1103/PhysRevLett.88.195004. (Cited on page 99.)
- [71] J. Candy, R. E. Waltz, and W. Dorland. The local limit of global gyrokinetic simulations. *Physics of Plasmas*, 11:L25–L28, May 2004. doi: 10.1063/1.1695358. (Cited on page 99.)
- [72] B. F. McMillan, X. Lapillonne, S. Brunner, L. Villard, S. Jolliet, A. Bottino, T. Görler, and F. Jenko. System Size Effects on Gyrokinetic Turbulence. *Physical Review Letters*, 105(15):155001–+, October 2010. doi: 10.1103/PhysRevLett.105.155001. (Cited on pages 99, 100, 102, and 126.)
- [73] A. Kallenbach, J. Adamek, L. Aho-Mantila, S. Äkäslompolo, C. Angioni, C. V. Atanasiu, M. Balden, K. Behler, E. Belonohy, A. Bergmann, M. Bernert, R. Bilato, V. Bobkov, J. Boom, A. Bottino, F. Braun, M. Brüdgam, A. Buhler, A. Burckhart, A. Chankin, I. G. J. Classen, G. D. Conway, D. P. Coster, P. de Marné, R. D’Inca, R. Drube, R. Dux, T. Eich, N. Endstrasser, K. Engelhardt, B. Esposito, E. Fable, H.-U. Fahrbach, L. Fattorini, R. Fischer, A. Flaws, H. Fünfgelder, J. C. Fuchs, K. Gál, M. García Muñoz, B. Geiger, M. Gemisic Adamov, L. Giannone, C. Giroud, T. Görler, S. da Graca, H. Greuner, O. Gruber, A. Gude, S. Günter, G. Haas, A. H. Hakola, D. Hangan, T. Happel, T. Hauff, B. Heinemann, A. Herrmann, N. Hicks, J. Hobirk, H. Höhnle, M. Hözl, C. Hopf, L. Horton, M. Huart, V. Igochine, C. Ionita, A. Janzer, F. Jenko, C.-P. Käsemann, S. Kálvin, O. Kardaun, M. Kaufmann, A. Kirk, H.-J. Klingshirn, M. Kocan, G. Kocsis, H. Kollotzek, C. Konz, R. Koslowski, K. Krieger, T. Kurki-Suonio, B. Kurzan, K. Lackner, P. T. Lang, P. Lauber, M. Laux, F. Leipold, F. Leuterer, A. Lohs, N. C. Luhmann, Jr., T. Lunt, A. Lyssoivan, H. Maier, C. Maggi, K. Mank, M.-E. Manso, M. Maraschek, P. Martin, M. Mayer, P. J. McCarthy, R. McDermott, H. Meister, L. Menchero,

- F. Meo, P. Merkel, R. Merkel, V. Mertens, F. Merz, A. Mlynek, F. Monaco, H. W. Müller, M. Münich, H. Murmann, G. Neu, R. Neu, B. Nold, J.-M. Noterdaeme, H. K. Park, G. Pautasso, G. Pereverzev, Y. Podoba, F. Pompon, E. Poli, K. Polochiy, S. Potzel, M. Prechtl, M. J. Püschel, T. Pütterich, S. K. Rathgeber, G. Raupp, M. Reich, B. Reiter, T. Ribeiro, R. Riedl, V. Rohde, J. Roth, M. Rott, F. Ryter, W. Sandmann, J. Santos, K. Sassenberg, P. Sauter, A. Scarabosio, G. Schall, K. Schmid, P. A. Schneider, W. Schneider, G. Schramm, R. Schrittweiser, J. Schweinzer, B. Scott, M. Sempf, F. Serra, M. Sertoli, M. Siccinio, A. Sigalov, A. Silva, A. C. C. Sips, F. Sommer, A. Stäbler, J. Stober, B. Streibl, E. Strumberger, K. Sugiyama, W. Suttrop, T. Szepesi, G. Tardini, C. Tichmann, D. Told, W. Treutterer, L. Urso, P. Varela, J. Vincente, N. Vianello, T. Vierle, E. Viezzzer, C. Vorpahl, D. Wagner, A. Weller, R. Wenninger, B. Wieland, C. Wigger, M. Willensdorfer, M. Wischmeier, E. Wolfrum, E. Würsching, D. Yadikin, Q. Yu, I. Zammuto, D. Zasche, T. Zehetbauer, Y. Zhang, M. Zilker, and H. Zohm. Overview of ASDEX Upgrade results. *Nuclear Fusion*, 51(9):094012, September 2011. doi: [10.1088/0029-5515/51/9/094012](https://doi.org/10.1088/0029-5515/51/9/094012). (Cited on page 99.)
- [74] F. Romanelli, M. Laxåback, and o. b. o. t. JET EFDA Contributors. Overview of JET results. *Nuclear Fusion*, 51(9):094008, September 2011. doi: [10.1088/0029-5515/51/9/094008](https://doi.org/10.1088/0029-5515/51/9/094008). (Cited on page 99.)
- [75] K. Lackner and N. A. O. Gottardi. Tokamak confinement in relation to plateau scaling. *Nuclear Fusion*, 30(4):767, 1990. (Cited on page 99.)
- [76] F. Hofmann, J. B. Lister, W. Anton, S. Barry, R. Behn, S. Bernel, G. Besson, F. Buhlmann, R. Chavan, M. Corboz, M. J. Dutch, B. P. Duval, D. Fasel, A. Favre, S. Franke, A. Heym, A. Hirt, C. Hollenstein, P. Isoz, B. Joye, X. Llobet, J. C. Magnin, B. Marletaz, P. Marmillod, Y. Martin, J. M. Mayor, J. M. Moret, C. Nieswand, P. J. Paris, A. Perez, Z. A. Pietrzyk, R. A. Pitts, A. Pochelon, R. Rage, O. Sauter, G. Tonetti, M. Q. Tran, F. Troyon, D. J. Ward, and H. Weisen. Creation and control of variably shaped plasmas in TCV. *Plasma Physics and Controlled Fusion*, 36:277–+, December 1994. doi: [10.1088/0741-3335/36/12B/023](https://doi.org/10.1088/0741-3335/36/12B/023). (Cited on page 101.)
- [77] O. Sauter, M. A. Henderson, F. Hofmann, T. Goodman, S. Alberti, C. Angioni, K. Appert, R. Behn, P. Blanchard, P. Bosshard, R. Chavan, S. Coda, B. P. Duval, D. Fasel, A. Favre, I. Furno, P. Gorgerat, J.-P. Hogge, P.-F. Isoz, B. Joye, P. Lavanchy, J. B. Lister, X. Llobet, J.-C. Magnin, P. Mandrin, A. Manini, B. Marlétaz, P. Marmillod, Y. Martin, J.-M. Mayor, A. A. Martynov, J. Mlynar, J.-M. Moret, C. Nieswand, P. Nikkola, P. Paris, A. Perez, Z. A. Pietrzyk, R. A. Pitts, A. Pochelon, G. Pochon, A. Refke, H. Reimerdes, J. Rommers, E. Scavino, G. Tonetti, M. Q. Tran, F. Troyon, and H. Weisen. Steady-State Fully Noninductive Current Driven by Electron Cyclotron Waves in a Magnetically Confined Plasma. *Physical Review Letters*, 84:3322–3325, April 2000. doi: [10.1103/PhysRevLett.84.3322](https://doi.org/10.1103/PhysRevLett.84.3322). (Cited on page 101.)

- [78] M. A. Henderson, R. Behn, S. Coda, I. Condrea, B. P. Duval, T. P. Goodman, A. Karpushov, Y. Martin, An. Martynov, J.-M. Moret, P. Nikkola, L. Porte, O. Sauter, A. Scarabosio, G. Zhuang, and the TCV team. Control of electron internal transport barriers in tcv. *Plasma Physics and Controlled Fusion*, 46 (5A):A275, 2004. (Cited on page 101.)
- [79] P. H. Rebut, P. P. Lallia, and M. L. Watkins. In IAEA, editor, *Proc. 12th Int. Conf. on Plasma Physics and Controlled Nuclear Fusion Research (Nice, 1988) vol 2*, page p. 191, 1989. (Cited on page 101.)
- [80] J. Wesson and J. W. Connor. *Tokamaks / John Wesson ; with contributions from J.W. Connor ... [et al.]*. Clarendon Press, Oxford ; New York :, 1987. ISBN 0198563280. (Cited on page 101.)
- [81] O. Sauter, S. Coda, T. P. Goodman, M. A. Henderson, R. Behn, A. Bottino, E. Fable, An. Martynov, P. Nikkola, and C. Zucca. Inductive current density perturbations to probe electron internal transport barriers in tokamaks. *Phys. Rev. Lett.*, 94(10):105002, Mar 2005. doi: 10.1103/PhysRevLett.94.105002. (Cited on pages 101 and 112.)
- [82] C. Zucca, O. Sauter, E. Asp, S. Coda, E. Fable, T. P. Goodman, and M. A. Henderson. Current density evolution in electron internal transport barrier discharges in TCV. *Plasma Physics and Controlled Fusion*, 51(1):015002–+, January 2009. doi: 10.1088/0741-3335/51/1/015002. (Cited on pages 101 and 102.)
- [83] A. Bottino, O. Sauter, Y. Camenen, and E. Fable. Linear stability analysis of microinstabilities in electron internal transport barrier non-inductive discharges. *Plasma Physics and Controlled Fusion*, 48:215–233, February 2006. doi: 10.1088/0741-3335/48/2/004. (Cited on pages 102, 108, and 110.)
- [84] X. Lapillonne, B. F. McMillan, T. Görler, S. Brunner, T. Dannert, F. Jenko, F. Merz, and L. Villard. Nonlinear quasisteady state benchmark of global gyrokinetic codes. *Physics of Plasmas*, 17(11):112321, November 2010. doi: 10.1063/1.3518118. (Cited on page 102.)
- [85] E. Fable, O. Sauter, S. Coda, T. P. Goodman, M. A. Henderson, H. Weisen, A. Zabolotsky, C. Zucca, and The TCV team. Inward thermodiffusive particle pinch in electron internal transport barriers in TCV. *Plasma Physics and Controlled Fusion*, 48:1271–1283, September 2006. doi: 10.1088/0741-3335/48/9/001. (Cited on pages 103 and 110.)
- [86] E. Fable. *Experimental and theoretical study of particle transport in the TCV tokamak*. PhD thesis, Lausanne, 2009. (Cited on pages 103 and 118.)
- [87] F. Merz and F. Jenko. Nonlinear interplay of TEM and ITG turbulence and its effect on transport. *Nuclear Fusion*, 50(5):054005–+, May 2010. doi: 10.1088/0029-5515/50/5/054005. (Cited on pages 103 and 109.)

- [88] C. Angioni, E. Fable, M. Greenwald, M. Maslov, A. G. Peeters, H. Takenaga, and H. Weisen. Particle transport in tokamak plasmas, theory and experiment. *Plasma Physics and Controlled Fusion*, 51(12):124017–+, December 2009. doi: [10.1088/0741-3335/51/12/124017](https://doi.org/10.1088/0741-3335/51/12/124017). (Cited on page [103](#).)
- [89] X. Lapillonne, S. Brunner, O. Sauter, L. Villard, E. Fable, T. Görler, F. Jenko, and F. Merz. Non-linear gyrokinetic simulations of microturbulence in TCV electron internal transport barriers. *Plasma Physics and Controlled Fusion*, 53(5):054011–+, May 2011. doi: [10.1088/0741-3335/53/5/054011](https://doi.org/10.1088/0741-3335/53/5/054011). (Cited on pages [103](#), [110](#), and [118](#).)
- [90] T. Görler, X. Lapillonne, S. Brunner, T. Dannert, F. Jenko, S. K. Aghdam, P. Marcus, B. F. McMillan, F. Merz, O. Sauter, D. Told, and L. Villard. Flux- and gradient-driven global gyrokinetic simulation of tokamak turbulence. *Physics of Plasmas*, 18(5):056103–+, May 2011. doi: [10.1063/1.3567484](https://doi.org/10.1063/1.3567484). (Cited on page [103](#).)
- [91] A. N. Karpushov, B. P. Duval, C. Schlatter, V. I. Afanasyev, and F. V. Chernyshev. Neutral particle analyzer diagnostics on the TCV tokamak. *Review of Scientific Instruments*, 77(3):033504–+, March 2006. doi: [10.1063/1.2185151](https://doi.org/10.1063/1.2185151). (Cited on page [108](#).)
- [92] M. Kammerer, F. Merz, and F. Jenko. Exceptional points in linear gyrokinetics. *Physics of Plasmas*, 15(5):052102, May 2008. doi: [10.1063/1.2909618](https://doi.org/10.1063/1.2909618). (Cited on page [109](#).)
- [93] D. R. Hatch, P. W. Terry, F. Jenko, F. Merz, M. J. Pueschel, W. M. Nevins, and E. Wang. Role of subdominant stable modes in plasma microturbulence. *Physics of Plasmas*, 18(5):055706, May 2011. doi: [10.1063/1.3563536](https://doi.org/10.1063/1.3563536). (Cited on page [109](#).)
- [94] P. B. Snyder, H. R. Wilson, J. R. Ferron, L. L. Lao, A. W. Leonard, T. H. Osborne, A. D. Turnbull, D. Mossessian, M. Murakami, and X. Q. Xu. Edge localized modes and the pedestal: A model based on coupled peeling-ballooning modes. *Physics of Plasmas*, 9:2037–2043, May 2002. doi: [10.1063/1.1449463](https://doi.org/10.1063/1.1449463). (Cited on page [112](#).)
- [95] F. Jenko, T. Dannert, and C. Angioni. Heat and particle transport in a tokamak: advances in nonlinear gyrokinetics. *Plasma Physics and Controlled Fusion*, 47:B195–B206, December 2005. doi: [10.1088/0741-3335/47/12B/S15](https://doi.org/10.1088/0741-3335/47/12B/S15). (Cited on page [125](#).)
- [96] F. Jenko and W. Dorland. Prediction of significant tokamak turbulence at electron gyroradius scales. *Phys. Rev. Lett.*, 89(22):225001, Nov 2002. doi: [10.1103/PhysRevLett.89.225001](https://doi.org/10.1103/PhysRevLett.89.225001). (Cited on pages [125](#) and [136](#).)
- [97] D. Told, F. Jenko, P. Xanthopoulos, L. D. Horton, E. Wolfrum, and ASDEX Upgrade Team. Gyrokinetic microinstabilities in ASDEX Upgrade edge

- plasmas. *Physics of Plasmas*, 15(10):102306, 2008. doi: 10.1063/1.3000132. (Cited on pages 130 and 131.)
- [98] F. Jenko, D. Told, P. Xanthopoulos, F. Merz, and L. D. Horton. Gyrokinetic turbulence under near-separatrix or nonaxisymmetric conditions. *Physics of Plasmas*, 16(5):055901, 2009. doi: 10.1063/1.3089603. (Cited on pages 130 and 131.)
- [99] P. J. McCarthy. The CLISTE interpretive equilibrium code. Technical Report IPP 5/85, IPP Garching, Germany, 1999. (Cited on page 130.)
- [100] F. Jenko, W. Dorland, B. Scott, and D. Strintzi. Simulation and theory of temperature gradient driven turbulence. In SIF, editor, *Theory of Fusion Plasmas*, Bologna, 2002. (Cited on page 135.)
- [101] T. Görler and F. Jenko. Scale separation between electron and ion thermal transport. *Physical Review Letters*, 100(18):185002, 2008. doi: 10.1103/PhysRevLett.100.185002. (Cited on page 136.)
- [102] B. B. Kadomtsev and O. P. Pogutse. Turbulence in Toroidal Systems. In A. M. A. Leontovich, editor, *Reviews of Plasma Physics, Volume 5*, volume 5 of *Reviews of Plasma Physics*, page 249, 1970. (Cited on page 136.)
- [103] C. S. Liu. Instabilities in a Magnetoplasma with Skin Current. *Physical Review Letters*, 27:1637–1640, December 1971. doi: 10.1103/PhysRevLett.27.1637. (Cited on page 136.)
- [104] T. Ohkawa. A transport model for alcator scaling in tokamaks. *Physics Letters A*, 67(1):35 – 38, 1978. ISSN 0375-9601. doi: DOI:10.1016/0375-9601(78)90560-1. (Cited on page 136.)
- [105] J. F. Drake, P. N. Guzdar, and A. B. Hassam. Streamer formation in plasma with a temperature gradient. *Phys. Rev. Lett.*, 61(19):2205–2208, Nov 1988. doi: 10.1103/PhysRevLett.61.2205. (Cited on page 136.)
- [106] Z. Lin, L. Chen, and F. Zonca. Role of nonlinear toroidal coupling in electron temperature gradient turbulence. *Physics of Plasmas*, 12(5):056125, 2005. doi: 10.1063/1.1894766. (Cited on page 136.)
- [107] W. M. Nevins, J. Candy, S. Cowley, T. Dannert, A. Dimits, W. Dorland, C. Estrada-Mila, G. W. Hammett, F. Jenko, M. J. Pueschel, and D. E. Shumaker. Characterizing electron temperature gradient turbulence via numerical simulation. *Physics of Plasmas*, 13(12):122306–+, December 2006. doi: 10.1063/1.2402510. (Cited on page 136.)
- [108] A. Bottino, A. G. Peeters, R. Hatzky, S. Jolliet, B. F. McMillan, T. M. Tran, and L. Villard. Nonlinear low noise particle-in-cell simulations of electron temperature gradient driven turbulence. *Physics of Plasmas*, 14(1):010701–+, January 2007. doi: 10.1063/1.2428280. (Cited on page 136.)

- [109] W. M. Nevins, S. E. Parker, Y. Chen, J. Candy, A. Dimits, W. Dorland, G. W. Hammett, and F. Jenko. Verification of gyrokinetic δf simulations of electron temperature gradient turbulence. *Physics of Plasmas*, 14(8):084501–+, August 2007. doi: 10.1063/1.2759890. (Cited on page 136.)
- [110] A. M. Dimits, W. M. Nevins, D. E. Shumaker, G. W. Hammett, T. Dannert, F. Jenko, M. J. Pueschel, W. Dorland, S. C. Cowley, J. N. Leboeuf, T. L. Rhodes, J. Candy, and C. Estrada-Mila. Gyrokinetic simulations of ETG and ITG turbulence. *Nuclear Fusion*, 47(8):817, 2007. (Cited on page 136.)
- [111] T. Hauff and F. Jenko. Streamer-induced transport in electron temperature gradient turbulence. *Physics of Plasmas*, 16(10):102306–+, October 2009. doi: 10.1063/1.3245163. (Cited on page 136.)
- [112] F. Jenko. On the nature of ETG turbulence and cross-scale coupling. *J. Plasma Fusion Res. Ser.*, 6(11), 2004. (Cited on page 136.)
- [113] F. Jenko and B. D. Scott. Numerical computation of collisionless drift wave turbulence. *Physics of Plasmas*, 6:2418–2424, June 1999. doi: 10.1063/1.873513. (Cited on page 144.)
- [114] M. J. Pueschel. *Electromagnetic Effects in Gyrokinetic Simulations of Plasma Turbulence*. PhD thesis, Westfälische Wilhelms-Universität Münster, 2009. (Cited on page 147.)
- [115] J. D. Callen, R. J. Groebner, T. H. Osborne, J. M. Canik, L. W. Owen., A. Y. Pankin, T. Rafiq, T. D. Rognlien, and W. M. Stacey. Analysis of pedestal plasma transport. *Nuclear Fusion*, 50(6):064004, June 2010. doi: 10.1088/0029-5515/50/6/064004. (Cited on page 151.)
- [116] J. D. Callen. Derivation of paleoclassical key hypothesis. *Physics of Plasmas*, 14(4):040701, April 2007. doi: 10.1063/1.2715564. (Cited on page 151.)
- [117] S. K. Rathgeber, R. Fischer, S. Fietz, J. Hobirk, A. Kallenbach, H. Meister, T. Pütterich, F. Ryter, G. Tardini, E. Wolfrum, and the ASDEX Upgrade Team. Estimation of profiles of the effective ion charge at ASDEX Upgrade with integrated data analysis. *Plasma Physics and Controlled Fusion*, 52(9):095008, 2010. (Cited on page 156.)
- [118] Python Software Foundation. Official python webpage. Electronic webpage, June 2011. URL www.python.org. (Cited on page 171.)
- [119] GENE Development team. *The Gyrokinetic Plasma Turbulence Code GENE: User Manual*. Max-Planck-Institut für Plasmaphysik, release 1.5 edition, 2011 February. (Cited on page 171.)

ACKNOWLEDGMENTS

It is a great pleasure to thank all the people who helped me along the way during my time as a doctoral student. First, I would like to thank my advisor, apl. Prof. Dr. Frank Jenko, for giving me the opportunity to complete both my diploma *and* my doctoral thesis in his group. During these four years at IPP, he was always available for advice and consultation, and his thoughtful guidance was crucial to the success of this work. I am also much indebted to Prof. Dr. Reineker for, once again without hesitation, accepting my thesis for reviewing.

All former and current members of our group, Matthias Kammerer, Florian Merz, Tobias Görler, Moritz Püschel, Thilo Hauff, Klaus Reuter, Mirjam Schneller, Hauke Doerk, Alexander Röder, Christoph Kowitz, Patrick Marcus, Angelo Limone, David Hatch, Alejandro Bañón-Navarro, Michael Oberparleitner, and Vasil Bratanov deserve special thanks for many interesting and compelling discussions, for providing their help on countless occasions, with problems of any imaginable kind, and for making every day at the institute worthwhile.

I am very grateful to Olivier Sauter and Lorne Horton for providing me with the input data used for the simulations in Chapters 5 and 6, along with their time for lengthy discussions about the data and their interpretation. The same is true for Elisabeth Wolfrum, Andreas Burckhart, Josef Schweinzer and Giovanni Tardini, but for projects that are not touched upon in this thesis. I would also like to thank our collaborators at the CRPP Lausanne, especially Stephan Brunner, for many helpful suggestions and discussions.

I would like to acknowledge the people at the Rechenzentrum Garching, especially Klaus Reuter, Tilman Dannert, and Ingeborg Weidl, for providing quick and competent solutions to any kind of computer problems that can appear during or at the very end of a PhD student's lifetime.

Many thanks go also to my careful proofreaders Tobias, David and Hauke, without whose countless suggestions and corrections this thesis would be much less readable.

Finally, I am very much indebted to my love, Sabrina, for staying at my side and continuously supporting me during the most important, laborious, but also rewarding time of my life.